Detection of high-energy transients with SVOM-ECLAIRs

Benjamin Arcier

THÈSE

En vue de l'obtention du

DOCTORAT DE L'UNIVERSITÉ DE TOULOUSE

Délivré par : *l'Université Toulouse 3 Paul Sabatier (UT3 Paul Sabatier)*

Présentée et soutenue le *07/10/2022* **par :**

Benjamin ARCIER

Detection of high-energy transients with SVOM/ECLAIRs

JURY

Jean-Luc ATTEIA	Astronome	Directeur de thèse
Giulia STRATTA	Chercheuse	Rapportrice
Bertrand CORDIER	Directeur de Recherche	Rapporteur
Jean-François OLIVE	Professeur d'Université	Président du Jury
Frédéric DAIGNE	Professeur d'Université	Membre du Jury
Andrea GOLDWURM	Directeur de Recherche	Membre du Jury
Natalie WEBB	Astronome	Membre du Jury
Philippe GUILLEMOT	Ingénieur de Recherche	Membre du Jury

École doctorale et spécialité :
ED SDU2E: Astrophysique, Sciences de l'Espace, Planétologie

Unité de Recherche :
Institut de Recherche en Astrophysique et Planétologie (UMR 5277)

Directeur de Thèse :
Jean-Luc ATTEIA

Rapporteurs :
Giulia STRATTA et *Bertrand CORDIER*

Acknowledgements

Ces trois années de thèse ont été une véritable plongée dans le monde de la recherche, me permettant d'en expérimenter ses innombrables qualités mais aussi ses défauts.

Ma volonté de faire une thèse en astrophysique remonte à ma rencontre avec Bernhard Brandl à TU Delft puis Emeric Le Floc'h au CEA Saclay. Sans ces rencontres, je n'aurai sûrement jamais songé à travailler 3 ans sur la mort spectaculaire de certaines étoiles de notre Univers. Je les en remercie.

Cette thèse a d'abord été permise grâce à la confiance que m'a accordé Jean-Luc Atteia lorsqu'il ma choisi comme étudiant. Tout au long de ma thèse, j'ai pu bénéficier de ses connaissances, mais aussi de sa pédagogie et sa bonne humeur. Je n'aurai pu rêver d'un meilleur directeur de thèse, que ce soit en terme d'excellence scientifique ou de qualité d'accompagnement.

Tout au long de ma thèse, j'ai travaillé avec les équipes de l'IRAP, du CEA Saclay, du LUPM ou encore de l'IAP sur ce merveilleux instrument (parfois un peu capricieux) qu'est ECLAIRs. Je remercie l'ensemble des ingénieurs et chercheurs concernés, au contact desquels j'ai énormément appris.

Cette thèse a été faite au sein de l'Institut de Recherche en Astrophysique et Planétologie, et je remercie donc toutes les personnes impliquées dans la vie de ce laboratoire. Je remercie aussi les organismes qui ont financé ma thèse: le CNES, l'Université Paul Sabatier, et l'état français qui a financé plus de 50% de mes études avec les bourses d'étude.

L'IRAP est un laboratoire plein de vie, au sein duquel j'ai tissé des liens avec des personnes formidables. Plus particulièrement, merci à Paul pour nos nombreux débats et soirées ensemble, Loulou pour nos soirées One Piece et Alix pour ton soutien et ton écoute (et bien sûr tes excellents gâteaux !). Merci aussi à mes deux partenaires IRL (In Rocket League ou In Real Life, au choix), JS IRAP - Rigoluto El Lama ("subscribe !") dit "le long" et Fwd:Fwd:Margot - Flofloban ("are you familiar with this country called ...") l'homme aux multiples retards et multiples excuses.

Merci à mes amis de Toulouse, de Poitiers, de La Rochelle et d'ailleurs, avec qui j'ai partagé bien des week-end et bien des vacances. Vous avez envahi la salle Coriolis (et le Zoom !) lors de ma soutenance, et cela restera pour moi un souvenir inoubliable.

Cette thèse est avant tout dédiée à ma famille: plus particulièrement à mes grand-parents pour m'avoir soutenu tout au long de mes études (financièrement, logistiquement mais surtout culinairement !). Vous m'avez suivi jusqu'à Delft en plein hiver pour pouvoir me voir soutenir mon Master, toujours avec "quelques" cannelés et magrets séchés en main. Merci à mes frères Alex, Nico et Thomas, loin des yeux mais toujours près du cœur. Vous êtes toujours là pour les moments qui comptent, et c'est le plus important. Merci à mon père l'apiculteur, le permagriculteur, le boulanger, plombier et électricien (sous réserve d'un Leroy Merlin pas loin ...) mais aussi l'expert Bâtiment, le directeur d'entreprise et surtout le capitaine de Fan D'Ango. Tu as inspiré, inspires et inspireras beaucoup de mes passions. Pour finir, je voudrais remercier ma mère qui m'a toujours accompagné, depuis mes premières additions jusqu'à la relecture de mon introduction de thèse. Ton soutien indéfectible, ton désir de me voir réaliser mes rêves jusqu'au bout mais aussi l'esprit critique que tu m'as transmis m'ont porté tout au long de mes études. Je pense que si l'espace m'a toujours fait autant rêver, c'est en grande partie grâce à vous.

Pour finir, je voudrais remercier celle qui m'accompagne maintenant depuis près de 9 ans. Celle au côté de laquelle j'ai grandis et appris, qui est venu me voir à Poitiers, à Toulouse, à Delft, à Paris pour enfin venir me retrouver à Toulouse. Cette thèse est aussi dédiée à toi Sonia.

Resumé

Les sursauts gamma sont des phénomènes transitoires extragalactiques qui continuent d'intriguer les scientifiques, 50 ans après leur découverte. Associés à des évènements violents comme la mort d'étoiles massives, ils se décomposent en deux phases : l'émission prompte, une bouffée de photons gamma durant quelques secondes, et l'émission rémanente, détectable dans les longueurs d'onde des rayons X, du visible et de la radio jusqu'à quelques jours après l'émission prompte. Comptant parmi les phénomènes les plus lumineux de l'Univers, les sursauts gamma sont extrêmement intéressants : ils font partie des sources cosmiques les plus lointaines observées, représentant un moyen unique de sonder les populations stellaires et le milieu extra- et intra-galactique aux plus hauts redshift. Cependant, en raison de leur courte durée et de l'imprévisibilité de leur apparition dans le ciel, l'étude des sursauts gamma reste un défi, même pour l'astronomie moderne.

Le satellite *SVOM*[1], qui sera lancé fin 2023, emporte deux instruments à champ large (ECLAIRs et GRM) et deux instruments à champ étroit (MXT et VT) pour détecter, caractériser et localiser les émissions promptes et rémanentes des sursauts gamma. *SVOM* bénéficiera aussi d'un suivi au sol grâce à trois observatoires terrestres dédiés (GWAC, C-GFT et COLIBRI) et d'un réseau d'antennes qui permet d'alerter la communauté scientifique quelques minutes seulement après la détection du sursaut gamma.

Mon travail s'est concentré sur ECLAIRs, un imageur spatial dans le domaine des rayons X durs. Grâce à sa caméra, son masque codé et son ordinateur embarqué, il détectera et localisera en temps quasi réel les émissions promptes des sursauts gamma. De part son seuil bas en énergie, ECLAIRs sera parfaitement adapté à la détection de populations de sursauts gamma intéressantes telles que les sursauts gamma très lointains.

Au cours de ma thèse, j'ai évalué les performances d'ECLAIRs dans l'espace : j'ai combiné les caractéristiques instrumentales mesurées pendant les calibrations avec des modèles de l'émission du fond du ciel, des sursauts gamma typiques et des sources X connues pour simuler avec précision les données attendues. Ces simulations ont été utilisées par exemple pour calculer le taux de détection de sursauts gamma attendu pendant la mission et comme support pour évaluer l'impact scientifique de divers paramètres de configuration de l'instrument.

Elles m'ont également servi de cadre pour développer un algorithme de détection au sol complémentaire aux logiciels de détection embarqués, puisque ECLAIRs aura la capacité unique de transférer au sol tous les événements détectés à bord.

Une autre application a été l'évaluation de la sensibilité d'ECLAIRs aux événements transitoires courts de haute énergie de notre Univers local ($z < 0.3$). Après avoir fourni une caractérisation de cette population, j'ai démontré qu'ECLAIRs sera capable d'en détecter la

[1]Space Variable Objects Monitor

grande majorité. J'ai également discuté des synergies potentielles avec d'autres instruments de *SVOM* et les observatoires multi-messagers pour l'étude de ces événements proches.

Dans le cadre d'un travail parallèle, j'ai exploré les connexions possibles entre les trous noirs créés lors des sursauts gamma longs et ceux impliqués dans les fusions de trous noirs binaires observées par les détecteurs d'ondes gravitationnelles. En comparant leur distribution en redshift et le taux attendu dans l'Univers local, j'ai montré que les sursauts gamma longs et les trous noirs détectés par ondes gravitationnelles sont très probablement deux populations distinctes.

Pour conclure, ma thèse a fourni un ensemble complet d'outils de simulation pour ECLAIRs avec des applications concrètes telles que le test du logiciel de vol et des pipelines *SVOM*. J'ai également montré que ECLAIRs sera capable de détecter et de localiser des populations uniques de sursauts gamma et d'autres évènements transitoires courts, permettant leur caractérisation multi-longueurs d'onde et multi-messagers par *SVOM* et les observatoires du monde entier.

Abstract

Gamma-Ray Bursts (GRBs) are extra-galactic transient phenomena that continue to puzzle scientists, 50 years after their discovery. Associated to violent events like the death of massive stars, they consist of two phases: the prompt emission, a burst of gamma-ray photons lasting typically few seconds and the afterglow, detectable in X-ray, visible and radio wavelengths up to few days after the prompt GRB. Being some of the most luminous phenomena in the Universe, GRBs are extremely interesting: they are among the farthest cosmic sources observed, representing a unique mean to probe stellar populations and the intra and inter-galactic medium at the highest redshifts. However, because of their short duration, their unpredictable times and sky localization, the study of GRBs remains challenging, even for modern astronomy.

The Sino-French mission *SVOM*[2], to be launched end of 2023, encompasses two wide-field (ECLAIRs and GRM) and two narrow-field (MXT and VT) instruments for detecting, characterizing and localizing the GRB prompt and afterglow emissions. *SVOM* also benefits from three dedicated ground telescopes (GWAC, C-GFT and COLIBRI) and an antennae network, allowing to alert the scientific community within few minutes after the prompt emission detection for an optimal follow-up.

My work focused on ECLAIRs, the wide-field hard X-ray telescope of *SVOM*. Using its coded mask and on-board computer, ECLAIRs will detect in near real-time the GRB prompt emission and get a crude localization from it. Thanks to its low energy threshold at 4 keV, the telescope will be perfectly suited for the detection of interesting GRB populations such as X-ray Flashes or high-redshift GRBs.

My thesis has been focused on the evaluation of ECLAIRs performances in space: I have combined instrumental effects with models of the background sky emission and GRB/X-ray sources to accurately simulate the instrument data stream. These simulations have been used for example to evaluate the sensitivity of ECLAIRs to various types of transients, to calculate the GRB detection rate expected during the mission, and as a support to evaluate the science impact of various configuration parameters of the instrument.

They have also been used as a framework for developing alternative trigger algorithm solutions to the on-board software, motivated by the unique ability of ECLAIRs to transfer all the events recorded on-board to the ground. Relying on simulated background orbits and GRBs, I have used a neural-network architecture suited for the anomaly detection on time series. This method may become part of an offline trigger able to detect transients missed by the on-board algorithm.

Another application presented in the manuscript is the evaluation of ECLAIRs sensitivity to short high-energy (HE) transients coming from our local Universe ($z < 0.3$). After

[2]Space Variable Objects Monitor

providing a characterization of this population, we demonstrate that ECLAIRs will be able to detect the large majority of it. We also discuss the potential synergies with other *SVOM* instruments and multi-messenger observatories.

As a side work, I have explored the possible connections between the BHs created during long GRBs and the mergers of binary black holes observed through gravitational waves (GW) emissions. This study was motivated by the release of the latest GW catalog GWTC-3, containing 79 BH mergers. From the comparison of their redshift evolution and expected rate, we have shown that these two populations are most probably distinct.

To conclude, my thesis has provided a complete set of simulation tools for ECLAIRs with concrete applications such as the testing of the flight software and the *SVOM* pipelines. I have shown that ECLAIRs will be able to detect and localize unique populations of GRBs and other short high-energy transients, enabling their multi-wavelength and multi-messenger characterization by *SVOM* and worldwide astronomical observatories.

Contents

List of Figures

List of Tables

Introduction FR

Les phénomènes dits "transitoires" (c'est à dire qui apparaissent dans le ciel pour une durée limitée) ont souvent été à l'origine de grandes avancées en astronomie. Par exemple, l'observation du transit de Vénus en 1761 et 1769 par des astronomes du monde entier a permis de mesurer la distance Terre-Soleil avec une précision inégalée pour l'époque. On peut aussi mentionner l'observation de la supernova de Tycho Brahe en 1572, remettant en question le concept Aristotélicien selon lequel le ciel au delà des planètes est immuable. A une époque plus récente, les supernovæ de type Ia ont permis de prouver que l'Univers était en expansion accélérée (Riess et al., 1998; Peebles & Ratra, 2003). Et plus récemment encore, la détection d'ondes gravitationnelles (Abbott et al., 2016, 2017a) émises lors de la fusion de deux trous noirs (difficilement observables par les moyens de l'astronomie classique) donne un nouveau regard sur ces derniers (e.g. Bavera et al., 2020; Volonteri et al., 2021).

Les sursauts gamma (GRBs, Vedrenne & Atteia 2009) sont des phénomènes transitoires découverts par hasard par les satellites américains *Vela* dans le contexte de la guerre froide. Ces satellites avaient été envoyés dans l'espace pour veiller au respect du traité de non prolifération des armes nucléaires qui interdisait en particulier les essais dans l'espace. Ils embarquaient des instruments sensibles aux rayonnements gamma émis lors des explosions thermo-nucléaires des bombes atomiques. Lorsque les données ont été dé-classifiées des années plus tard, la communauté scientifique a découvert des bouffées de photons gamma de quelques dizaines de secondes, provenant non pas de la Terre ou du Soleil, mais de l'espace. C'est ainsi que le premier sursaut gamma GRB 670702 a été découvert (Klebesadel et al., 1973). Au total, environ 500 GRBs seront détectés lors des missions *Vela*.

La mission *CGRO* (pour Compton Gamma-Ray Observatory), lancée en 1991 et emportant l'instrument gamma BATSE (Fishman et al., 1989), permettra de glaner plus d'informations concernant ces phénomènes. Les observations (e.g. Meegan et al., 1992) de BATSE semblaient montrer que les progéniteurs de GRBs étaient à des distances cosmologiques, même si ce résultat était alors débattu, notamment en raison des niveaux d'énergie requis ($\sim 10^{54}$ erg correspondant à 10^{47} J). C'est afin d'expliquer les propriétés des GRBs détectés par BATSE (énergie requise, variabilité temporelle, spectre non-thermique) que le modèle standard des GRBs voit le jour (e.g. Rees & Meszaros, 1992). Celui-ci explique l'émission gamma prompte observée par BATSE par des chocs internes très intenses entre des couches de matières éjectées à différentes vitesses au sein de jets relativistes par un moteur central très compact (un trou noir ou une étoile à neutron en rotation rapide). Le modèle standard prédit aussi l'apparition d'une émission rémanente suivant l'émission prompte, expliquée par les chocs entre les couches de matière éjectées et le milieu interstellaire (chocs externes). On attend de l'émission rémanente la production de photons dans l'intégralité du spectre

lumineux, permettant son observation avec des télescopes X ou optiques et donc une bien meilleure localisation de la source du GRB. Cependant, de part le faible champs de vue des instruments X et visibles, la localisation de l'émission rémanente demande d'avoir en premier une position approximative du GRB. Or, la localisation de l'émission prompte par BATSE était trop lente et trop peu précise pour obtenir cette position à temps.

BATSE a aussi permis de découvrir une bi-modalité dans la distribution des durées des émissions promptes de GRBs (Kouveliotou et al., 1993; Dezalay et al., 1992). Celle-ci semblait composée de sursauts courts d'une durée caractéristique de quelques dixièmes de secondes et de sursauts longs d'une durée de quelques dizaines de secondes. Cette bi-modalité suggérait une nature différente des sursauts courts et longs, mais il n'y avait à ce moment là encore aucune preuve tangible.

Il faudra attendre la fin des années 1990 et la mission *BeppoSAX* (Boella et al., 1997a) pour avoir une localisation de l'émission prompte à la fois précise et rapide. Cela a été permis grâce à la technologie du masque codé de l'instrument WFC (Jager et al., 1997) embarqué sur le satellite couplée à l'analyse automatique des données au sol. Cette méthode a permis de détecter la première émission rémanente d'un sursaut gamma avec des instruments X et visibles. L'observation de l'émission rémanente seulement quelques heures après l'émission prompte a permis de localiser précisément le sursaut gamma (à quelques secondes d'arc près). C'est ainsi que la première mesure de décalage vers le rouge d'un GRB a pu être faite, ($z = 0.835$, Metzger et al. 1997, correspondant à un évènement qui s'est produit il y a 7 milliards d'années) confirmant ainsi l'origine cosmologique de ces phénomènes.

Cette localisation précise obtenue a aussi permis de mieux comprendre l'origine des GRBs longs. La mission *HETE-2* (Ricker et al., 2003) montrera que les GRBs de cette catégorie sont quasi-systématiquement accompagnés de supernovæ de type Ibc (Stanek et al., 2003; Hjorth et al., 2003) et qu'ils se produisent majoritairement au cœur des galaxies naines, dans des zones à fort taux de formation stellaire (Le Floc'h et al., 2003; Fruchter et al., 2006). Les GRBs longs seraient donc produits par l'effondrement du cœur d'une étoile massive en rotation rapide.

Pour les GRBs courts, l'émission rémanente est demeurée indétectable pour les instruments de *BeppoSAX* et *HETE-2*. Il faudra attendre la mission Neil Gehrels Swift Observatory (*Swift*, Gehrels et al. 2004a), lancée en 2004, afin d'avoir plus d'indices sur leur origine. Cette mission est équipée d'un instrument à grand champ de vue, BAT (pour Burst Alert Telescope, Barthelmy et al. 2005a) et de deux instruments à champ de vue étroit, XRT (X-Ray Telescope Burrows et al. 2005) et UVOT (Ultra-violet Optical Telescope Roming et al. 2005). Grâce à sa capacité de re-pointage exceptionnellement rapide, *Swift* a pu pointer ses instruments XRT et UVOT seulement quelques minutes après la détection de l'émission prompte, et ainsi observer la première émission rémanente de GRBs courts (Gehrels et al., 2005) avant que celle-ci ne devienne trop peu lumineuse. On découvre que ces sursauts sont localisés dans tous les types de galaxies, avec ou sans formation stellaire, suggérant une origine liée à des astres vieux (Belczynski et al., 2006). La théorie connectant les GRBs courts à la fusion de deux étoiles à neutron rencontre un franc succès. Cependant, il faudra attendre 2017 et la détection du GRB court GRB 170817A, coïncidant avec la détection

d'ondes gravitationnelles (Abbott et al., 2017b; Abbott et al., 2017), pour confirmer l'origine des GRBs courts.

Les précédentes missions spatiales servent maintenant de référence pour les futures missions vouées à l'observation des GRBs. *BeppoSAX*, *HETE-2* et *Swift* ont montré qu'il faut être capable de rapidement détecter et localiser l'émission prompte d'un sursaut gamma si l'on veut effectuer des observations de l'émission rémanente et obtenir une position précise du progéniteur. Cela demande aux satellites de pouvoir repointer rapidement dans la direction de l'émission prompte et d'échanger rapidement des informations avec le sol. Les missions *BATSE* et *Fermi* (Meegan et al., 2009a) ont aussi souligné l'importance de la caractérisation spectrale de l'émission prompte, ceci afin d'en apprendre plus sur l'origine des phénomènes physiques à l'œuvre, demandant des instruments couvrant une gamme d'énergie la plus large possible.

Même si de grandes avancées ont été faites depuis la découverte des GRBs il y a 50 ans, il reste encore beaucoup d'interrogations. Le chapitre 1 illustre ainsi la difficulté d'expliquer certaines observations en utilisant le modèle standard des GRBs. Ces dernières années, les détections de GRB 178017A (conjointe avec l'onde gravitationnelle GW 170817, Abbott et al. 2017b; Abbott et al. 2017) et GRB 190814C (conjointe avec des photons au delà du TeV, MAGIC Collaboration et al. 2019a) ont aussi démontré qu'une large collaboration scientifique est nécessaire si l'on veut être en mesure de percer les mystères des GRBs. Celle-ci permettrait la mise en place d'observations couvrant l'intégralité du spectre lumineux (multi longueurs d'ondes) et des porteurs d'informations potentiels (multi-messager).

C'est dans ce contexte que *SVOM* (Space-based multi-band astronomical Variable Objects Monitor, Wei et al. 2016), mission franco-chinoise dédiée à l'étude des GRBs et prévue pour fin 2023, va opérer. *SVOM* embarque 2 instruments grand champ de vue (ECLAIRs Godet et al. 2014 et GRM Wu 2021) pour détecter, caractériser et localiser l'émission prompte des GRBs. Le satellite sera ensuite capable de se re-pointer en direction de cette localisation afin d'utiliser ses 2 autres instruments à champ de vue étroit (MXT Mercier et al. 2018 et VT Fan et al. 2020) afin de détecter, caractériser et localiser précisément l'émission rémanente de ces mêmes GRBs. En plus de ces 4 instruments, *SVOM* possède aussi 3 observatoires dédiés au sol (GWAC Han et al. 2021, C-GFT Niu et al. 2022, COLIBRI Fuentes-Fernández et al. 2020), permettant un suivi dédié de chacun des GRBs observés. L'intégralité de la mission a été construite dans le but de maximiser le suivi des sursauts détectés grâce à sa stratégie de pointage anti-solaire : une détection de GRBs se fera systématiquement dans une zone du ciel immédiatement observable par les télescopes au sol. La mission et les différents instruments qui la compose sont décris dans le Chapitre 2.

Ma thèse s'intéresse principalement à l'étude des performances du télescope X-dur de *SVOM*, ECLAIRs (Godet et al., 2014). Ce télescope est issu de la collaboration entre plusieurs laboratoires français (APC, CEA, IAP, IRAP, LUPM), avec la responsabilité scientifique confiée à l'IRAP et la maîtrise d'œuvre assurée par le CNES. ECLAIRs est un télescope à masque codé avec un large champ de vue de 90×90 deg^2 : couplé à son Unité de Gestion pour le Traitement Scientifique (UGTS, Schanne et al. 2019), cette technologie permettra de détecter et de localiser (avec une précision de quelques arc-minutes) en temps quasi-réel l'émission prompte des GRBs. Le plan de détection de l'instrument (Nasser et al.,

2014; Bajat et al., 2018a; Lacombe et al., 2018), comprenant 80×80 pixels en Tellure de Cadmium (CdTe), rend l'instrument sensible de 4 à 150 keV, permettant une détection de populations particulièrement intéressantes comme les GRBs à haut décalage vers le rouge. Grâce à l'ensemble de ces caractéristiques, ECLAIRs détectera environ 50 GRBs par an (Antier-Farfar, 2016), avec un suivi dédié par les autres instruments de *SVOM* pour la large majorité d'entre eux. ECLAIRs est décrit plus en détail dans le Chapitre 3.

J'ai effectué ma thèse pendant l'assemblage et la campagne de test du modèle de vol de ECLAIRs. Le chapitre 4 présente ma participation à la validation du modèle de masse de ECLAIRs, ainsi qu'à la caractérisation de phénomènes instrumentaux observés pendant les tests.

Ma thèse s'est concentrée autour de la simulation du comportement de ECLAIRs dans l'espace, unifiant le travail entrepris depuis plusieurs années par plusieurs laboratoires (Antier-Farfar, 2016; Mate et al., 2019; Dagoneau, 2020). Le chapitre 5 présente ainsi des simulations dites astrophysiques (bruit de fond du ciel, sources X, GRBs) couplées à des simulations de la chaîne de transmission d'informations de ECLAIRs (comportement de l'UGTS et de l'électronique de ECLAIRs). Ces simulations ont contribué à la validation du plusieurs composantes du logiciel de vol, mais aussi à l'actualisation du taux de détection de GRBs.

Comme ECLAIRs sera capable de transférer au sol l'intégralité des évènements enregistrés à bord, cela donne l'opportunité de développer des algorithmes de détection au sol, s'affranchissant des contraintes qu'aura l'algorithme de détection à bord d'ECLAIRs. J'ai ainsi développé mon propre algorithme de détection que j'ai entraîné, validé et testé grâce aux simulations présentées au chapitre 5. Le chapitre 6 traite d'une approche novatrice, utilisant un réseau de neurones avec un apprentissage semi-supervisé adapté aux séries temporelles, afin de compléter les performances de détection de l'algorithme de bord.

Le travail de simulation effectué a aussi permis de mieux comprendre les populations astrophysiques qui seront visibles par l'instrument ECLAIRs. Le chapitre 7 reprend le travail publié dans le journal *Astrophysics and Space Science* (Arcier et al., 2020). Il traite des performances de détection de ECLAIRs pour un échantillon de phénomènes transitoires courts de haute énergie provenant de l'Univers local ($z < 0.3$), montrant que l'instrument sera capable de détecter la large majorité de l'échantillon constitué. En plus d'apporter une caractérisation détaillée de cette population, j'ai aussi développé de potentiels synergies que pourrait avoir ECLAIRs avec les autres instruments de *SVOM* et les observatoires du monde entier.

Pour finir, le chapitre 8 présente une étude indépendante de *SVOM* publiée dans le journal *The Astrophysical Journal* (Arcier & Atteia, 2022). Il porte sur les populations de binaires de trous noirs observées à l'aide des ondes gravitationnelles et sur les trous noirs formés pendant les GRBs longs. L'augmentation du nombre d'évènements du catalogue d'ondes gravitationnelles GWTC-3 (The LIGO Scientific Collaboration et al., 2021b) a permis d'étendre les résultats de Atteia et al. (2018). Mon travail montre ainsi que les deux populations ne sont probablement pas liées, et ouvre la voie pour des études futures utilisant les observations O4 et O5 de LIGO, Virgo et KAGRA (Abbott et al., 2018a).

Chapter 1

Gamma-Ray Bursts

After a brief introduction to transient events in Sec. 1.1, this chapter presents the GRB phenomenon. Sec. 1.2 narrates the observational and theoretical progresses in the field, emphasizing the important lessons learned for future GRB missions such as *SVOM* presented in Chapter 2. These progresses have allowed the creation of the standard model presented in Sec. 1.3. Section 1.4 describes the observed properties of GRB phenomenology nowadays, showing how they deviate from the standard model and the necessity for future missions to gather more observations. Finally, Sec. 1.5 presents the content of this thesis and the work performed during these last 3 years.

Contents

1.1 Transient events as unique tools for observing the Universe

In his astronomical treatise *De caelo*, Aristotle describes a cosmos divided into two regions: the sub-lunar world, where we are living, and the sup-lunar world, the world of the sky and celestial bodies. According to the scientist and philosopher, this sup-lunar world is composed of ether and completely motionless and is divine by nature. For this reason, the only objects able to move or change in the sky are the ones belonging to the sub-lunar world.

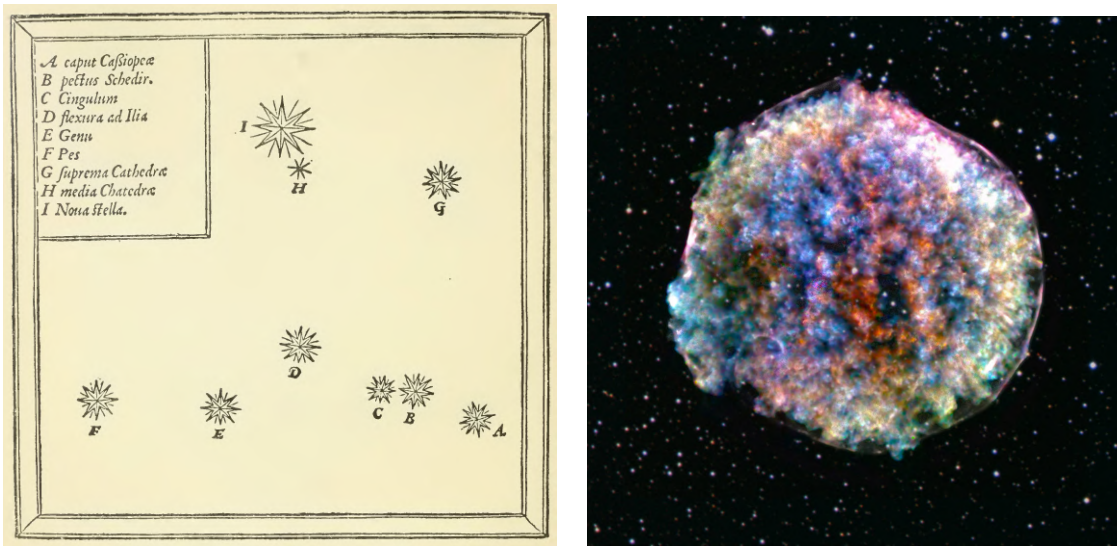

(a) (b)

Figure 1.1. (a) Map of the Cassiopeia constellation, showing the SN 1572 position relatively to stars (label I). Credit: De Stellar Nova, 1573 (b) The remnant of SN 1572, seen by Chandra. Credit: NASA/CXC/Rutgers/J.Warren & J.Hughes et al.

The supernova SN 1572 observed the 11^{th} of November 1572 in the Cassiopeia constellation by Tycho Brahe (see the manuscript annotations in Fig. 1.1(a)) has completely changed this apprehension of the cosmos. This event manifestation was a new star in the sky with an apparent magnitude of -4, brighter than Venus at this period of the year. A few months later, this object was not visible anymore to the naked eyes (its remnant is still visible with X-ray telescopes, see Fig. 1.1(b)). After months of observations, the position of this object relative to the other stars in the sky has not moved, while the parallax method indicated a distance greater than the moon and the other planets' distances. Tycho Brahe concluded that this object could not be a planet, therefore belonging to the domain called by Aristotle the sup-lunar world. The SN 1572 observation represents one of the most critical changes in the history of astronomy, breaking one of the axioms of the Aristotelian dogma: the sub-lunar world can change. It also shows two crucial characteristics of transient observations: the observation is limited in time, and its sky localization is unpredictable.

Thanks to the observation, characterization, and follow-up of transient events, remarkable discoveries have been made. Supernovae Ia have, for example, contributed to increase our understanding of the Universe. These particular supernovae display a recognizable spectrum pattern, consisting of strong iron emission lines and silicon absorption lines. Their progenitors are white dwarfs exceeding the Chandrasekhar mass because of mass transfer from a companion star. Since the progenitors of such supernovae explode at the same mass (~ 1.4 $M_\odot$, thus having similar initial conditions), they have similar lightcurves and peak luminosities. Visible at up to $z \sim 1$, they have been used as one of the ladders for the distance estimation in the Universe. Thanks to their unique properties, SNIa have also been used to demonstrate the acceleration of the Universe expansion (Riess et al., 1998; Peebles & Ratra, 2003), which dramatically changed the cosmological theories: to explain this acceleration, a dark energy accounting for $\sim 70\%$ of the Universe energetic content seems to be required.

However, one of the most puzzling transient phenomena observed remains the γ-ray bursts (GRBs). Observable from across the Universe, these phenomena consist of brief and intense flashes of γ-ray photons (the prompt emission) followed by a multi-wavelength emission (from X-ray to radio) lasting up to several months (the afterglow emission). The diversity of observed properties, the complex physics at stake, and the limited observations prevent scientists from completely grasping the nature of GRBs. However, being some of the most luminous phenomena in the Universe, they are fascinating: among the farthest cosmic sources observed, they represent a unique mean to probe stellar populations and the intra- and inter-galactic medium at the highest redshifts. Nonetheless, because of their short duration, unpredictable times, and sky localization, the study of GRBs remains challenging, even for modern astronomy. These events and their observations are the centers of interest in this thesis.

1.2 A small history of γ-ray bursts

This section attempts to summarize the main observational and theoretical progress along the years in the γ-ray burst domain, starting from the years of the phenomenon discovery in the 70s to the launch of the *Fermi* satellite at the beginning of 2008. During this period, we have obtained a global view of the phenomenon, which has led to the construction of the GRB standard model presented in Sec. 1.3. At the end of each subsection, we have outlined in italic some of the lessons learned.

1.2.1 Discovery of γ-ray bursts

Like many scientific discoveries (radioactivity, penicillin, cosmic microwave background, ...), γ-ray bursts were discovered accidentally in the late 1960s. To limit the proliferation of nuclear weapons from other countries, the United States of America, the United Kingdom, and the USSR signed a treaty in Moscow in August 1963, partially prohibiting nuclear weapon tests. This interdiction was valid on the ground, the sea, but also in space. While the ground and sea tests could be detected via various tracers such as seismic activity, the air composition, or hydro-acoustic monitoring, space tests were much more difficult to spot:

the γ-ray photons emitted during the explosion are absorbed by the Earth's atmosphere. The only way to detect a nuclear explosion in space was to have a satellite equipped with a γ-ray instrument. This is how the *Vela* program was created: by launching several pairs of satellites in a common circular orbit with γ-ray scintillators on-board, it was possible to detect a burst of gamma-rays and have an estimation of the γ-ray emitter position via triangulation methods.

In the end, no nuclear explosion was reported during the mission. However, several unexpected signals from space were detected, with a signature and localization different from solar flares or nuclear explosions. Among them GRB 670702[1], the first GRB detected on 2^{nd} of July 1967 (Klebesadel et al., 1973). After the discovery of the first GRB by the Vela satellites, $\sim$ 500 additional GRBs were discovered by the various instruments on US and Soviet satellites (Higdon & Lingenfelter, 1990), with a localization precision above dozens of square degrees.

The InterPlanetary Network (IPN), a group of satellites carrying instruments tailored for GRB detection, has also been used. The satellites were in orbit around the planets of the solar system, allowing them to have large baselines to perform the localization with triangulation methods. Several months were required for gathering and analyzing the data from all the satellites, but it allowed to obtain sub-arcminute localizations for dozens of GRBs (Atteia et al., 1987).

Nonetheless, as the localization was either too imprecise or obtained too late, no electromagnetic counterparts were discovered from the GRBs in frequencies lower than the gamma. At that time, the central question was about the GRB origin and whether galactic or extra-galactic sources emitted GRBs: the rough isotropy and the deficit of low fluence GRBs from the nominal $N(>S) \propto S^{-3/2}$ law expected from a Euclidean geometry (Higdon & Lingenfelter, 1990) seemed to point toward a cosmological origin. However, the data were too scarce to settle the debate properly.

Some people realized that the luminosity of GRBs would be limited by the electron-positron pair production condition, which raised the "compactness problem." This problem was especially troublesome for the cosmological origin of GRBs, where highly energetic phenomena were required.

The observation of the first GRBs set the characteristics for the next GRB missions: an instrument with a large FoV, sensitive to the hard X-ray / γ-ray, was required to maximize the number of detections. Moreover, a fast and accurate localization of such events appeared mandatory to learn more about these events' origins.

[1]The naming of the GRBs is based on a convention, where GRB YYMMDDA has been detected in year 19YY or 20YY, month MM, and day DD. An additional letter 'A,' 'B', ... is added to account for the detection sequence. Note that the first GRB happening during a day might not contain the letter 'A,' as it is the time the event is acknowledged as a GRB that matters.

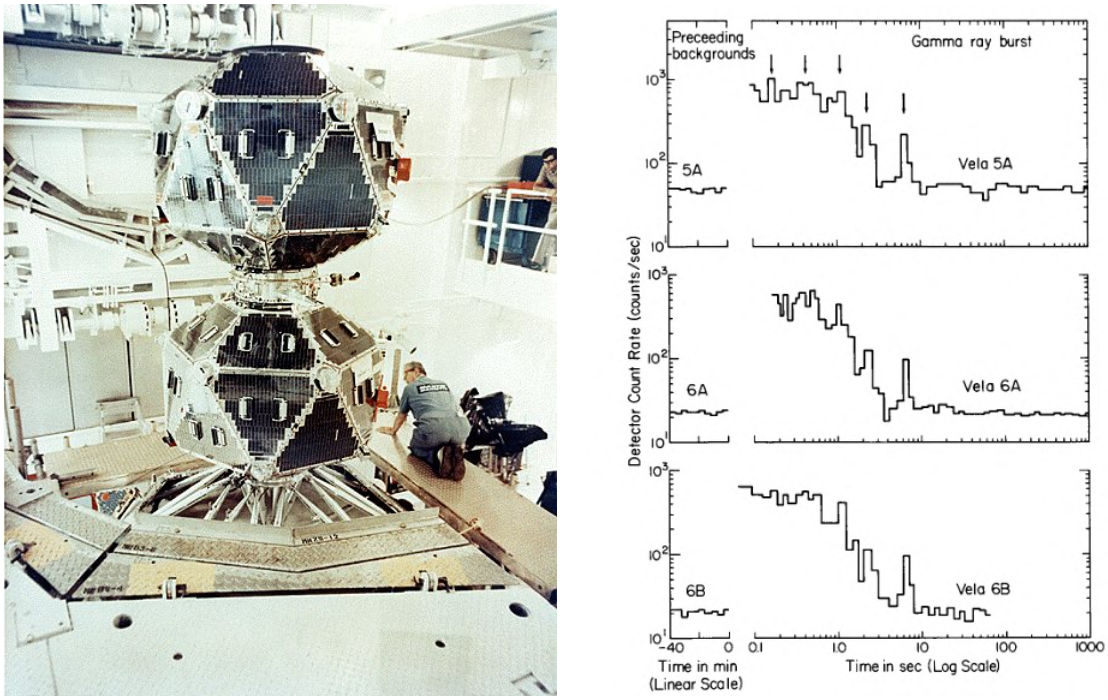

(a) (b)

Figure 1.2. (a) Vela-5A/B Satellite in Clean Room. Credit: https://heasarc.gsfc.nasa.gov/ (b) Lightcurve of GRB 670722, one of the first burst detected by the *Vela* mission. Credit: Klebesadel et al. 1973

1.2.2 γ-ray bursts without a localization

The launch of the *CGRO* spacecraft on 5th April 1991 with the BATSE instrument on-board brought new clues on the GRB origin and physics. The BATSE instrument was sensitive in the 25 keV – 100 MeV energy range, with a field of view covering the whole sky available (the Earth was partially occulting the FoV as it was in low Earth orbit) and a detection sensitivity of 3×10^{-8} erg cm^{-2} for a 1 sec GRB (several orders of magnitudes better than the *Vela* detectors). Although no lower frequency counterparts were detected by the follow-up instruments (the localizations were still too poor), the 2704 GRBs detected (Fishman et al., 1994) allowed to get better statistics on the prompt emission properties.

The extra-galactic origin became more and more plausible, mainly because of the highly isotropic distribution of the GRB angular position and the fluence distribution (Meegan et al., 1992). Finally, the non-thermal spectrum of GRBs was confirmed, leading to the definition of the BAND function (Band et al., 1993) as a convenient way to fit GRB spectra in the 10 keV - 10 MeV energy range.

As the extra-galactic origin was getting more and more credit, researchers tried to explain how such powerful events could be created despite the compactness problem. The standard *fireball shock model* had been theorized (Rees & Meszaros, 1992), setting up several elements of the current framework of the GRB theory. This is the model presented in Sec. 1.3: the

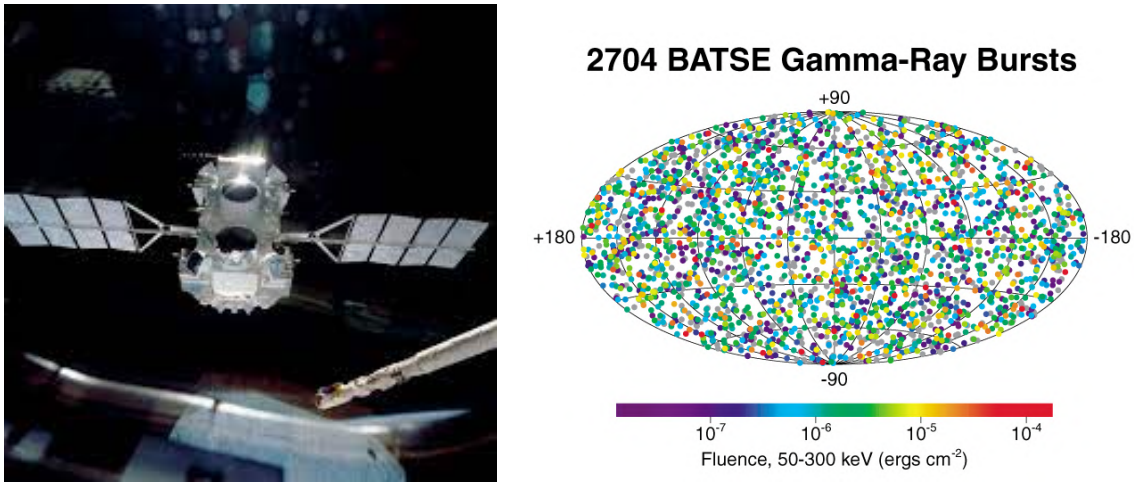

(a) (b)

Figure 1.3. (a) The Compton Gamma-Ray Observatory released by the Atlantis shuttle's remote manipulator system. Credit: https://www.nasa.gov/ (b) BATSE all-sky plot of GRB locations. Credit: https://heasarc.gsfc.nasa.gov

non-thermal spectrum of GRBs was explained by the internal, external, and reverse shocks that accelerate baryons, emitting photons via synchrotron radiation or inverse Compton scattering. Some people also argued that a highly magnetized neutron star could power a GRB (Usov, 1992; Thompson, 1994) by converting the spin energy through a magnetic field to accelerate matter, explaining the non-thermal spectrum by a magnetically dissipative photosphere. It was also at this period that the collapsar model (the collapse of a single Wolf-Rayet star with rapid rotation) was introduced as a potential progenitor for long GRBs.

Finally, there were predictions (Mészáros & Rees, 1997) about the afterglow emission of the GRB created by the external shock of the fireball in the circumburst medium. γ-ray astrophysicists were expecting a multi-wavelength emission lasting several days. However, the prompt emission localization was too poor, and the IPN triangulation was obtained too late to make such observations.

The CGRO/BATSE mission and the GRB missions in the Interplanetary Network (IPN) have underlined the diversity of observed GRBs in terms of energetic and spectral characteristics. Therefore, to properly characterize the spectrum of the prompt emission, it appeared necessary to have an instrument with an extensive energy range. Moreover, more than 2000 *additional bursts have been found on the ground with an off-line analysis, showing the importance of such analysis: until this day, the BATSE catalog is the catalog with the lowest peak flux completeness thanks to this (Stern et al., 2001). Finally, a rapid a precise localization from the γ-ray instruments was necessary to point narrow-field instruments toward the emission site and catch the theorized afterglow.*

1.2.3 Fast and accurate GRBs localizations

The launch of *BeppoSAX* (Boella et al., 1997a) in 1996 and *HETE-2* (Ricker et al., 2003) in 2000 drastically improved the localization precision of the GRBs. These satellites encompassed coded mask telescopes (see Chapter 3) able to give a localization of the prompt emission, so narrow field instruments could be pointed to the GRB direction only a few hours after the prompt emission detection. The localization algorithms were made on-board on the *HETE-2* mission, while it was made on the ground for *BeppoSAX*. With this method, the first X-ray and optical afterglows were detected for GRB 970228 (Wijers et al., 1997) and the first radio afterglow for GRB 970508 (Frail et al., 2000). Their precise localization allowed to point ground optical telescopes toward the afterglow, making GRB 970228 the first GRB with a potential host galaxy and a measured redshift ($z = 0.695$, although there was still a controversy about the association with the host galaxy). The detection of the afterglow of GRB 970508 afterglow and the measurement of its redshift ($z = 0.835$, Metzger et al. 1997) from the afterglow absorption lines confirmed the cosmological origin of long GRBs. Thanks to the afterglow observations, standard afterglow models have been complexified, introducing effects such as stratified circumburst media (e.g., stellar wind environments), continuous energy injection, stratification of the Lorentz factor, effects of the jet collimation and its transition from relativistic to non-relativistic velocity.

Moreover, the quick and accurate detection of afterglow emissions from GRBs also led to the discovery of "Dark" GRBs (e.g. Piro et al., 2002), which are X-ray bright GRBs with no optical afterglow emission.

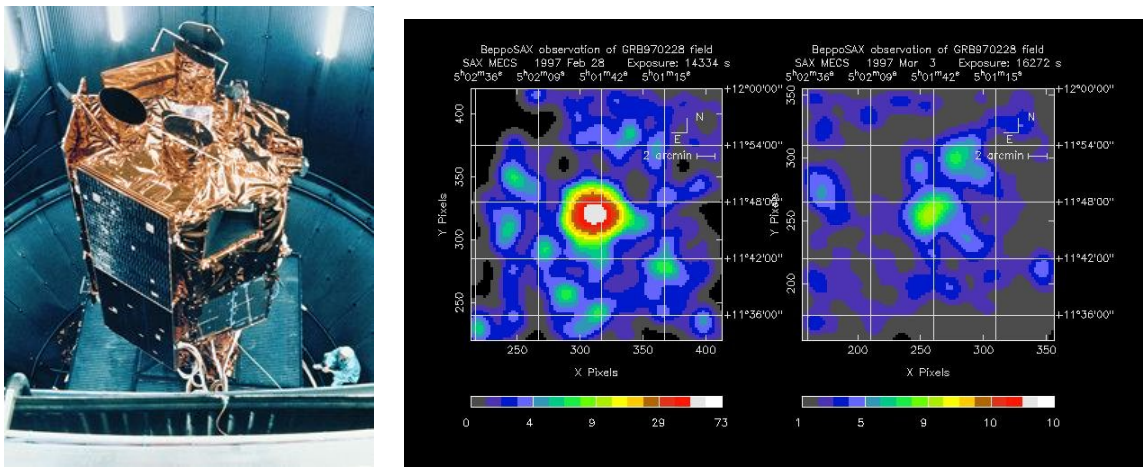

(a) (b)

Figure 1.4. (a) The BeppoSAX spacecraft during testing. Credit: Agenzia Spaziale Italiana (b) First X-ray afterglow observed within 6 hours after the prompt emission by the *BeppoSAX* X-ray camera. The image on the right is the same field 3 days after, where the source is almost completely faded. Credit: BeppoSAX team

With the enhanced localization precision, Type Ic broad-line SN have been detected and associated with nearby long GRBs: first GRB 980425 seen by *BeppoSAX* (Tinney et al., 1998; Galama et al., 1998) and later GRB 030329 by *HETE-2* (Stanek et al., 2003; Hjorth et al., 2003). While the former was an unusual low-luminosity long GRB in a nearby galaxy ($z = 0.0085$, Tinney et al. 1998), the association of a typical long GRB GRB 030329 ($z = 0.168$, Greiner et al. 2003) with a Type Ic SN confirmed this result. Le Floc'h et al. (2003); Fruchter et al. (2006) found that long GRBs are preferentially found in active star-forming regions of sub-luminous galaxies so that they might be associated with the death of a certain type of massive stars. This contributed to confirm the collapsar model as the standard theoretical framework for producing long GRBs.

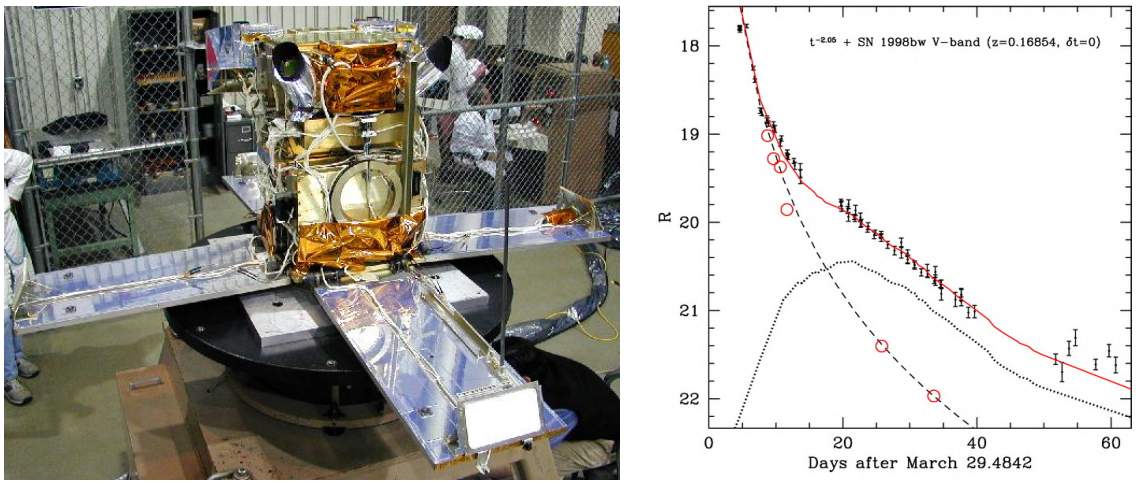

(a) (b)

Figure 1.5. (a) The HETE-2 spacecraft during mass properties testing. Credit: https://www.nasa.gov/ (b) The supernova associated with GRB 030329: the red curve corresponds to the observations and is produced by the superposition of the afterglow continuum (dashed line, constrained by spectroscopy with the red squares) and a SN 1998bw-like supernova scaled to the GRB redshift (dotted line). Credit Matheson et al. 2003

The low-energy thresholds of the WFCs on-board *BeppoSAX* and FREGATE on-board *HETE-2* allowed the detection of events that emit most of their photons, the hard X-rays. The so-called X-ray Flashes (XRFs) and X-Ray Rich (XRRs) GRBs seem to form a continuum with the GRBs, being the low-energy soft tail of the GRB population (Barraud et al., 2005; Sakamoto et al., 2005).

Alternatives to the standard model have also emerged during this period, invoking the fireball photosphere (explaining the hard low-energy photon index exceeding the synchrotron line of death found in some GRBs) or a Poynting flux dominated outflow as dominant radiation sources of the prompt emission.

HETE-2 and BeppoSax showed the importance of a quick and accurate localization of the prompt emission. This localization enables the detection of the afterglow, which usually

leads to the GRB's precise localization, with the redshift measurement and host galaxy identification. Such observations give access to the burst's energetic, in addition to its localization, giving clues about the nature of its progenitor. Moreover, having a γ-ray instrument sensitive to low energies ($\sim$ keV) allows the detection of soft events such as the XRFs and XRRs, whose nature remains, until this day, puzzling.

1.2.4 Quick localization and observation of GRBs

The *Neil Gehrels Swift Observatory* mission (*Swift*, Gehrels et al. 2004a) was launched in November 2004 and remains active until this day. It encompasses one wide-field instrument (the hard X-ray coded mask telescope BAT, Barthelmy et al. 2005a) and two narrow field ones (the X-ray camera XRT and the visible camera UVOT, see Roming et al. 2005; Burrows et al. 2005).Thanks to its capability to slew towards the target in less than a minute, *Swift* can point its narrow-field instrument towards the prompt emission to observe the afterglow way quicker than ever before.

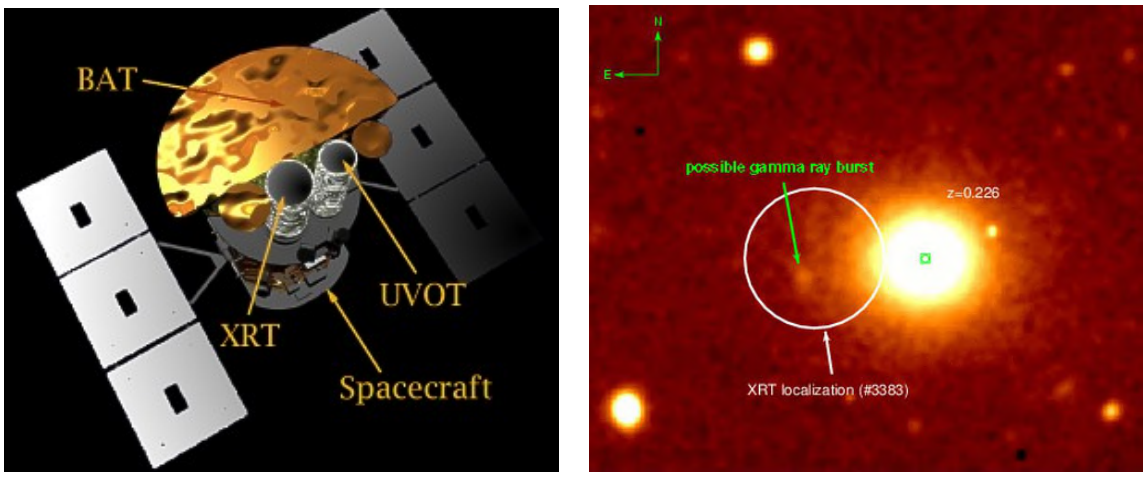

(a) (b)

Figure 1.6. (a) The Swift spacecraft with its 3 on-board instruments. Credit: NASA (b) Afterglow localization of GRB 050509B, one of the first short GRB afterglow detected by *Swift*. Credit: UC Berkeley/WIYN Telescope

These early-time observations have enabled the first detection of the faint short GRB afterglows, leading to the identification of their host galaxies (see the typical red galaxy in Fig. 1.6(b)). It turns out that short GRBs originate from all types of galaxies, with or without star formation, suggesting a different nature from long GRBs.

Swift/XRT early observations have also allowed to discover the steep and shallow decay phases of the X-ray afterglows, observed before the other decay phases identified with previous missions. They have also allowed the discovery of X-ray flares within the afterglow phase, X-ray plateaus, and the complex chromatic behavior of some GRB afterglows, all suggesting that the standard external shock framework is not sufficient to describe the diversity of afterglow behavior observed.

The quasi-systematic follow-up of GRBs from the first minutes after their detection has also allowed to obtain a large number of redshifts from these events, from low redshift GRBs such as GRB 060218 or GRB 111005A to very high redshift ones such as GRB 090423 or GRB 090429B. Increasing the sample of GRBs with an associated redshift has allowed to put more statistically significant constraints on the energetic of GRB phenomena.

The early observation of GRB afterglows has opened lots of questions, stressing the importance of rapid localization and slew capabilities for future multi-wavelength missions. The systematic multi-wavelength follow-up of GRBs was also crucial to obtain redshifts and host galaxies information. Finally, the increase in sensitivity and rapid follow-up disclosed the diversity of phenomena observed in GRBs' prompt and afterglow emissions.

1.3 The Gamma-Ray bursts standard model

The standard model has been built to explain the spectral and temporal properties of GRBs' prompt and afterglow emissions: how to alleviate the compactness problem, explain the non-thermal spectrum of the GRBs, and the high temporal variability of the prompt emission and the diversity of the afterglow behavior.

Figure 1.7 is a schematic representation of the standard model emission. This schema shows the case of a collapsar as a progenitor, but the standard model can also be applied for neutron star mergers, although some parameters will change to explain the observed properties.

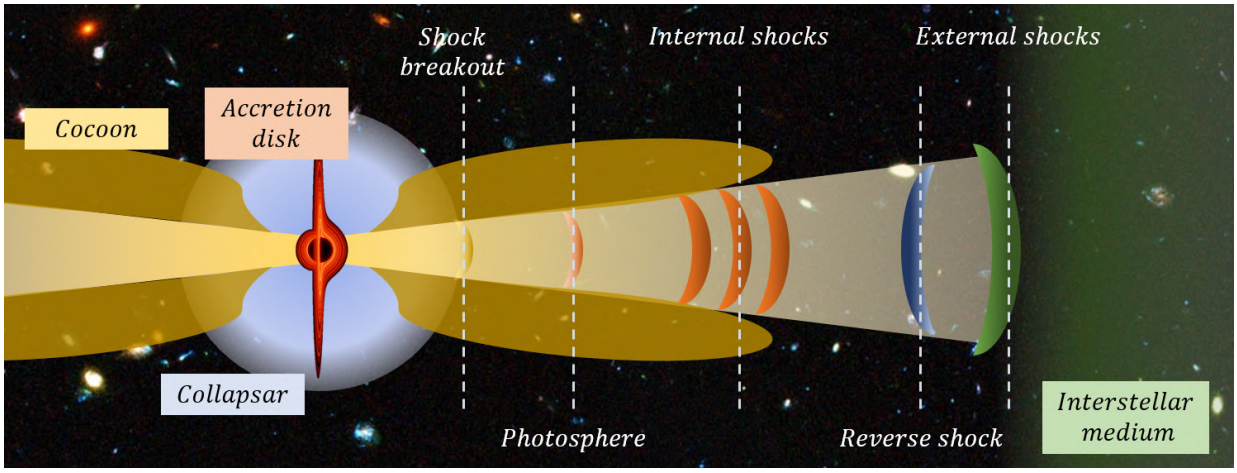

Figure 1.7. The standard model schematic for a collapsar.

A central engine is formed during the formation of a black hole (created, for example, during the collapse of a massive star or the merger of neutron stars). This central engine is thought to be either a black hole or a rapidly rotating neutron star. The matter surrounding the central engine is not supported by the internal pressure anymore and collapses towards it. In the case of the collapsar, the star is rapidly rotating to form the accretion disk so that the matter does not directly fall into the black hole. The central engine pumps energy from the accretion disk via mechanisms currently not well understood (possibly the magnetic field

from the spinning black-hole with for example the Blandford-Z effect and/or the neutrino emission from the accretion disk). This energy is probably transferred into heat energy, which is then converted into kinetic energy via the adiabatic expansion of the ejecta (fireball model). Thanks to this expansion, shells of matter are ejected from the central engine with a building velocity that reaches relativistic speeds (typically $\Gamma \sim 100$). Recent realistic models also suggest that magneto-hydrodynamic effects could also take place for the jet formation (e.g. Zhang, 2018).

When the matter pierces the stellar envelope, some high-energy photons might be expected via a shock-breakout. This phenomenon is predicted mainly for supernovae but might have also been observed to explain particularly long nearby GRBs such as GRB 060218 (Campana et al., 2006). While the jet crosses the stellar envelope (or the matter surrounding the merger), its interaction with it can create a cocoon. The emissions from this cocoon are challenging to model, as they require dedicated hydrodynamical simulations, including relativistic effects and photons/particles interactions. However, its strong influence on jet collimation and structure is acknowledged.

At a certain distance from the central engine, the shells of matter lose density and become optically thin, allowing the emission of the photons trapped inside: the radius at which this is happening is called the photosphere. The spectrum of the photons emitted at the photosphere for generic fireball scenarios is expected to be thermally distributed (e.g. Hascoët et al., 2013), although some sub-photospheric shocks could make it non-thermal (e.g. Beloborodov, 2017).

Because of the activity variations from the central engine, the ejected shells may have different Lorentz factors: at some point, the faster shells catch up with the slower ones, producing relativistic shocks called the "internal shocks" (Daigne & Mochkovitch, 1998). During these shocks, charged particles are accelerated to reach very high energies. These particles are thought to emit highly energetic photons through inverse Compton scattering and synchrotron emission, creating the prompt emission and its non-thermal spectrum. Magnetic re-connections could also play a key role in the emission of the prompt-emission photons (Beniamini & Giannios, 2017).

Since the shells are moving at relativistic speed, the beaming effect from special relativity plays a key role in the phenomena, narrowing the emission within a cone of angular size $\theta \sim 1/\Gamma$ and blue-shifting the spectrum. Note that this angle is different from the jet angle $\theta_j \sim 5 - 10°$(Goldstein et al., 2016; Lamb et al., 2021), and narrower ($\theta \sim 0.5°$ for $\Gamma = 100$). This implies that the only visible part of the jet is the part facing the observer, which emphasizes the importance of the viewing angle θ_v and reduces the impact of the jet angle θ_j as long as the shells have a high Lorentz factor (typically $\Gamma > 10$).

Once the shells reach the interstellar medium, they decelerate through "external shocks," creating the afterglow emission observable in the whole spectrum. These external shocks can also be accompanied by reverse shocks propagating back into the shells. The afterglow emission depends on many factors, such as the initial shock conditions (jet energy and magnetization, initial Lorentz factor), the external medium density evolution (stellar wind environment, classic interstellar medium, dense medium), and also effects from the jet

itself (jet opening angle, viewing angle, jet structure). Through the shocks, the shells decelerate, decreasing the influence of the beaming effect and allowing for lower energy emission, forming the X-ray and/or optical and/or radio afterglow.

1.4 Phenomenological description of a γ-ray burst

Section 1.2 has described how the different missions have increased our understanding of the γ-ray bursts, and Sec. 1.3 has introduced the GRB standard model. In this section, we present GRBs' current observational properties. We emphasize that GRB observed properties are complex and diverse, suggesting that the emission mechanisms are more complex than the picture of the standard GRB model presented above.

1.4.1 Prompt emission observations

The prompt emission relates to the first phase of the GRB, defined as *the temporal phase during which sub-MeV emission is detected by the GRB triggering detectors above the instrumental background emission level.* Nonetheless, the definition is not limited to the sub-MeV emission, as optical counterparts or supra-GeV emissions have also been detected during this phase. The sub-sections below describe the observational properties of the GRB prompt emission.

Temporal characterization

The GRB prompt emission lightcurves have diverse shapes and durations, exhibiting an irregular behavior. Some bursts have a single spike; others display several spikes that can be separated by up to several minutes, and there are even some bursts with an irregular extended emission. Most spikes exhibit a sharp rising phase with a shallower exponential decay, for which several authors have tried to create a parametrization (e.g. Norris et al., 1996; Kocevski et al., 2003; Norris et al., 2005). A small fraction of GRBs also has a precursor emission, typically softer than the main burst. Usually, its properties are similar to the ones from the main-episode emission, although the presence/absence of this precursor is entirely independent of the main emission properties.

Historically speaking, one of the most important temporal properties of GRB prompt emission was the measurement of its duration, T_{90} (the time interval inside which the detector collects 90% of the total GRB photon fluence). The first T_{90} observed by *PHEBUS* and *BATSE* (Dezalay et al., 1996; Kouveliotou et al., 1993) had two peaks, one for short-duration (~ 0.2 seconds) and another for long-duration (~ 20 seconds) GRBs. Moreover, it seemed that the short-duration GRBs had a harder spectrum than the long-duration ones. However, as this quantity is related to the energy range and instrument sensitivity, the *CGRO*/BATSE T_{90} distribution is different from the one obtained by *Swift*/BAT or *Fermi*/GBM. There have been some indications that the T_{90} distribution may even contain a third, intermediate duration class, although there is no strong evidence to support a distinct physical origin.

Short and long GRBs seem to have distinct origins, while some outliers exist, such as short GRBs with extended emissions such as GRB 050709 (Fox et al., 2005; Jin et al., 2016), long GRBs without supernova associated such as GRB 060614 (Gehrels et al., 2006) or short GRBs with an associated supernova GRB 200826A (Ahumada et al., 2021). Therefore, the prompt emission duration is not a sufficient criterion to infer the GRB progenitor origin.

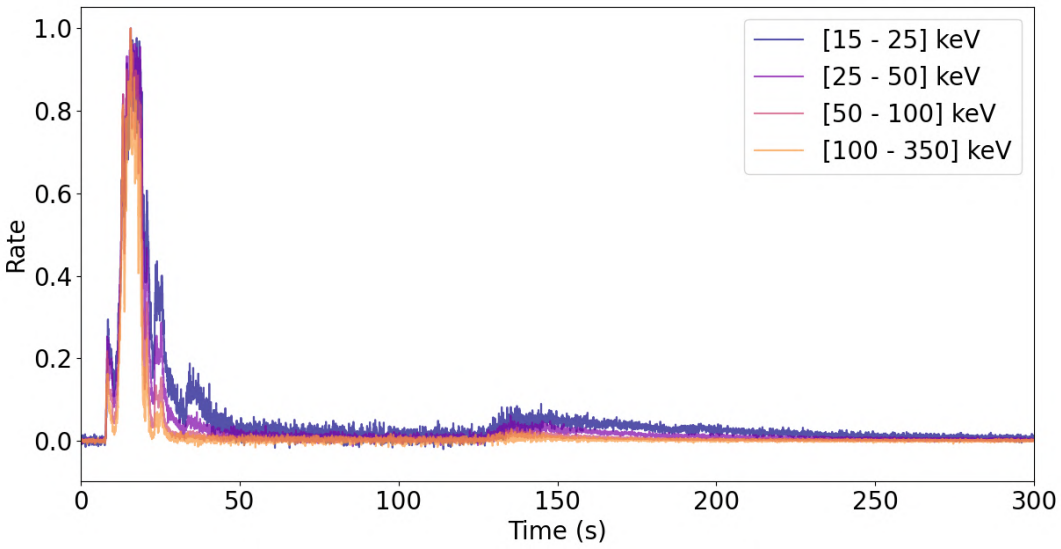

Figure 1.8. Examples of normalized lightcurve from GRB 130427A in different energy ranges. Credit: Adapted from *Swift*/BAT catalog

An important aspect of GRB lightcurves is their morphology variation relative to the energy bands in which they are observed. In most cases, the higher the energy, the narrower the spikes. The energy dependence of a GRB pulse width, $w(E)$, is a power-law function of the energy ($w(E) \propto E^{-\alpha}$), with typical index values of $\alpha \sim 0.3 - 0.4$ (Norris et al., 2005; Liang et al., 2006). This effect must be considered when observing high-redshift GRBs since the prompt emission detected in the sub-MeV range can come from energies up to 10× higher, reducing the typical pulse width by a factor of 2. This variation of morphology is illustrated in Fig. 1.8. The lightcurves, drawn from different energy ranges from the *Swift*/BAT instrument, have their intensity normalized relative to the peak. The extended emission is seen up to hundreds of seconds after the first spike is visible, mainly in the low energy ranges. Although the main spike has the same morphology for all the energies considered, the relative intensities of the intermediate spikes greatly vary depending on the energy range (see around ~ 30 seconds, for example).

Finally, it has been noticed that GRB lightcurves exhibit a spectral lag for energies below 10 MeV, especially for long GRBs: the emission in the softer band tends to be delayed with respect to the one observed in the harder bands. However, this property is not usually observed for short GRBs, where the spectral lag is not significant and even negative for some cases (Norris & Bonnell, 2006; Yi et al., 2006).

Spectrum

The main spectral characteristic of the GRB prompt emission is the non-thermal nature of its spectrum, already observed by *BATSE* (Band et al., 1993). That means there is a power-law distribution in flux at high energy instead of the expected exponential decay from the thermal spectrum.

The spectrum of a GRB prompt emission is often described by the photon spectral shape $N(E)$ [ph cm^{-2} keV^{-1}]. The fluence obtained from a given spectral shape can therefore be calculated as :

$$\int_{E_{\rm min}}^{E_{\rm max}} N(E)\ E\ {\rm d}E\ \left[{\rm erg\ cm^{-2}}\right] \tag{1.1}$$

The spectrum is normalized using the values $E_{\rm piv}$ [keV] and $A_{\rm norm}$ [ph cm^{-2} keV^{-1}]. The energy $E_{\rm piv}$ is often chosen depending on the spectral range of the instrument (e.g. 100 keV for *Swift*/BAT and *Fermi*/GBM for example), while $A_{\rm norm}$ is found during the spectral fit, corresponding to the normalization of a given spectral shape. When observations with a sufficient number of photons and within a sufficiently large energy band are available, the prompt emission spectrum is often well characterized by the Band model and its 3 parameters α, β and $E_{\rm peak}$ (Band et al., 1993) expressed as:

$$N(E)\ \left[{\rm ph\ cm^{-2}\ keV^{-1}}\right] = A_{\rm norm} \begin{cases} (E/E_{\rm piv})^{\alpha} \exp\left[-\frac{(\alpha+2)E}{E_{\rm peak}}\right] & \text{for } E < \frac{(\alpha-\beta)E_{\rm peak}}{\alpha+2} \\ (E/E_{\rm piv})^{\beta} \exp(\beta-\alpha) \left[\frac{(\alpha-\beta)E_{\rm peak}}{(\alpha+2)E_{\rm piv}}\right]^{\alpha-\beta} & \text{elsewhere} \end{cases} \tag{1.2}$$

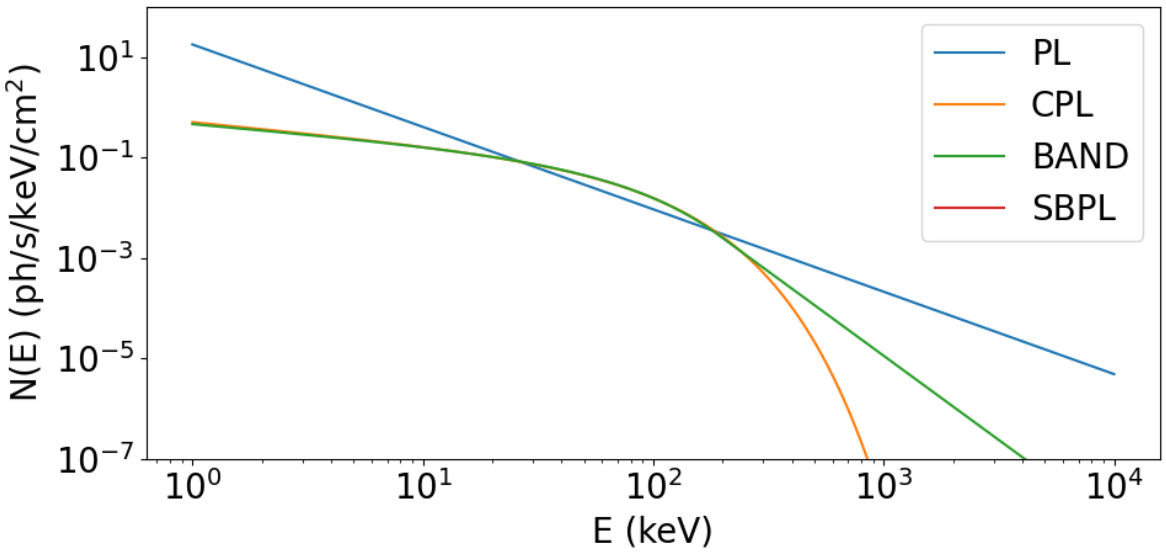

Figure 1.9. Examples of spectral fits for GRB 180314A observed by Fermi/GBM

The peak energy $E_{\rm peak}$ spans for over 3 decades of energy, ranging from $\sim$ 10 keV (Sakamoto et al., 2004) for XRFs to $\sim$ 10 MeV for the hardest bursts observed (Ackermann et al., 2010). However, this characterization is mostly available when the spectrum is measured

over a large energy range. For example, an instrument with an energy range between 15 and 150 keV, measuring a burst that has a spectrum following a BAND spectrum with parameters $(\alpha, \beta, E_{\rm peak}) = (-1, -2.3, 500\ {\rm keV})$, will struggle to constrain the peak energy and the β slope as they have little influence inside its energy coverage. For this reason, two models with fewer parameters are usually employed for instruments with smaller energy ranges, such as *Swift*/BAT (Lien et al., 2016):

- The comptonized model has 2 parameters α and $E_{\rm peak}$ and its formulation is:

$$N(E) = A_{\rm norm} \left(E/E_{\rm piv}\right)^{\alpha} \exp\left[-\frac{(\alpha+2)E}{E_{\rm peak}}\right] \tag{1.3}$$

- The power-law has a single parameter α and can be expressed as:

$$N(E) = A_{\rm norm} \left(E/E_{\rm piv}\right)^{\alpha} \tag{1.4}$$

Such spectral characterizations are primarily due to a lack of measurements rather than a physical reality: these models should be used with caution when calculating quantities such as the isotropic energy. The main risk is a miss-calculation of some quantities extrapolating the spectrum outside the energy range within which it has been measured.

The advent of the *Fermi* mission, with the GBM (Meegan et al., 2009a) and LAT (Atwood et al., 2009) instruments, has allowed a deep spectral characterization of the bursts over more than 6 orders of magnitude (from 10 keV to 10 MeV). Some GRB spectra dominated by a thermal component have been discovered, although the majority remain dominated by non-thermal emission. Moreover, a sub-dominant thermal component has been observed for some GRBs, suggesting that the prompt emission could have several emission mechanisms. For example, Guiriec et al. (2011) suggest that the photosphere emission could create the thermal component from the ejecta. High-energy observations by LAT also enabled the discovery of a high-energy component for some GRBs, suggesting a second $E_{\rm p}$ in the range $1 - 100$ GeV.

Finally, the spectral evolution during a GRB prompt emission mainly exhibits two types of evolution patterns. The first one is a hard-to-soft pattern, where the peak energy of the spectrum tends to decrease during the duration of the burst. The second one is an intensity tracking pattern, where the peak energy increases during the rising phase of the peaks. These two behaviors can also be seen in different peaks of the same GRB.

Very high-energy counterparts

GRB 190114C has been the first GRB with a joint detection between a γ-ray instrument and a very high energy gamma-ray detector at TeV energies by MAGIC (MAGIC Collaboration et al., 2019a) (and in space by *GBM* and *Swift*). Other very high-energy detections have also been made (Abdalla et al., 2019; de Naurois, 2019; Fukami et al., 2022), but with photons below the TeV energy. The spectral analysis up to ultra-high energies has allowed to identify an additional component in the afterglow emission, probably due to the inverse Compton up-scattering of synchrotron photons by high-energy electrons (MAGIC Collaboration et al., 2019b). Further simultaneous detections will enable to study the variability and spectral

shapes at very high energy, providing stringent limits on the jet bulk Lorentz factor and the nature of the processes involved (hadronic or leptonic interactions).

However, the attenuation of γ-ray photons via photon-photon pair production interactions with the extragalactic background photons make such detections difficult.The Cherenkov Telescope Array (CTA, Cherenkov Telescope Array Consortium et al. 2019), with its enhanced sensitivity in the energy range 10 GeV - 100 TeV, will most likely contribute to other conjoint detections of GRBs in the future (Inoue et al., 2013).

Energetic

From the spectral characterization of a GRB prompt emission and its redshift, it is possible to compute its isotropic energy, expressed as:

$$E_{\rm iso}\ [\rm erg] = \frac{4\pi D_{\rm L}^2(z)}{1+z} \int_{1/(1+z)}^{10^4/(1+z)} E\ N(E)\ \mathrm{d}E \tag{1.5}$$

The isotropic energy is used to compare the energetic of the bursts, assuming that the progenitor emits isotropically. This quantity is widely distributed among the GRBs, ranging from 10^{47} erg (for GRB 170817A, see Abbott et al. 2017) up to $\sim 10^{55}$ erg (for GRB 220101A, see Atteia 2022), with a possible cut-off in the distribution above $\sim 2 \times 10^{54}$ erg (Atteia et al., 2017). Nonetheless, the isotropic emission assumption is not exact since GRBs are produced by a jet-like emission. Therefore, some studies have tried to correct the beaming emission, considering the measured beaming angle when available. While this treatment narrows down the energy distribution, it remains still wide, contradicting the possibility of a "standard" energy reservoir (Frail et al., 2001).

There have been claims about a correlation between the energetic of the burst and the intrinsic peak energy of the prompt emission for long GRBs (Amati, 2006). This relation would allow the long GRBs to be used as "standard candles," similarly to what is done with SN Ia. However, several studies (Collazzi et al., 2012; Heussaff et al., 2013) have shown that this correlation is only partly accurate, being affected by significant selection effects.

Other relations linking the GRBs have also been found, such as the Ghirlanda relation (Ghirlanda et al. (2010), correcting the $E_{\rm iso}$ by the beaming factor effect) or the Yoneteku relation (Yonetoku et al. (2004), the relation between the peak luminosity and the spectral peak energy). However, they have also been challenged by other studies (Band & Preece, 2005; Shahmoradi & Nemiroff, 2011).

Polarization

The prompt emission polarization of GRBs could be one of the keys to identify the physical processes at stake in the GRB relativistic jets. For example, theoretical models involving synchrotron radiation from large-scale magnetic fields expect a linear polarization degree of up to 50% (Lyutikov et al., 2003). Predictions for photo-spheric emission and the associated polarization degree have also been made, expecting a polarization degree as high as 50% in the low energy range (Lundman et al., 2018). Under certain magnetic field conditions

(magnetic field lines aligned, little turbulence), the average polarization degree could be around 40% for a sample of GRBs (Toma, 2013).

For this reason, several missions aiming to measure the polarization of GRB prompt emission have been developed. One of the most successful is probably POLAR, where 55 GRBs have been detected (Kole et al., 2020). For these GRBs, the polarization on the time-integrated spectrum between 30 keV and 750 keV seems to be very low or null. These results are in tension with the ones obtained from the *AstroSAT* mission (Chattopadhyay et al. 2019 claim to have polarization degrees of up to 50% for some GRBs) or the *INTEGRAL* mission ((Götz et al., 2009) have found a polarization of $\sim 40\%$ on GRB 041229A). Future missions such as POLAR-2 (Hulsman, 2020) or eXTP (Zhang et al., 2016) might bring new observations to settle the crucial question of GRB prompt emission polarization.

1.4.2 Afterglow emission observations

As explained before, the afterglow emission was discovered as soon as it became possible to get fast and precise estimations of the prompt emission localization. This emission is observed in all wavelengths, from the hard X-ray to the radio, and its properties depend on the wavelength range considered. This part quickly summarizes the current observation status of this phenomenon.

X-ray afterglow

The large majority of bursts observed by *Swift*/BAT have an X-ray afterglow observable by *Swift*XRT. After the observations of hundreds of X-ray afterglows, a *canonical-lightcurve* (Zhang et al., 2006) has been created as a tentative to synthesize the behavior of the afterglows (see Fig. 1.10). Note that the five components of the canonical lightcurve are not observed for all GRBs, and some afterglows are entirely different from this model. The canonical X-ray afterglow is decomposed into the following parts:

A steep decay phase, with a temporal slope ranging from ~ -3 to ~ -10. This phase lasts between 10^2 and 10^3 seconds, explaining why the *Swift* mission was the only one able to detect it. Thanks to its fast repointing capabilities, Barthelmy et al. (2005b) discovered that this phase might be linked to the "tail" of the prompt emission. This decay follows the behavior predicted by the "curvature effect": the photons received being produced by internal shocks at higher latitudes relatively to the line of sight. This emission is received later, creating a signal dimmer than the prompt emission. This phase also exhibits a strong hard-to-soft spectral evolution which the curvature effect can explain under some assumptions on the prompt emission spectral shape.

The second part is the shallow decay phase, which can eventually become a plateau in some cases. In this phase, the slope of the X-ray afterglow lightcurve is almost constant for about $10^3 - 10^4$ sec. As discussed in Sec. 1.2, the physical reasoning behind this phenomenon remains debated among the science community, but it would involve a continuous energy injection from the central engine, either a black hole or a magnetar.

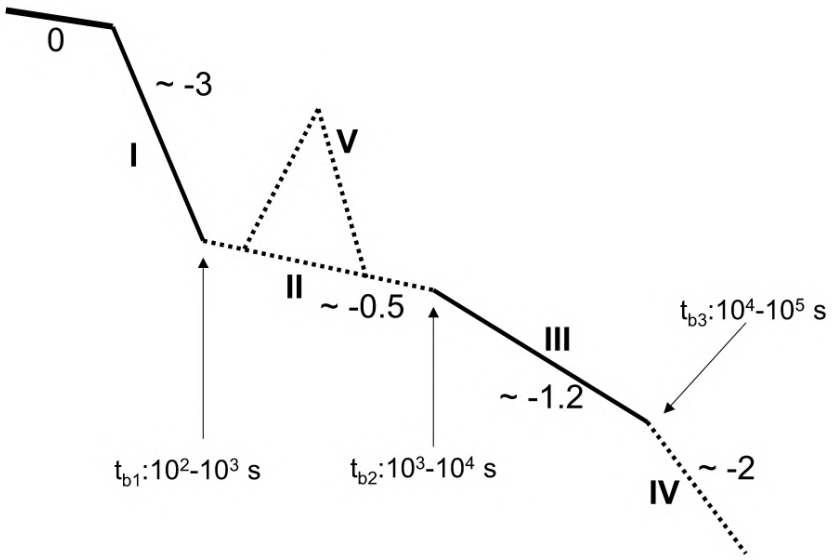

Figure 1.10. The canonical lightcurve description proposed by Zhang et al. (2006), containing the 5 components observed in GRB afterglows. Optional components are shown with dotted lines.

The third and fourth parts are essential in the afterglow characterization. Assuming that external shocks explain the afterglow, the break between the third and fourth phases is the jet break. Because of its deceleration by the interstellar medium, the Lorentz factor of the ejecta has a relativistic beaming angle that increases. This opening allows the observer to receive photons from higher latitude sites that were not previously in the line of sight (because of the relativistic beaming effect), explaining the relatively slow decay from the third phase. However, at some point, the relativistic beaming angle becomes more significant than the jet opening angle of the GRB, meaning that the de-boosting of the emission is not compensated anymore by the additional emission from higher latitudes. The time of this break allows the estimation of the jet opening angle if the redshift is also measured.

The fifth phase consists of the X-ray flares usually observed during the plateau phase, characterized by rapidly rising and falling lightcurves (although some have been observed up to 10^6 seconds after the prompt emission). At least one flare is observed in one-third of the GRBs, and the GRBs with flares exhibit on average ~ 2.5 flares in their afterglow. The fluence of these flares is variable, ranging from less than a hundredth of the prompt emission to greater than the prompt fluence. Nevertheless, many scientists noticed the flares and the prompt emission similarities, arguing that these two phenomena could be coming from the same site. Duque et al. (2021) explain, for example, that the early X-ray flares (typically happening $\leqslant 1000$ seconds after the prompt emission) could be produced by geometrical effects, the flares being "de-boosted" and delayed spikes of the prompt emission.

Optical afterglow

Usually, GRB optical afterglows can be decomposed into an early (within the first few hours after the burst) and late time (after a couple of hours) component. The early time afterglow has a complex behavior, displaying different features depending on the GRBs. Figure 1.11 shows some of these features, with, for example, optical flares that might be correlated to the prompt emission, early optical flashes (probably related to the external reverse shock), re-brightening and shallow/steep decay phases (similar to X-ray afterglows). As is the case for the X-ray afterglow, the early optical afterglow behavior might originate from both the external forward shock, the external reverse shock, or late-time outflows due to late central engine activity.

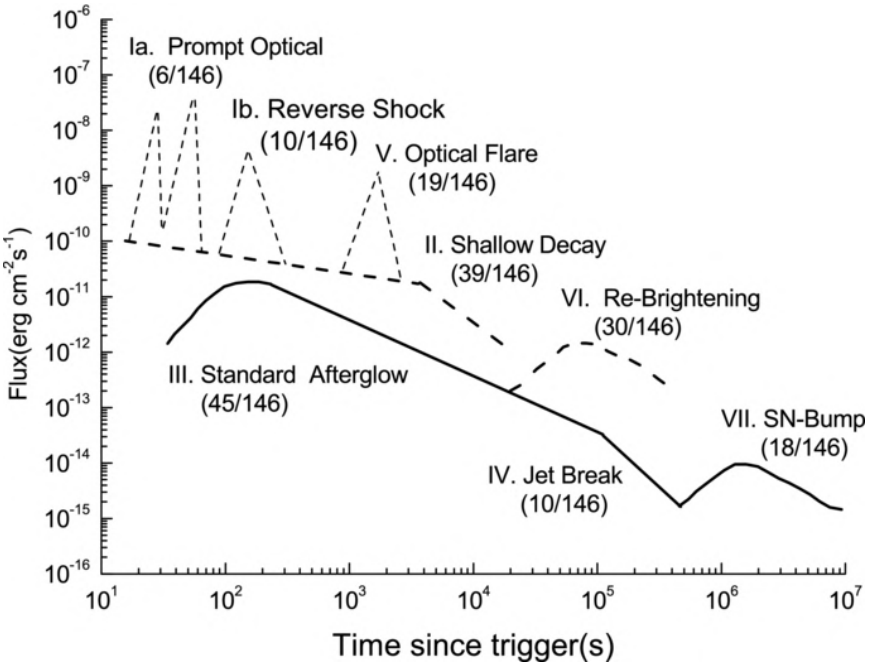

FIGURE 1.11. Schematic lightcurve of multiple optical emission components proposed by Li et al. (2012).

The late-time optical afterglow has a behavior that is much more regular and typically consists of a two-segment power-law decay, with a normal decay in $\sim t^{-1}$ that transitions into a steeper decay $\sim t^{-2}$. This break is explained by the same geometrical effect as the break observed in the X-ray afterglow. The jet break is thus expected to be achromatic.

By comparing the temporal evolution in the X-ray and optical bands, the chromatic or achromatic nature of the temporal breaks within the GRB afterglow can be investigated. An achromatic behavior happens when the X-ray and optical afterglows have a temporal break at the same time. On the other hand, a chromatic behavior happens when a break is identified in one band and not the other (or at a different time). Within the standard afterglow model, an achromatic behavior is expected because of hydrodynamical or geometrical effects. However, a chromatic break is much more difficult to explain within this framework unless there is a spectral index change across the temporal break (which is rare for X-ray afterglows).

Therefore, considering different emission sites for the optical and X-ray afterglow emissions is a potential explanation for this chromatic behavior.

Although most GRB afterglows have X-ray components, a good fraction of them $\sim 30-50\%$ do not have detectable optical counterparts. Removing the bias induced by the lack of deep observations from telescopes, the fraction of dark GRBs is estimated at around $\sim 10\%$ (e.g. Greiner et al., 2011). These so-called "optically-dark" GRBs are defined as GRBs with optical afterglows fainter than predicted by synchrotron model emission scaled with the X-ray flux. The main explanations for such phenomena are the high extinction of the host galaxy dust, the neutral-hydrogen absorption from the intergalactic medium for very distant GRBs, or an intrinsic lack of visible emission.

Radio Afterglow

The radio afterglows are particularly interesting to observe because of their slow evolution. Unlike X-ray or visible afterglows, they peak days to a few months and up to a year after the prompt emission (e.g. van der Horst et al., 2006). Therefore, they allow to follow the full deceleration of the ejecta in the circumburst medium, giving unique information about its global kinetic energy.

Using Very Long Baseline Interferometry (VLBI), the radio observations of the GRB 970508, GRB 030329, or GRB 170817A afterglows have allowed to measure the relativistic expansion of the jet, constraining the source size and its evolution (Galama et al., 1998; Granot et al., 2005; Troja et al., 2018). For GRB 130427A, radio observations of the afterglow have identified the reverse shock and its spectral evolution over time (Laskar et al., 2013; van der Horst et al., 2014).

1.4.3 Redshift determination

As explained earlier, the redshift determination of GRBs has been made possible with the detection of their visible afterglows. There are two possibilities for determining a redshift: it can be inferred from absorption lines from the host galaxy in the afterglow emission or the emission lines of the potentially identified host galaxy lying in the localization error box.

The first method is the most precise: it identifies galactic absorption lines in the continuum of the visible afterglow spectrum. Figure 1.12 from Kawai et al. (2006) shows on the upper spectrum the oxygen, carbon, and silicate lines in addition to the Lyman-α break in the visible afterglow of GRB 050904. Two objects create these absorption lines at different redshifts: one at $z = 4.84$ is responsible for some carbon lines, while the host galaxy creates the others at $z = 6.295$. The lower spectrum represents the one-sigma error of the upper spectrum. However, these observations require having a telescope able to gather enough light to perform the spectroscopic observations, which is for high-redshift GRBs mostly restricted to the 8-meter class on-ground and the HST in space. Moreover, as the afterglow fades rapidly, the observation has to be carried out quickly. Considering the availability of such telescopes, the localization of the GRB (it has to be on the side of the night hemisphere and visible for the telescope), and the instrumental constraints, it is sometimes impossible to have timely observations.

A photometric estimation is also possible with broad-band afterglow observations by observing the Lyman-α break. The hydrogen gas in the host galaxy and along the line of sight absorbs photons with wavelengths shorter than 121.6 nm, creating a deficit of photons that can be seen in the inset of Fig. 1.12. A photometric redshift can be determined by correctly identifying the so-called Lyman-α break. While the accuracy is less than for an absorption redshift, it also has less stringent constraints. For high-redshift galaxies, the Lyman-α break is shifted towards the near-infrared, observed at 973 nm at $z = 7$. Therefore, observing this break for high-redshift objects requires sensitive instruments in the visible and near-infrared wavelengths.

However, as explained before, a fraction of GRBs ($\sim 10\%$) do not have a detectable optical afterglow. Therefore, the method based on the optical afterglow is, in that case, not applicable.

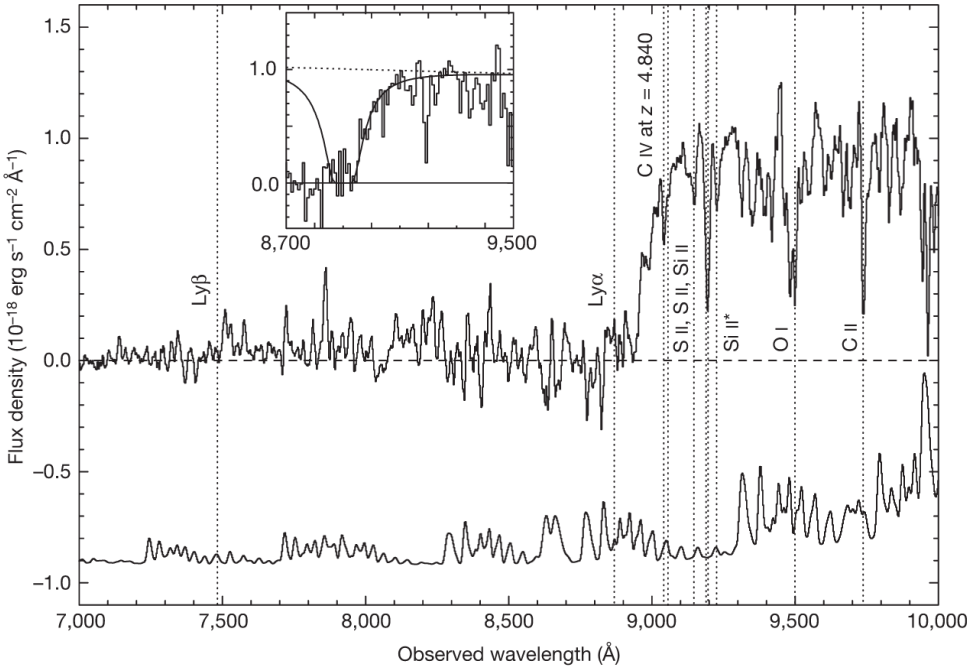

FIGURE 1.12. Example of absorption lines on the GRB 050904 afterglow spectrum. Credit: Kawai et al. (2006)

The second method to get the redshift of the GRB progenitor does not use the visible afterglow but the association with a host galaxy. Observing the error boxes from the X-ray afterglow makes it possible to identify one or several galaxies and calculate the chances of alignment for a given host galaxy. When these chances are sufficiently low to ensure this is not a simple coincidence, the GRB is associated with the host galaxy, and the redshift may be determined directly from the host galaxy by conventional methods (spectroscopic or photometric observations). However, this method is sometimes difficult to apply for very high-redshift galaxies, as the host is sometimes too faint to be detected. As a result, a foreground host can be mistakenly associated with a GRB coming from such an invisible background galaxy.

The *Swift* mission has been able to retrieve the redshift of $\sim 30\%$ of the GRBs detected by BAT. However, this sample is probably biased: it is, for example, complex to determine the redshift of a GRB with an afterglow that fades too quickly or is not bright enough in the visible wavelengths (e.g., dark GRBs). The Extended-BAT6 (Salvaterra et al., 2012b) or the SHOALS (Perley et al., 2016) catalogs have tried to mitigate the biases by introducing cuts in flux and fluence. However, these solutions are only half satisfying.

1.4.4 Supernovae and Kilonovae

As described before, GRBs are divided into two categories based on their prompt emission durations. Although it has been shown (see discussion about the prompt emission duration above) that this duration is insufficient to characterize the burst's origin, long GRBs have often been associated with supernovae and star-forming galaxies, suggesting that most of them are associated with the collapsar model.

Supernovae are the most ancient extra-solar transient phenomena observed. They have been divided into different categories, depending on the emission lines identified in their spectrum. Long GRBs are associated with the so-called Ibc supernovae, which originate from the core collapse of stripped massive stars (e.g. Stanek et al., 2003; Galama et al., 1998). They can be recognized thanks to their lack of hydrogen lines (ejected before the explosion by stellar winds) and display lines from elements such as oxygen, calcium, and magnesium.

As explained in Sec. 1.2, supernovae have been the smoking gun for the association of long GRBs with collapsars. However, the association of supernovae with long GRBs is only possible for a sub-sample of them: spectroscopically identifying a SN is only possible up to $z \leqslant 0.5$. It is also possible to match templates of Type Ic SN light curves with the photometric re-brightness observed in the afterglow $\sim 15 - 20$ days after the burst to increase this horizon to $z \leqslant 1$. Nonetheless, most long GRBs do not have a supernova association, as they happen at distances too high for detecting the SN.

For the long GRBs with an associated supernova, Figure 1.13 from Berger (2014) shows the distribution of SN peak magnitudes for long GRBs: the spread is more or less contained within one magnitude. The histogram on the left of the plot also shows the typical distribution for local Type Ic, showing that SN associated with long GRB are more luminous than an average supernova.

Nonetheless, few nearby long, e.g., GRBs GRB 060614 (Gehrels et al., 2006) and GRB 060505 (Fynbo et al., 2006) have no associated supernova down to ~ 7 magnitudes lower than the bulk of the SN associated with long GRBs. These long GRBs probably did not have a supernova associated with them (Jin et al. 2015 claim the detection of a kilonova). This indicates that at least some long GRBs might have progenitors with properties different from the collapsars.

Short GRBs, on the other hand, are thought to be associated with the merger of neutron stars. This time, the smoking gun has been the association of a gravitational wave detection GW 170817, from a NS-NS merger (Abbott et al., 2017b), with the simultaneous detection

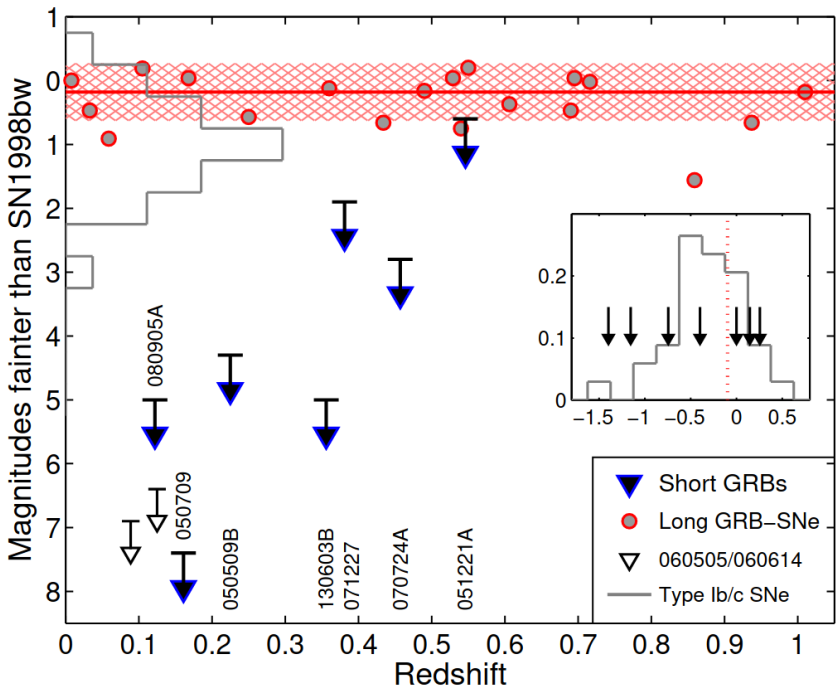

Figure 1.13. Supernovae associated with long and short GRBs relative to the peak absolute magnitude of the canonical long GRB-SN 1998bw. Credit: Berger 2014

of a short GRB, GRB 170817A (Goldstein et al., 2017a), and later an associated kilonova AT2017gfo (Tanvir et al., 2017). The kilonovae, a thousand times more powerful than a classical nova (explaining their denomination), are SN-like transients powered by the radioactive decay of the highly neutron-rich material (Metzger et al., 2010) ejected during NS mergers. Heavy radioactive elements are formed via rapid neutron capture nucleosynthesis, called r-process. These newly synthesized elements undergo nuclear fission, heating the ejecta, which then radiates this energy as thermal emission. Some potential kilonovae had already been observed in previous short GRBs (e.g. Hjorth et al., 2005; Troja et al., 2018; Fong et al., 2016a), but their observation remains difficult. Compared to supernovae, the kilonovae are dimmer and evolve faster: they peak between a few hours and one day after the GRB, depending on the wavelengths (the lower the wavelength, the sooner the peak).

To illustrate the difficulty of the SN/KN detection and their association with long/short GRBs with current observatories, let me briefly develop an example: GRB 211227A is a long GRB that was detected by *Swift*/BAT (Beardmore et al., 2021). Lü et al. (2022) claimed that this burst could be analogous to GRB 060614, considering that no SN has been seen down to stringent limits, and the claimed distance $z = 0.228$ (Malesani et al., 2021). They also consider that this redshift is too high to be able to detect the potential KN emission. However, several arguments confuse this picture: first, the optical afterglow has not been detected, so the redshift was determined from a potential host galaxy lying in the XRT localization error box. Second, the observations made by (Malesani et al., 2021), not mentioned in the paper, lead to an upper limit for the detection of a kilonova at

R-band Vega magnitude of $R = 24.5$. According to the kilonova templates presented in Lü et al. (2022), this observation carried $\sim 20,000$ sec after the burst should have detected the kilonova.

Therefore, this GRB might have happened in a galaxy at a higher redshift (e.g., $z > 1$), the identified host being a foreground galaxy that happened to be within the XRT FoV. In that case, the non-detection of the SN and KN for limits up to $R = 24.5$ would be easily explained, as the signal from both the SN and the KN would be too faint to be detected.

1.4.5 Multi-messenger astronomy

These recent years, astronomy has entered the multi-messenger era: observations are carried out thanks to electromagnetic emission but also gravitational waves, very high-energy particles (and photons), and neutrinos. The GRB science can benefit from this in many aspects.

Ultra High-energy cosmic rays

Ultra High-energy cosmic rays (UHECRs) have been observed by the Pierre-Auger observatory (Abraham et al., 2004) since 2005. Over the years, growing pieces of evidence seem to show that UHECRs above 8×10^{18} eV are emitted from extragalactic sources (Pierre Auger Collaboration et al., 2017). From this time, the search for potential progenitors of extragalactic UHECRs has intensified.

Because of the acceleration mechanisms happening during the internal and external shocks, GRBs have been seen as promising candidates for UHECRs (Vietri, 1995; Waxman, 1995). Murase et al. (2008) proposed that low-luminosity GRBs could favor even more the production of such particles, as the lower radiation luminosity would allow the heavy nuclei to more easily survive inside the sources. The connection of GRBs with UHECRs could constrain more the prompt and afterglow emission mechanisms.

However, the UHECRs are slower than the photons, so several thousands of years are expected between the GRB detection and the associated UHECRs: the detection of a prompt GRB emission with the associated UHECRs is not possible, removing the possibility of having a smoking-gun proof as for gravitational waves. Nonetheless, indirect signatures of these particles could be detected in the very-high energy portion of the spectrum.

Neutrinos

High-energy neutrino emissions are predicted within the standard model of GRBs, produced by the interaction of the baryons in the jet with the fireball photons in the internal or external shock regions. The fact that neutrinos barely interact with their surrounding could be used to probe the innermost region of the GRB central engine and assess the fraction of baryons within these regions. However, the detection of a high-energy neutrino coming from a GRB has not been made yet by the current most sensitive neutrino telescopes, IceCUBE (Abbasi et al., 2011) and ANTARES (Adrián-Martínez et al., 2013). Even by stacking the observations from the epochs coincident with GRB detection by γ-ray observatories, no

conclusive indication of detection has been found (Aartsen et al., 2015): classical GRBs might not be strong neutrinos emitters, implying some limits on the hadrons production for the GRB jets. Moreover, no neutrino has been found for the low-luminosity GRB 170817A by *IceCube*, *ANTARES* and the *Pierre Auger Observatory* (Albert et al., 2017), but this is consistent with model predictions of short GRBs observed at a large off-axis angle.

The IceCube collaboration has discovered an isotropic emission of high-energy neutrinos (IceCube Collaboration, 2013; Aartsen et al., 2014; Guetta et al., 2020) that is not correlated with any electromagnetic or cosmic-ray anisotropy. The plausible explanation is that high-energy neutrinos are of an extragalactic origin. The currently preferred progenitors of such TeV neutrinos are energetic events that are, however not too powerful (Murase & Ioka, 2013; Senno et al., 2016), such as choked jets and low-luminosity gamma-ray bursts (similar to candidates for UHECRs).

Gravitational Waves

Gravitational waves (GWs) are phenomena with essential implications in astrophysics. Predicted in 1916 by Einstein's general relativity, GWs are spacetime distortions created by accelerated masses, propagating through space at the speed of light. The currently detected signals of GWs are transient and are emitted by BHs and/or neutron stars (NSs) in close orbits: since they lose energy by emitting GWs, they inspiral closer and closer to each other to the point where they eventually merge into a BH or a high-mass NS. This last phase is detected thanks to giant Michelson interferometers (LIGO Scientific Collaboration et al., 2015; Acernese et al., 2015), monitoring the mirrors' spacing changes for distances as small as $\pm\ 2 \times 10^{-18}$ m. There have been 3 observation runs for the moment, conducted by the LIGO-Hanford, LIGO-Livingston, and VIRGO interferometers, called O1, O2, and O3, that have detected ~ 100 events in total (Abbott et al., 2019, 2020; The LIGO Scientific Collaboration et al., 2021b). The following observation run will start around Mars 2023, with the addition of the Japanese interferometer KAGRA (Abbott et al., 2018a).

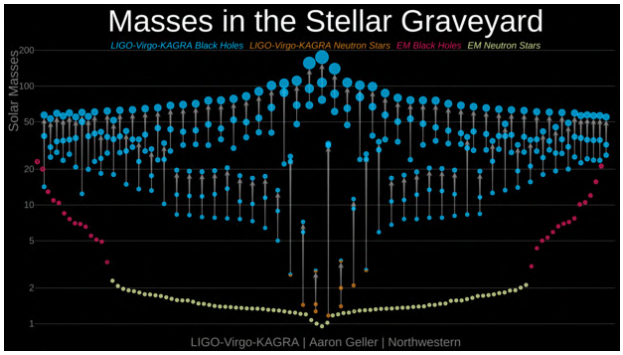

FIGURE 1.14. Masses of announced gravitational-wave detections of black holes and neutron stars. Credit: LIGO-Virgo / Aaron Geller / Northwestern University.

The three GW catalogs released (Abbott et al., 2019, 2020; The LIGO Scientific Collaboration et al., 2021b) had many consequences on the understanding of stellar BHs that traditional

photon-based observations had not given. Massive black holes with masses above 100 $M_\odot$ have been discovered (see Fig. 1.14 with the mass properties of the detected mergers), although the models struggle to form such objects because of the instabilities in the stellar core (e.g. Belczynski et al., 2016; Volonteri et al., 2021). The majority of BBH mergers observed through gravitational waves do not have high rotational speed (The LIGO Scientific Collaboration et al., 2021a), on the contrary of the ones detected in High-Mass or Low-Mass X-ray binaries (see Fishbach & Kalogera 2021 but also Belczynski et al. 2021a): this raises questions about the evolution mechanisms of binary system of massive stars, supposing that the BBH mergers observed are the products of massive binary star systems.

The multi-messenger observation of GW 170817 simultaneous with the detection of GRB 170817A (Abbott et al., 2017b; Abbott et al., 2017; Goldstein et al., 2017a) was a revolution in the GRB astrophysics (see Fig. 1.15(a) and 1.15(b) for the images of such a detection). Observed on the 17^{th} August 2017, a short GRB was detected at the same time and localization as the merger of two neutron stars. The implications of such a detection are numerous: the smoking gun for the association of short GRBs with neutron star mergers, an independent measurement of the cosmological constant H_0 (Abbott et al., 2017a), a constraint on the measurement of the velocity of gravitational waves or the investigation of the equivalence principle and Lorentz invariance (Abbott et al., 2017b). The discovery of similar events is highly pursued by some potential future γ-ray observatories such as *SVOM*.

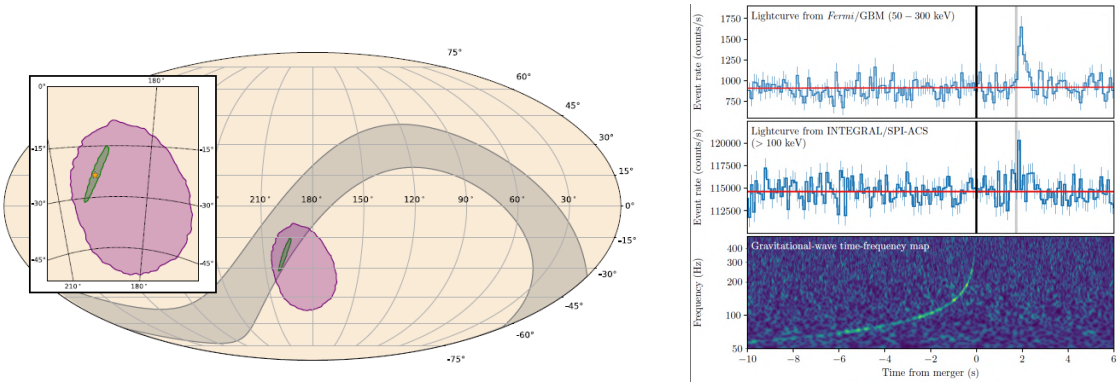

(a) (b)

Figure 1.15. (a) Final localization obtained for GW 170817: the green contour represents the LIGO-Virgo localization, the purple one the targeted search from *Fermi*/GBM. Credit: https://www.ligo.org/science (b) Joint detection of GRB 170817A with lightcurve from *Fermi*/GBM and *INTEGRAL*/SPI-ACS and GW 170817 with time-frequency map from LIGO-Hanford and LIGO-Livingston Credit: https://www.ligo.org/science

Moreover, the association or lack of association of a GW transient signal with some GRB events could help to shed some light on some puzzling GRB events, such as the SN-less long GRBs. GW interferometers, at their designed sensitivity, will be able to detect merger events up to $z \sim 1$, allowing them to probe a volume of Universe large enough to detect coincident on-axis GRBs potentially.

1.5 Thesis presentation

Previous missions can be used as references for the next generation of GRB observatories. For example, *BeppoSAX*, *HETE-2* and *Swift* have demonstrated the necessity to rapidly detect and localize the GRB prompt emission to be able to detect the afterglow emission and get a precise localization of the progenitor. For this reason, the spacecraft should be able to quickly repoint itself towards the prompt emission direction and quickly exchange information with the ground. Furthermore, the *BATSE* and *Fermi* (Meegan et al., 2009b) missions have also stressed the importance of the spectral characterization of the prompt emission to learn more about the physical phenomena at stake, requiring instruments with extensive spectral coverage.

Despite the advances made since the GRBs discovery 50 years ago, there are still many interrogations. This chapter has illustrated how the standard model struggles to explain some observations. The last years and the detection of GRB 170817A (with the gravitational wave event GW 170817 Abbott et al. 2017) and GRB 190814C (with photons beyond the TeV MAGIC Collaboration et al. (2019a)) have shown that an extensive scientific collaboration is necessary to shed some light on the GRBs mysteries, requiring multi-wavelength and multi-messenger coverage of the GRB events.

It is in this context that *SVOM* (Space-based multi-band astronomical Variable Objects Monitor, Wei et al. 2016), a Franco-Chinese mission dedicated to the study of GRBs and planned for the end of 2023, will operate. *SVOM* encompasses 2 wide field instruments (ECLAIRs Godet et al. 2014 and GRM Wu 2021) to detect, characterize and locate the prompt emission of GRBs. The satellite will then be able to slew towards this location in order to point its 2 other narrow field of view instruments (MXT Mercier et al. 2018 and VT Fan et al. 2020) to detect, characterize and locate precisely the afterglow emission of these same GRBs. In addition to these 4 instruments, SVOM also has 3 dedicated ground-based observatories (GWAC Han et al. 2021, C-GFT Niu et al. 2022, COLIBRI Fuentes-Fernández et al. 2020), allowing a dedicated follow up of each observed GRB. The whole mission has been built to maximize the follow-up of the detected GRBs thanks to its anti-solar pointing strategy: a GRB detection will be systematically made in an area of the sky immediately observable by ground-based telescopes. The mission and the different instruments that compose it are described in Chapter 2.

My thesis is mainly interested in studying the performances of the *SVOM* hard X-ray telescope, ECLAIRs (Godet et al., 2014). This telescope is the result of a collaboration between several French laboratories (APC, CEA, IAP, IRAP, LUPM), with the scientific responsibility at IRAP and the project management ensured by the CNES. ECLAIRs is a coded mask telescope with a large field of view of $90 times 90$ deg^2: coupled with its Unité de Gestion pour le Traitement Scientifique (UGTS, Schanne et al. 2019), this technology will allow to detect and localize (with an accuracy of a few arc-minutes) in near-real time the prompt emission of GRBs. The detection plane of the instrument (Nasser et al., 2014; Bajat et al., 2018a; Lacombe et al., 2018), consisting of 80×80 pixels in Cadmium Telluride (CdTe), makes it sensitive from 4 to 150 keV, allowing the detection of particularly interesting populations such as GRBs at high redshift. Thanks to all these features, ECLAIRs will

detect ~ 50 GRBs per year, with a dedicated follow-up by the other instruments of *SVOM* for most of them. ECLAIRs is described in more detail in Chapter 3.

I did my thesis during the assembly and the test campaign of the ECLAIRs flight model. Chapter 4 presents my contribution to the validation of the ECLAIRs mass model and the characterization of instrumental phenomena observed during the tests.

My thesis focused on the simulation of the behavior of ECLAIRs in space, unifying the work of several years from several laboratories (Antier-Farfar, 2016; Mate et al., 2019; Dagoneau, 2020). Chapter 5 presents the so-called astrophysical simulations (sky background, X-ray sources, GRBs) coupled with simulations of the information transmission chain of ECLAIRs (behavior of the UGTS and the electronics of ECLAIRs). These simulations contributed to the validation of several components of the flight software and also the update of the GRBs detection rate.

As ECLAIRs can transfer to the ground all the events recorded on board, this allows the development of ground detection algorithms, freed from the constraints that the on-board detection algorithm ECLAIRs will have. I thus developed my own detection algorithm, which I trained, validated, and tested thanks to the simulations presented in Chapter 5. Chapter 6 deals with an innovative approach, using a neural network with semi-supervised learning adapted to time series to complete the detection performances of the on-board algorithm.

The simulation work carried out has also allowed to understand better the astrophysical populations that will be visible by the ECLAIRs instrument. Thus, Chapter 7 presents a paper published in the journal *Astrophysics and Space Science* (Arcier et al., 2020). It deals with the detection performances of ECLAIRs for a sample of high-energy transients coming from the local Universe ($z < 0.3$), showing that the instrument will be able to detect the large majority of them. In addition to providing a detailed characterization of this population, I also developed potential synergies that ECLAIRs could have with other instruments of *SVOM* and observatories around the world.

Finally, Chapter 8 presents an independent study of *SVOM*, published in the journal *The Astrophysical Journal* (Arcier & Atteia, 2022). It focuses on populations of binary black hole mergers observed with gravitational waves and black holes formed during long GRBs. The increase in the number of events in the GWTC-3 gravitational wave catalog (The LIGO Scientific Collaboration et al., 2021b) has extended the results of Atteia et al. (2018). My work thus shows that the two populations are probably unrelated and paves the way for future studies using the O4 and O5 observations of LIGO, Virgo, and KAGRA (Abbott et al., 2018a).

Chapter 2

The *SVOM* mission

The Space-based multi-band astronomical Variable Objects Monitor (SVOM) is a sino-french mission principally dedicated to the study of GRBs. The mission and its context are presented in Sec. 2.1, the on-board and ground-based observatories in Sec. 2.2 and Sec. 2.3. Section 2.4 presents the observing strategy of *SVOM* and the consequences on the mission duty cycle. Finally, Sec. 2.5 presents the ground antenna network that allows the communication with *SVOM*.

Contents

2.1 Mission presentation

The SVOM mission was approved after a governmental agreement between France and China in 2014: it is a collaboration between the China National Space Administration (CNSA), the Chinese Academy of Sciences, and the french Centre National d'Etude Spatiales (CNES). In France, the CNES is in charge of the project management of the french payload (the ECLAIRs and MXT instruments), the VHF antennae network, and the SVOM French Science Center. The mission includes major instrumental contributions from Chinese and French laboratories, such as the Institut of High-Energy Physics (IHEP) and the National Astronomical Observatory of China (NAOC) in China and the Institut de recherche sur les lois fondamentales de l'univers (IRFU) and the Institut de recherche en astrophysique et planétologie (IRAP) in France, among others.

The *SVOM* satellite will be launched at the end of 2023 from the Chinese base of Xichang, on a quasi-circular orbit with an inclination of 30° and an altitude of 625 km (corresponding to an orbital period of 96 min).

As shown in Fig. 2.1(a), the *SVOM* satellite encompasses two wide-field instruments (ECLAIRs and GRM) and two narrow field ones (MXT and VT). Moreover, three dedicated ground-based observatories (COLIBRI, C-GFT, and GWAC) are used for the detected transients follow-up or the prompt emission detection (for GWAC).

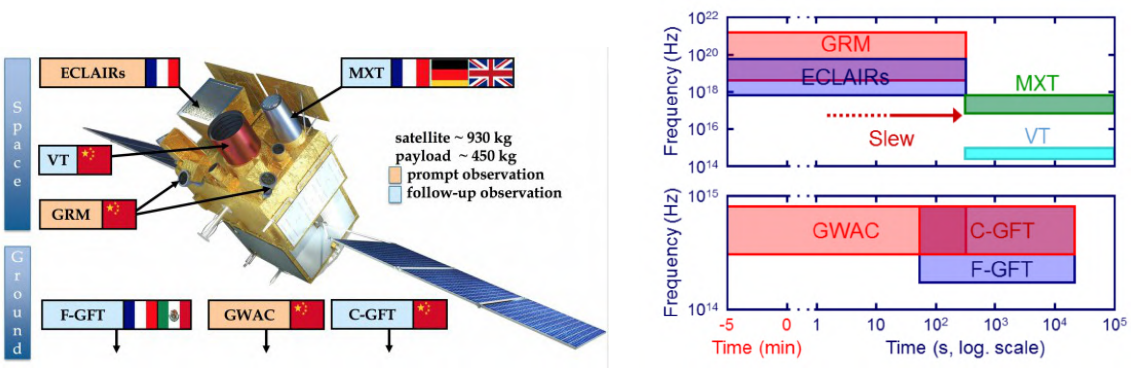

(a) (b)

Figure 2.1. (a) The SVOM satellite and associated instruments. Credit: www.svom.eu (b) *SVOM* spectral coverage of the GRB prompt and afterglow emission, as a function of time. Credit: Wei et al. (2016)

The *SVOM* spacecraft can re-point itself without ground intervention, based on the alerts distributed by the on-board instrument ECLAIRs. This automatic slew allows observing the earliest moment of a GRB, maximizing the probability of localizing it precisely as explained in Chapter 1. The sequence of observation of a GRB with *SVOM* is represented in Fig. 2.1(b) and can be described as follows:

(1) The wide-field instruments ECLAIRs and GRM monitor the sky, looking for GRB prompt emission in the hard X-ray and the γ-ray for GRM. When they detect a

new transient source, ECLAIRs gives an estimated sky position of the GRB, and transmits it to the satellite. It is important to note that a detection by GRM only will not lead to an accurate position determination. In case of detection (with or without precise localization), an alert is always transmitted to the science community with the first information retrieved from the burst.

(2) If the detection is made with a sufficient Signal-to-Noise Ratio (SNR), the *SVOM* satellite slews towards the target, pointing its narrow field instruments MXT and VT. These instruments detect the first epochs of the afterglow and narrow the localization error box to a few arc seconds. Moreover, the dedicated *SVOM* ground observatories also observe the ECLAIRs error box within a few tens of seconds after the detection.

(3) The refined localization obtained along with some of the burst characteristics are transmitted to the science community so that other observatories can perform dedicated follow-ups.

2.2 SVOM on-board instruments

This section presents the 4 on-board instruments of *SVOM*.

2.2.1 ECLAIRs

ECLAIRs is a wide FoV instrument, developed by IRAP, the Commissariat à l'Energie Atomique (CEA), the laboratory AstroParticules et Cosmologie (APC) and the Institut d'Astrophysique de Paris (IAP) under the supervision of CNES. It is a hard X-ray coded mask telescope, sensitive in the $4 - 120$ keV, aiming at detecting, characterizing, and localizing the prompt emission of the high-energy transients. The coded mask technology allows a relatively large FoV (2 sr) to maximize the number of GRBs detected (≈ 65 GRB yr^{-1}) with a localization precision (90% confidence level of 12 arcmin at detection limit) good enough to enable follow-up observations. Moreover, the detection and localization are made in near real-time thanks to the instrument on-board computer, allowing to perform this follow-up as soon as the burst has been detected. ECLAIRs characteristics are discussed more in detail in Chapter 3.

2.2.2 Gamma-Ray burst Monitor

The Gamma-Ray burst Monitor (GRM) is the second wide-field instrument on-board the *SVOM* satellite, dedicated to the detection and characterization of the GRBs prompt emission (Wu, 2021). The instrument has been developed at IHEP in Beijing and is composed of three scintillation detectors called Gamma-Ray Detectors (GRDs) (see Fig. 2.2(a)). Each GRD (see Fig. 2.2(b)) consists of a scintillation crystal of sodium iodide (NaI), with an individual surface of 200 cm^2 and a thickness of 1.5 cm, read by a photomultiplier. When an incoming γ-ray photon interacts with the scintillator material, it generates several optical photons whose signals are amplified by a photomultiplier tube attached to the crystal. As for ECLAIRs, each GRD can count the interacting photons one by one, recording their

arrival time and energy with temporal and spectral resolutions of respectively < 20 μs and 16% at 60 keV.

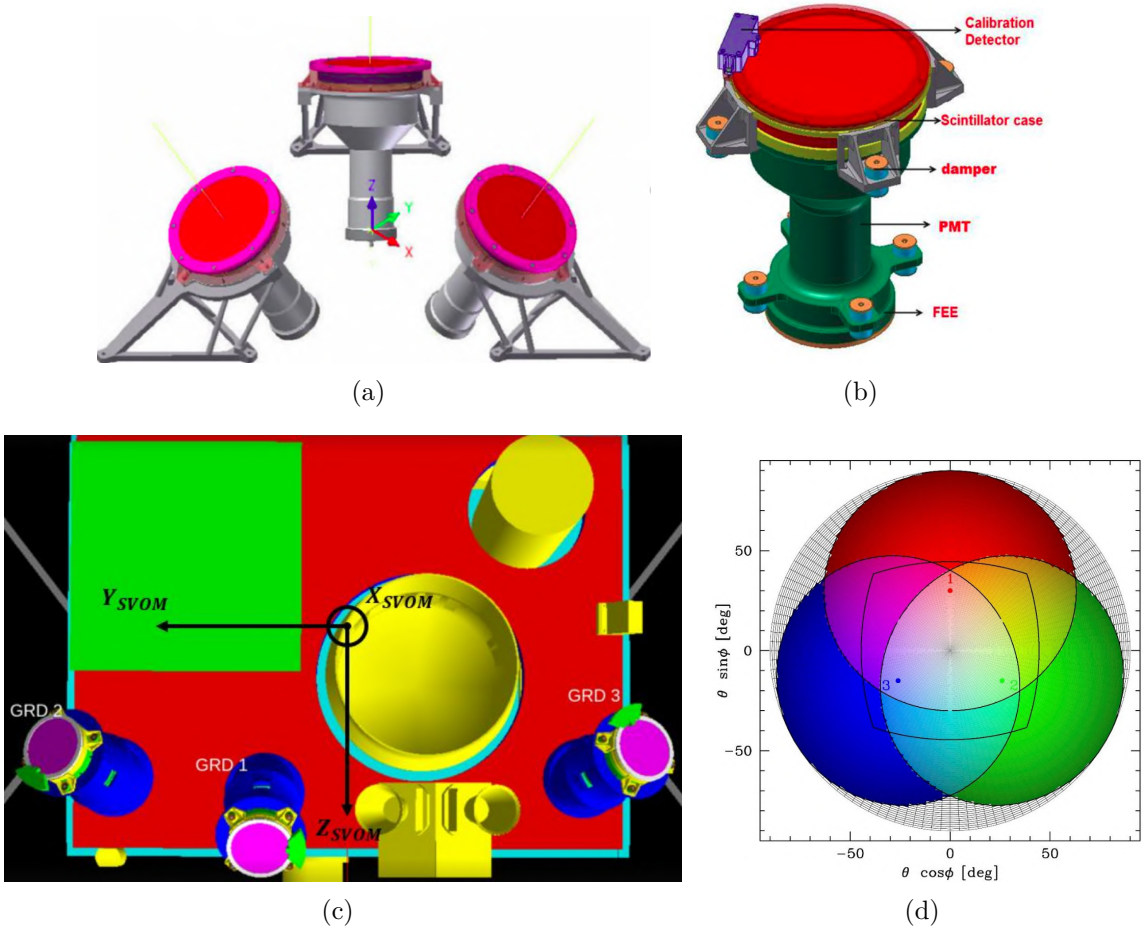

Figure 2.2. (a) The GRM CAD model, consisting of three GRDs (b) Detail on one GRD (c) GRDs localization on the SVOM platform with pointing directions spaced by 30° with respect to ECLAIRs pointing direction. (d) The three GRDs FoV (blue, green, and red) compared to the ECLAIRs instrument FoV represented by the square. Credit: (abc) IHEP (d) F. Daigne

Each GRD has an individual FoV of ~ 3.4 sr, pointing towards a direction inclined of 30 deg with respect to the ECLAIRs axis and spaced from each other in the perpendicular plane of 120 deg. Their physical location on the satellite platform can be seen in Fig. 2.2(c). The total field of view of GRM is 5.6 sr, combining the 3 GRDs. The intersection of the FoV of at least 2 GRDs is 2.8 sr, and the intersection of the FoV of the 3 GRDs is 1.0 sr. As shown in Fig. 2.2(d), they completely include the ECLAIRs FoV within the combination of their FoV.

Trigger algorithm of GRM

As for ECLAIRs, GRM has an on-board trigger system analyzing in real-time the counts received by the three GRDs. The trigger is based on 4 energy stripes ($15-50$ keV, $50-300$ keV, $300-1000$ keV and $1000-5000$ keV) and 3 timescales (0.1 sec, 1 sec and 4 sec). For each GRD the SNR is defined as:

$$SNR_{\mathrm{GRD_i}}(t,\Delta t,\Delta E)=\frac{C_{\mathrm{GRD_i}}(t,\Delta t,\Delta E)-C_{\mathrm{GRD_i}}(t-\Delta t_{\mathrm{bkg}},\Delta t_{\mathrm{bkg}},\Delta E)\times\frac{\Delta t}{\Delta t_{\mathrm{bkg}}}}{\sqrt{C_{\mathrm{GRD_i}}(t-\Delta t_{\mathrm{bkg}},\Delta t_{\mathrm{bkg}},\Delta E)\times\frac{\Delta t}{\Delta t_{\mathrm{bkg}}}}} \quad (2.1)$$

The quantity $C_{\mathrm{GRD_i}}(t,\Delta t,\Delta E)$ represents the number of counts received by the $\mathrm{GRD_i}$ in the energy stripe ΔE during the time interval $[t,t+\Delta t]$. The subtracted term at the numerator of Equ. 2.1 represents the background estimation made on a timescale of $\Delta t_{\mathrm{bkg}}=16$ sec for the same GRD and energy stripe. The background at time t is estimated based on the counts received on the time interval $[t_i(t)-\Delta t_{\mathrm{bkg}},t_i(t)]$, where $t_i(t)$ is the 16 seconds time interval containing the time t.

The GRM triggers when the SNRs of at least two GRDs exceed the thresholds defined for the same time interval and energy stripe. There are $3\times4=12$ adjustable thresholds for each GRD, one per timescale and energy range. The GRBs' crude localization (within 15×15 deg^2) will only be performed when the 3 GRDs simultaneously trigger.

Thanks to this algorithm, GRM will detect >90 GRBs per year (see Sec. 5.6.2). GRM is expected to detect some short hard bursts that are either undetectable for ECLAIRs or not within its FoV. However, detecting a GRB with GRM alone does not trigger a slew request to the *SVOM* instrument, as the localization precision is too poor. The detection alert is nonetheless transmitted to the ground.

Synergies with ECLAIRs

This instrument nicely complements ECLAIRs thanks to its more extensive energy range (from 15 keV to 5 MeV). The majority of the GRBs detected by ECLAIRs will also be detected by this instrument, allowing an extensive spectral characterization (Bernardini et al., 2017), lacking, for example, for the *Swift*/BAT instrument as explained in Sec. 1.4.1. The hard spectral bands of GRM also allow computing hardness ratios between ECLAIRs and GRM, which might be determinant for classifying the bursts.

Moreover, when ECLAIRs receives a trigger signal from GRM, it is possible to lower its detection algorithms thresholds (see 3.5), as the probability for ECLAIRs to detect a burst is increased. This might increase the number of GRBs seen by both ECLAIRs and GRM.

2.2.3 Micro-channel X-Ray Telescope

The Micro-channel X-Ray Telescope (MXT, Götz et al. 2014; Mercier et al. 2018) has been developed by the CEA and IJCLab, in collaboration with the Leicester University in UK

and the Max-Planck Institut für Extraterrestrische Physik (MPIE) in Garching Germany, under the supervision of CNES.

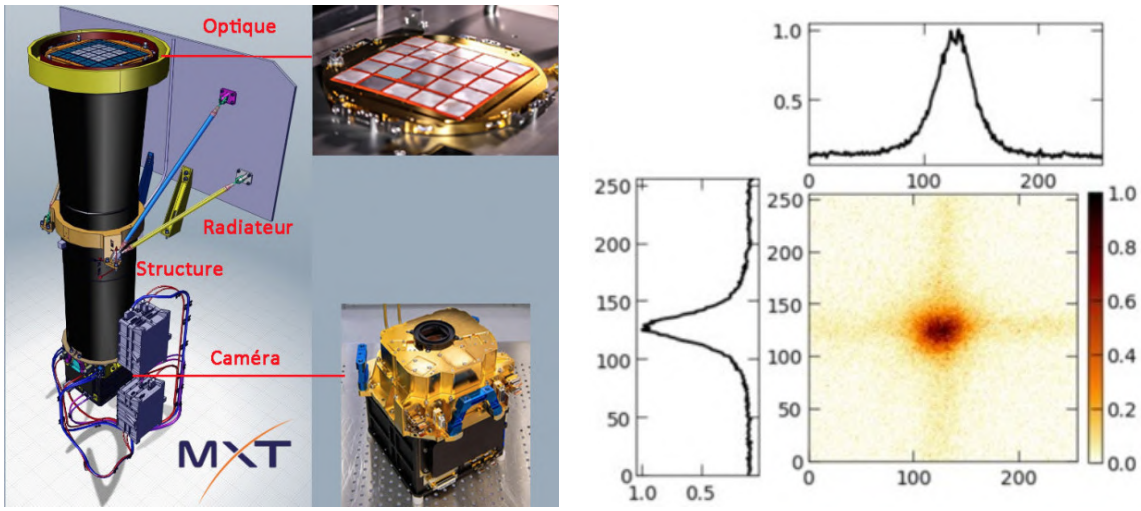

(a) (b)

Figure 2.3. The Microchannel X-ray Telescope CAD model with its main components (a) and its specific point spread function (b). Credit: CEA/CNES

MXT (whose major components can be seen in Fig. 2.3(a)) is a so-called *lobster-eye* telescope[1]: micro-pore optics of 40 microns are arranged in a configuration that focuses the X-ray beam onto the 256×256 pnCCD detector. The Wide-field X-ray Telescope (WXT, Liao et al. 2017) equipping the future Einstein-Probe spacecraft also share the same technology. MXT has been calibrated at the PANTER X-ray facility where many other instrument from X-ray missions such as *XMM-Nexton*, *Spektr-RG*, *Suzaku* or *Swift* have also been calibrated.

The telescope has an energy range of $0.2 - 10$ keV and an energy resolution of ~ 75 eV at 1.5 keV. With an effective area equal to 23 cm^2 at 1 keV, MXT has a detection sensitivity of 10^{-12} erg cm^{-2} s^{-1} for 10 ksec of observations. With such sensitivity, GRB afterglows will typically be observable by the instrument up to 24h after the prompt emission detection. The FoV of MXT is 1.1×1.1 deg^2, large enough to contain the raw localization error box of ECLAIRs entirely. The localization precision of the afterglow emission is expected to be below 1 arcmin, going as low as 13 arcsec for the 50% brightest GRBs, within 5 minutes of the trigger. MXT can ask for a second slew of the satellite towards the refined localization when necessary, improving the afterglow detection and localization performances of *SVOM*.

Moreover, MXT will measure the absorption along the line of sight of GRB afterglows, both from the intergalactic medium and from the host galaxies. The instrument will also be able to measure the spectral index of the afterglow emission and even the prompt emission in the case of very long duration bursts, overlapping the ECLAIRs energy range.

[1] https://www.svom.eu/en/portfolio/mxt-langouste/

2.2.4 Visible Telescope

The Visible Telescope (VT, Wu et al. 2012; Fan et al. 2020) is dedicated to the follow-up of the optical afterglow emission (see Fig. 2.4(a)). The telescope has been developed by the XIOPM (Xi'an Institute of Optics and Precision Mechanics).

The VT is a Ritchey-Chretien telescope with a primary mirror of 40 cm. It has a 26 × 26 arcmin^2 FoV, large enough to contain more than 90% of ECLAIRs localization error boxes. The instrument will be able to localize the afterglow emission of the GRB with a sub-arc-second precision, giving a localization error box small enough so that the 8-meter class telescopes can point towards it and measure its spectrum.

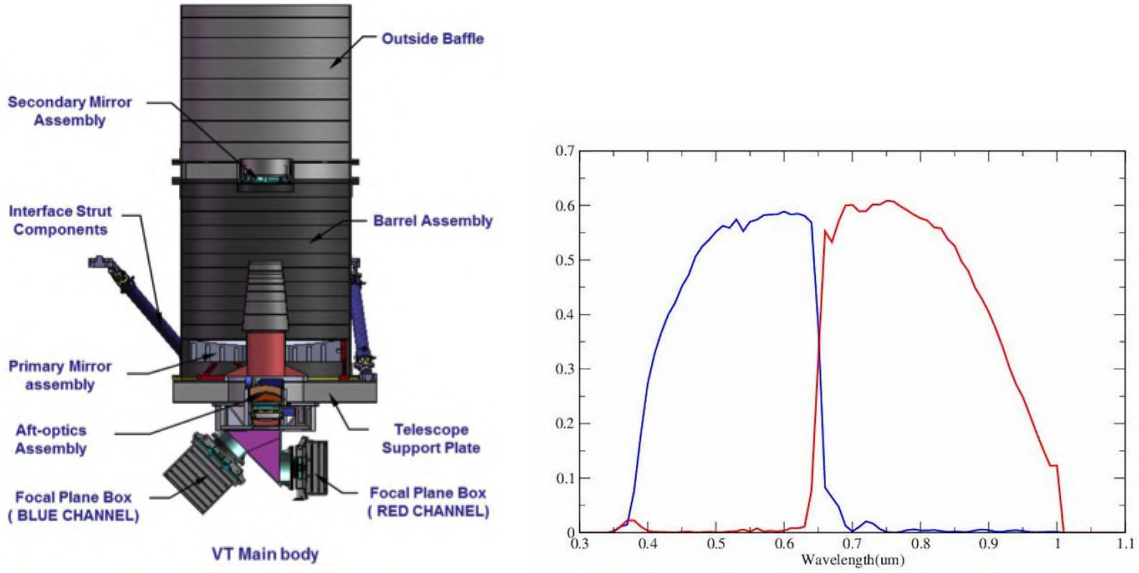

(a) (b)

FIGURE 2.4. (a) The Visible Telescope CAD model and (b) its spectral response for the blue and red filters. Credit: NAOC

The telescope's focal plane is equipped with two CCD cameras with 2048 × 2048 pixels. They cover the blue and red optical wavelengths (respectively $450 - 650$ nm and $650 - 1000$ nm), reaching a magnitude in the visible of 22.5 in 300 seconds exposure. A dichroic beam splitter separates the two channels, allowing simultaneous observation with both cameras. As we can see in Fig. 2.4(b), the quantum efficiency of the VT CCD detectors in the red channel is close to 50% at 0.9 μm, which allows the detection of GRB afterglows in the beginning of the near-infrared (NIR).

Only 3.5% of the redshifts determined with *Swift* are above $z \sim 5$, representing $\sim 1\%$ of the GRBs detected by *Swift*/BAT. However, theoretical calculations predict a fraction of high-z GRBs among the detected GRBs of 5 to 7% (Salvaterra, 2015). A possible explanation is that the optical images provided by the visible telescope UVOT on-board *Swift* are not sensitive enough to quickly identify the visible rising afterglow for high-redshift GRBs, as UVOT does not cover the NIR. As this afterglow is required to get a position precise enough

so that ground telescopes can perform spectroscopic observations and measure a redshift, high-z GRBs could be under-represented among *Swift* GRBs with a redshift. Therefore the VT, covering the NIR, will most likely increase the number of high-z GRBs detected.

2.3 SVOM ground-based observatories

In addition to the instruments presented above, the *SVOM* mission has 3 ground observatories dedicated to the prompt emission observation and the afterglow follow-up of *SVOM* GRBs. They are presented in this section.

2.3.1 GWAC

The Ground-based Wide-Angle Cameras Network (GWAC-N, Han et al. 2021) is composed of nine GWAC-A (GWAC Arrays) and several robotic, multi-band, small FoV telescopes (GWAC-F60A/B and GWAC-F30). It has been designed to simultaneously search for the optical prompt emission of GRBs detected by the ECLAIRs and GRM instruments. The GWAC-A will point towards the central part of the ECLAIRs FoV: its FoV will represent $\sim 12\%$ of the total ECLAIRs FoV. The GWAC-A will attempt to detect the prompt and/or afterglow emission from the GRBs, while the narrower FoV instrument will automatically validate and follow the detected candidates.

Figure 2.5. Panoramic view of GWAC installation at Xinglong Observatory (Beijing, China) showing 4 GWAC-A mountings (right) and the 60 cm and 30 cm telescopes (left). Credit: NAOC

The nine GWAC-A mounts are equipped with two types of cameras:

- There are 4 Joint Field of View (JFoV) cameras with an individual FoV of $\sim 12.8 \times 12.8\,\mathrm{deg}^2$. These cameras consist of a refractive lens with an aperture of 180 mm, which is equipped with 4k × 4k CCD cameras. Using these four cameras available for one GWAC-A telescope, the collective FoV reaches $\sim 25 \times 25\ \mathrm{deg}^2$. The limiting magnitude of these cameras in the R-band is 16 mag for a 10 s exposure, reaching a typical magnitude of 18 when stacking the images.
- The Full Field of View (FFov) camera has an aperture of 3.5 cm and covers roughly the same FoV as the 4 JFoV cameras. This camera is used to guide and extend the optical flux coverage to ~ 6 mag in the R-band at the bright end.

The system is also used for Target of Opportunity (ToO) observations to search for the optical counterparts of transient events or gravitational waves detection from LIGO/Virgo interferometers. They have already participated in the search of such counterparts during the O2 and O3 runs, leading to the emission of several GCNs such as Wang et al. (2020); Turpin et al. (2020a,b).

2.3.2 C-GFT

The Chinese Ground Follow-up Telescope (C-GFT) has a 1.2-meter diameter primary mirror and is based on an existing telescope located at the Jilin observatory. Two instruments equip the telescopes: one at the Cassegrain focus and one at the primary focus. The secondary mirror can be manually moved to use one instrument or another. The C-GFT will reach a sensitivity of 20 mag at 10σ in the r-band for 300 seconds exposure time during new moon nights.

FIGURE 2.6. Dome at the Jilin Observatory (left) and the C-GFT telescope (left). Credit: Jilin Observatory

The instrument at the Cassegrain-focus has a field of view of 21×21 arcmin^2 and is sensitive in the $400 - 950$ nm wavelength range. The instrument has 3 SDSS filter channels (g, r, and i), each equipped with low read time CMOS-CCD cameras with a size of $2\text{k} \times 2\text{k}$ (Niu et al., 2022). It will be able to take exposures in the 3 channels simultaneously. The primary-focus instrument covers a larger FoV of 1.5×1.5 deg^2 thanks to its $4\text{k} \times 4\text{k}$ camera.

The telescope will be exceptionally responsive to *SVOM* alerts thanks to the robotic control, real-time data, and communication systems.

2.3.3 COLIBRI

COLIBRI is the 1.3-meter robotic telescope under french responsibility (Fuentes-Fernández et al., 2020), located in San Pedro Mártir, Baja California, Mexico. The telescope has a sensitivity of ~ 22 in the r-band for a 300 seconds exposure at 10σ. It will be able to point to any source in the sky in less than 30 seconds, allowing to study the first minutes of GRB afterglows. COLIBRI has two cameras, DDRAGO and CAGIRE (CApturing Grb InfraRed Emission). An illustration of the telescope can be found in Fig. 2.7(a).

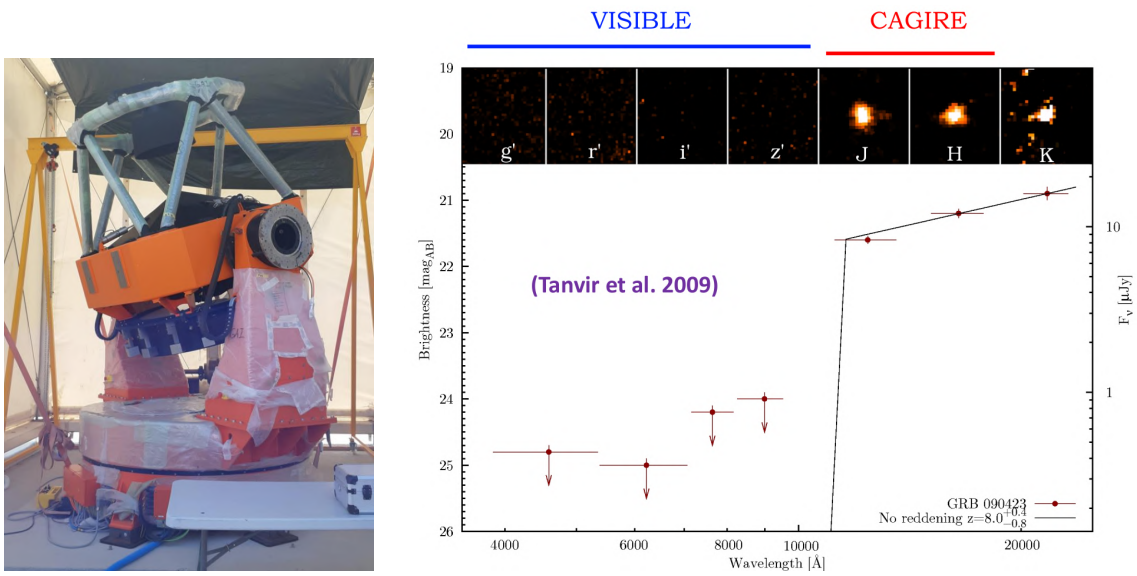

(a) (b)

FIGURE 2.7. (a) The COLIBRI telescope. Credit: OHP (b) Photometric observations of a GRB 090423 ($z = 8.0^{+0.4}_{-0.8}$) from Tanvir et al. (2009)

The DDRAGO instrument observes in two channels, a blue one (Pan-STARRS g, r and i filters) and a red one (z and y filters). It has a FoV of 26×26 arcmin^2 with two $4\text{k} \times 4\text{k}$ CCD detectors.

CAGIRE is a NIR camera located at the same Nasmyth focus of COLIBRI, allowing observations between 1.1 and 1.8 μm with a FoV of 21×21 arcmin^2. The instrument is equipped with a LYNRED sensor with 2048×2048 15 μm pixels and incorporates an automated reduction and analysis system (Nouvel De La Flèche et al., 2022). The motivation is to detect and monitor GRB afterglows up to redshift ~ 11, where the Lyman break at $\lambda = 91.2$ nm is translated towards the NIR bands.

CAGIRE and DDRAGO will operate conjointly thanks to a dichroic splitting the beam between visible and NIR light. A combination of such afterglow observations will enable a photometric estimation of the redshift for high-z GRBs, as illustrated in Fig. 2.7(b).

2.4 The SVOM observation strategy

SVOM observation strategy has been defined carefully to take into account the space environment's constraints and optimize the follow-up from ground observatories. This section defines the three observation programs for the *SVOM* mission and describes the B1-law, which is the attitude pointing law. It also briefly explains the consequences of the orbit and pointing of *SVOM* on the instruments' observations.

2.4.1 The Core, General and ToO programs

The *SVOM* observation program is divided into three categories: the *Core Program*, the *General Program* and the *Target of Opportunity* (*ToO*) *Program*. The fraction of the observation time allocated for each category can be found in Fig. 2.8(a). The programs are defined as follows:

- the *Core Program* regroups observations related to the detection and characterization of the prompt and afterglow emission of GRBs detected by *SVOM* instruments.
- The *ToO Program* of *SVOM* manages unplanned observations of transient and variable sources. It corresponds, for example, to the follow-up observation of a portion of the sky following a GW (ToO Multi-Messenger), FRB, or galactic SN alert. The scientific community can apply for ToOs, and their scientific interests will be evaluated by the *SVOM* PIs. Once the observations are accepted, they can be performed within several hours.
- The *General Program* (GP) deals with observations that have been pre-planned, open to all scientists answering the *SVOM* yearly calls for observation proposals. A Time Allocation Committee evaluates them based on their scientific merit. GP observations consist, for example, of the monitoring of X-ray sources or the observation of the Virgo cluster. The GP considers the constraints set by the Core program, allowing pointing only towards sources close (i.e., within 5° to 10°) to the B1 attitude law. Nonetheless, observations outside the B1-law constraint during 10% of the GP useful time could be allowed to increase the scientific interest of the program.

2.4.2 B1-law for the Core program

The *Core* program constrains the attitude law of the satellite with an anti-solar, out of the galactic plane, pointing strategy: this attitude law is called the "B1-law". Figure 2.8(b) illustrates the exposition time of a sky portion in galactic coordinates over one year when the *SVOM* satellite follows this law. The main advantages of such a pointing are the following:

(1) The instruments' optical axes are pointed at a maximum of $\sim 45°$ from the anti-solar direction, preventing sun rays from altering the instruments' sensitivity or damaging them. Moreover, when a transient is detected and located by ECLAIRs, an immediate follow-up from ground observatories is possible since it is night-time on this side of the planet.

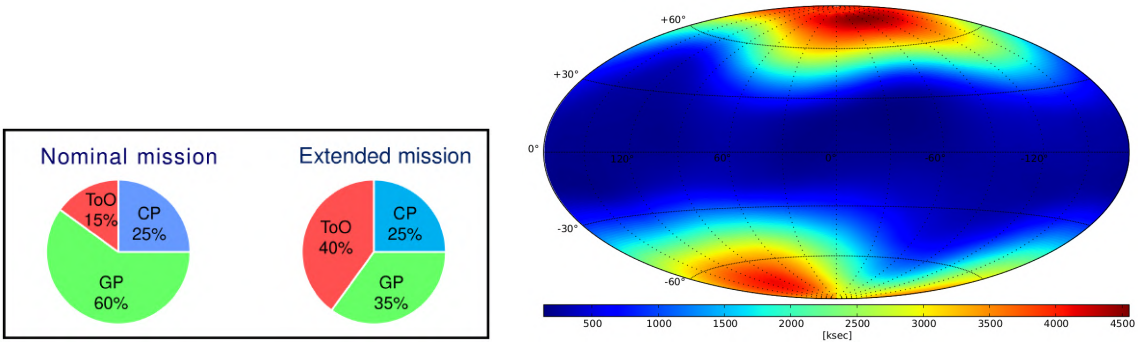

(a) (b)

FIGURE 2.8. *SVOM* pointing strategy with (a) Fraction of dedicated observing time for the three programs, for the nominal and extended mission (b) Sky exposure (ksec) in galactic coordinates for ECLAIRs Credit: Wei et al. (2016)

(2) Pointing within the galactic plane (defined as galactic latitudes $|b| < 10°$) is avoided by ECLAIRs when possible, as most of the intense X-ray sources are located there (see the X-ray sources map from Dagoneau 2020 on Fig. 5.7). Such objects within the ECLAIRs and/or GRM FoV might perturb the trigger algorithms and decrease the sensitivity.
(3) The extremely intense X-ray source Sco-X1 is retained outside the ECLAIRs FoV.
(4) The most observed regions in the sky are also the ones observable by large ground telescopes such as the VLTs, GTC, Keck 1&2, Subaru, Gemini, ...

2.4.3 Consequences of SVOM attitude and orbit

The pointing law of *SVOM* and the low-Earth orbit characteristics have two significant consequences on the observations of *SVOM*.

Earth transit within the FoV

The Earth transits systematically in the FoV of *SVOM* instruments, meaning that the background seen by the instrument is highly variable (illustrated in Fig. 5.2 for example). This variable background has to be taken care of in the trigger algorithms of ECLAIRs and GRM, with, for example, the implementation of a background estimation when calculating the SNR. Precedent gamma-ray missions (*HETE-2*, *Swift*, *Fermi*) also have a low-Earth orbit, which has inspired the ECLAIRs and GRM algorithms.

ECLAIRs and GRM trigger algorithms will be deactivated when the Earth is entirely inside their FoV. In total, $\sim 30\%$ of the GRBs will be missed by ECLAIRs and GRM because they will occur at sky locations occulted by the Earth. Figure 2.9 illustrates how the available FoV varies with each orbit. The combination of ECLAIRs and the 3 GRDs represents the FoV for which the maximum GRB signal can be collected for each instrument. The two GRDs combination represents the FoV in which a burst could trigger the GRM algorithms.

Because of its large FoV and the absence of imaging, GRM will also be perturbed by the X-ray sources rising in their FoV. The trigger of GRM will be deactivated when GRM exits the Earth's shadow so that the bright X-ray sources appearing inside GRM FoV do not create false alarms. Therefore, the duty cycle of GRM is even more impacted than ECLAIRs for some galactic pointing of *SVOM*.

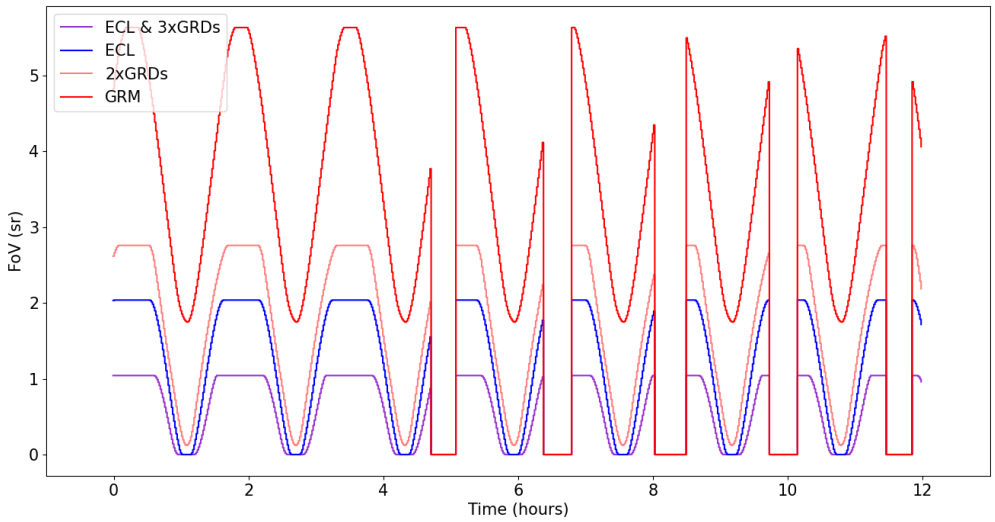

Figure 2.9. FoV of the intersection of ECLAIRs and the 3 GRDs, ECLAIRs, the intersection of at least 2 GRDs and the GRM for half a day.

SAA crossing

The satellite crosses the South Atlantic Anomaly (SAA), a region around the Earth where the concentration of trapped protons and electrons is much higher. The background becomes so large that it prevents any observation inside this zone. Moreover, the so-called activation effect creates an additional noise component that persists and decay for several tens of minutes after exiting it (e.g. Hajdas et al. 2004 for the *RHESSI* mission, Biltzinger et al. 2020 for the *Fermi*/GBM mission or He et al. 2020 for the simulations on GRM). The on-board trigger algorithms of ECLAIRs and GRM will be deactivated during this phase, and the high-voltage applied on the detection plane will be switched off for the longest SAA crossings to prevent the polarization of the detection plane.

The field of view available evolution relatively to time is illustrated in Fig. 2.9 for 12 hours of orbits (the abrupt decreases of the FoV represent the SAA crossing). It is estimated that the ECLAIRs and GRM instruments will lose $\approx 20\%$ of their observing time because of the SAA. While some orbits will cross the SAA when the satellite points towards the Earth (thus with fewer consequences on the duty cycle), some, like the one illustrated in Fig. 2.9, will have the SAA crossing right when the instrument FoV is maximum.

Taking the SAA and the Earth transit, ECLAIRs and GRM can detect GRBs during $\sim 50\%$ of their observing time.

2.5 The ground stations network

The observation strategy of *SVOM* has been built to maximize the follow-up of the detected GRBs from the ground. Here we briefly describe how the *SVOM* communicates its information with ground stations and how this information can be broadcast to the scientific community.

2.5.1 GCN system

The Gamma-Ray Coordinates Network (GCN) is a system that distributes the locations of GRBs and other transients detected and reports the follow-up observations. As GRB astronomy is a domain where the timing of the observations is crucial, this network has been created to inform the potential observers as soon as possible.

The GCN Notices send the location of the GRB/transients without any humans-in-the-loop, meaning that the notice is distributed to the users with a $2-10$ seconds delay depending on the real-time downlinks constraints. On the other hand, the GCN Circulars allow the GRB community to distribute messages to the entire GRB community. They are prose-style messages that the follow-up observers write.

A typical use-case for the GCN system is, for example, a *Swift*/BAT alert that triggers GCN Notices containing the burst localization, followed a few minutes later by a GCN Circular detailing the follow-up of the XRT and UVOT instruments on-board.

2.5.2 VHF stations

The Very High Frequency (VHF) ground network is composed of 47 stations scattered as homogeneously as possible around the Earth's surface (see Fig. 2.10). They ensure a near real-time space-ground link availability for 80% of the time.

Once a GRB is detected by ECLAIRs or GRM, the alert signal is transmitted to the ground network receptors within $\sim$ 10 seconds via radio emission (between 137 and 138 MHz). When a ground VHF station detects a signal from SVOM, these telemetry packets are sent via the Internet to the French Science Center (FSC), where the original message is reconstructed and immediately transmitted to the *SVOM* robotic telescopes. The original message is also distributed with the GCN Notices to the scientific community.

Thanks to the stations' localization, the time interval between the GRB on-board detection and the message reception by the robotic telescopes is below 30 seconds. This strategy will also allow large telescopes (i.e., 8-m class) to carry out spectroscopic observations of the afterglow within minutes of a burst detection by ECLAIRs in 65% of the cases (Wei et al., 2016).

In addition to the alert transmitted through the VHF network and the potential GRB localization, a few scientific information, such as the raw ECLAIRs lightcurves or the triggered energy band and timescale, are also sent to the ground. From these data are extracted level 0 scientific products (e.g., fluence, peak-flux, T_{90}, hardness ratio for ECLAIRs

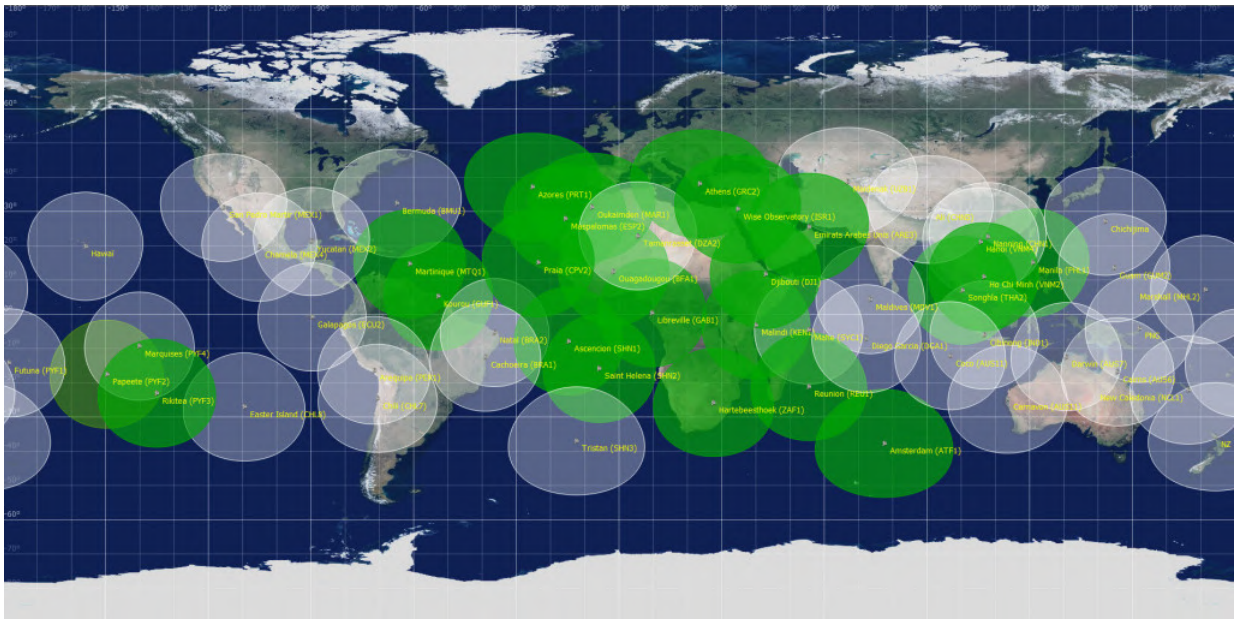

FIGURE 2.10. The 47 VHF stations localization. Color coding is for the stations deployed (green) and to be deployed (grey) on May 1st 2021. Credit: CNES

and GRM, classification of the transient), automatically sent into GCN Notices. These information can also be verified by the Burst Advocate (BA) and communicated to the science community through GCN Circulars, $\sim 30 - 60$ min after the trigger.

Some alerts can also be transmitted through the Beidou network via inter-satellite communications. Information such as trigger information in case of detection, position and sub-images are sent through this mean.

2.5.3 X-band and S-band stations

The bandpass transmitted through the VHF stations is limited, meaning that the information transmitted with this frequency is basic. Therefore, X-band and S-band stations are used to communicate a larger volume of information.

There are 2 French and 3 Chinese S-band stations scattered around the globe. Both are used to upload the ToO observation requests to the satellite, with a maximum latency of 12 hours. However, as *SVOM* might also use the Beidou system to communicate with the ground, this latency could be reduced to < 5 hours. The 3 Chinese stations will also be used for routine telecommand upload, as *SVOM* will have 4 passes per day. These telecommands can be, for example, configuration changes of the on-board instruments or modifications of the flight software.

The allocation of the S-band bandpass is 3 Mbit each for the ECLAIRs and MXT instruments, 4 Gbits each for the VT and GRM. A large majority of the S-band data is allocated to the

status of the plateform (9 Mbit), payload management interface (0.5 Gbits) and VHF/X-band telemetry health-check (4 Gbit).

For the X-band stations, there are 3 X-band stations located at Kourou, HBK, and Sanya, allowing 6 passes per day for a mean inter-pass duration of 4 hours. For each pass, *SVOM* will be able to transmit 18 Gbits of raw data, with a maximum data latency of 24 hours for the core program. The transmitted X-band data for ECLAIRs are of the following nature:

- Even if there is no detection, the ECLAIRs instrument will send all the raw data registered on-board to the ground to analyze them more in-depth, using the so-called "off-line analysis" (see 3.5).
- In case of detection, the raw events received by the instrument around the trigger are kept and stored, to be sent as soon as possible to the ground. This allows a refined analysis compared to the VHF data, where the bandpass only allows the transmission of a few data.

For information, the X-band data allocation for the 4 *SVOM* instruments is the following: 18 Gbit for ECLAIRs, 4 Gbit for MXT, 22 Gbit for GRM and 30 Gbit for the VT. 0.1 Gbit are dedicated to the PDPU, and a margin of 9.9 Gbit is allocated.

2.6 Context of the mission

The *SVOM* mission will operate in a multi-messenger context, in synergy with other observatories presented in Fig. 2.11.

2.6.1 Precise localization of GRBs

On the one hand, *SVOM* will increase the follow-up opportunities for GRBs, being another γ-ray spacecraft with multi-wavelength capabilities in space. Moreover, although the *Swift* mission and its instrument BAT (Barthelmy et al., 2005a) still operate successfully (since the end of 2004, despite it having been designed for an 18 months mission), the on-board instruments are getting old: only half its detection plane is functional, and there have already been failures on some critical component such as one of its reaction wheel (Cenko, 2022). *INTEGRAL* (Ubertini et al., 2003; Vedrenne et al., 2003) provides some precise localization, but the mission is planned to be decommissioned in the coming years after more than 20 years of operation. *Fermi* (Meegan et al., 2009a) does not have any coded mask and is, therefore, most of the time unable to derive accurate localization from the prompt emission observation. The same applies to the Konus-Wind network or the recently launched *GECAM* mission.

On the other hand, the next generation of multi-wavelength missions such as the Transient High Energy Sky and Early Universe Surveyor (*THESEUS*, Amati et al. 2018) or the Transient Astrophysics Probe (*TAP*, Camp & Transient Astrophysics Probe Team 2018) are expected to be launched not before the middle of 2030.

Nonetheless, the Einstein Probe mission (Yuan et al., 2022), which will share the VHF network of the *SVOM* mission, will also be able to detect and localize GRBs thanks to

Figure 2.11. Multi-messenger panorama of space- and ground-based observatories that might detect or follow transient events.

its instrument WXT (Liao et al., 2017) and FXT (Chen et al., 2020). But for these two reasons, *SVOM* will be the focus of the GRB community in the coming years, as it will be part of the few instruments able to provide sufficiently precise localization to perform ground follow-up observations.

2.6.2 Gravitational-waves observatories

The synergy with gravitational wave observatories allows the detection of events similar to GRB 170817A/GW 170817 (Abbott et al., 2017b). The O4 run of aLIGO/aVirgo starts by mid of 2023, and will last for ~ 1 year (Abbott et al., 2018b). *SVOM* should be operational before the end of 2023, and could benefit from this synergy during its first months of observation. However, *SVOM* will more likely evolve in the O5 run context around its third year of operation in 2026. In this context, the LIGO-India (Saleem et al., 2022) and KAmioka GRAvitational wave detector (KAGRA, Kagra Collaboration et al. 2019) might be operational, narrowing down the localization error boxes of some GW events, easing their follow-up.

2.6.3 Neutrinos detectors

As explained in Sec. 1.4.5, neutrino detections are critical to constrain the physics of GRB jets. IceCUBE (IceCube Collaboration, 2013) and the version 2.0 of KM3Net (Adrián-Martínez et al., 2016) will increase the simultaneous survey time of γ-ray instruments and neutrino detectors, increasing the chances of simultaneous detections or constraining even more the neutrino emission of GRBs in case of non-detection.

2.6.4 Vera-Rubin Observatory

The Vera-C.-Rubin Observatory (Ivezić et al., 2019) will also be available during the *SVOM* operations, expected to start its operation by 2023. This 8.4 meter telescope will survey the southern sky in three days, providing about 6 million alerts per night to the scientific community about optical and NIR transient observed. To categorize and filter these alerts, algorithms called "brokers" have been created. This allows to provide to the science community alerts centered around a science theme (here, the GRBs). The *SVOM* community is particularly involved with one broker called FINK (Möller et al., 2021). Combined with the off-line trigger capabilities of ECLAIRs (see Sec. 3.5), it might enable the discovery of orphan afterglows, supernovae, or kilonovae related to GRBs. The Zwicky Transient Facility (ZTF, Bellm et al. 2019; Graham et al. 2019), currently operating with a strategy similar to the Vera-Rubin Observatory, will also contribute to delivering some alerts that could be followed with *SVOM* ToO program.

2.6.5 Next generation observatories

SVOM will operate in a context where a whole new panel of next-generation instruments will be available. At very-high-energy, the Cherenkov Telescope Array (CTA, Cherenkov

Telescope Array Consortium et al. 2019), the High- Altitude Water Cherenkov Observatory (HAWC, Albert et al. 2020) and the Large High Altitude Air Shower Observatory (LHAASO, di Sciascio & Lhaaso Collaboration 2016) will be operational around the same period. In the X-rays, the extended ROentgen Survey with an Imaging Telescope Array (eROSITA, Predehl et al. 2021) will allow faster identification of new sources by establishing a reliable map of the X-ray sky. The James Webb Space Telescope (JWST) has been successfully launched at the end of 2021 and can perform deep observations in the near- and mid-infrared, allowing the detection and characterization of high redshift afterglows and host galaxies. In the radio, the Australian SKA Pathfinder (ASKAP, Johnston et al. 2008) or MeeRKAT (Jonas, 2009) will be able to characterize the radio afterglows, while the Canadian Hydrogen Intensity Mapping Experiment (CHIME, CHIME/FRB Collaboration et al. 2018) or the program Commensal Real-time ASKAP Fast Transients Survey (CRAFT, Macquart et al. 2010) on ASKAP could associate some high-energy transients with Fast Radio Bursts (FRBs) detections.

The next generation of extremely large telescopes will also start to operate beginning at the end of 2027 (Skidmore et al., 2015; Bernstein et al., 2018; Hook, 2009). Thanks to their gigantic mirrors and the adaptive optics system, their instruments will perform diffraction-limited observations with incredible sensitivity and spectral resolution.

Chapter 3

The ECLAIRs instrument

ECLAIRs is one of the two wide field γ-ray instrument in the *SVOM* platform. The purpose of the instrument is to detect, localize and characterize the GRBs prompt emission. ECLAIRs is the accomplishment of almost two decades of dedicated work from approximately one hundred persons from french laboratories, CNES, and the space industry. It is also the instrument on which this thesis is focused. This chapter describes some of the main components of ECLAIRs in Sec. 3.1, then it goes into the details of photons detection in Sec. 3.2, Sec. 3.3 and Sec. 3.4. Finally, the GRB detection algorithms related to the ECLAIRs instrument are explained in Sec. 3.5, while the instrumental effects observed on the detection plane are presented in Sec. 3.6.

Contents

3.1 ECLAIRs components

The hard X-ray imager ECLAIRs comprises several key components, illustrated in Fig. 3.1 and discussed in this section. Each of the components has a specific task that is explained more in detail in the subsections below:

- The detection planeand the Electronique de Lecture Secteur (ELS) take care of the detection of the incoming photons, the measurement of their energy, and the pre-processing of the data before sending them to the on-board computer of ECLAIRs.
- The Unité de Gestion et de Traitements Scientifiques (UGTS) controls ECLAIRs, ensuring that the detection planeand the ELS are behaving nominally. It is also responsible for GRBs detection and localization by applying trigger and deconvolution algorithms to the data sent by the ELS.
- The coded mask and the shielding are responsible for the modulation of the photon repartition on the detection plane. Because of their opacity to hard X-ray photons, a point source in the sky will project the mask pattern on the detection plane, which the UGTS uses for the detection and localization of the GRB.

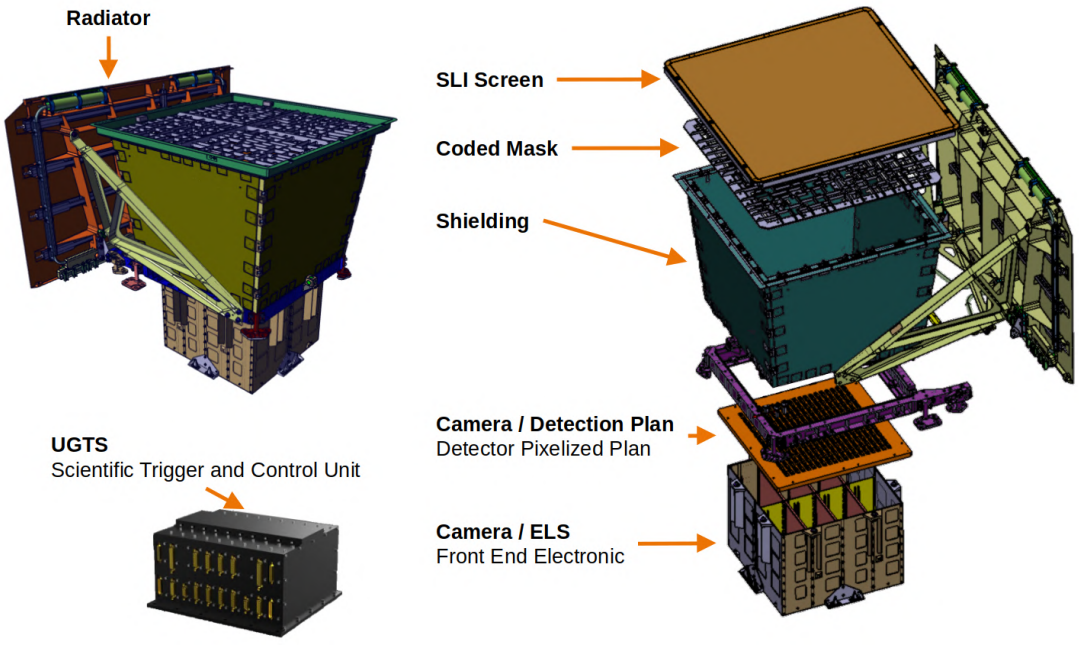

Figure 3.1. Anatomy of the ECLAIRs instrument. Source: CEA/CNES Application Specific Integrated Circuits

The global characteristics of the ECLAIRs instrument can be found in Table 3.1 .

Table 3.1 . Main characteristics and expected performance of *SVOM*/ECLAIRs

Measured property	Value
Energy range	4 – 150 keV
Mode of operation	Photon counting
Time resolution	20 μs
Detecting area	$\sim$ 1000 cm^2
Detectors	CdTe
Number of detectors	6400
Size of detectors	4 mm $\times$ 4 mm $\times$ 1 mm
Energy resolution (median)	$<$ 1.6 keV @ 60 keV
Field of view (half-coded / full)	0.9 / 2.0 sr
Coded mask dimensions	54 cm $\times$ 54 cm
Coded mask open fraction	40 %
Coded mask element size	10.4 mm
Detector-Mask distance	46 cm
Telescope PSF	52 arcminute FWHM
Expected performance	**Value**
Effective area at 20 keV	$\sim$ 400 cm^2
Background level (empty sky)	$\sim$ 4000 cts s^{-1}
Point source localization (90% confidence)	13 arcminute @ SNR = 7
Limiting flux for a 20 s long on-axis GRB	1.5×10^{-8} erg cm^{-2} s^{-1}
Dead time	$\leq$ 5% for 10^5 cts s^{-1}

3.1.1 The detection plane

The detection planeis the detection plane of the instrument, where the photons coming from astrophysical sources are detected. The IRAP teams have developed the detection planeand its electronic (e.g. Nasser et al., 2014; Bajat et al., 2018b,a; Lacombe et al., 2018, 2019). It consists of 80 $\times$ 80 pixels of cadmium telluride (CdTe) spaced by 0.5 mm with an individual pixel area of 4 $\times$ 4 mm^2 and a thickness of 1 mm, forming a detection plane with a geometric surface of 1296 cm^2. This detection plane is divided into 8 sectors containing 25 XRDPIX detectors each (see Fig. 3.2(b)). An XRDPIX is composed of 32 pixels and has its own Application Specific Integrated Circuit (ASIC) for detecting and shaping the signal produced by the photon or particle interactions (see Sec. 3.2 after). The golden grid seen on Fig 3.2(b) is used to apply the high-voltage ($-$300 V) to the CdTe, necessary for the charge carriers transport (see Sec 3.2). The detection plane of ECLAIRs allows an energy resolution better than 1.6 keV at 60 keV, in addition to an energy coverage from 4 to 150 keV.

Figure 3.3 shows the numeration conventions of the sectors, XDPIX modules, and pixels of the detection plane. The plate on which the XRDPIX are mounted is made in AlBeMet, an

alloy of aluminum and beryllium with excellent mechanical and thermal properties with a density ~ 1.4 times lower than aluminum. The detection plane is controlled in temperature thanks to heat-pipes that can be seen on the top of Fig. 3.2(a), maintaining a temperature around $\sim -20°C$. The heat carried by the heat-pipes is rejected to space by the radiator.

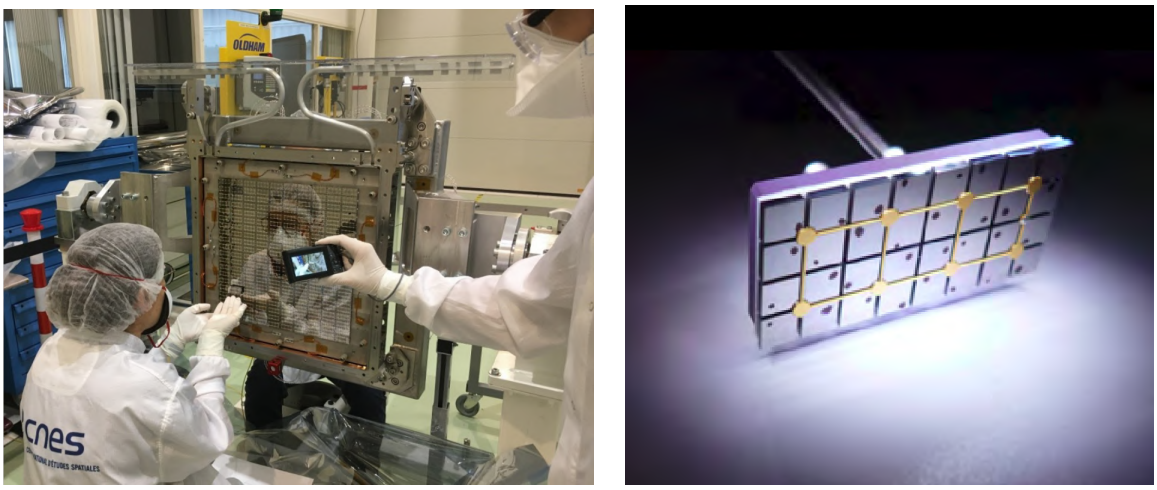

(a) (b)

Figure 3.2. (a) Detection plane of the instrument, the ELSs are located behind it. Source: CNES/IRAP (b) Close-up of one of the XRDPIX. Source: K. Lacombe

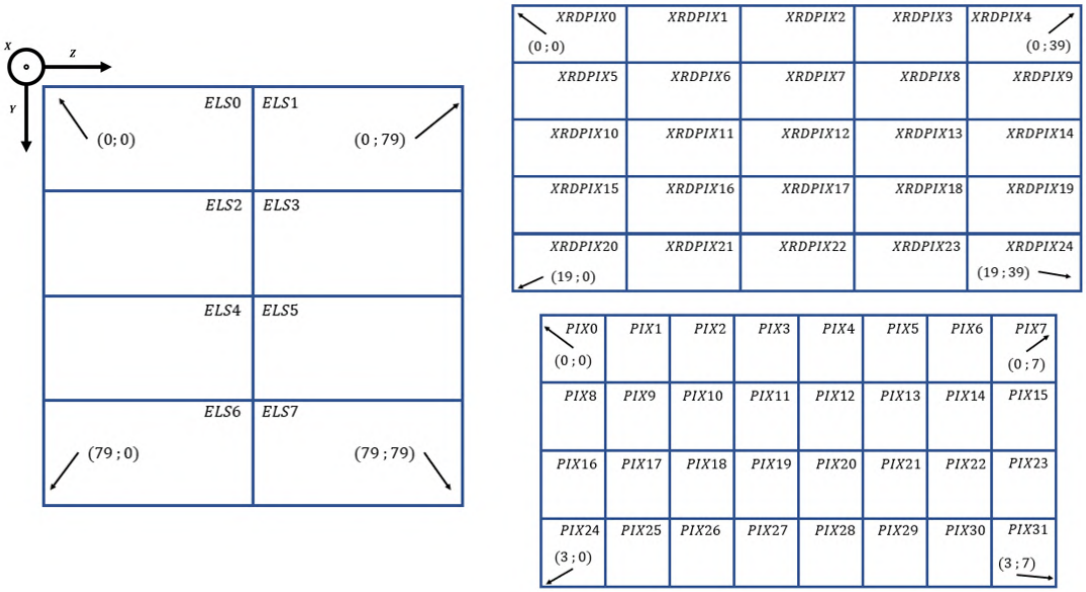

Figure 3.3. Convention of the detection plane for the whole detection plane (left), one sector (top right) and one XRDPIX (bottom right)

The CdTe conductors offer a good spectral resolution at the expense of a loss of sensitivity to energies above ~ 1 MeV. For this reason, they are perfect candidates for instruments

such as ECLAIRs: the broad spectral coverage is sacrificed to get the low energy threshold, a larger detecting area, a good energy resolution, and localization precision. Due to their high mean atomic number and density, CdTe detectors have been particularly used in high-energy astrophysics, as it provides a good quantum efficiency for energies < 200 keV and the possibility to use them at non-cryogenic temperatures. Germanium has better characteristics (higher charge mobility and efficiency) than CdTe, but Germanium detectors require cryogenic temperatures to work. The necessity to keep ECLAIRs simple, light, and compact prevented using a cryostat. Several X- and γ-ray missions are using this technology:

- The IBIS instrument mounted on the *INTEGRAL* mission spacecraft has a 2621 cm^2 detection plane populated by detectors made in CdTe, with an individual thickness of 2 mm. The detection plane, called ISGRI, is sensitive to energies from 15 keV to 10 MeV.
- A variant of this material, the CdZnTe, populates the *Swift*/BAT detection plane (Barthelmy et al., 2005a). It comprises 256 modules, each composed of 128 pixels with an individual surface of 4×4 mm^2 and a thickness of 2 mm. The global detection surface is 5240 cm^2, for an energy coverage from 15 to 150 keV and an energy resolution of 3.3 keV at 60 keV.
- The CZTI instrument on the *Astrosat* mission (Bhalerao et al., 2017) also uses 64 CdZnTe detectors with dimensions 39.06×39.06 mm^2 and a thickness of 5 mm, themselves divided into 16×16 pixels. The global detection surface is 976 cm^2, for an energy coverage from 20 to 200 keV and an energy resolution of ≈ 6 keV at 60 keV.

The ECLAIRs detection surface is approximately 2 times smaller than for *INTEGRAL*/IBIS and 4 times smaller than for *Swift*/BAT. However, its unique feature is the low energy bound of the instrument reaching 4 keV. This sensitivity to low energies is crucial and has driven many design choices for the instrument.

3.1.2 Electronique de Lecture Secteur

By construction, the 8 sectors work almost independently, and so do the corresponding electronics[1]. The 25 XRDPIX populating the sectors is controlled by the Electronique de Lecture Secteur (Sector-Reading Electronic, ELS) that also exchanges information with the UGTS (Unité de Gestion de Traitement Scientifique, see dedicated section after). The ELS is also in charge of maintaining the high voltage on the XRDPIX and coding the event's energy. One ELS is composed of five boards (doubled in cold redundancy) with distinct functions to perform these functions.

Pre-Processing

The pre-processor card contains a Field Programmable Gate Array (FPGA) NanoXplore, a programmable logic circuit. This board controls the two other ELS cards and communicates

[1]There is a link implemented between the sectors to correct the cross-talk effect, inhibiting the detections of modules one a sector adjacent to another that is detecting something.

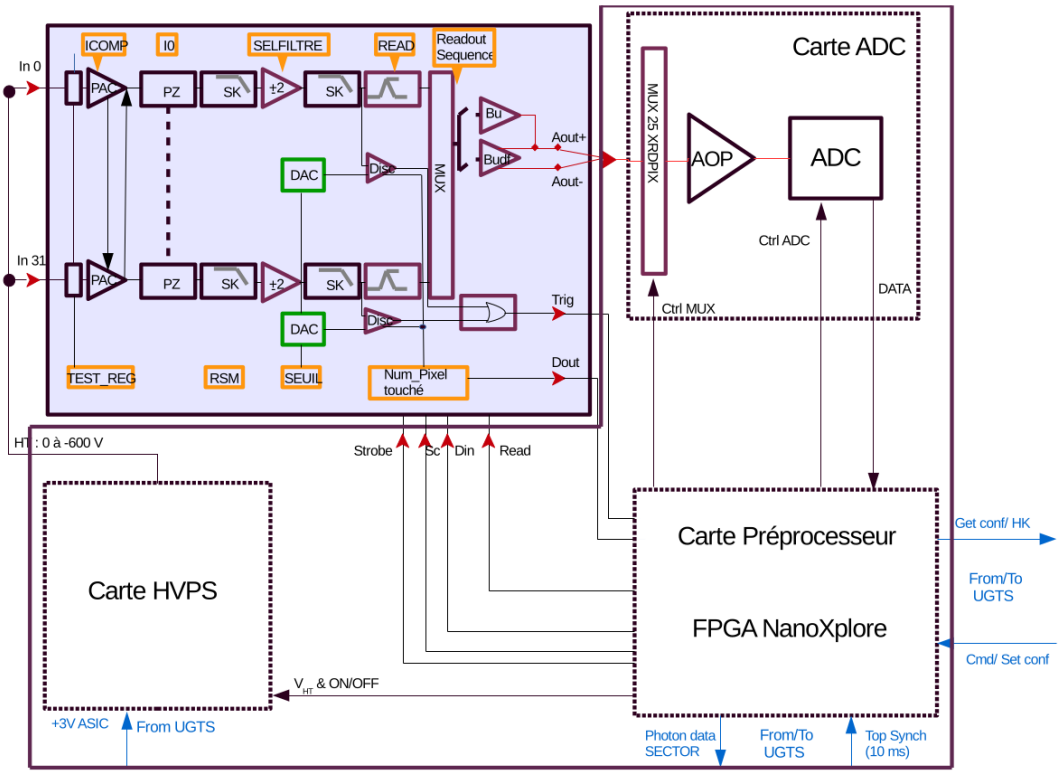

Figure 3.4. Schema of the sector electronic, including the XRDPIX ASIC (in the shaded blue part) and the ELS electronic with the LV/HVPS, ADC and Pre-processing cards. Source: Bajat (2018)

with the 25 associated ASICs in the 25 XRDPIX. When this circuit receives the analogical detection signal (created by a photon detection) from one of the 25 ASIC modules (the *Trigger* signal), it sends a reading command to this ASIC. It also programs the multiplexer from the ADC card, depending on the multiplicity of the events (see after in Sec. 3.2). Merging two pieces of information from the ADC card and the XRDPIX ASIC, the card sends coded frames containing the information about the detected event to the UGTS through the photon link, with a format depending on the event type. (see Sec. 3.4). The card also has some monitoring functions: it maintains the communication with the UGTS (see after) through the UART (Universal Asynchronous Receiver Transmitter) link to send HouseKeeping (HK) information about the internal tensions and temperature of the electronic. The card can send the required high voltage to the LV/HVPS card to maintain the XRDPIX polarization with these information.

LV/HVPS

The LV/HVPS (Low Voltage / High-Voltage Power Supply) card is responsible for the polarization of the XRDPIX, by distributing a high voltage to each detector via a grid inside the XRDPIX. This tension enables the electrons/holes movement generated by the photon/detector interaction (see in Sec. 3.2). The high-voltage can be set to different values

by the pre-processor card, ranging from 0 to −600V. The value directly affects the behavior of the detection plane, as more noisy pixels are created for high polarization voltages (below −450V). The card contains numerous filters to reduce the input noise so that the power supply of an XRDPIX is stabilized. The LV/HVPS card is also responsible for the supply of a 3V voltage to the XRDPIX ASIC, used by the Pre-Amplificator of Charges (PAC).

Analogic-Digital Convertor

Finally, the Analogic-Digital Convertor (ADC) card reads the output of the XRDPIX ASICs (A^+_{out}, A^-_{out}) and digitizes the analogic signal to encode the energies of the registered events. The pre-processing card at the entrance of the card controls the multiplexer, preventing the reading of the energies in the case of large multiple events (creating MEA and MEE, see Sec. 3.4).

Thanks to these cards, the ELS can analyze each event happening on the detection plane, dating them with a time resolution of 20 μs and coding their energy with a resolution of 0.15 keV.

3.1.3 Unité de Gestion et de Traitements Scientifiques

The "Unité de Gestion et de Traitements Scientifiques" (UGTS) is the on-board computer of ECLAIRs. The system is in charge of the ECLAIRs instrument control (reception and treatment of commands received, collection of the HKs, thermal management of the detection plane, noisy pixels treatment), the acquisition and storage of the events in the instrument memory, and the scientific treatment of such data (trigger algorithms as in Sec. 3.5, VHF alerts creation, GRB localization and slew request for the satellite). The UGTS consists of 10 cards, including 6 cards for the ELS energy supply (4×1 cards for 4 pairs of ELS, plus 2 cards for the power supply management), 2 for the input/output information management, and 2 for the calculation. Each card is in cold redundancy: they are duplicated, so if one fails, a ground command can be sent to switch and use the other.

The calculation card consists of an FPGA and a double-core Leon 3 CPU, with a clock of 80 MHz, delivering a calculation power of about 2×50 Mflops, encompassing 256 MB of RAM and 4 MB of memory dedicated to the software use and configuration.

The flight software of the UGTs has been developed at CEA/IRFU with the participation of the "Département d'Astrophysique" (DAp) and the "Département d'Electronique des Détecteurs et d'Informatique pour la Physique" (DEDIP).

3.1.4 Coded mask and the shielding

A classical optical telescope uses a system of reflection and refraction to concentrate a collimated beam of light on the instrument detection plane. However, refraction techniques are almost impossible to use in the hard X-ray/γ-ray, as the photons at this energy barely deviate from their initial trajectory. The reflection techniques that focus the light with the "lobster-eye" or the Wolter (used in XMM-Newton or Chandra) optical system also barely work for hard X-ray and γ-ray photons, as they go through the reflector if the incidence

angle is too high. Moreover, the FoV obtained by such optical systems is limited, which is problematic for a GRB-detector instrument.

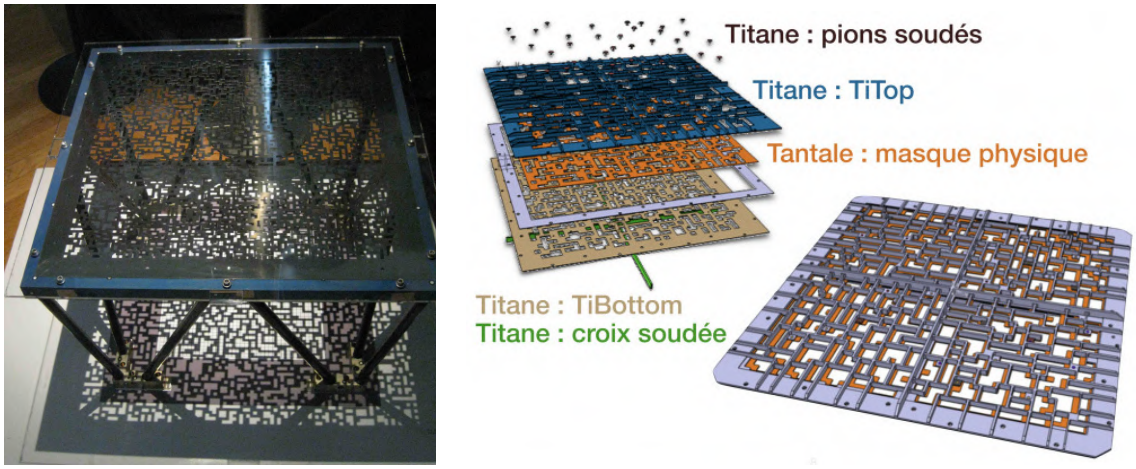

(a) (b)

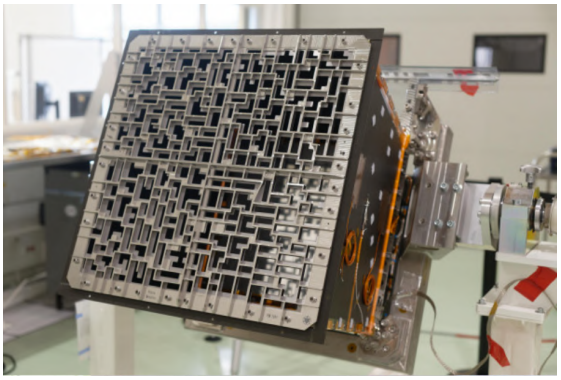

(c)

Figure 3.5. (a) Principle of the shadowgram illustrated with the coded mask prototype. Source: APC/CEA (b) Representation of the elements constituting the ECLAIRs coded mask. Source: APC (c) Coded mask and shielding of the instrument during the assembly and test campaign. Source: CNES/IRAP/CEA

The approach has to be different: instead of focusing the beam of light, a coded mask instrument uses the shadow projected by the beam on the detection plane, creating what is called a shadowgram (see Fig. 3.5(a) with the shadowgram projected by the light). The mask and shielding materials are opaque below 120 keV, preventing photons from going through it. Therefore, almost all photons detected on the detection plane have gone through the mask, meaning that the shadowgram obtained is coded by the mask pattern. It is possible to reconstruct a representation of the sky image that has projected the shadowgram using a deconvolution algorithm (see Section 3.5.1 for more information on the process).

This technique has been used on several other instruments for hard X-ray and γ-ray telescopes: *Granat*/SIGMA and ART-P (Sunyaev et al., 1990; Paul et al., 1991), *Beppo-SAX*/WFC (Jager et al., 1997), *INTEGRAL*/JEM-X, IBIS and SPI (Lund et al., 2003; Ubertini et al., 2003; Vedrenne et al., 2003), *Swift*/BAT (Barthelmy et al., 2005a) and *Astrosat*/CZTI (Bhalerao et al., 2017).

The ECLAIRs coded mask has been designed and made by the APC. The mask is self-supporting to maximize its efficiency for low energies: the holes in the coded mask pattern are empty instead of being filled with a material more or less transparent to X-rays. However, this premiere in space puts strong constraints on the rigidity of the mask, as it will have to endure the mechanical vibrations of the launch. The mask is therefore composed of a 0.6 mm tantalum mask surrounded by two thicker masks made in titanium (see Fig. 3.5(b)). 10 mm ribs of titanium have been added to the top and bottom layers, in addition to a 16 mm thick titanium cross to hold the structure. Some titanium pawns are welded, maintaining the top and bottom titanium layers together. Tantalum pellets cover them to ensure X-ray opacity.

The shielding has been manufactured by CNES and is made of copper and lead glued on a carbon fiber support, preventing the large majority of hard X-ray photons from going through it. The shielding components, excited by high-energy photons and particles in space, will also emit photons through the fluorescence process. These photons will be used for the on-flight energy calibration.

3.2 Photons detection in ECLAIRs

After describing the sub-systems composing ECLAIRs, we present the physical mechanisms involved in X-ray photons detection. X-ray and γ-ray photons carry much higher energies than optical or infrared photons. Thanks to this energy and the low flux received in space, ECLAIRs can detect the hard X-ray photons one by one and measure for each their position, time of arrival, and energy.

This section presents the physical processes that allow the detection of photons by ECLAIRs and the measurement of their energy.

3.2.1 Physics of the interaction of photons with ECLAIRs detection plane

The physics of hard X-ray photon interactions with the detection plane of ECLAIRs is complex, and its exact modeling requires dedicated Monte-Carlo simulations with GEANT4 (see 4.1 for more detail). The three major interactions between photons and matter are the photoelectric effect, the Compton effect, and the pair production. Within the ECLAIRs energy range (typically 4 – 150 keV) and with a detection plane made in CdTe, the dominant effect is the photoelectric effect.

3.2.2 The photo-electric effect

During such an interaction, the incoming photon gives its entire energy $E_i = h\nu$ to an electron located in the innermost electronic layer of the atom (most of the time, the K or L shell). This electron is ejected from the electronic cloud with a kinetic energy $E_{d,1} = E_i - E_K$, where E_K is the binding energy of the K-shell electron's electronic layer. It then deposits all its energy within the detector. However, the atom is left in an excited state because of the missing electron from its inner layer. Thus, the atom undergoes one of the two following mechanisms to reach a more stable state:

- An electron from the external electronic layer replaces the missing internal layer electron. By decreasing its energy level, the electron emits an X-ray fluorescence photon, whose energy corresponds to the energy levels difference between the external and internal electronic layers. For example, a fluorescence photon from the M-shell carries an energy $E_{i,2} = E_K - E_M$. This photon can again interact with a detector or escape.
  - If the fluorescent photon interacts with the detection plane, it transfers its energy to another electron ($E_{d,2} = E_{i,2} - E_L$). In this case, almost all the energy $E_i \approx E_{d,1} + E_{d,2}$ is deposited in the detector.
  - However, if the fluorescence photon escapes the material, only the energy transmitted to the first escaping electron $E_{d,1} = E - E_K$ is deposited in the detector. The energy from the second photon $E_{d,2}$ is lost.
- The atom can also re-arrange its electronic cloud so that the exceeding energy is re-distributed among the electrons. Some electrons of the external layers can acquire through this process energies high enough to escape the atom; they are called Auger electrons. The kinetic energy of these electrons is equal to $\sum E_{e_i} \approx E_K$, so that almost all the energy $E_i \approx E_{d,1} + \sum E_{e_i}$ is deposited on the detection plane.

The probability of having fluorescence photons or Auger electrons emission depends on the atomic number and the interaction shell. In the energy range considered, for the CdTe, the typical fluorescence yields are $\sim 85\%$ for the K-shell and $\sim 5\%$ for the L-shell (Krause, 1979).

The fluorescent photon might also deposit its energy on a pixel different from the initial photon, creating two coincidental events. These events are seen as multiples by the detector or even as two individual single events if the two pixels are from different ELS.

3.2.3 Generation of electron-hole pairs and charge collection

Energetic electrons generated by the photon interaction interact with the semiconductor material, creating electron-hole pairs by ionization mechanisms. An electron of energy E_d creates on average $N = E_d/\bar{\epsilon_w}$ electron-hole pairs, where $\bar{\epsilon_w} = 4.42$ eV is the mean energy required for a pair creation inside the CdTe.

Once the electron-hole pairs are created, they are respectively transported to the anode and cathode thanks to the electric field generated by the high voltage applied with the grid. The times t_n and t_p required for the electrons and holes to reach the anode and cathode

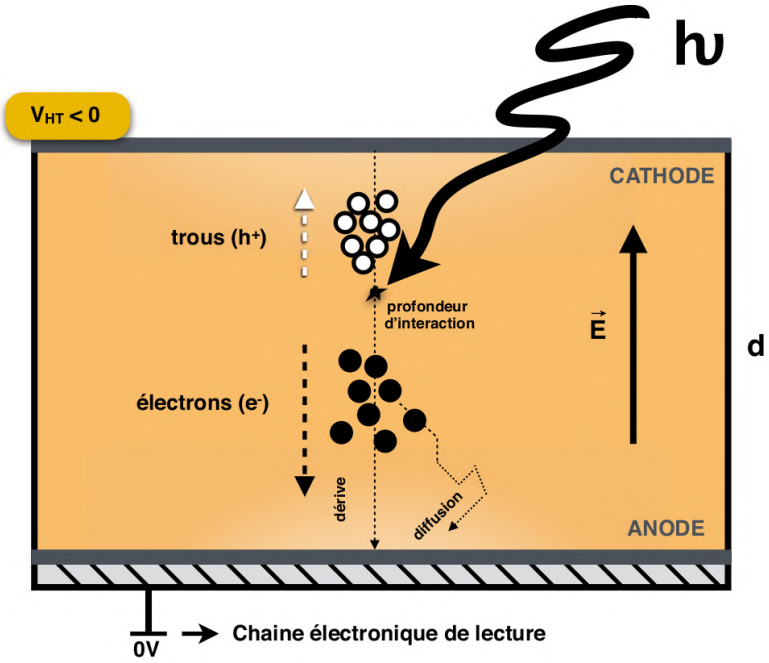

Figure 3.6. Representation of the interaction of a photon with a CdTe semiconductor, creating the charges carriers clouds. Source: Nasser (2015)

are called the transit times. They depend on the carriers' mobility in the semiconductor, μ_n and μ_p, the voltage applied to the electrodes V_{HT}, the thickness of the semiconductor material d, and the depth of the photon interaction z with the formula:

$$t_n = \frac{d-z}{\mu_n V_{HT}/d} \text{ and } t_p = \frac{z}{\mu_p V_{HT}/d} \tag{3.1}$$

The transit of the electron and hole charges at the anode and cathode creates an inducted current, $I_n(t)$ and $I_p(t)$. Assuming that there is no charge loss during the migration of the electrons and holes, it is possible to retrieve the charges Q_{anode} and $Q_{cathode}$ deposited by the holes and the electrons by integrating the induced currents. By summing the two contributions, it is possible to retrieve the number of electron/hole couples created by the ejected electron, therefore finding the energy transmitted by the photon to this electron E_d:

$$Q_{anode} + Q_{cathode} = 2Nq = 2\frac{E_d}{\bar{\epsilon_w}}q \tag{3.2}$$

3.2.4 Generation of the trigger signal and energy measurement

The charges collected are measured at the anode and converted by the Charge Pre-Amplifier (PAC) to a voltage. This voltage is shaped thanks to a filtering stage (shown as the PZ, SK, and SELFILTRE in Fig.3.4) to facilitate the measurement of its peak. The measured

voltage amplitude is compared to a threshold value (called the SBN threshold, see in Sec 3.6): if the voltage created from the collected charges exceeds this value, the signal *trigger* is activated. This signal freezes the ASIC module during a time $t_{freeze} \approx 9.6$ μs so that the charges have time to be entirely collected (the peak of the signal is not missed) without any interference. After this time, the state of the ASIC is fixed, and the FPGA from the pre-processing card reads the channels of the ASIC that have activated the *Trigger* signal. Finally, the peak of the signal voltage is detected, measured, and sent to the ADC card to be numerically encoded.

3.3 The ECLAIRs response matrices

The instrument response describes the interactions of an instrument with the incoming photons. It considers the effects described in Sec. 3.2, such as the photons-detector interactions (e.g., photoelectric or Compton mechanisms, energy deposited, fluorescence) and the charge collection process. By inversing this instrument response, it is possible to retrace the properties of the photons from the events recorded on the detection plane that have created them (using, for example, XSPEC Arnaud 1996). Therefore, the instrument response is crucial to construct and adequately analyze the data from an instrument.

In the X- or γ-Rays astronomy, the instrument response is usually modeled via the following response files:

(1) The Ancillary Response File (ARF) contains a table of area values for several energy ranges. It gives the area available for the instrument to detect a photon at an incident energy $E_{\rm in}$.
(2) The Instrument Response Function (IRF) describes the variation of the ARF relatively to the incident angle of the photons.
(3) The RMF, most of the time coupled with the energy resolution of the instrument, described the repartition of the energies deposited by incoming photons of energies $E_{\rm in}$.

This section describes how these files are generated.

These files have been created by M. Yassine, using *GEANT4* simulations of the ECLAIRs instrument from L. Bouchet. They have been correlated with actual observations of the ECLAIRs instrument, as discussed in detail in Sec. 4.1. These files follow the OGIP format that can be found at https://heasarc.gsfc.nasa.gov/docs/heasarc/caldb/docs/memos/cal_gen_92_002/cal_gen_92_002.html

3.3.1 GEANT4

GEANT4 simulates the passage of particles or photons through matter (Allison et al., 2016). The algorithm draws individual photons and follows the product of their interaction using a Monte-Carlo process. If one interaction deposits energy on the detection plane of ECLAIRs, GEANT4 considers that an event has been detected. The detected events are

stored in a table with the energy, position, and multiplicity, along with another file storing the corresponding photons.

3.3.2 The Ancillary Response File

The ARF is a vector (see its representation on Fig. 3.7(a)), for which each component $A_{eff}(E_i - E_{i+1})$ [cm^2] represents the efficiency area of ECLAIRs available to detect photons within an energy range $[E_i - E_{i+1}]$. The ARF is constructed as follows: starting from an on-axis point source at an infinite distance from the instrument, photons in the energy range $[E_i - E_{i+1}]$ are sent towards the detection plane. The ARF bin $A_{eff}(E_i - E_{i+1})$ [cm^2] is then defined as the ratio between the number of photons with such energy detected divided by the number of photons sent towards the detection plane, multiplied by the detection plane surface of 1296 cm^2.

The values of the ARF depend on the interaction efficiency of the 1296 cm^2 detection plane with the high-energy photons. Because of the mask opacity, the available detection surface for on-axis photons below $\sim$ 80 keV is reduced by the opening fraction of the mask (0.397), down to 514 cm^2. Moreover, not all the incoming photons deposit an energy on the detection plane: the higher the energy of the photons $E_{\rm in}$, the less likely their interaction. This explains why the ARF decreases at high energies, despite the mask becoming more transparent at these energies. Finally, the ARF also considers the absorption of materials in front of the detection plane: for example, the SLI and MLI contribute to reduce the efficiency at low energy as they absorb the incoming photons. This is one of the reasons why the ARF drastically reduces for energies below 4 keV.

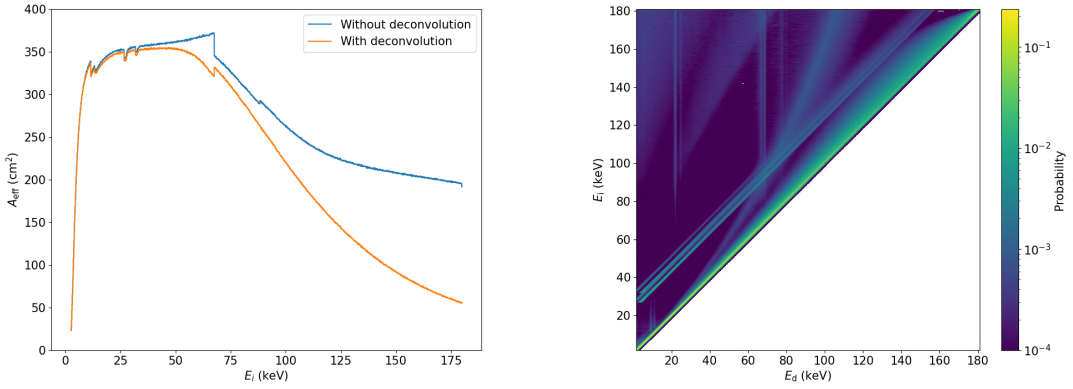

(a) ARF

(b) RMF with energy resolution

Figure 3.7. Representation of the ARF and RMF files of ECLAIRs. The color coding on the RMF represents the probability for an event with an incident energy $E_{\rm in}$ to deposit an energy $E_{\rm dep}$ on the detection plane.

As shown in Fig. 3.7(a), there are two versions of the ARF matrix. The one without deconvolution is built from all the events generated on the detection plane. However, the

one with deconvolution is obtained by selecting only some of the events near the source location (the deconvolution process is explained more in detail in Sec. 3.5). By making a deconvolution of the shadowgram obtained from the events generated, an image of the ECLAIRs FoV is obtained. In this image, only the counts near the on-axis location (the position of the photons source) are considered. As shown in Figure 3.7(a), this process has a consequence of lower ARF values above 50 keV. Indeed, the events created at this energy are, for some of them, generated by Compton scattering with the mask material. As these events are not coded on the shadowgram, they are considered as background events during the deconvolution process and are not taken into account in the ARF construction.

3.3.3 The Instrument Response File

The IRF (Instrument Response File) describes how the instrument ARF changes relative to the direction of the incoming photon represented by θ and ϕ. The IRF can be defined as follow:

$$IRF(E, \theta, \phi) = \frac{ARF(E, \theta, \phi)}{ARF(E, 0, 0)} \tag{3.3}$$

This IRF is a data-cube of $199 \times 199 \times 2$, where the two first dimensions are equal to the number of sky pixels and the last dimension the two energy bins. The sky pixels have been created to provide a discretization of ECLAIRs FoV: each sky pixel represents a sky surface (different depending on the sky pixel location).

3.3.4 The Redistribution Matrix File

The RMF (Redistribution Matrix File) describes the stochastic processes involved in the energy deposition on the detection plane of a photon with an incident energy E_{i}, creating an event with an energy E_{d}. The construction of this matrix requires modeling the interactions of photons/matter finely. Figure 3.8 illustrates this energy redistribution: in orange are the photons emitted by the Am-241 and the Fe-55, and in blue, the energy of the events generated by these photons once the instrument response is applied. The peaks observed in the blue curve between 30 and 40 keV (although no orange photons are emitted in this energy range) are the escape peaks of Cd and Te. The inner electrons ejected by the photo-electric effect carry only a part of the incident photon energy, $E_d = E_i - E_{K_\alpha}$. In case the unstable atom de-excites with the emission of a fluorescence photon that successfully escapes the detection plane, the energy E_{K_α} is lost. The peaks between 30 and 40 keV therefore correspond to the initial photon energy at $E_i = 60$ keV, minus the energy E_{K_α} of the telluride and the cadmium, respectively at 27.5 and 23.2 keV.

An RMF matrix is constructed through GEANT4 simulations by simulating photons within a given energy interval $E_i - E_{i+1}$ and observing the distribution of the energy deposited E_d by these photons. The operation is repeated for $E_i \in \{2.5 - 180\}$ keV to obtain a good representation of the photon interactions within the ECLAIRs instrument. The final result is a matrix of dimension $N \times M$, N being the number of bins of simulated photon energies E_i and M the number of bins of deposited energy E_d, that can be seen in Fig. 3.7(b).

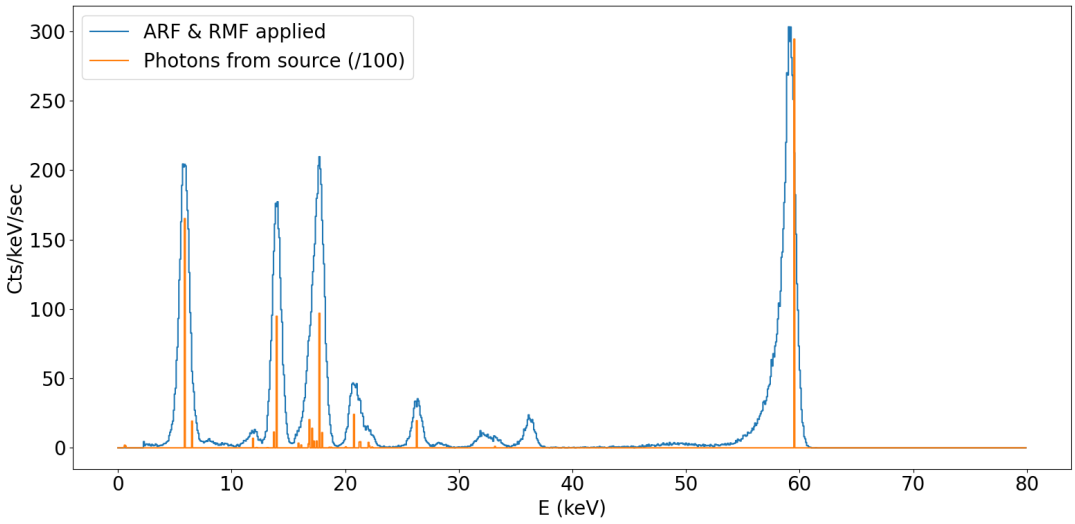

FIGURE 3.8. Application of ARF, RMF, and energy redistribution for Am-241 and Fe-55 sources. The orange peaks come from the photons emitted by the radioactive sources (mainly at 13.95, 17.75 and 59.54 keV for Am-241 and 5.9 keV for Fe-55), while the blue curve corresponds to the spectrum measured once the ARF and RMF applied.

3.3.5 The energy resolution

During the creation of electron-holes pairs explained in Sec. 3.6, statistical fluctuations or the imperfection of the charge collection induces an incertitude in the measurement of the energy deposited by a photon. The energy resolution file accounts for this incertitude. In practical for ECLAIRs, the energy redistribution and energy resolution are grouped into the RMF.

As a first estimation, this energy resolution can be assumed Gaussian with a full width at half maximum expressed as:

$$\Delta E_m \approx \sqrt{\Delta E_{stat} + \Delta E_{elec}^2 + \Delta E_{collec}^2} \tag{3.4}$$

The term ΔE_{stat} accounts for the fluctuation of the number of electron-hole pairs created by a given electron. When a photon transmits a kinetic energy E_d to an electron, the number of electron-holes pairs created is subject to statistical uncertainty according to a Poisson distribution, multiplied by a factor F, called the Fano factor. The uncertainty on measured energy of this electron E_m can be expressed as $\Delta E_{stat} = F\epsilon_w E_d$ with $F = 0.2$ in the case of ECLAIRs. The term ΔE_{elec} represents the incertitude of the energy measurement generated by the electrical components of the circuit, influenced, for example, by the leaking current of the PAC, the capacities involved in the filtering stages, and the time required to shape the signal. The final term ΔE_{collec} describes the energy resolution because of the variation in the efficiency of the charges collection. Figure 3.8 shows that for low-energies, the energy resolution looks like a Gaussian.

However, the peak around 60 keV in Fig. 3.8 shows that at higher energies, the energy resolution cannot simply be expressed as a Gaussian (see the low energy tail that appears). The explanation is that photons with higher energies interact deeper than low-energy photons in the CdTe. As shown in Fig. 3.6, the deeper the interaction, the longer the path for the holes to reach the cathode. Therefore, the collection of the holes charges is affected by two effects:

(1) Their traveling velocity is ~ 10 times lower than the electrons, creating a loss called the ballistic loss. The holes take ~ 0.4 μs to cross the 1 mm of the CdTe pixel, while it only takes ~ 0.04 μs for the electrons. As the energy measurement is made at a time $t_{peaking}$ after the trigger, some holes might not have sufficient time to reach the cathode and contribute to the collected signal.
(2) The holes have a mean free path in the CdTe that is > 2 order of magnitude lower than the electrons: during their migration towards the cathode, they have a much higher probability of interacting with recombination or trapping sites. During these interactions, they disappear and are not collected at the cathode, creating some charge losses.

Therefore, a low-energy photon interacting close to the cathode induces few electron losses and almost no hole losses, while a high-energy photon interacting close to the anode creates more hole losses and almost no electron losses. The charge carriers lost cannot be used to measure the photon energy, meaning that the measured energy underestimates the incoming photon energy, creating this low-energy tail.

3.4 Classification of the events by the ELS

As presented in Sec. 3.1, the ELS are responsible for the detection and the arrival time, energy measurement, position, and multiplicity measurements of the photons interacting with the detection plane. Here we describe how the events are classified depending on their positions and multiplicity.

3.4.1 Classification mechanism

The events registered by the ELS are classified into several categories according to the logic diagram from Fig. 3.4. First, there are the single events (SE) and multiple events (ME). Multiple events happen when several detectors or pixels trigger within the anti-coincidence window, with a duration of ~ 1 μs. This happens, for example, when a fluorescence photon interacts with another pixel. There is also the possibility of an independent photon interacting with the detection plane at the same time, although it is improbable considering the observed rates and the anti-coincidence window size. A single event is the opposite of a multiple event, happening when a single detector triggers during the anti-coincidence window and the energy is deposited on a single pixel. It is important to note that if two events happen simultaneously on two ELS, they are not considered as multiples but as two single events.

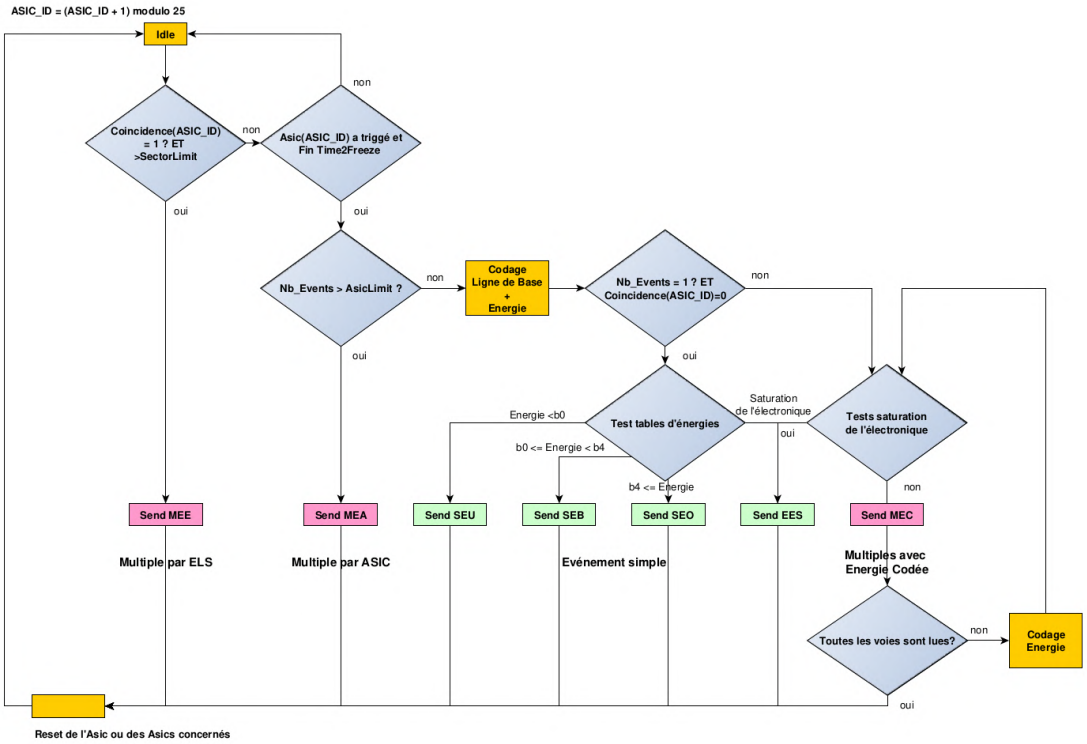

Figure 3.9. Schema of the detection algorithm for reading the events inside the ASICS. Source: ECL-ICD-112-493-IRAP

Based on the energy measured by the electronic, single events are classified into different categories. The SEB (Single Event in Band) events are single events used by the trigger algorithm. They fall inside one of the 4 adjacent energy bands, defined by 5 energy boundaries in the UGTS. The SEU and SEO (Single Event Underflow and Overflow) events have also their energy encoded, except that this energy does not fall within the 4 energy bands. An event with an energy below the lowest band limit is classified as an SEU, while one above the highest band limit is classified as an SEO event. The SES (Single Event Saturated) are events happening when the energy either saturates the electronics during the energy measurement or when a trigger signal is associated with no channel.

Multiple events also have sub-categories, which are defined according to the number of events composing them and the location of these events. The MEC (Multiple Events Coded) events involve a small number of detector hits (usually two), whose energy is encoded by the electronics. MEE and MEA (Multiple Events ELS and ASIC) events involve many simultaneous hits: while the multiple events are still counted on the detection plane, the individual energy of the events is not encoded. There are limits on the detection plane (typically 2 for the MEA limit and 3 for the MEE limit) corresponding to the limit of simultaneous events per ELS (respectively per ASICS) for which the system stops creating MEC and instead creates MEE (respectively MEA).

For example, if a multiple event creates 3 events on 3 different ASICs, it will be considered as a single MEE event. However, if it creates 2 events on the same ASIC and one additional

event on another ASIC, it does not exceed the MEA and MEE limits and the 3 events will be stored as MEC events. Finally, creating 3 events on the same ASIC will make this event a single MEA event.

3.4.2 Format of the ELS frames

As it has been shown before, several types of events can be transmitted by the ELS to the UGTS. Moreover, one event type is not related to photon interactions, called the Time Frame Events (TFEs). The UGTS sends these TFEs to each ELS every 10 ms. When an ELS receives a TFE, it immediately includes it in the data flow and resets its internal clock, allowing it to tag individual photons relative to the Time Frame Events.

We summarize below the event frames sent to the UGTS by the ELSs.

- The ASIC output is the first important variable: it encodes the nature of the event. This value ranges from 0 to 24 for SE and MEC events (depending on the ASIC impacted), 25 for MEA, 26 for MEE, and 28 for TFE events. The system makes the difference between MEC and SE thanks to an extra bit.
- The SE and MEC frames contain information about the ASIC number, the pixel number on which the event is happening, the time of arrival relative to the last TFE, the energy of this event encoded into channels, and the band in which the event is located.
- For MEE and MEA, time is still encoded in addition to the number of events generated by this multiple, but not the energy. The ASIC on which the multiple event is detected is stored for MEA events. However, the ASIC numbers are not stored in the case of MEE events.
- For TFE, there are two pieces of information: the number of events registered on one of the 800 pixels over the last 8 seconds and the pixel number for which this information is given. The pixel number is incremented by 1, from 0 to 799

The energy in the SE and MEC events is encoded on 10 bits ranging from 0 to 1023 in channels (CHAN). There is a linear relation specific to each pixel, allowing to convert a channel into energy. J-P Dezalay has measured this conversion from calibrations with radioactive sources.

Figure 3.10 illustrates the distribution of the two coefficients of this linear relationship. The energy E of a SE or a MEC on a pixel XY can then be calculated as:

$$E(XY) = \frac{CHAN - b(XY)}{a(XY)} \tag{3.5}$$

Something important to note is that all the events whose energies exceed the channel 1023 are stored in this channel. In order to compute a correct spectrum, it is therefore essential to remove the events coming from the channel 1023.

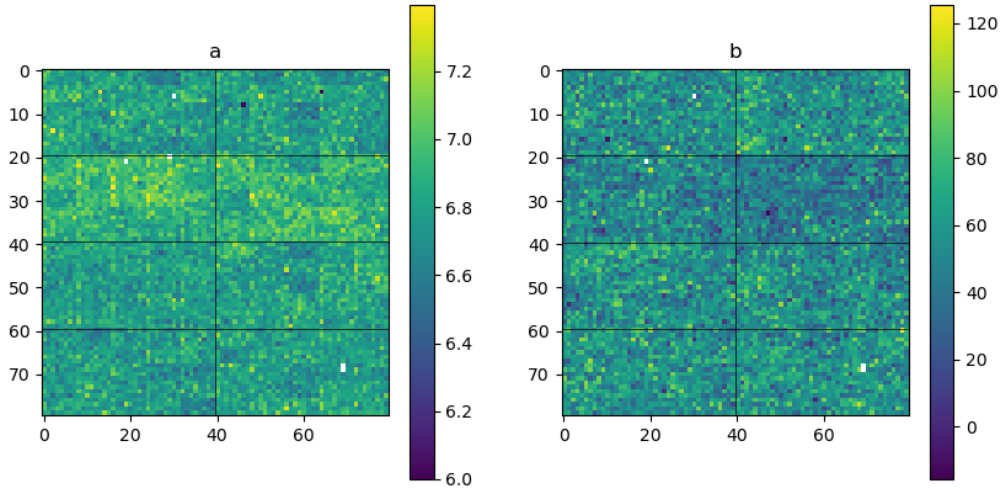

FIGURE 3.10. a and b coefficients calibrated during the PFM campaign.

3.5 γ-ray bursts detection algorithms

The characteristics of the photons detection and their energy measurement presented above are used to characterize in real-time the photons received by the UGTS, allowing ECLAIRs to detect and localize GRBs. The manifestation of a GRB on the detection plane is as follows:

(1) An excess of counts in some or all the ECLAIRs energy bands compared to the expected signal from the background emission.
(2) The appearance of a new source in the sky image, obtained by deconvolving the shadowgram projected by the GRB on the detection plane.

ECLAIRs has two self-triggering systems that detect these two manifestations without any ground intervention. We introduce in this section the two trigger systems implemented on-board, each using the deconvolution process presented below. We also mention a third trigger system based on the offline analysis of the raw data sent to the ground by *SVOM* through the X-band.

3.5.1 The deconvolution process of ECLAIRs coded mask

The coded mask technology of ECLAIRs is the solution to obtain a hard X-ray instrument with a large FoV while still having a localization precision of a few arc minutes. As explained in Sec. 3.1, the coded mask forces the photons coming from a point source in the sky to project a specific pattern on the detection plane called the shadowgram. The deconvolution is an arithmetic process that uses the characteristics of the coded mask: applied on the shadowgram projected by the GRB on the detection plane, this method

allows to reconstruct the 199×199 sky image seen by the instrument responsible for this projection of the shadowgram. The main components involved in the deconvolution process are:

- The detector image D with dimensions 80×80. This image can be corrected from the non-flatness due to the background or Earth transit, creating a corrected detector image $\tilde{D}$ with dimensions 80×80. Assuming that the number of counts on each pixel in the detection plane is following the Poisson distribution, the variance of the corrected detector image can be assumed to be equal to the detector image, so that $\mathrm{Var}(\tilde{D}) \approx \tilde{D}$.
- This detector image can be weighted with a matrix W to compensate for effects such as noisy pixels (by disabling them for the deconvolution) or non-uniformity of the detection plane at low energies.
- The mask matrix filled with integers, with 0 for the opaque parts and 1 for the holes. This mask is then linearly interpolated from a 46×46 array to a 120×120 array M so that the physical size of the interpolated mask pixels has the same physical size as the pixels of the detection plane. The pixel values from this matrix are floats, ranging from 0 to 1 because of the interpolation. From this interpolated mask M, the arrays G^+ and G^- can be constructed. The computation of these two arrays relies on the mean opening of the mask α, equal to 0.4 in the case of ECLAIRs. The array G^+ is defined as the values of $(1/\alpha M - 1)$ for $M > \alpha$ and 0 elsewhere, whereas G^- is defined as $(1/\alpha M - 1)$ for $M < \alpha$ and 0 elsewhere.
- The matrix A normalizes the counts on the shadowgram to get a correct flux of the sources located in the center of sky pixels.
- The matrix B allows to get a flat sky image if the noise is flat with a null mean without sources

It is possible to estimate the number of counts received from each sky pixel using the defined matrices above with the equation (Goldwurm, A. et al., 2003):

$$C_{\mathrm{cnt}}(i,j) = \left(\frac{\left[G^+ \star \left(\tilde{D} \times W \right) \right]}{A} - \frac{B \times \left[G^- \star \left(\tilde{D} \times W \right) \right]}{A} \right)(i,j) \tag{3.6}$$

And the variance of each pixel as:

$$C_{\mathrm{var}}(i,j) = \left(\frac{\left[G^{+2} \star \left(\tilde{D} \times W^2 \right) \right]}{A^2} - \frac{B^2 \times \left[G^{-2} \star \left(\tilde{D} \times W^2 \right) \right]}{A^2} \right)(i,j) \tag{3.7}$$

So that the image SNR for a given sky pixel can be computed as:

$$SNR_{\mathrm{im}}(i,j) = \frac{C_{\mathrm{cnt}}(i,j)}{\sqrt{C_{\mathrm{var}}(i,j)}} \tag{3.8}$$

In these equations, the operator $\star$ represents a convolution between two quantities, while the operator $\times$ represents the product term by term of the two matrices.

This SNR formulation can be compared with the one presented in Sec. 3.5.2. In the hypothesis of a large number of counts N_c from a source in the sky, the illuminated pixels will have $C_{var} \propto N_c$ and $C_{cnt} \propto N_c$, which means that $SNR_i \propto \sqrt{N_c}$. It is different from the count SNR, where in the same case, there will be $SNR_c \propto N_c$. In practice, it means that for $N_c >> 1$, the count SNR will be larger than the image SNR. However, the two of them are equivalent for the lower number of source counts (or the image SNR can even be higher).

3.5.2 The count trigger

The count trigger algorithm (developed by CEA (Schanne et al., 2019)) analyzes the counts received on the detection plane by the UGTS. This algorithm is based on the construction of lightcurves, which are histograms of the number of events received within a time interval Δt. The count trigger algorithm creates lightcurves for different timescales (Fig. 3.11(a)), energy stripes (Fig. 3.11(c)) and detection plane zones (Fig. 3.11(c)). Using these constructed lightcurves, it fits a quadratic function to predict the count expected by the instrument during the next epochs. The algorithm then tries to detect if the counts received during the next epochs are in excess compared to the prediction: the background prediction B is compared with the real count C received for a given timescale, energy stripe, and zone via a signal-to-noise ratio (SNR). The definition of this SNR is as follows:

$$SNR_c = \frac{C - B}{\sqrt{B}} \tag{3.9}$$

If this ratio SNR_c exceeds a threshold previously defined for a given timescale, energy stripes, and zone, a shadowgram of the detection plane is created for these selected parameters. This shadowgram is then de-convoluted (via the process explained before) to create an SNR image of the sky, where the value $SNR_i(i, j)$ is defined from Equation 3.8.

The algorithm searches on the created sky SNR image if there are some sky pixels exceeding a defined threshold (~ 6.5) and localizes this excess. This threshold is calculated as the ratio between the $SNR_i(i, j)$ value of a sky pixel divided by the standard deviation of the pixel value of the image. If these pixels are not located at the position of a known source (Crabe, Sco-X1) and if the Earth does not obscure them, the count trigger considers that it has detected a transient. Furthermore, if the pixel value exceeds another threshold (~ 8), ECLAIRs transmits a slew request to the satellite so that *SVOM* can point its narrow field instruments towards this sky direction.

The energy stripes used by the trigger algorithm combine the ECLAIRs energy bands. For example, one stripe might be the combined energy bands $\{0, 1, 2, 3\}$ (typically $4 - 120$ keV), another might be $\{2, 3\}$ ($50 - 120$ keV) and another one $\{0\}$ ($4 - 15$ keV).

The threshold and the bands/stripes to use for the count trigger algorithm are still under discussion because they have many implications:

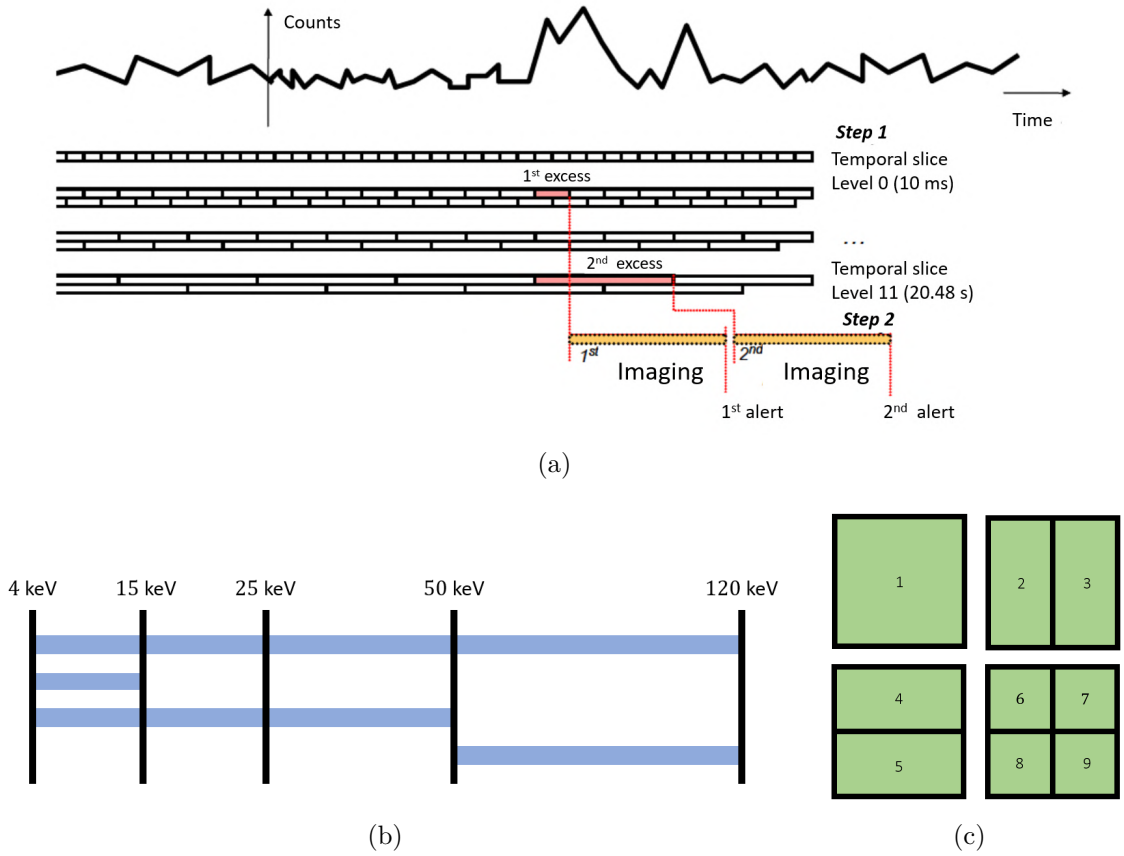

FIGURE 3.11. (a) Schema of the count trigger algorithm with the timescales used (b) Definition of the 4 energy stripes with the 4 energy bands, using the 5 specified energy boundaries (c) Segmentation of the detector zones

- The count threshold choice impacts the rate of the sky image production. The UGTS system can make an image through the deconvolution process every 2 seconds. Therefore, the count threshold should be chosen so that the image deconvolution is not requested at a higher rate. Moreover, as the number of expected GRBs is around 1 to 2 per week, a count threshold leading to the production of hundreds of thousands of images per week does not make sense.
- For the image thresholds, the values to be applied depend on the desired FA rate. Because of the statistical fluctuations of the counts on the detection plane and the reconstructed of the sky image, the image SNR can be high, even without any source in the instrument FoV. This is especially true on the edges of the sky image. For this reason, the image threshold has been chosen so that the FA rate does not exceed one per day, and the edges of the sky image have been removed from the analysis.
- The energy bands and stripes used are the only ones available at the UGTS level. Consequently, they are also used to construct the VHF alert products. The

calculation of the level 0 scientific products (quick T90, hardness ratio, peak flux) depends on these values.

- As it has been shown in Sec. 3.6, the detection plane has instrumental effects at low energy. The thresholds and stripes should therefore be selected to mitigate such effects.

3.5.3 The image trigger

The image trigger is different from the count trigger as it only relies on the source SNR in the image. Instead of selecting the shadowgram for which the count SNR was the highest (for a given zone, energy range, and timescale), the image trigger algorithm systematically creates sky images from the shadowgrams obtained every 20.48 seconds for each energy stripe. This is made possible because the system only creates one image every ~ 5 seconds, which is feasible with the UGTS CPU performances.

With such long timescales, the shadowgram has to be cleaned from the non-flat background which increases the variance of the sky image. The two reasons for the image's non-flatness are the Earth's obscuration in some sky directions and the fact that pixels see different quantities of the sky depending on their locations on the detection plane. Therefore, the cleaning aims at removing the non-flatness of the background from the shadowgram, thanks to a fitting process or wavelet approach (Dagoneau et al., 2020).

The sky images are then summed up to obtain sky images integrated from 40.96 to 1310.72 sec, corresponding to ~ 20 minutes of maximum exposure. For each of these images, the image trigger algorithm looks for an SNR excess in the image, excluding the already known X-ray sources positions and part of the sky masked by the Earth (similar to the second phase of the count trigger). If an excess is discovered with an SNR above a given threshold, the image trigger algorithm sends the information to the *SVOM* satellite.

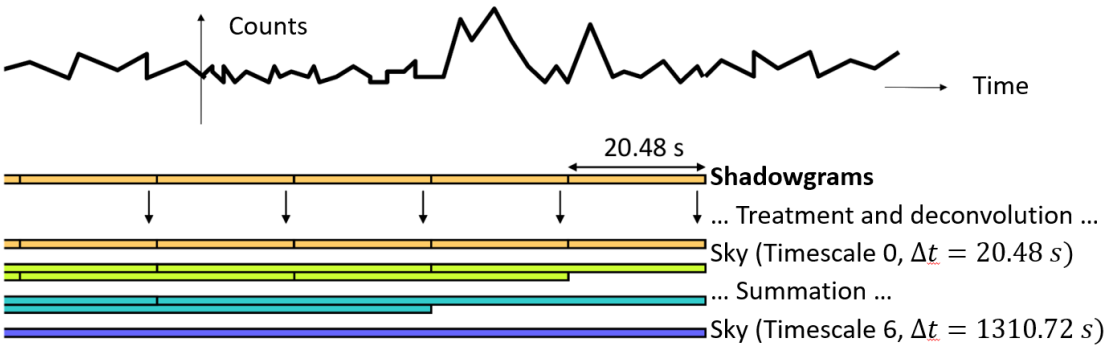

FIGURE 3.12. Chronograph of the image trigger algorithm. Source: Dagoneau (2020)

The long timescales used for the image trigger algorithm are well adapted to detecting ultra-long GRBs (Dagoneau et al., 2020), whose prompt emission can last several thousands of seconds (e.g. $\sim 2,000$ sec for GRB 100316D Starling et al. 2011): a timescale of up to 1310.72 sec can be crucial there for the detection.

3.5.4 The offline trigger

The ECLAIRs instrument will send all the raw events registered on-board to the ground. This feature is unique and will be the first one for a GRB mission: *BATSE* was, for example, only sending continuous lightcurves to the ground, while *Swift* is only able to send the events around a time of interest (Tohuvavohu et al., 2020). Having an offline trigger offers several unique possibilities.

First, there are limits imposed on the UGTS. Because of the required space qualification of the components, the on-board computers on the satellite cannot have as much processing power, memory, or storage as the ground computers. Having an offline trigger allows a re-analysis of the events without these limitations.

Second, the on-board trigger's design must be robust enough to limit the number of false alarms (FA). A FA leading to an unjustified slew will waste observing time and resources. Typically, the on-board trigger must have a FA rate below 1 per week (without a slew request) and below 1 per month with a slew request. For this reason, the threshold levels discussed above for the on-board trigger algorithms will be conservative. On the ground, the constraints on the FA rate are less important: the consequences of a false detection will probably be limited to the intervention of a burst advocate or the run of an automatic pipeline.

Third, the on-board trigger has periods where it will not be operational (e.g., observations of specific "ToOs" for which the on-board trigger will be disabled, specific periods of instrument calibrations, or during the "slews"). The events are still recorded, but the on-board trigger algorithms are not functional because of the additional complexities created by such situations (e.g., the complex background evolution during slews). By running the offline trigger during these moments, approximately a month of additional observations per year could be used for the GRB detection (Bouchet & Atteia, 2016). Moreover, as explained before, the on-board trigger algorithms do not consider some sky locations corresponding to known X-ray sources or Earth-masked locations. This prevents the on-board algorithm from detecting events such as Terrestrial Gamma-ray Flashes (TGFs), objects of interest for other scientific communities.

Fourth, the offline trigger can provide the opportunity to use combined data from several instruments for the GRB search. This can be the other *SVOM* γ-ray instruments, like the GRM and GWAC, but also the gravitational waves alerts from LIGO/Virgo, the neutrinos from IceCube or KM3NeT, and the optical data from Vera Rubin Observatory. Having several independent searches can decrease the individual SNR of each instrument required to make a detection. Moreover, the possibility to derive upper limits on the gamma-ray counterparts for the LIGO/Virgo GW alerts or neutrino alerts can set some constraints on the models or narrow down the error box position of the event. Another example of synergy is the case of SNe detection by Vera Rubin observatory, where the offline trigger will be able to search for precursors such as shock breakouts prior to the main reported events when they fall within the ECLAIRs FoV. Finally, for the optical afterglow detected by the Vera Rubin observatory, ECLAIRs will also be able to constrain the existence of a prompt emission to determine whether these afterglows were orphans.

Chapter 6 shows a possible implementation of the offline trigger in adequation with points 1, 2, and 3. Ph. D. Miguel Llamas-Lanza's work consists of implementing all these points.

3.6 Instrumental effects

The ECLAIRs characteristics that have been presented have assumed an ideal, noiseless behavior. However, during the test campaigns, the detection plane and its electronics have displayed some instrumental effects, some expected and others not. This section describes these effects and their potential consequences on the on-board trigger algorithms. A GitLab project simulating these effects, called `dpix-effects`, is available at https://drf-gitlab.cea.fr/eclgrm-fr/dpix-effects.

3.6.1 Impact of SBN configuration

As explained in Sec. 3.2, the SBN threshold sets the minimum voltage that should be collected (corresponding to the energy deposited) during a photon/detection plane interaction. A photon is detected and registered on a given pixel only if its energy exceeds its energy threshold. This threshold is chosen independently for each pixel, depending on their sensitivity to electronic noise. For example, pixels 8 and 16 of each XRDPIX module have been identified as noisy because of their location next to the trigger signal wire (creating an effect called cross-talk), and it was necessary to increase their SBN value from ~ 16 to ~ 30. (see left panel of Fig. 3.13).

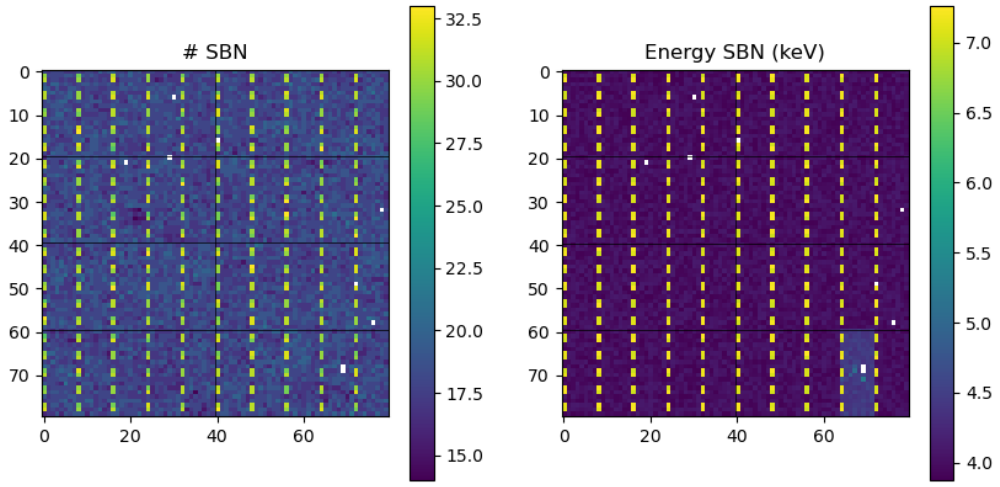

Figure 3.13. (left) SBN values used for the TXG PFM test sequence. (right) Energies corresponding to the SBN values obtained with the Equation 3.10.

The correspondence between the SBN command and the energy threshold has been calibrated for every pixel (Godet, 2022). This linear relation is characterized by two coefficients α and β, so that:

$$SBN(XY) = \alpha E_{\mathrm{SBN}} + \beta \tag{3.10}$$

Taking the previous example, the corresponding threshold energy for the pixels 8 and 16 with an SBN value of 30 is ~ 7 keV, meaning that these pixels are not sensitive to events that have an energy below 7 keV. The map threshold energies can be seen on the right panel of Fig. 3.13.

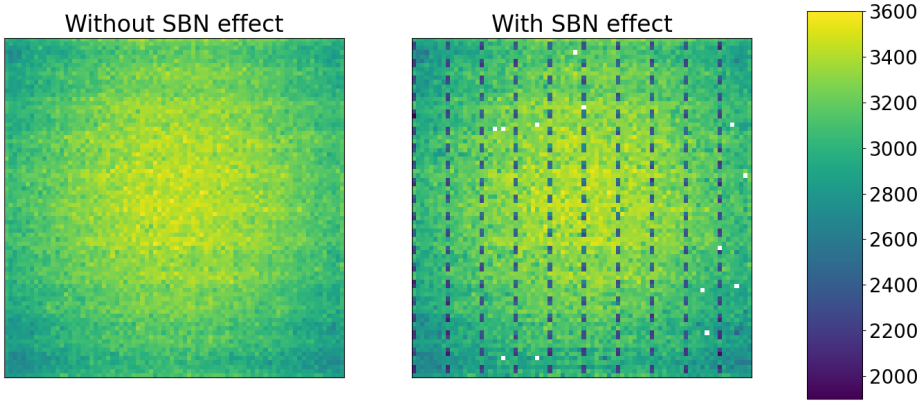

Figure 3.14. Shadowgram obtained for two background orbits composed only of CXB, in the $4 - 150$ keV energy range (left) without the influence of the PFM SBN configuration and (right) with its influence.

Astrophysical background simulations (performed with PIRA, see Sec. 5.2.1) or GRB simulations (see Sec. 5.3.1) do not take into account the SBN configuration, which is necessary to have simulations as realistic as possible. Therefore, all the simulated events with an energy E_m smaller than the pixel energy threshold $E_{\mathrm{SBN}}(XY)$ need to be filtered out.

Figure 3.14 illustrates the impact of the SBN. For a simulated CXB background accumulated over 11760 seconds, a shadowgram is constructed with single events between 4 and 150 keV. The same operation is performed after the SBN filtering. Fig. 3.14 shows the inhomogeneities on the detection plane, created because some pixels are de-activated (white pixels in the image) but also because some pixels on the detection plane are not sensitive to energies below 7 keV. These homogeneities completely disappear as soon as the events have all energies above ~ 7 keV.

Since each pixel has its energy threshold, the efficiency of the detection plane for energies below 7 keV is inhomogeneous. Figure 3.15 shows the efficiency of each pixel relative to a

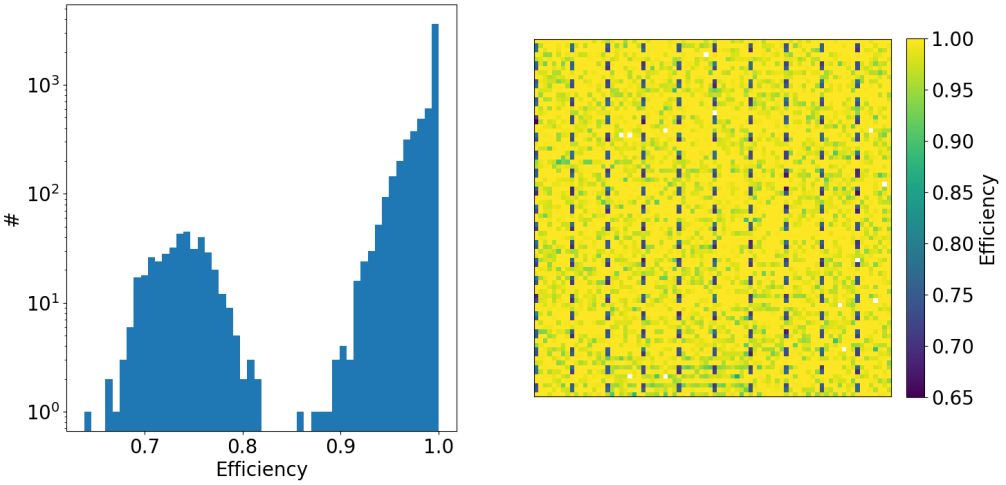

Figure 3.15. Impact of the PFM SBN configuration on the detection plane efficiency for a CXB background between 4 and 150 keV. (left) Histogram of the efficiency of the 6400 pixels on the detection plane and (right) map of the detection plane efficiency

CXB background in the energy range $4 - 120$ keV: it can be constructed by making the ratio (right/left) between the two maps presented in Fig. 3.14. The map clearly shows that a large majority of the pixels have an efficiency of 1.0, while the ones with an SBN value of ~ 30 have an efficiency of around 0.75. The same efficiency map can be done in different energy bands: for example, in the energy range $15 - 120$ keV, this map would be homogeneous with all pixel efficiencies set to 1.0, as the SBN thresholds do not have any effect.

These inhomogeneities are considered inside the weight matrix W, so that the deconvolution process is not affected by the patterns created by the different SBN values (see Sec. 3.5 before). This matrix W should be computed for all the energy stripes used in the ECLAIRs trigger algorithm.

3.6.2 The SLE noise

The SLE noiseis an instrumental effect noticed from the first test campaign of ECLAIRs. It has been attributed to the heat-pipes because of the strong time correlation of their operation with the noise intensity. This noise is mainly characterized by its spatial distribution, where the pixels on the vertical edges of the detection planeseem to be more sensitive and by its presence at low energy (< 10 keV for SE events). Figures 3.16(a) and 3.16(b) show the spatial distribution of the low-energy events from a test performed on the flight model of ECLAIRs (*ECL0_TVAC_20211005_094231*): this noise is principally distributed on the top left and right corners. On the contrary, the detection plane is completely homogeneous when events with energies above 10 keV are taken, as shown in Fig. 3.17(a) and 3.17(b). Section 4.3 presents a more detailed discussion about this noise properties.

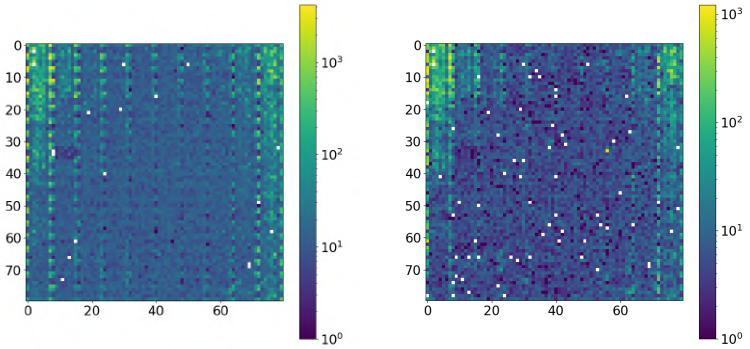

(a) SE < 10 keV (b) MEC < 13 keV

Figure 3.16. (a) Single events (SE) and (b) Multiple events (MEC) distribution from *ECL0_TVAC_20211005_094231* for energies below 10 and 13 keV respectively, showing the spatial distribution of the SLE noise.

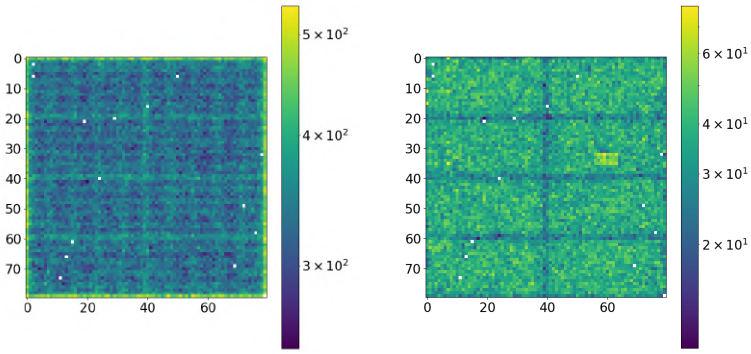

(a) SE > 10 keV (b) MEC > 13 keV

Figure 3.17. (a) Spatial distribution for the same test as for Fig. 3.16(a) and 3.17(b) but with the events energies greater than 10 and 13 keV.

Overall, if the SLE noisewere to happen once in space, it would potentially impact the performances of the on-board trigger algorithms. Because of the location of the noise on the sides of the detection plane and the relatively high count rate on these pixels, the deconvolution process would not perform as expected. The main consequence would be that for low energy stripes affected by the SLE noise(typically with a lower energy boundary below 8 keV), and particularly for the shortest timescales (from 10 to 80 ms due to the SLE noiseproperties), the counts might often exceed the count thresholds defined. It would lead to a systematic deconvolution process, which should be avoided not to monopolize the UGTS processing power. Therefore, these count thresholds would be increased to prevent false detections due to this noise, reducing the sensitivity of ECLAIRs to potential transients with short timescales. The other solution would be to inhibit the pixels on the side of the detection plane for the low-energy stripes, which then impacts the instrument's sensitivity

and its FoV. However, the consequences would be more limited for the offline trigger, where practical solutions such as the one presented in Sec. 4.3 can be applied.

3.6.3 Non-homogeneity of the XRDPIX response at low energy

The PFM test campaigns also showed that the detection plane is unexpectedly inhomogeneous at low energies (without considering the SBN effect discussed above). Figure 3.18(a) shows the spatial distribution of the XRDPIX on the detection plane, the color coding representing their manufacturing batches. We can see that the XRDPIX equipping the PFM detection plane come from 3 different batches that we will call A, B, and C.

Figure 3.18(b) shows the spatial distribution of the counts received during the test around the main emission line of a radioactive source (Fe-55 at 5.9 keV). The XRDPIX that count less than the others around 5.9 keV are spatially correlated with the green XRDPIX (B batch) from Fig. 3.18(a). The histogram on the left of Fig. 3.18(a) shows that the efficiency loss is around $\sim 20\%$. The reason behind this loss of efficiency at low energy are still under investigation: it could be related to the thickness of the cathode contact.

As explained before, inhomogeneities of the detection plane can have consequences on the on-board trigger algorithms. However, dedicated studies performed at CEA (by W. Xie and N. Dagoneau) seem to indicate that the inhomogeneities created by the different batches impact marginally the performances of the count rate and image trigger algorithms.

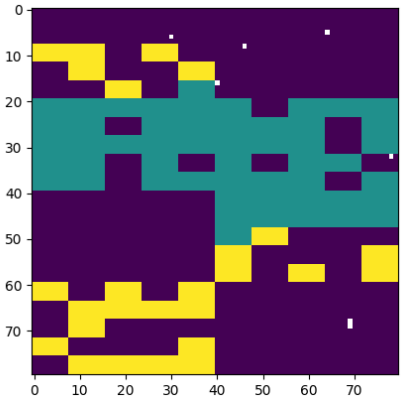

(a)

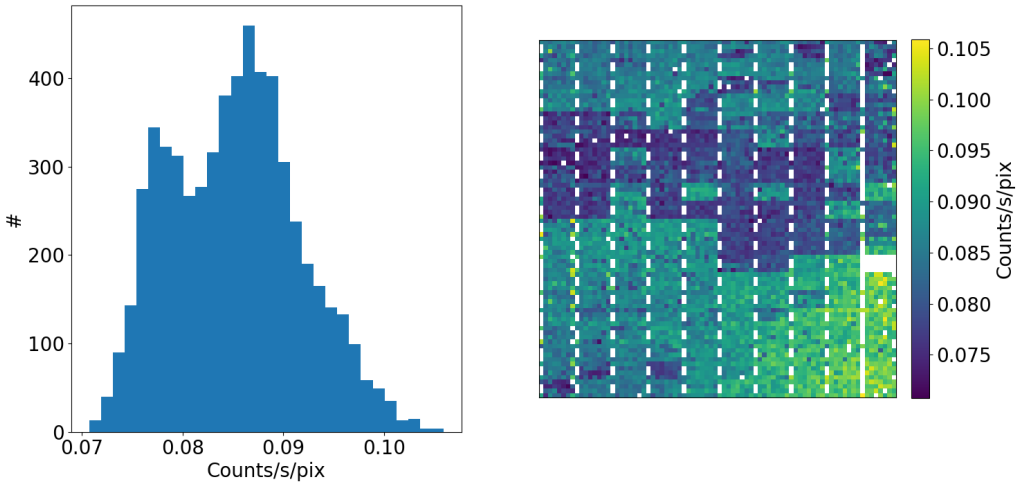

(b)

Figure 3.18. (a) Distribution of the XRDPIX by batches, in purple the ones from A, in green the ones from B batch, and in yellow the ones from C batch (b) Shadowgram of the detection plane in the energy range $4 - 8$ keV obtained from *CE4_Test_PFM8_Fe-55_20210407_204402*

Chapter 4

Instrumental contributions to ECLAIRs

This chapter details my instrumental contributions to ECLAIRs. The first contribution presented in Sec. 4.1 shows the methodology applied to validate the GEANT4 model of ECLAIRs at low energy thanks to the flight model test campaign results. Then Sec. 4.2 describes the investigation of the origin of an unexplained spectral line observed during ECLAIRs test campaign. Finally, Sec. 4.3 shows a characterization and potential mitigation of the SLE noise presented in Sec. 3.6.

Contents

4.1 Calibration of ECLAIRs response with GEANT4 simulations

The response files presented in Section 5.4 are generated with GEANT4 simulations made by Manal Yassine and Laurent Bouchet (Yassine, 2021), based on the mass model of the ECLAIRs instrument in flight conditions. To ensure that these simulations accurately describe ECLAIRs, the mass model of ECLAIRs should be confronted with real tests performed during the PFM test campaign. Note that the mass model used for this comparison is a bit different, as it describes the ECLAIRs instrument in the vacuum chamber instead of integrated on the *SVOM* satellite.

The calibration of the energy response has been done under the supervision of Laurent Bouchet with the support of his Ph.D. student Miguel Llamas Lanza. The purpose of this calibration was to compare the efficiency of ECLAIRs with the one predicted via GEANT4 simulations for several test sequences and several X-ray sources. I have created the scripts that allow reading the test data and eliminating their instrumental biases. I have also taken care of the normalization of the GEANT4 simulations and the application of the instrumental effects on them so that these simulations can be compared with the tests. The GitLab project, called `PFM_DPIX_data_analysis`, is available at https://drf-gitlab.cea.fr/lanza/pfm_dpix_data_analysis.

4.1.1 Set-up for ECLAIRs test campaign

There are two configurations of ECLAIRs used for calibrating the GEANT4 model. These configurations have been used during the test campaign #1 and #4.

The first configuration for campaign # 1 consists of the Flight Model (FM) detection plane, coupled with the FM UGTS (flight software 3.2.2). The second configuration for campaign # 4 consists of the FM detection plane with the shield on the sides, in addition to the external SLI layer and the SLI layer within the TXG cavity. It is coupled with the FM UGTS (flight software 3.3).

4.1.2 Reading and preparing the test files

The first step of this comparison consists in reading the test data, retrieving the events for the calibration, and creating a spectrum that can be compared to other tests. The GEANT4 simulations ECLAIRs only consider the physical interactions photons-matter, while the electronic effects also play a role for the real tests. For this reason, several effects seen on the detection plane and presented in Sec. 3.6 need to be mitigated as much as possible to accurately reconstruct the spectrum. As these effects appear especially in the low-energy range, tests using sources such as Fe-55 or Zn-65 (with their main emission line at low energy) need a thorough analysis.

- To handle the non-homogeneity of the detection plane, modules with lower efficiencies are tracked and suppressed from the analysis
- Pixels located on the detection plane side with a visible column effect have been removed from the analysis.

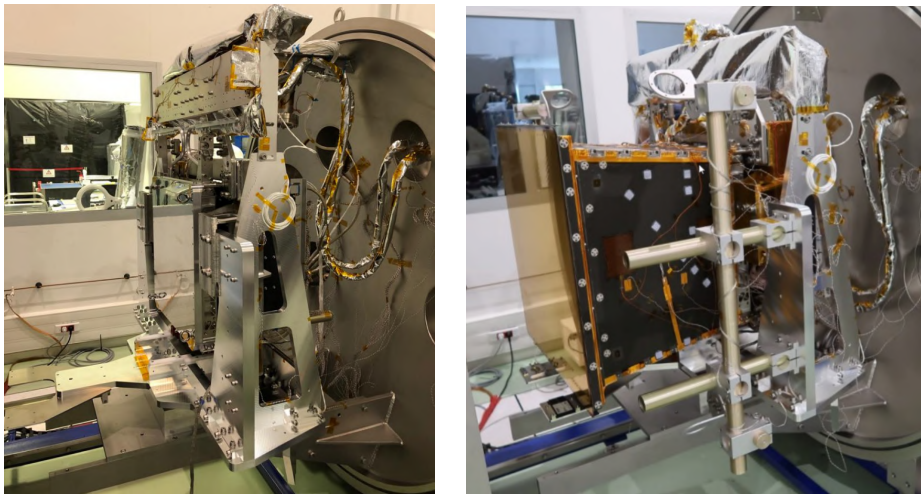

(a) CE1 (b) CE4

Figure 4.1. Configurations used in CE1 and CE4 tests. Credit: CNES/IRAP

- Pixels with an energy threshold above 4 keV have also been removed from the analysis for low-energy sources to limit the SBN impact on the measurement of the spectral lines.

An example of clean-up is shown in Fig. 4.6, where pixels impacted by one of the 3 types of in-homogeneities defined above have been removed.

The spectrum is then created from the spectral files generated by the DPIX studio during the acquisition of the tests. These files contain the number of counts per pixel and channel for all the test duration. Finally, a linear relation calibrated on precedent tests allows converting the channels into energies, using the formula presented in Sec. 3.2.

Finally, the spectrum $S(E)$ [counts/s/keV/pix] is normalized by the acquisition duration and the number of available pixels to be comparable with the MC simulations.

4.1.3 Comparison with GEANT4 simulations

The GEANT4 simulations have been made by L. Bouchet, simulating the set-up of the different tests inside the vacuum chamber to be as close as possible to the real tests conditions. This section describes how the GEANT4 simulations are treated to become comparable with the tests.

Methodology

From the list of events created with GEANT4, we want to build a normalized spectrum $S_{\mathrm{G4}}(E)$ that can be compared with the one from the tests. However, these GEANT4 simulations do not incorporate any time dependency: the spectrum obtained with a GEANT4 simulation is computed for a given photon number $N_{\mathrm{ph,G4}}$ in units of [counts/keV/pix]. Therefore, to compare this spectrum with the spectrum obtained from the tests, we have

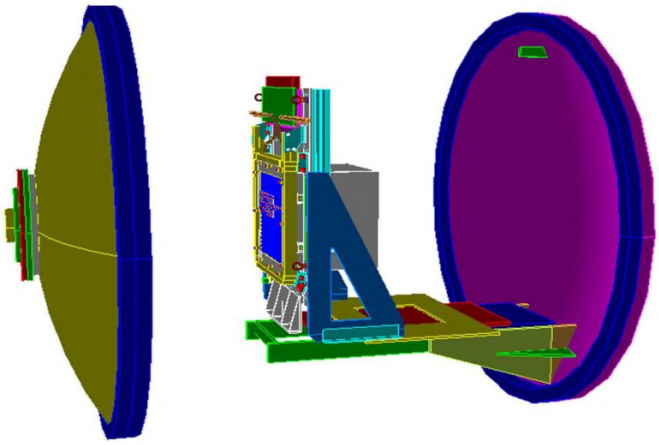

Figure 4.2. GEANT4 mass model of the PFM detection planein the vacuum chamber. The radioactive source is placed in front of the camera in the source holder on the left part of the vacuum chamber. Credit: L. Bouchet

to normalize it by duration during which the $N_{\mathrm{ph,G4}}$ GEANT4 photons would have been emitted by the radioactive source.

Radioactive sources used

Radioactive sources emit photons at a rate that depends on their activity and the nature of the source. For a given source, the probability of emitting a photon at given energy during decay is described by a quantity called the branching ratio. Figure 4.3 shows the expected photon energy pondered by the activity and the branching ratio for the radioactive sources used to calibrate the detection plane.

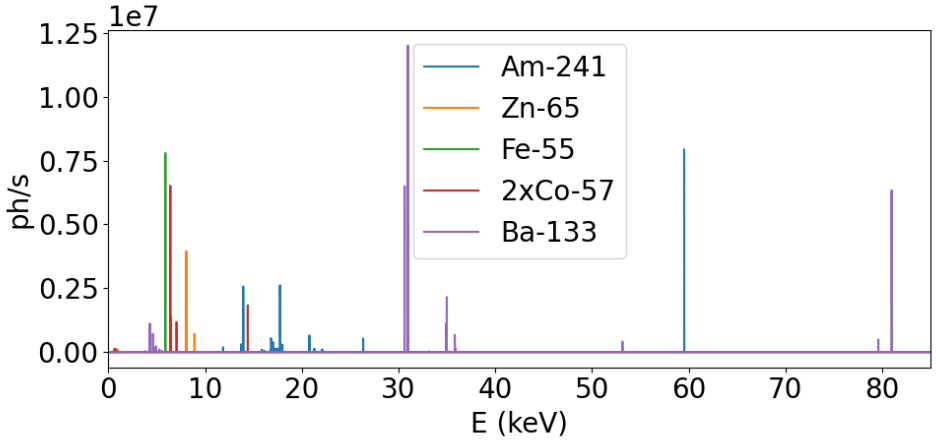

Figure 4.3. Expected photon rate emitted isotropically by the radioactive sources used for the calibration, for a duration of 100 seconds for Ba-133 and the two sources of Co-57 and 10 seconds for the others.

Application of the energy resolution on GEANT4 simulations

As explained in Sec. 3.6, the measurement of the energy deposited by the photons on the detection plane has some incertitudes, mainly created by the randomness of the charge collection, the charge loss at high energy, and the electronic noise. These effects are not considered in the GEANT4 simulations: the output of such simulations can be seen in Fig. 4.4, where we can see the lines created by the photons-matter interactions. These lines are visible because most of the processes in this energy range (fluorescence, radioactive sources emissions) are happening at discrete energies.

Therefore, the energy resolution must be applied to make the GEANT4 simulations comparable to the tests. The method used is identical to the one developed for the astrophysical simulations in Sec. 5.4.

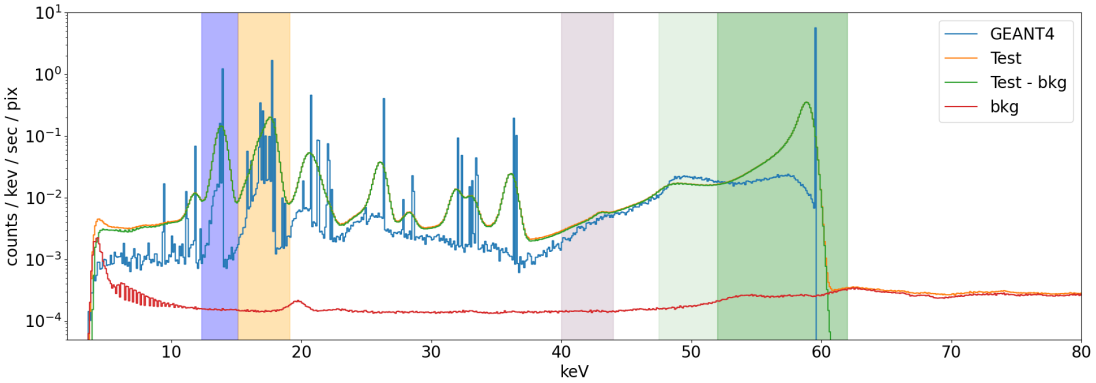

Figure 4.4. Example of Am-241 test (*CE1_PFM3-Am241_bis_20210211_190244*) compared to GEANT4 simulations without the ECLAIRs energy resolution.

Normalization of the spectrum

The activity of a source with half-life $t_{1/2}$ can be calculated for a given Δt, representing the time between the moment the activity A_0 has been measured and the activity $A(\Delta t)$ when the source is used. This decay is essential to consider when comparing simulations with the real tests, especially for sources such as Zn-65 with a half-life of a few hundred days ($t_{1/2} \sim 200$ days).

Once calculated, this activity should be multiplied by the sum of all the branching ratios ($b_{\mathrm{tot}} = \sum_{\mathrm{E_i}} b_{\mathrm{E_i}}$, with $\mathrm{E_i}$ representing all the possible photon energies the source can release) to obtain the number of photons emitted by the radioactive source per second.

$$R_{\mathrm{ph}} \ [\mathrm{ph/s}] = A(\Delta t) \times b_{\mathrm{tot}} \tag{4.1}$$

Using this photon rate, it is possible to estimate the equivalent duration of a given GEANT4 simulation that draws $N_{\mathrm{ph,G4}}$ photons by computing the ratio:

$$dt_{\mathrm{G4}}\ [\mathrm{s}] = \frac{N_{\mathrm{ph,G4}}}{R_{\mathrm{ph}}} \tag{4.2}$$

This duration dt_{G4} can be used to normalize the GEANT spectrum. It is then possible to compute the ratio between the two in a given energy range using the two normalized spectra $S(E)$ calculated from the tests and $S_{\mathrm{G4}}(E)$ calculated from the GEANT4 simulations. This ratio $\eta_{E_0-E_1}$ is computed around the main emission lines of the radioactive sources within the energy range $[E_0, E_1]$ (see Table 4.1 for the energy ranges used). If the GEANT4 simulations successfully reproduce the reality, then this ratio should be close to 1.

$$\eta_{E_0-E_1} = \frac{\int_{E_0}^{E_1} S_{\mathrm{G4}}(E)\mathrm{d}E}{\int_{E_0}^{E_1} S(E)\mathrm{d}E} \tag{4.3}$$

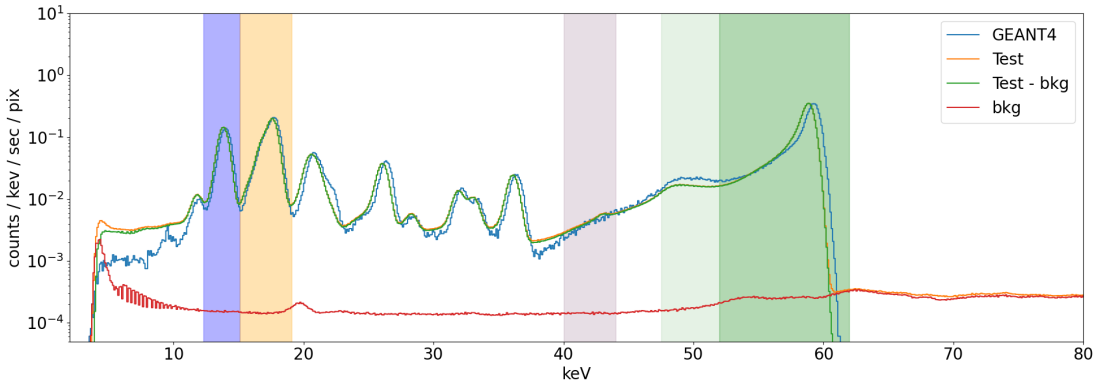

Figure 4.5. Example of Am-241 test (*CE1_PFM3-Am241_bis_20210211_190244*) compared to GEANT4 simulations with the ECLAIRs energy resolution.

Figure 4.1.3 shows the comparison between one test and its corresponding GEANT4 simulation. The blue, yellow, and green bands represent the energy ranges around the Am-241 emission lines, while the fair purple and fair green are the continuum used as a reference for the lines.

4.1.4 Results

Table 4.1 shows the obtained ratios for several tests and sources, with most of the ratios within ±10% of 1, showing a good agreement between the GEANT4 simulations and the tests.

However, several outliers can be identified. The test *CE4_Test_PFM8_Fe-55_20210407_204402* is the most important, with a deficit of almost 50% of events in the tests data: the GEANT4 model predicts an efficiency too high for this energy range compared to the one observed during the tests. There are two possibilities: either the GEANT4 model does not properly

Table 4.1 . Ratio obtained for the PFM-detection planecalibration, using several radioactive sources and tests.

Test name	Source	Emin [keV]	Emax [keV]	Line [keV]	Ratio G4/test
CE1_PFM3-Zn65_20210215_211658 CE4_PFM8_Zn-65_20210408_231621	Zn-65	6	10.5	8.13	0.98 0.97
CE1_PFM3-Fe55_20210212_172228 CE4_Test_PFM8_Fe-55_20210407_204402	Fe-55	4	8	5.96	1.05 1.56
CE1_PFM3_2xCo57_20210217_155258	Co-57	5 12.5 105 125	8 16 125 140	6.47 14.41 122.1 136.5	0.87 0.93 0.93 1.23
CE1_PFM3-Ba133_20210216_182839	Ba-133	6.2 28 32.4 70	10.5 32.4 37 82	8.35 30.86 35.14 80.90	0.98 1.09 1.00 1.04
CE1_PFM3-Am241_bis_20210211_190244	Am-241	12.3 15.1 52	15.1 19.1 62	13.93 17.5 59.54	1.00 1.07 1.02

reproduce the instrument response at low energy, or the lower value measured during the test is due to an external effect not taken into account in the simulations.

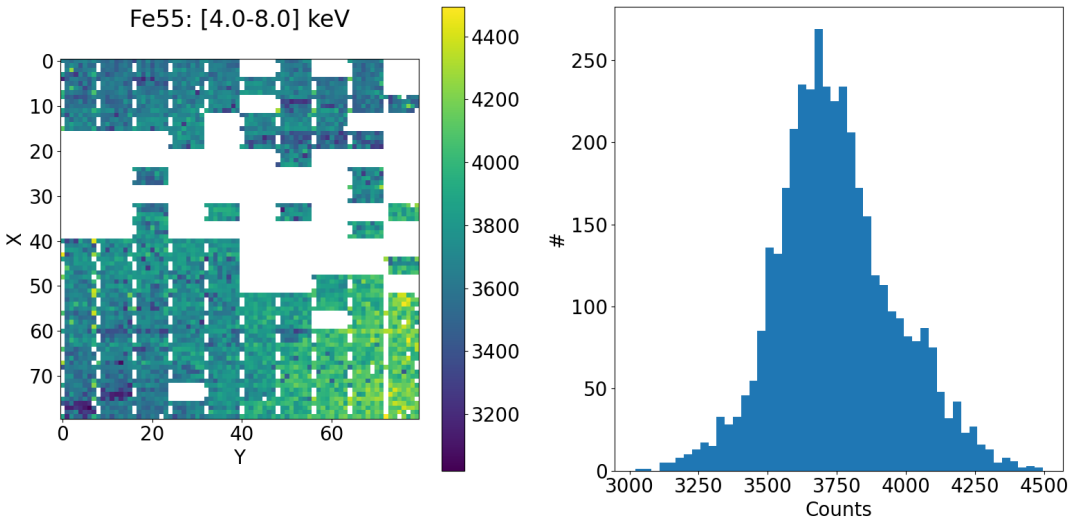

Figure 4.6. Shadowgram used for the comparison of *CE4_Test_PFM8_Fe-55_20210407_204402* with GEANT4 simulations.

Figure 4.6 shows that the Fe-55 line intensity is not uniformly distributed on the detection plane, with a gradient ranging from the bottom right of the shadowgram to the top left. The histogram of values shows that the lower and upper parts have counts differing by $\sim 20\%$ maximum, which is not enough to explain the 50% deficit of events in the test data. Therefore, the reasons behind this deficit remain yet unknown, and are still being investigated.

Nonetheless, the excellent agreement between the other tests and the GEANT4 simulations allows us to be confident in the response files created for ECLAIRs.

4.2 Investigation of the mysterious 20 keV line

During the PFM test campaign, a spectral line at 20 keV has been noticed, as shown on the spectrum presented in Fig. 4.7(a). The line even appears on the spectrum of background noise acquisition of the instrument, and its presence remains unexplained by the GEANT4 simulations. This section aims to characterize this line properties to unveil its origin.

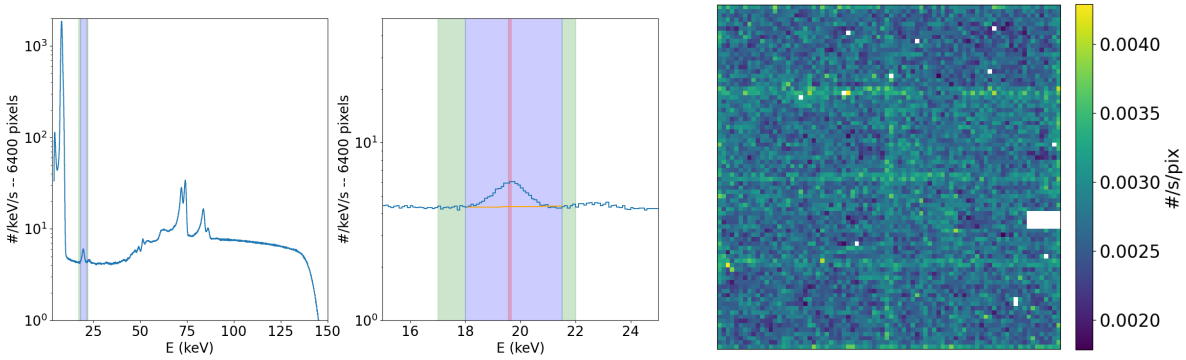

(a) (b)

Figure 4.7. (a) Spectrum from test *CE4_PFM8_Zn-65_20210408_231621*, with a close up on the 20 keV line (b) Detection plane image for SE in the energy range $18 - 21.5$ keV obtained from the same test

Figure 4.7(b) shows a detection plane image of SE events considering energies around the energy of the line: the spatial distribution of the line is more or less homogeneous. This gives a first clue on the localization of the material that generates this line: it has to be homogeneously seen by the detection plane.

Figure 4.8 shows the comparison between the intensity of the continuum below the line (interpolated between the two green bands from Fig. 4.7(a)) compared to the intensity of the 20 keV line for various tests. The former is calculated as the integral of the orange curve in the energy range delimited by the blue band, while the latter is the integral of the difference between the blue and orange curves in the same energy range. The tests used for Fig. 4.8 encompass three different configurations: the PEQM test campaign, the PFM tests in Signe-3 at CNES, and the PFM tests for the whole camera at Airbus Defense & Space.

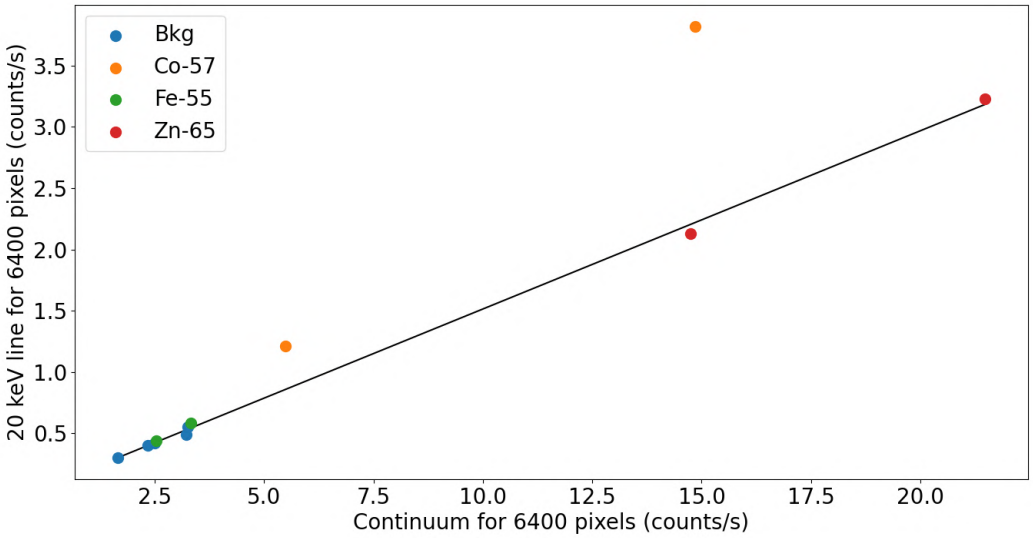

Figure 4.8. Evolution of the 20 keV line intensity relative to the continuum value, for several tests and configurations.

Figure 4.8 illustrates that for tests with sources emitting below 20 keV (green and red dots for Fe-55 and Zn-65) and tests without any source (blue dots), there is a scaling relation between the continuum and the 20 keV line intensity. Moreover, if we see tests with a source that emits at higher energy (e.g., the Co-57 at 122 keV with orange dots), we can see that the line intensity increases compared to the scaling relation.

Since the intensity of the line increases relative to the background, the physical phenomena observed is most likely fluorescence. The material emitting these fluorescent photons is excited by the background continuum (i.e., muons, high-energy photons, particles): the more intense the continuum, the more photons released. The presence of a Co-57 source increasing even more the line intensity indicates that the material releasing this 20 keV line is also excited by the high-energy photons. If the physical phenomenon was a radioactive decay from a material, it should not be affected by the presence of a source or by changes in the continuum. As the intensity of the line compared to the continuum did not change from the PEQM to the last PFM tests (despite the addition of the mask, shielding, different material for the belt, and different vacuum chambers), it is safe to assume that this line comes from the detection plane itself, potentially the electronic behind.

Moreover, the fact that the line is a fluorescence line at 20 keV also restrains the potential emitter candidates. The Molybdenum has an emission at 19.6 keV from its K_β line. However, the K_α lines at 17.4 and 17.5 keV are 10× more likely to happen: if this material was responsible for the 20 keV line, a much more important line at $\sim$ 17.5 keV should be visible. The Rhodium is another candidate, with K_α lines at 20.22 and 20.07 keV. According to GEANT4 simulations made by L. Bouchet, 5% of Rhodium in the Al203 ASIC ceramics excited by a muon background would be enough to explain the 20 keV line.

Nonetheless, the origin of this line remains unsolved for the moment, as the presence of such a quantity of Rhodium in the ASIC ceramics has not been confirmed by the manufacturer. Finally, this line is too weak to have any perturbation on the behavior of ECLAIRs: this investigation aimed mainly at better understanding the instrument and its components rather than fixing this line emission. However, it might be possible to use this line for the in-flight calibration.

4.3 Characterization and mitigation of ECLAIRs SLE noise

As described in Sec. 3.6, the SLE noise might impact the performances of ECLAIRs trigger algorithms if it were to happen on-flight. In the context of my thesis, I have contributed to the study of this noise by proposing a characterization to measure its intensity and a method to remove the events generated by such a noise.

The presentation from Guillemot (2022) shows that the temperature gradient between the condenser and the evaporator of the heat-pipes are correlated with the apparition of the noise. However, its physical origin remains until this point unknown: we do not know whether it is mechanical (micro-vibrations), thermal (temperature gradients within the detection plane), or radiative (even though this possibility is not very credible). Its characterization might help to shed some light on its origin. It also enables laying the ground for a mitigation algorithm for this noise based on its characteristics. This section describes more in detail the SLE noise while also proposing a method for mitigating its impact.

4.3.1 *ECL0_TVAC_20211005_094231*

The test *ECL0_TVAC_20211005_094231* has been used for the majority of the illustrations of this analysis. However, the noise characteristics noise identified here also apply to other tests.

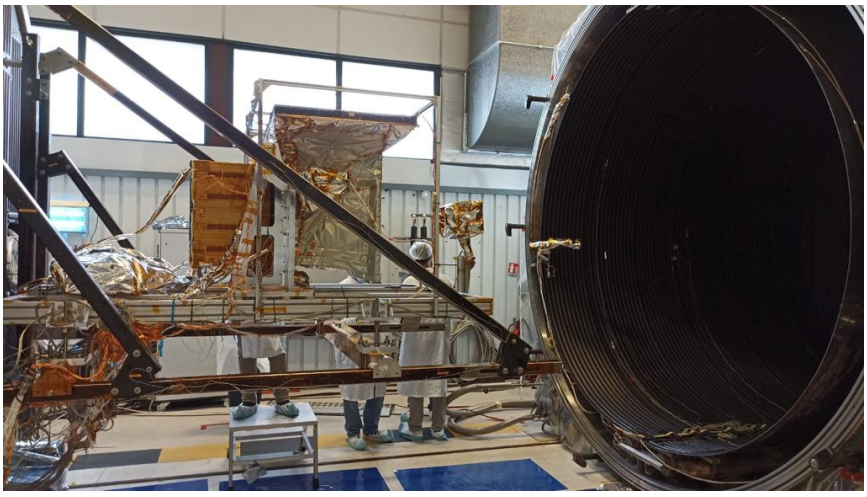

Figure 4.9. Configuration for *ECL0_TVAC_20211005_094231*: TXG with mask.

The configuration for this test, illustrated in Fig. 4.9, is the PFM detection planewith mask, shielding, and the 2 SLI layers. This is connected with the PFM UGTS with the version 5.0 of the flight software. The events have been recovered thanks to the real-time monitoring from IRAP Electrical Ground Support Equipment (EGSE) DPIX Studio.

The test measures the background noise in the SIMDIA thermal vacuum chamber at Airbus Defense & Space (ADS). The thermal management of the instrument is made thanks to the ECLAIRs radiator, located in front of the radiative plate from the vacuum chamber. Therefore, the test conditions are the closest to the flight conditions ECLAIRs has experienced during its test campaigns.

4.3.2 *CE4_Test_PFM0_20210407_101542*

The test *CE4_Test_PFM0_20210407_101542* has been mainly used for the temporal characterization of this analysis. The configuration for this test is similar to the one illustrated in Fig. 4.1(b), is the PFM detection planewithout the mask but with shielding, and the 2 SLI layers. This is connected with the PFM UGTS with the version 3.3 of the flight software. The events have been recovered thanks to the real-time monitoring from IRAP Electrical Ground Support Equipment (EGSE) DPIX Studio.

The test measures the background noise in the SIGNE3 thermal vacuum chamber at CNES. The thermal management of the instrument is made thanks to the cold plate.

4.3.3 Characterization

The counts received from the SLE noise are concentrated near the detection plane edges. Therefore, the events from there (the red area from Fig. 4.10) are dominated by the events induced by the SLE noise. On the contrary, the noisy barely influences the middle part (orange area in Fig. 4.10). By comparing the spectrum, time difference distribution, and spatial repartition of the events from these two zones, I have disentangled the specific SLE noise properties from the background ones.

Spectral

The spectral properties of the events are different depending on the area they belong to, both for SE and MEC events. The color coding from the spectra of Fig. 4.11(a) and 4.11(b) is related to the location of the events taken to create the spectrum, either belonging to the orange or red zone from Fig. 4.10. These two figures show that the SLE noise (characterized by the red curve) is mainly seen at low energy, below 8 keV for the SE events and 15 keV for the MEC events. Moreover, we can also see from the orange curve that this noise is almost absent for the events located in the middle of the detection plane. It can be noticed that the MEC events also have a 3 peaks structure, which is investigated further during the spatial characterization.

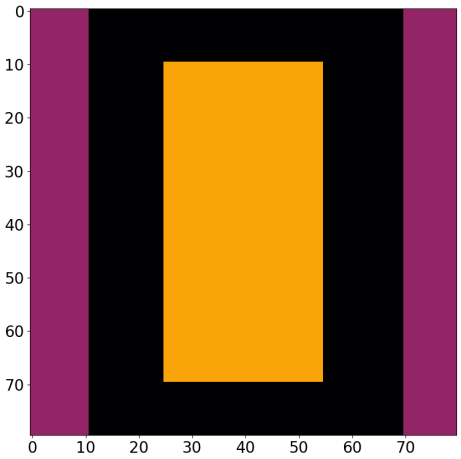

Figure 4.10. Localization zones used for the characterization of the SLE noise.

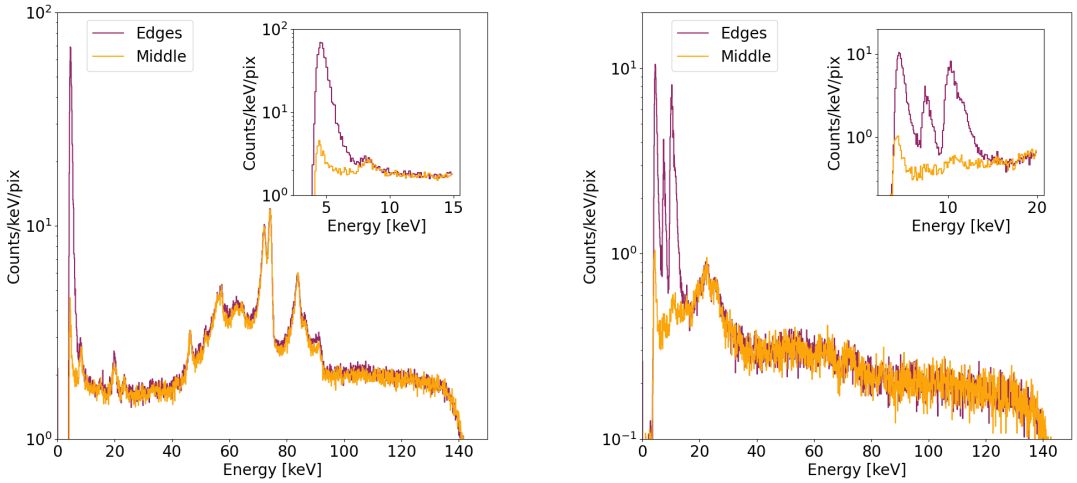

(a) SE spectrum

(b) MEC spectrum

Figure 4.11. (a) SE and (b) MEC Spectrum from *ECL0_TVAC_20211005_094231*. The color coding is associated with the colors of the zone from Fig. 4.10.

Spatial

The MEC spectrum contains 4 peaks illustrated in Fig. 4.12(a) with the four different colors. By taking only events with energies coming from one of those peaks, the maps on Fig. 4.12(b) and 4.12(c) have been created. For example, the top left maps of Fig. 4.12(b) and 4.12(c) are created from all the MEC events with energies in the first blue peak (between

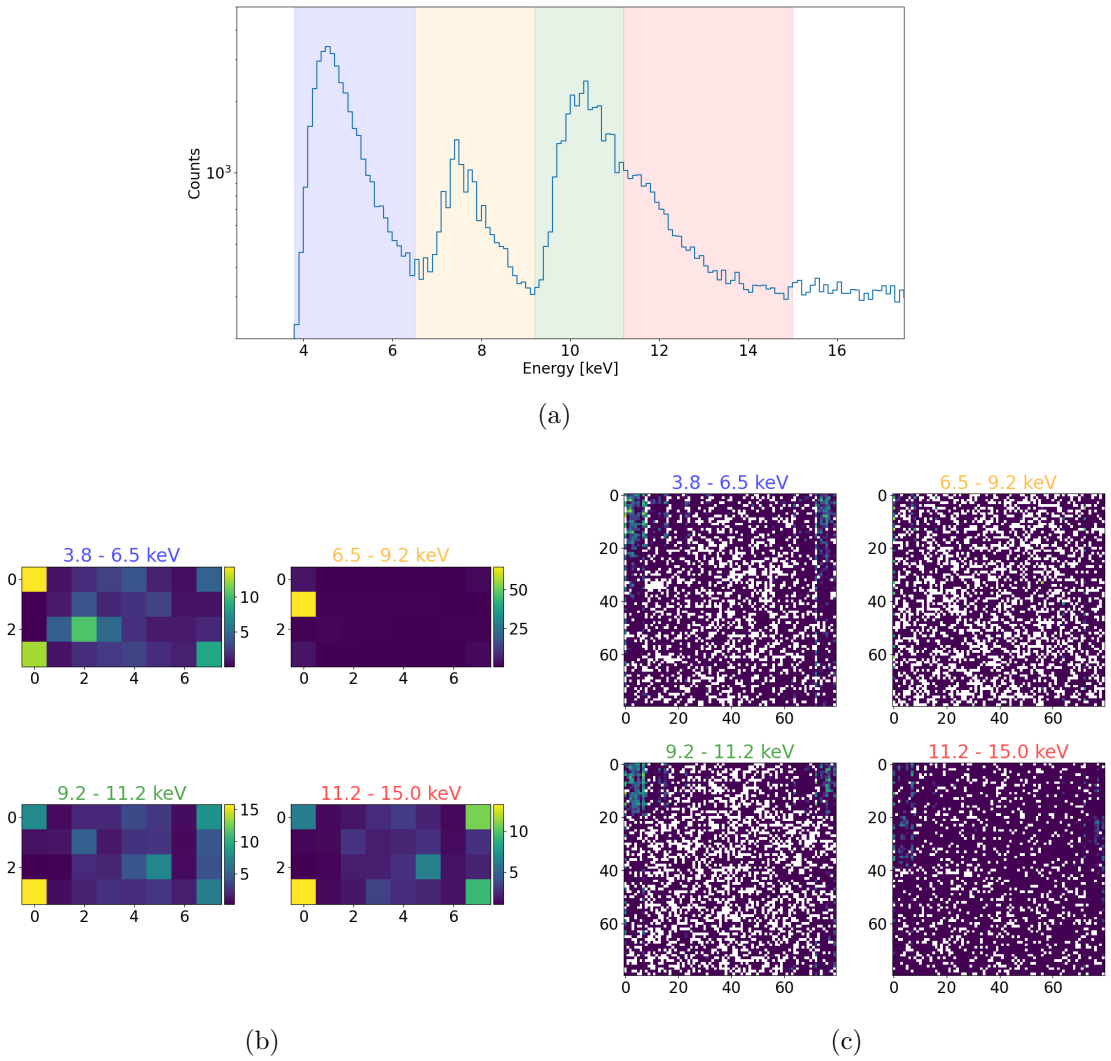

FIGURE 4.12. (a) Spectrum of MEC events obtained for the whole detection plane, with the color stripes delimiting 4 spectral regions (b) Relative number of counts on the XRDPIX modules from events originating from the spectral region selected (c) Detection plane image from events originating from the spectral region selected.

3.8 and 6.5 keV). As shown in Fig. 4.12(b), depending on the energy of the MEC events considered, the pixels of the XRDPIX impacted are different. This is especially true for the spike between 6.5 and 9.2 keV, where more than 50% of the MEC events with such energy are from the pixel 8. At the detection planescale shown in Fig. 4.12(c), the global spatial distribution of the events also changes depending on the energy considered: they seem more located on the top of the detection plane between 9.2 and 11.2 keV compared to the events between 3.8 and 6.5 keV or between 11.2 and 15.0 keV. These different XRDPIX and detection planelocations that depend on the energy considered are probably a manifestation

of the physical phenomena responsible for the SLE noise. However, we have not been able to explain it.

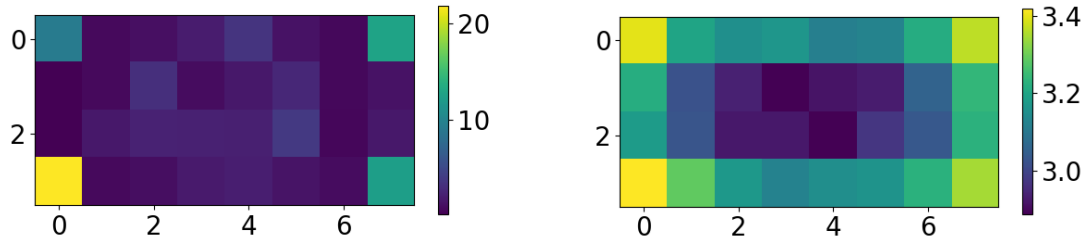

(a) E < 10 keV (b) E > 10 keV

Figure 4.13. Distribution of SE events on the XRDPIX, considering events with energies (a) below 10 keV and (b) above 10 keV.

For single events, the SLE noise does not have a spatial distribution changing with the energy. Figures 4.13(a) and 4.13(b) have been created by making a 2D histogram of the SE events (recorded with an energy respectively below 10 keV and above 10 keV) using the XRDPIX number of each of these events. However, Fig. 4.13(a) shows that, considering only SE events with an energy below 10 keV (so largely dominated by the SLE noise), 50% of the events are located in the XRDPIX corners (pixels $0, 7, 24$ and 31). We can see that this is a real particularity: when considering only SE events with energies above 10 keV (removing the large majority of the noisy events), Fig. 4.13(b) shows that the counts on the XRDPIX are homogeneously distributed. Therefore, the SLE noise seems linked to an effect particularly affecting the corners of the XRDPIX.

Temporal

Finally, the temporal properties of the SLE noise are also remarkable. The test *CE4_Test_PFM0_202104* is perfect for illustrating these temporal properties of the SLE noise: the first $\approx 6,000$ seconds are perturbed by an intense SLE noise, while the remaining of the test is (almost) free from it.

Here we define a "burst" as the occurrence of more than 10 coded events (SE and/or MEC) within a time interval of 10 ms. As the rate for this test without SLE noise is estimated to ~ 170 cnts s^{-1}, having such a burst because of statistical variations is unlikely ($< 0.0001\%, 6\sigma$ assuming a Poisson distribution for the counts received).

Figure 4.14 shows a light-curve of the number of bursts, per periods of 100 seconds. The number of bursts is drastically reduced after $6,000$ seconds, the moment when the SLE noise is reduced. For this reason, we conclude that the SLE noise manifests itself at least partially through the emission of intense bursts lasting a few ms.

It is confirmed by the construction of the time difference distribution. For each SE event, the time difference $\delta t(i)$ [sec] for the event i arriving at time $T(i)$ with the previous event arriving at time $T(i-1)$ and the next one arriving at time $T(i+1)$ is computed as:

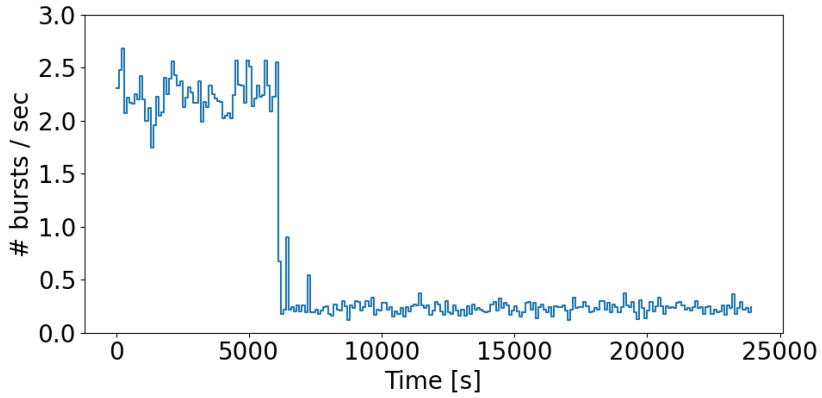

FIGURE 4.14. Evolution of the number of bursts relatively to time.

$$\delta t(i) = \frac{T(i+1) + T(i-1) - 2T(i)}{2} \tag{4.4}$$

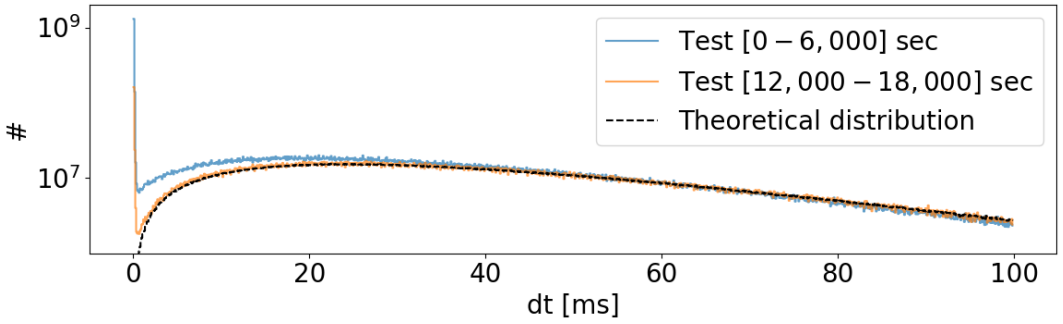

FIGURE 4.15. Time difference between the events from *CE4_Test_PFM0_20210407_101542* for two periods, compared to the theoretical expectation without noise.

The distribution of time differences $\delta t(i) = T(i+1) - T(i)$ for events created by a physical process producing events at a rate $\dot{N}$ follows an exponential distribution, with parameter $\lambda = \dot{N}$. The theoretical distribution plotted as the dashed black line on Fig. 4.15 is the sum of two independent exponential distributions. The theoretical rate $\dot{N} = \lambda$ for these two distributions has been adjusted to be as close as possible to the rate expected during the test without the SLE noise. For this reason, it has been calculated using the pixels from the orange zone of the detection plane for the period $[12,000 - 18,000]$ seconds, where the SLE noise is almost absent. If a physical process creates the events received on the detection plane, they are expected to follow the same curve as the theoretical curve. However, there is a spike on the left side of the distribution, both for the time interval $[0 - 6,000]$ seconds and $[12,000 - 18,000]$ seconds: an unphysical process is at work during the test.

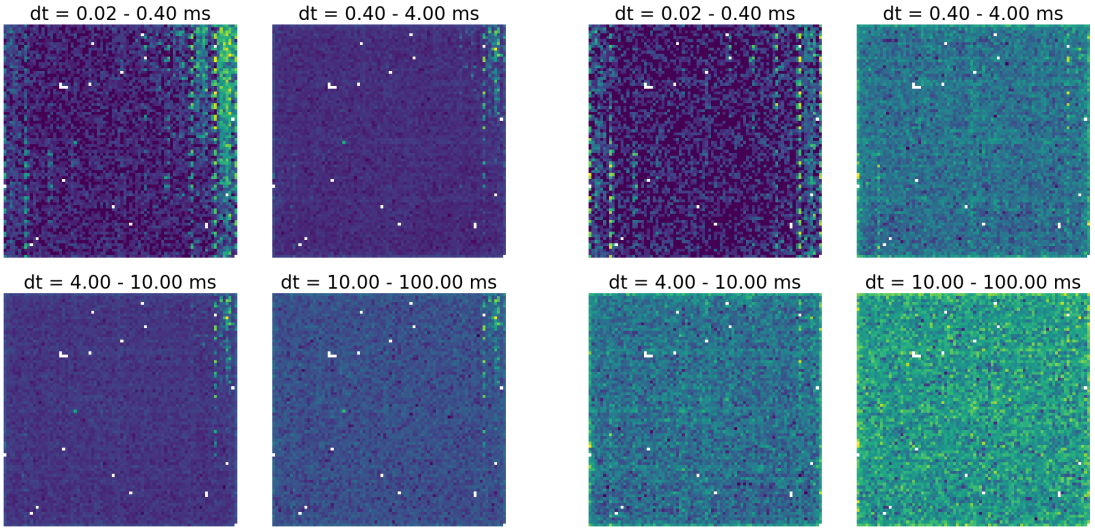

(a) 0–6,000 (b) 12,000–18,000

Figure 4.16. Spatial distribution of the events belonging to different time intervals

Moreover, Fig. 4.15 shows that the time difference distribution from the blue curve (the time interval with dominant SLE noise) deviates from the theoretical distribution, even for time differences as long as 30 ms. The behavior is different for the orange curve (created from events with a non-dominant SLE noise), where the deviation from the theoretical distribution only appears at the smallest time differences.

Figure 4.16(a) shows the spatial repartition of the events, depending on the bin of time difference they belong to, for the time interval $[0 - 6,000]$ seconds. Even for events with a time difference in the range of $10 - 100$ ms, the SLE noise is still visible on the right-end side of the detection plane. On the contrary, considering the time interval $[12,000 - 18,000]$ seconds from Fig. 4.16(b), we see that the detection plane image only has visible SLE noise for the first time difference interval, $dt \in [0.02 - 0.4]$ ms. The remaining of timescales have spatial distributions that do not seem affected by the SLE noise.

Figure 4.17 shows the time difference distribution for another test, where there is no evolution along the test. However, we notice that the distribution deviates from the theoretical one starting from ~ 10 ms. The deviation is not as intense as the first part of *CE4_Test_PFM0_20210407_101542*, but more important than the second part of this test. Overall, this indicates that the temporal signature of the SLE noise varies with its intensity. The higher this intensity, the more events with higher time differences appear (perhaps coming from cross-talk or column effects induced by the increased count rate on some pixels created by the SLE noise).

Summary

In conclusion, we have identified the following characteristics of the SLE noise events:

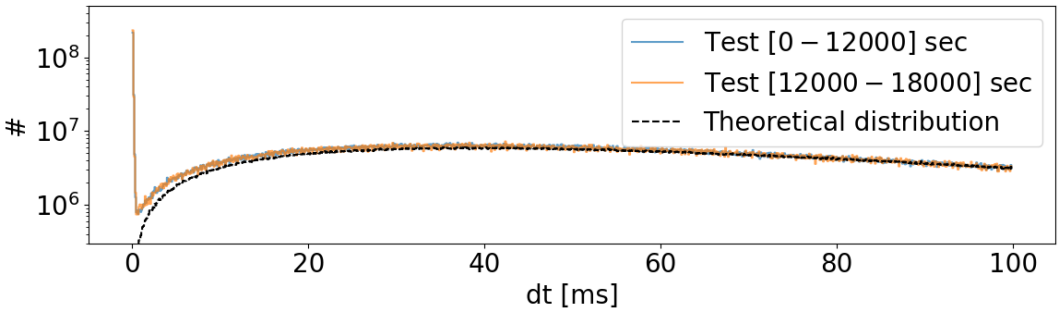

Figure 4.17. Time difference between the events from *ECL0_TVAC_20211005_094231* for two periods, compared to the theoretical expectation without noise.

(1) An energy below 10 keV for SE and 15 keV for MEC.
(2) A spatial repartition at the detection plane level which varies in time but is nonetheless principally located on the edges of the detection plane.
(3) The majority of the SLE noise SE and MEC events affect the edges of the XRDPIX
(4) A significant fraction of the SLE noise events are generated through spikes of a few milliseconds, a characteristic that appears clearly in the time difference distribution by an important excess of events at very low time differences.
(5) High-intensity SLE noise seems to have two components, one that appears only within bursts and mainly affects the corner pixels of XRDPIX, and another one with much higher time differences.

4.3.4 Mitigation method

To limit the influence of the SLE noise on the data, we propose a method to remove the SE events generated by this noise, using its properties presented in the above section. The purpose of this method is to calculate the likelihood, for each event in the dataset, that it has been generated by the SLE noise. For calculating this likelihood, it uses three characteristics identified in the SLE noise: the time difference distribution, the energy distribution, and the pixel distribution on an XRDPIX for such events.

The method is based on the assumption that a section of the detection plane is unperturbed by the SLE noise, while this noise dominates the other one. The orange and the red zones from Fig. 4.10 are used, respectively unperturbed and dominated by this noise. On the one hand, events from the orange zone can be used as a reference for the expected energy, time difference, and XRDPIX position distribution. On the other hand, events from the red zone can be used as a real-time characterization of the SLE noise.

Time difference likelihood

This likelihood $\mathcal{L}_{\delta t}$ is based on the time difference distribution of the detection plane events. This distribution is created using all the events from the test (blue distribution in Fig.

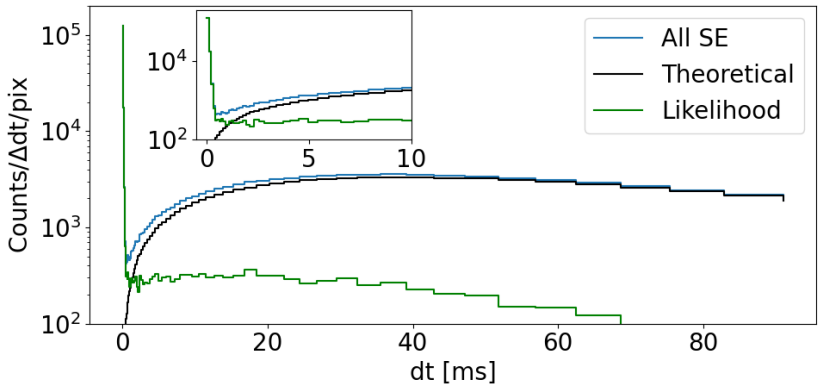

Figure 4.18. Time difference likelihood created from the difference between the time distribution of the test and the theoretical time distribution. The distributions are normalized by the time difference bin size and per pixel.

4.18), using the Equ. 4.4 presented in Sec. 4.3.3. The other distribution, represented with the dashed black line in Fig. 4.18, is the theoretical distribution expected from a constant background (determined with the same method as in Sec. 4.3.3). This distribution is subtracted from the time difference distribution of all the events on the detection plane, giving the likelihood of a given event with a time difference δt to originate from the SLE noise (in green in Fig. 4.18).

Energy likelihood

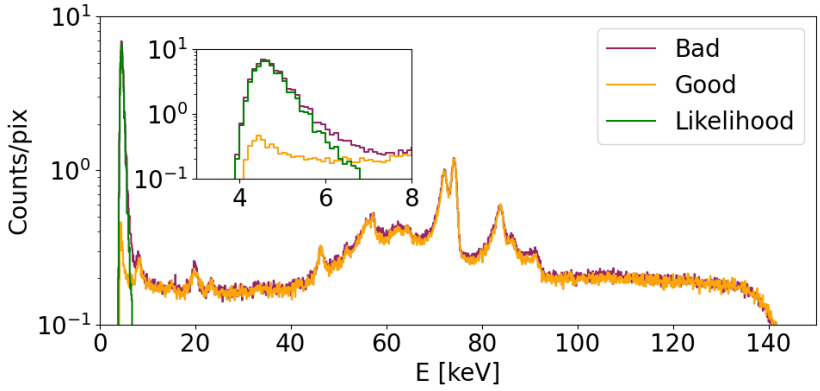

Figure 4.19. Energy likelihood created from the subtraction of the so-called bad and good energy distributions. The distributions are normalized per pixel.

The energy likelihood $\mathcal{L}_E$ is determined from the difference in the energy distribution of the events belonging to the orange and red zones. Figure 4.19 shows the likelihood in green, with the spectral distribution from the good and bad zones in orange and red.

Pixel likelihood

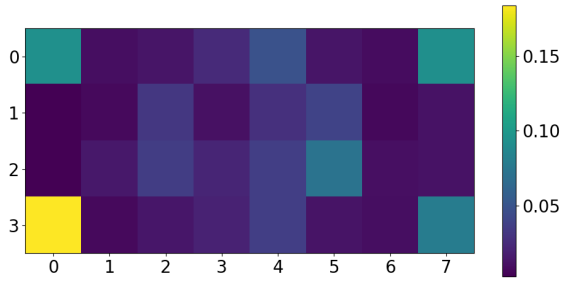

Figure 4.20. Pixel likelihood created from the events spatial distribution on the XRDPIX pixels.

The SLE noise completely dominates the events from the red zone, and the expected distribution of the XRDPIX locations is uniform (see Sec. 4.3.3). Therefore, the pixel likelihood $\mathcal{L}_{pix}$ is determined by creating a histogram of the XRDPIX locations of events below 10 keV belonging to the red zone, normalized by the number of events used. The likelihood obtained is shown in Fig. 4.20.

Global likelihood computation

Once these likelihoods are obtained, we associate a likelihood to each SE event of the test. From the SE event properties E_i, δt_i and PIX_i, the corresponding likelihoods $\mathcal{L}_E(E_i)$, $\mathcal{L}_{\delta t}(\delta t_i)$ and $\mathcal{L}_{pix}(PIX_i)$ are obtained by linearly interpolating the likelihoods created beforehand. The global likelihood $\mathcal{L}(E_i, \delta t_i, PIX_i)$ is then obtained by multiplying these three individual likelihoods.

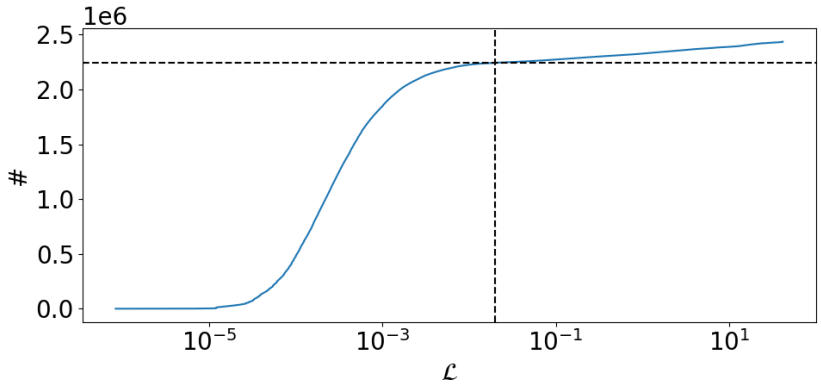

Figure 4.21. Cumulative distribution of events relative to their likelihood.

The events can then be classified based on this likelihood value. The higher it is, the more likely the SLE noise generated the event. Based on this classification, the events with the highest likelihood must be removed. The number of events to remove can be defined in two different ways:

(1) Figure 4.21 illustrates a cumulative distribution of the likelihood of the events, the vertical black line being an arbitrary threshold. All the events with a likelihood above are removed, representing $\sim 200,000$ events ($\sim 7.9\%$). For the case of *CE4_Test_PFM0_20210407_101542*, with the exact same threshold, $500,000$ events ($\sim 8.0\%$) are removed.
(2) From the events in the orange area and assuming that the counts are isotropic on the detection plane, it is possible to predict the expected number of events N_{nohp} for the test if there was no SLE noise. This quantity is compared to the actual number received during the test N_{hp}, and so the $\Delta N = N_{hp} - N_{nohp}$ events with the highest likelihood are removed. The values found are $207,000$ ($\sim 8.5\%$) and $495,000$ ($\sim 7.9\%$) for the two tests considered.

4.3.5 Results

Figure 4.22 shows the application of this method on the test *ECL0_TVAC_20211005_094231*. The panel on the left represents the detection plane image taken during the whole test in a logarithmic scale. The influence of SLE noise is visible, represented by the increased counts on the edges by more than one order of magnitude. The middle panel shows a detection plane image formed by the events kept with the method, while the right panel shows the events removed. The detection plane image of the cleaned events is mostly uniform, meaning that most SLE noise events have been removed (see how they are located on the sides on the left panel).

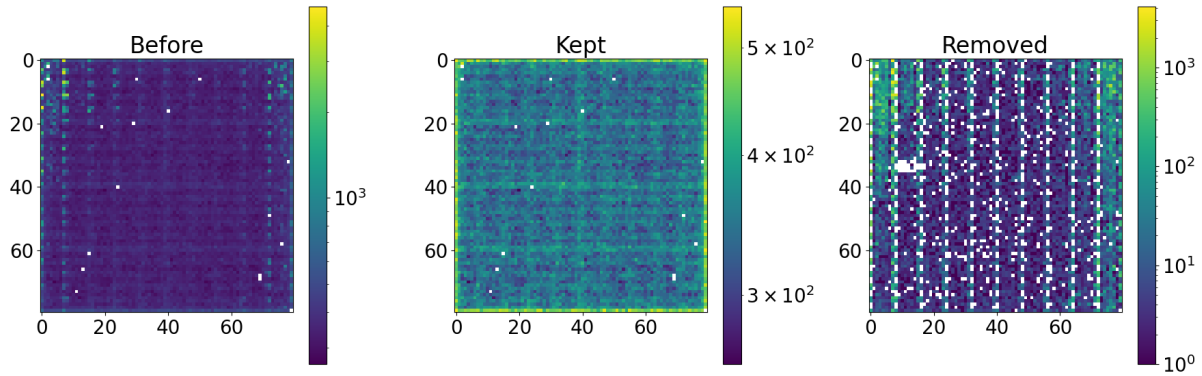

Figure 4.22. Detection plane image from *ECL0_TVAC_20211005_094231* cleaned with the method with the image before cleaning (left), after cleaning (middle) and the events removed (right)

Moreover, Fig. 4.23 and 4.24 show that the events almost follows the spectral and temporal distributions expected from a noise-free test. It is comparable with for example the middle events from Fig. 4.11(a) and the theoretical distribution of Fig. 4.15. The method efficiently removes the SLE noise events, but it also has a low number of false positive events (standard background events mistaken for SLE noise events).

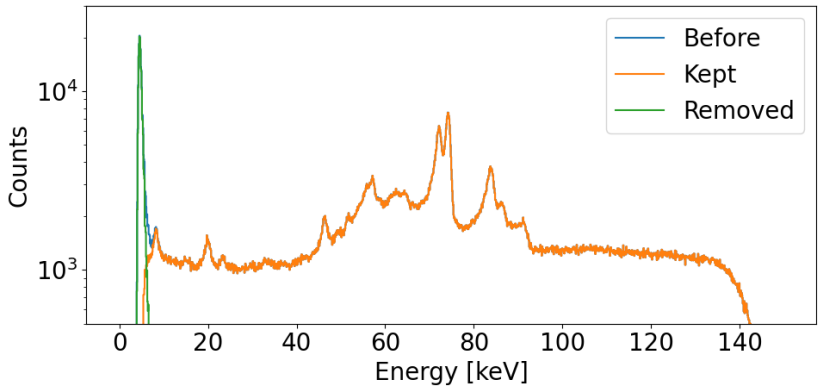

Figure 4.23. Spectrum from *ECL0_TVAC_20211005_094231* before and after cleaning

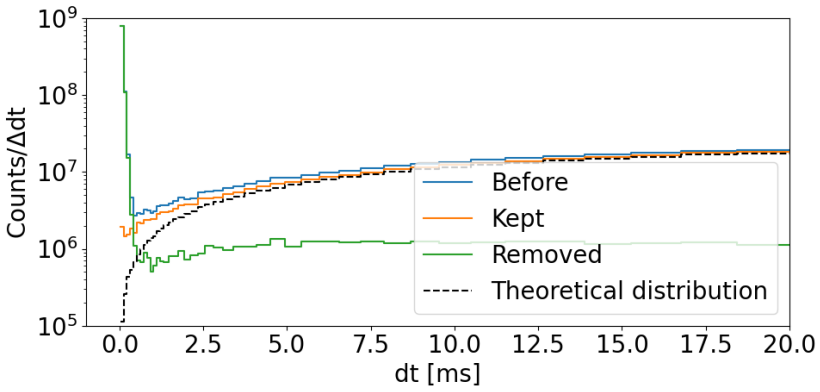

Figure 4.24. Time interval difference from *ECL0_TVAC_20211005_094231* before and after cleaning

Figure 4.25 shows another illustration of the same method (with the same threshold parameters) applied to another background test, *CE4_Test_PFM0_20210407_101542*. As we can see, despite the different spatial structures of the noise, the method successfully removes the SLE noise.

4.3.6 Perspectives

This study paves the way for a deeper analysis to prepare for the ECLAIRs on-flight data exploitation, in case the SLE noise is still present once *SVOM* in space.

Application on simulated data

The method presented for the SLE noise removal is promising, but it has been mostly tested on the background tests for the moment. The next step would be to combine these tests with astrophysical simulations and see how the method performs and how many "astrophysical"

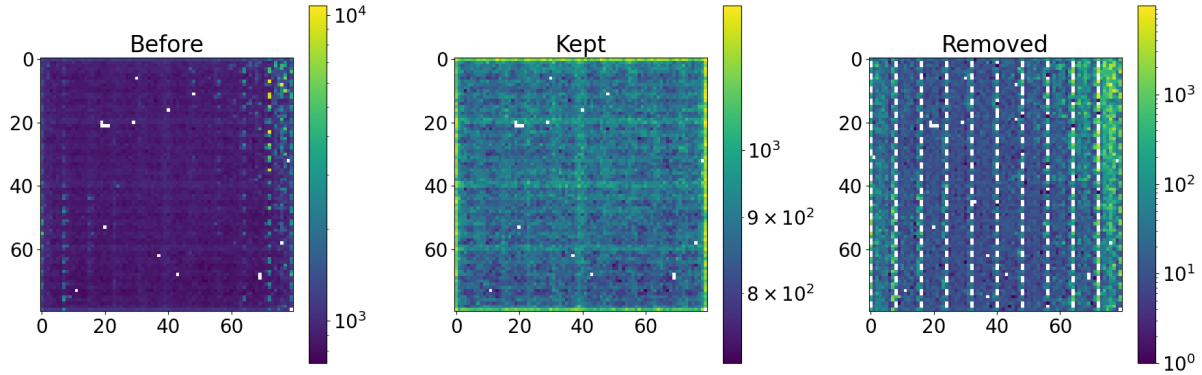

Figure 4.25. Same method applied on *CE4_Test_PFM0_20210407_101542*

photons are removed by mistake. The final validation of this method would be to test it with real flight-data if the SLE noise is still present.

The method is developed here for SE, but it can also be applied to MEC by changing the differential time distribution by another time-related indicator.

Unsupervised classification approach

This method relies on the choice of a threshold or an expected number of events to remove and might therefore be more complicated to apply to real data. Another approach would be to use unsupervised classification methods such as the K-means, Spectral Clustering, Agglomerative Clustering, or Gaussian Mixture (Pedregosa et al., 2011). However, this requires a dedicated, thorough analysis of the data structure and a comparison of the performances of the methods to identify the one that suits the problem the most.

4.3.7 The EIC HW

The EIC hardware (EHW) has been built from the spare XRDPIX modules that have not been integrated into the ECLAIRs FM. It consists of two fully populated sectors (corresponding to ELS 2 and 3), connected to the flight spare of the UGTS. The hardware is controlled through the CNES software OCTAVE, and tested inside the Signe3 vacuum chamber from CNES.

The purpose of the EHW is to perform extensive tests in vacuum conditions with real hardware. It is the ideal way to study some instrumental anomalies that might happen when ECLAIRs will be in orbit: the EHW is a complement to the Banc Validation Système (BVS) described in Sec. 5.7. If the SLE noise were to happen in space, the EHW would be the opportunity to characterize it even more and investigate its origin.

During all the test campaigns, the detection plane was in a vertical position (see Fig. 4.1(a) for example) to be able to face the source holder. However, the heat-pipes are not working nominally in this position, as the gravity directly impacts the fluid diffusion inside

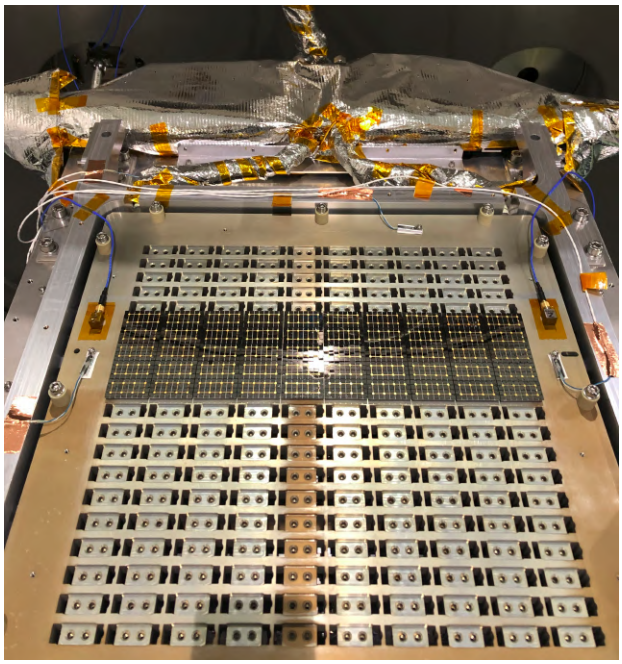

Figure 4.26. The EIC Hardware, in the horizontal configuration.

them: it generates micro-vibrations at the evaporator level (Guillemot, 2022). These micro-vibrations do not appear in the horizontal configuration where gravity has less influence on the heat-pipes fluid, a configuration that is also more representative of the flight conditions.

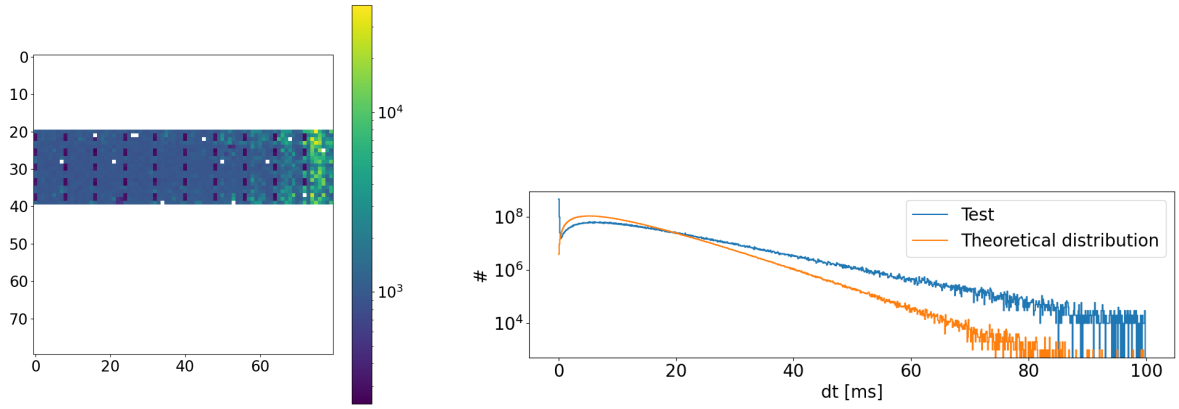

(a) Detection plane image

(b) Time difference distribution

Figure 4.27. Characterization of the EHW test in the horizontal position *CE99_Test_bruit_de_fond_20220505_171104*

The test *CE99_Test_bruit_de_fond_20220505_171104* has therefore been performed with the detection plane in the horizontal configuration. No SLE noise has been detected in this configuration: the detection plane image of Fig. 4.27(a) does not have excess counts on the edges. The time difference distribution of Fig. 4.27(b) follows exactly the expected

theoretical distribution. The spectrum has not been built, as the CHAN to energy relation for EHW XRDPIX has not been calibrated yet.

Using the same test set-up but for a vertical configuration, the SLE noise reappears with the usual signature for *CE99_Test_EHW0_20220609_200015*, noticeable by the increase of counts on the detection planes edges (see Fig. 4.28(a)) and the increase of counts compared to the theoretical distribution for the low time difference intervals (see Fig. 4.28(b)).

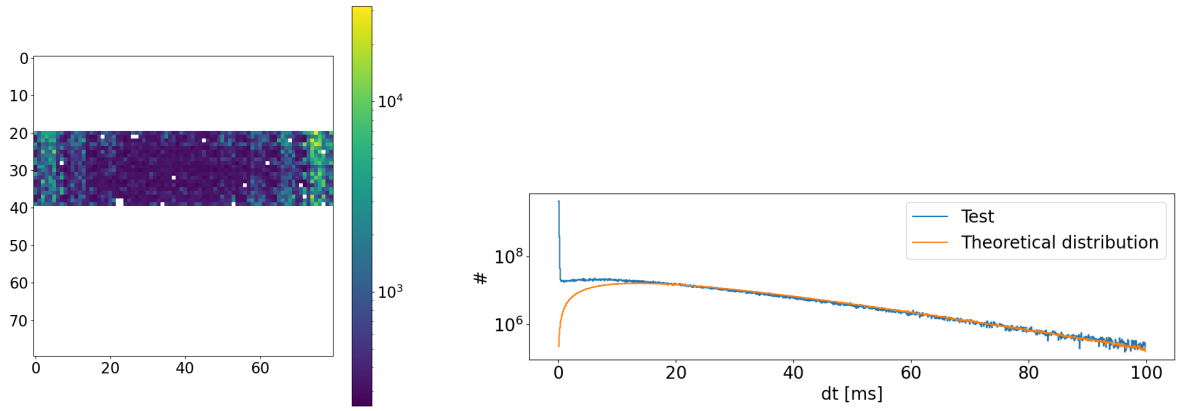

(a) Detection plane image

(b) Time difference distribution

Figure 4.28. Characterization of the EHW test in the horizontal position *CE99_Test_bruit_de_fond_20220505_171104*

As gravity is the potential cause for the malfunction of the heat-pipes in the vertical position, this test suggests that the SLE noise might not appear once the satellite is in-space.

Chapter 5

Astrophysical simulations of *SVOM*/ECLAIRs and GRM

Simulating the performances of the two wide-field instruments of *SVOM* has many applications, from the testing of the *SVOM* pipelines to the validation of ECLAIRs flight software, to the prediction of the GRB rate (alert and/or slew) expected by ECLAIRs and/or the GRM instrument. These simulations generate a list of events expected on the detection plane. The properties of such events change depending on the source of the events (background, GRB, X-ray source) and the context of ECLAIRs, and this Chapter shows how they are simulated.

First, the astrophysical background expected during the flight (see Sec. 5.2), which is the most important source of events to simulate as ECLAIRs sensitivity is background limited. On top of this background, GRBs and X-ray sources (see Sec. 5.3 and Sec. 5.4) can be simulated to assess the detection performances of the trigger algorithms, for example. It is also possible to add instrumental effects measured during the test campaign (presented in Sec. 3.6) to test their influence on the algorithm behavior. A wrap-up package of these simulation tools, `eclgrm-simulation`, will be presented in Sec. 5.5. Moreover, some applications of these simulation tools are presented in Sec. 5.6.

In the last part of this Chapter, we briefly discuss ways to add more detailed effects, like the instrument dead time, to these simulations. The methodology employed to add these effects is presented in Sec. 5.7.

Contents

5.1 Format of the simulation outputs

Before going more into details about the simulations, it is essential to describe the properties of these simulated events. They are defined as follows:

- `eventID` is the event's time in seconds. It is given relatively to the starting time of the simulation, which is an absolute time encoded with the ISO 8601 time time format (ISOT).
- `energy` is the energy of the event in keV that has been measured on the detection plane.
- For ECLAIRs simulations, `X` and `Y` are the coordinates in the detection plane of the pixel that triggered. The values are comprised between 0 and 79.
- For GRM simulations, the `GRD` keyword is the GRD on which the event has been detected. The values are between 1 and 3, corresponding to the 3 GRDs.
- `effMult` is the multiplicity of the event: this parameter describes how many events have been created by a given incoming photon/particle. While multiple events are quite frequent for ECLAIRs, they are extremely rare for GRM as it requires interaction with two GRDs that are distant of ~ 1 meter.
- `procID` traces the origin of the photon or particle that has created the event. A `procID` of 0 is associated with photons coming from the CXB, 1 for Albedo, 2 for Reflection, 3 for SAA Protons, 4 for SAA Electrons, 5 for X-ray Sources, 6 for GRBs, 7 for instrumental noise and 8 for cosmic particles. This origin is not available in reality but helps for some simulations' applications.

The purpose of the simulations is to generate a list of events for which the properties are distributed according to the environment of ECLAIRs in space.

5.2 Astrophysical background in hard X-ray/γ-ray

The sensitivity of ECLAIRs and GRM is limited by the background counts, which are dominated by the cosmic X-ray background CXB (measured by former missions such as *INTEGRAL* Churazov et al. 2007 or *Swift* Ajello et al. 2008 in both the ECLAIRs and GRM energy range). There are also additional components from the CXB reflection on the Earth's atmosphere (Churazov et al., 2007) and from the Albedo, which is the interaction of cosmic rays with the Earth's atmosphere (Sazonov et al., 2007; Ajello et al., 2008). As this background represents the majority of counts that the two instruments will receive, it is necessary to correctly simulate it to have a proper estimation of its evolution during the *SVOM* orbit.

5.2.1 `pira-bkg` and the ECLAIRs background

The dynamical evolution of the background along the orbit is simulated with `pira-bkg` (Mate et al., 2019), a software relying on a pre-computed database of photons/particles-instrument interactions simulated using the *GEANT4* toolkit (Allison et al., 2016). I have contributed to improving `pira-bkg` during my thesis, adding the cosmic ions as potential event sources, the

possibility to use it for the GRM instrument, or the modularity to ease its installation and use. The GitLab project is available at https://drf-gitlab.cea.fr/eclgrm-fr/pira-bkg.

The pre-computed interactions between the photons/particles and the detection plane simulated by GEANT4 are stored in two databases. The first, called the source photons, contains the photons simulated by GEANT4 that have successfully interacted with the detection plane. It contains the properties of these photons, i.e., their incoming direction or energy. One or several events (depending on the event multiplicity), each corresponding to these photons, are stored in the other database, the detection planeevents. These events have properties described in Sec. 5.1.

However, *GEANT4* events are not dated and do not consider the position and attitude context of ECLAIRs. This is the purpose of the `pira-bkg` software, drawing events from these two databases to calculate the dynamic background of the instrument based on the position of *SVOM* in its orbit and its orientation relative to the Earth's position.

The attitude and orbit information (AAV/PVT) used in `pira-bkg` have been provided by Jean Jaubert from CNES. They contain the pointing (quaternions) and position (in Cartesian coordinates in the Earth referential frame) of the *SVOM* spacecraft and their evolution along the time during the 3 years of the nominal mission.

The procedure for `pira-bkg` to calculate the background is as follow:

(1) Starting from the *SVOM* attitude and orbit information, it calculates various quantities, like the RA/Dec coordinates of the instrument line of sight, its angle with respect to the Earth, or the latitude and longitude of the satellite.
(2) For each background component (CXB, Albedo, Reflection, ...), the algorithm calculates the expected events rate, assuming an isotropic emission.
(3) The algorithm is then going to loop on each time-step of the attitude and orbit files. For each time step and each background component, the algorithm selects events in the GEANT4 database depending on the attitude and orbital context:
    (a) Using the calculated rate, `pira-bkg` draws the required number of photons in the GEANT4 database for each background component.
    (b) Some of the photons drawn are discarded based on their incoming direction: CXB photons only come from sky directions not obscured by the Earth, whereas reflection and albedo photons only come from the Earth. Has a consequence a change of the rate from each of these individual components depending on the pointing of ECLAIRs relatively to the Earth.
    (c) The events corresponding to the remaining photons are stored (with the information presented in Sec. 5.1), and the algorithm loops on another simulation time-step.
(4) The algorithm merges the events obtained from all the background components and writes them in a *.fits* file, along with the corresponding attitude information.

Figure 5.1, associated with Fig. 5.2, shows an example lightcurve and how the expected count rate evolves relatively to the Earth position in the FoV: the Albedo and Reflection count rates are maximum when the Earth is in the FoV (as the large majority of such events

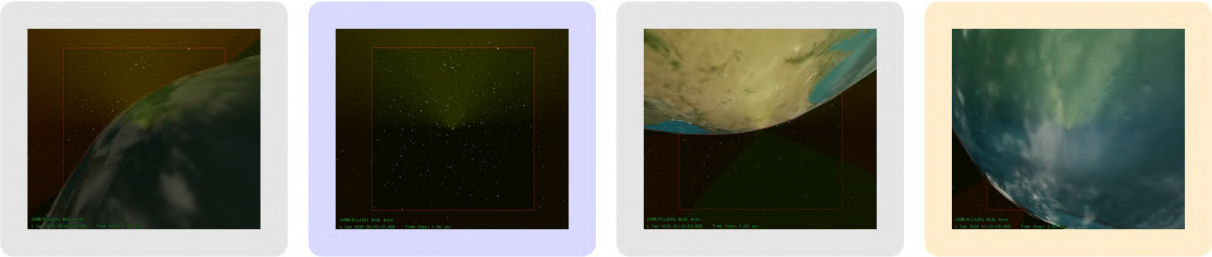

Figure 5.1. Simulation of ECLAIRs FoV, with the Earth: exiting the FoV (left), out of the FoV (middle left), entering in the FoV (middle right), and almost covering the FoV (right). Credit: CEA/H. Triou

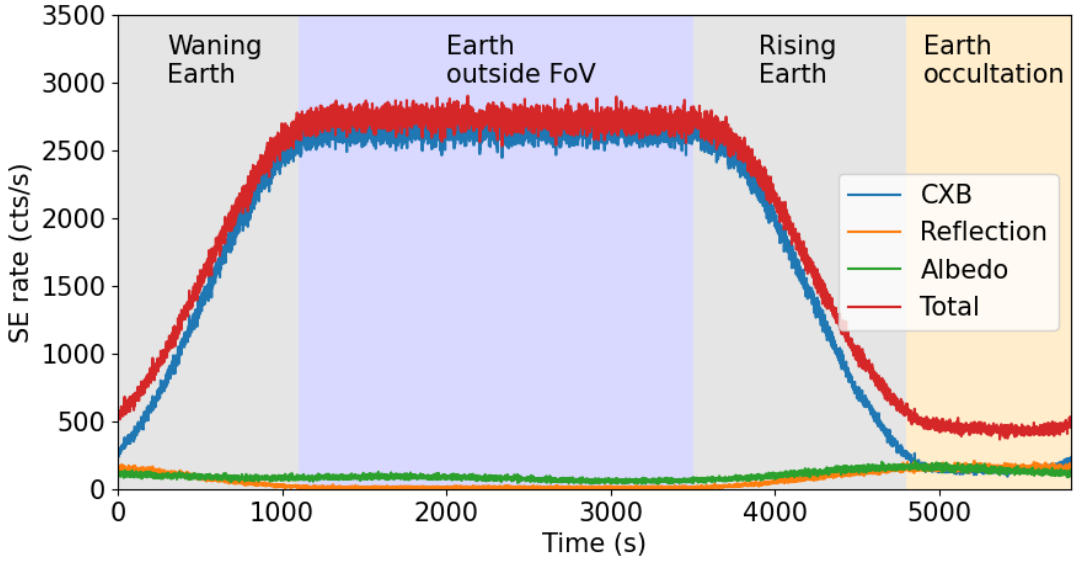

Figure 5.2. Example of single events lightcurve between 4 and 150 keV from an orbit generated by `pira-bkg`: the 4 zones delimited correspond to the 4 FoV images above from Fig. 5.1.

come from the Earth), while the CXB is maximized when the Earth is outside the FoV (as the CXB events come from the sky).

Figure 5.3 shows that the astrophysical background spectral properties also change depending on the Earth's position within the FoV: when the Albedo and Reflection dominate the counts (orange curve), the spectrum becomes much harder than for a CXB-dominated case (blue curve). The CXB intensity is also more dependent of the Earth position in the FoV, as the large majority of events are coming from the FoV of ECLAIRs. On the other hand, as the reflection and the albedo have much harder spectrum, the proportion of events coming from outside the FoV of ECLAIRs is also higher, meaning that the Earth position has less impact on the background intensity.

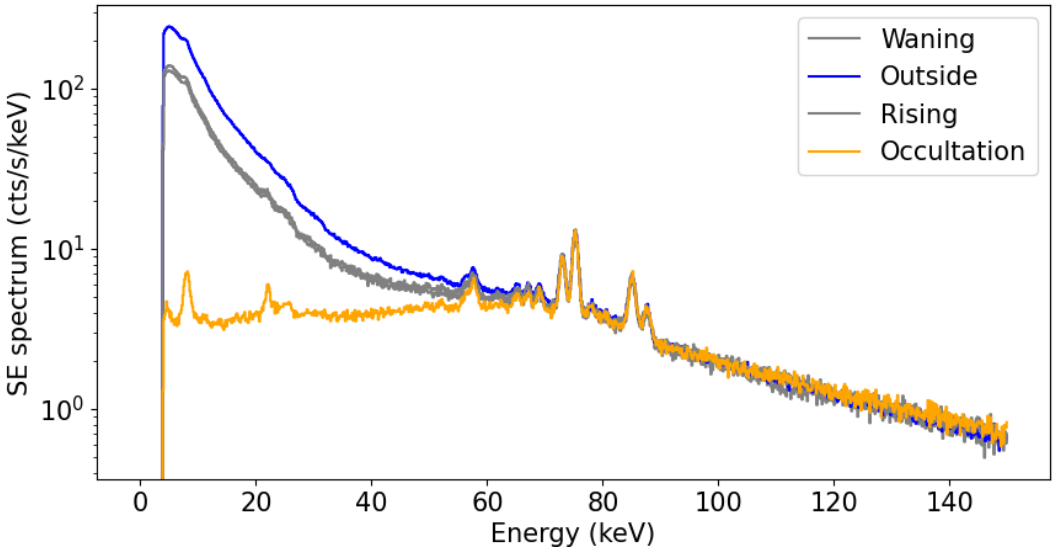

Figure 5.3. Example of the spectrum of Single Events count from an orbit generated by PIRA: the 4 graphs correspond to the 4 FoV images above from Fig. 5.1. The waning and rising spectra are almost indistinguishable.

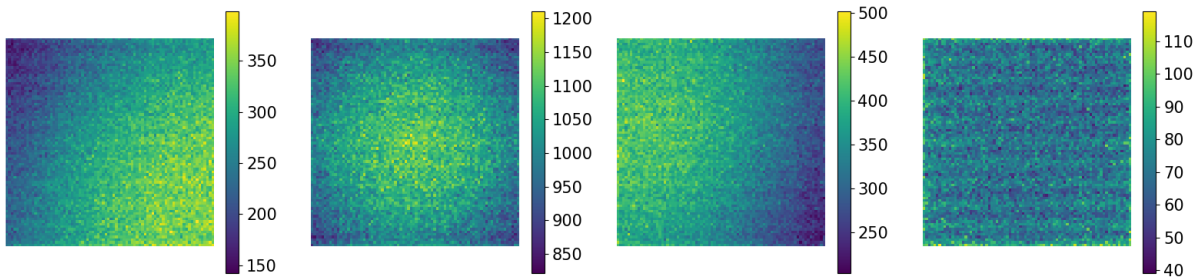

Figure 5.4. Example of shadowgram of Single Events counts from an orbit generated by PIRA, the 4 images corresponding to the 4 FoV images above from Fig. 5.1

Finally, Fig. 5.4 illustrates how the counts' repartition on the detection plane changes relative to the Earth's position within the FoV. The partial occultation of the ECLAIRs FoV by the Earth induces a gradient of counts on the detection plane. For long exposures (typically for $\delta t > 20.48$ sec), this gradient needs to be removed so that it does not perturb the image trigger algorithm (see Sec. 3.5).

5.2.2 On the development of `pira-bkg` for GRM

Although `pira-bkg` has initially been developed for ECLAIRs, it is possible to apply the same algorithm for the other *SVOM* γ-ray instrument, GRM. This implementation has been made with the joint efforts of L. Bouchet (IRAP), A. Maiolo (LUPM), F. Piron (LUPM),

and myself. GEANT4 databases have been generated for GRM for the CXB, Reflection, and Albedo from a mass model built by the Chinese team. The orientation conventions have been harmonized to be compatible with the SVOM conventions (Arcier, 2022), used for the attitude calculations.

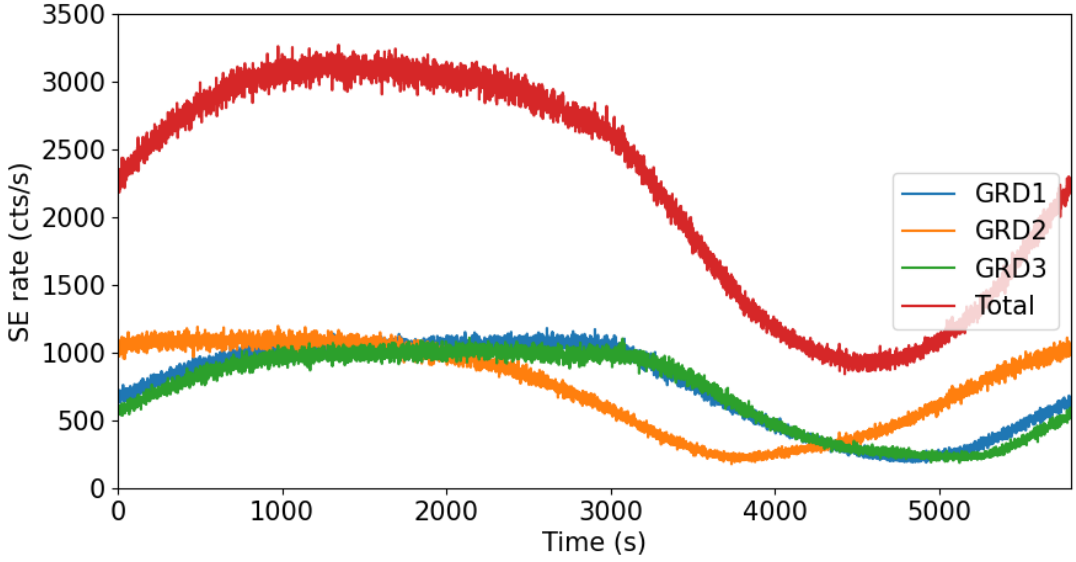

Figure 5.5. Example of lightcurve of Single Events count from an orbit for GRM generated by `pira-bkg`

He et al. (2020) have performed a static analysis of the GRM expected background, which can be compared with the early results obtained with `pira-bkg` applied to the GRM.

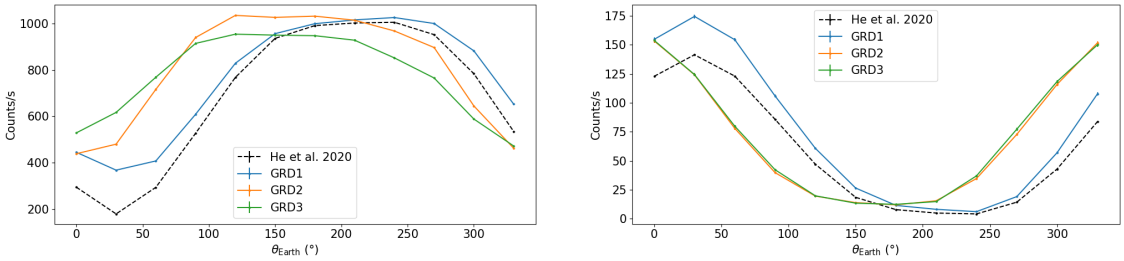

(a) CXB (b) Reflection

Figure 5.6. Comparison between the received rates from He et al. (2020) and the ones predicted by `pira-bkg` for the 3 GRDs in the $15 - 5,000$ keV energy range, for different angles relatively to the Earth.

Figures 5.6(a) and 5.6(b) show that the CXB and Reflection intensities have the same evolution as He et al. (2020) simulations relatively to the θ_{Earth}, the angle between the SVOM line of sight and the Earth. This means that the conventions and the Earth masking have been correctly implemented on `pira-bkg`.

However, a constant difference of $\sim 20\%$ remains between the two curves. This difference probably comes from the input spectrum considered for `pira-bkg` and the GEANT4 simulations used to create the databases. It is under investigation by A. Maiolo and F. Piron at LUPM, in collaboration with the IHEP team.

5.2.3 Perspectives

Overall, `pira-bkg` is now implemented for both ECLAIRs and GRM, but some work remains to be done. First, large GEANT4 databases need to be created for GRM, allowing to perform long-duration simulations. More detailed simulations for ECLAIRs taking into account the *SVOM* mass model are also planned, increasing the accuracy of the existing ones.

Moreover, the activation of the ECLAIRs and GRM material, created by the particle interactions during an SAA crossing, has not been modeled yet. As explained before in Sec. 2.4, Biltzinger et al. (2020) or He et al. (2020) have estimated the impact of such activation by a double exponential decay, showing that the increase of counts is non-negligible on the overall background. In He et al. (2020), one GRD received ~ 1000 counts/s because of CXB, Albedo and Reflection (when the Earth is located at the opposite side of the satellite). The additional background due to the SAA activation ~ 100 seconds after the SAA represents a count rate of ~ 300 counts/s. Even without any SAA crossing, they expect the activation to add approximately 10% of noise. Therefore, the activation effect needs to be added to the simulations to get a more realistic estimation of the count rate once in space. Nonetheless, as ECLAIRs is sensitive to up to 150 keV, the activation problem might matter less. The Hard X-ray Modulation Telescope mission (*HXMT*, (Zhang et al., 2020b)) might provide more information on the impact of activation within the ECLAIRs energy range.

Finally, these simulations will be beneficial for performing conjoint estimation of ECLAIRs and GRM background noise for a given attitude scenario. Combined with X-ray source simulations discussed in Sec. 5.3, they might be used by the *SVOM* community to provide realistic calibration scenarios during the commissioning phase.

5.3 Generation of X-ray sources and high-energy photons

On top of the expected background, the primary sources of γ-ray or X-ray photons in space will be GRBs or X-ray sources. This section describes how the photons incoming towards the ECLAIRs and/or GRM instruments from such sources are generated.

5.3.1 grbsimulator

This tool was developed by F. Daigne and S. Antier (Antier-Farfar, 2016). Starting from a lightcurve and a spectrum of an already detected GRB, `grbsimulator` simulates the photons emitted by the transient. The algorithm calculates the number of photons to be simulated (using a normalized spectrum), and draws the photons randomly from this spectrum, attributing to each an `energy` and a `time` tag.

The same GRB can also be simulated at different redshifts: the code takes into account the time dilation effect of the lightcurve and the redshift of the spectrum, in addition to the decrease of the GRB photon fluence. The Gitlab project of the code, called `grbsimulator`, is maintained by David Corre and available at https://drf-gitlab.cea.fr/eclgrm-fr/grb-simulator.

Input data

The input data of `grbsimulator` consist of a spectrum and a lightcurve.

The lightcurve input format is a three columns table, with `tmin` and `tmax` representing the edges of the bins and `Nph` a number of photons inside this bin. The normalization of the lightcurve is done thanks to the spectrum provided.

The spectral characteristics of the GRB are expressed as follows:

- `tmin` and `tmax` represent the time interval between which the spectrum is applicable. It is possible to set several lines with different times to account for the spectral evolution of the burst.
- `spectrum_type` represents the spectral model used. As discussed in Chapter 1, several types of spectral shapes can be used to characterize the prompt emission. They are represented here by letters `S, P, C, B` and `G`, respectively for the SBPL, Power-law, Compton, Band, and Glog spectral shapes.
- `sp_param_1...5` are the parameters associated with the spectral shapes defined above. They represent respectively the normalization coefficient $A_{\rm norm}$ (ph/s/cm^2/keV), the high- and low-energy slopes (α and β), the peak energy $E_{\rm peak}$ (keV) and the additional parameter Δ for the SBPL law.

Moreover, as shown in Sec. 1.4.1, the spectrum depends on an additional parameter, the pivot energy $E_{\rm piv}$ [keV], specified directly inside the code. The normalization coefficient given in the spectral characteristics file must agree with the value provided inside the code. Throughout the thesis, the value has been set to $E_{\rm piv} = 100$ keV for all the simulations using `grbsimulator`.

Output data

The output of `grbsimulator` used in the remaining simulations presented in this chapter is the photon draw file. This file contains the expected photons in the energy range $[2.5 - 180]$ keV incoming on-axis toward the 1296 cm^2 envelope of the detection plane of ECLAIRs. The number of photons equals the source photon fluence multiplied by the surface area of ECLAIRs. The energy range has been chosen to share the exact energy boundaries of the ARF and RMF files.

Each photon has two properties, an energy `E` in keV and a relative time of arrival `T` in seconds. There are also other outputs, such as the application of the trigger algorithms on the GRB or the computation of its detection probability by BATSE. However, these outputs have not been used in the framework of this thesis.

The case of GRM

From the same input data, the same operations can be performed for the GRM instrument. A photon draw file is generated containing the expected photons in the energy range $[8 - 10,000]$ keV arriving on-axis toward the 200 cm^2 detection surface of one GRD.

5.3.2 Addition of X-ray sources from catalogs

In addition to the transient sources that appear in the sky, the constant X-ray sources must also be taken considered. Primarily located in the galactic plane, they can significantly increase the count rate of ECLAIRs (and GRM) when they are inside the FoV (for ECLAIRs, having the Crab within the FoV adds $\sim$ 500 cnts/s, Sco-X1 $\sim$ 6000 cnts/s. For information, the CXB, Reflection, and Albedo contribute to $\sim$ 3000 cnts/s when the Earth is not obscuring the FoV). Figure 5.7 shows the distribution of these X-ray sources in galactic coordinates, where we can see that the majority of them are located towards the galactic center, except for the Crab nebula.

The inventory of the visible X-ray sources and their spectral properties can be found in Dagoneau (2020). The use of this catalog and the simulation in the Gitlab project of `eclgrm_data_simulator`, at https://drf-gitlab.cea.fr/eclgrm-fr/eclgrm_data_simulator.

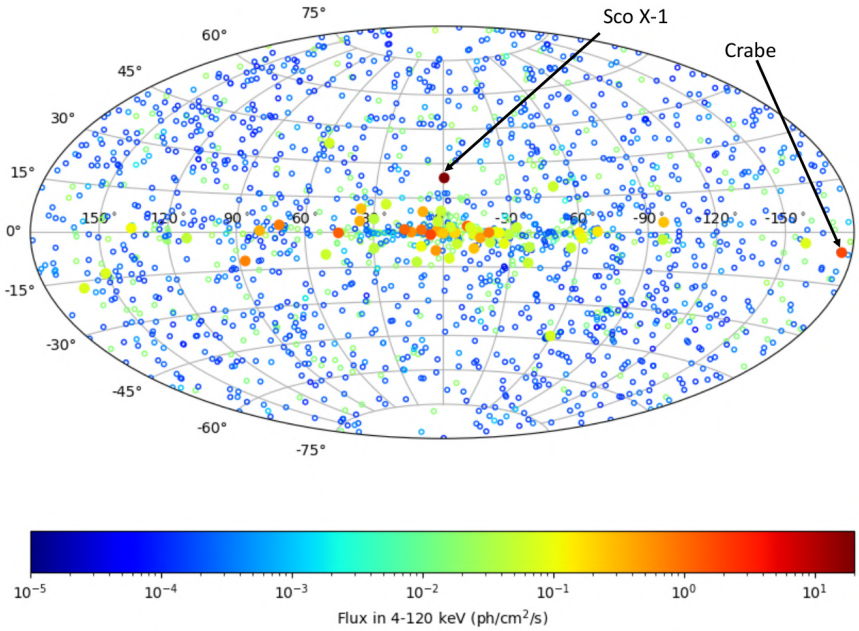

FIGURE 5.7. Distribution of the X-ray sources in galactic coordinates. The color coding is from the expected flux in the energy band $4 - 120$ keV in ph/cm^2/s. Credit: Dagoneau (2020)

The algorithm, starting from the attitude file generated by `pira-bkg`, searches for X-ray sources within the FoV of the instrument considered (ECLAIRs and/or GRM). Then, for each of the selected sources, the photon list of events arriving in the detection area of the

instruments is created. Finally, the time of arrival of each photon and its energy are drawn using the flux and spectral shape provided in the X-ray source catalog.

5.4 Application of instrument response

Once the photon list is simulated (either from an X-ray source or a GRB), the interaction between these photons and ECLAIRs (or GRM) detection plane is simulated. In the ECLAIRs case, a ray-tracing of these photons is performed to account for the mask pattern. Then the response matrices ARF, RMF, and IRF are applied to account for the redistribution and detection efficiency of ECLAIRs and/or GRM.

Note that for the background simulations from `pira-bkg`, only the energy resolution needs to be applied, as the efficiency and redistribution are already taken into account by the GEANT4 simulation.

5.4.1 Photons ray-tracing

The design of coded-mask telescopes ensures that the photons interacting with the detection plane have crossed the coded mask. Assuming an opacity of the mask of 100%, all photons that do not cross mask holes are stopped and cannot interact with the detection plane. For point sources such as GRB or X-ray sources, the mask pattern is projected on the detection plane, forming a coded pattern called a shadowgram.

The purpose of the ray-tracing algorithm is to simulate this projection by associating, to each photon, a position on the detection plane. This position depends on the photon arriving angle and its position relatively to the coded mask. The quantities θ_s and ϕ_s represent the relative sky angles between the pointing direction of ECLAIRs and the source direction. For an astrophysical source with a stable pointing of the instrument, these quantities remain constant over time: θ_s and ϕ_s are the same for all the photons generated. However, in the case of a slew, as the pointing of the instrument and therefore these quantities evolve: θ_s and ϕ_s depend on the time the photons arrive on the instrument.

Infinite distance ray-tracing simulations

The infinite distance ray-tracing was first implemented by S. Mate during his thesis and maintained by me during these 3 years. This ray-tracing implementation is based on the ECLAIRs General Program Python library, `ecpi`, which contains the mask pattern information and some routines used in the algorithm. The ray-tracing algorithm is illustrated in the left panel of Fig. 5.8, and works as follows:

(1) Random positions are drawn at the surface of the detection plane. The number of positions drawn, N, is equal to the number of photons in the `grb-simulator` *PhotonDraw.fits* file, reduced by a factor $\cos\theta_s$.
(2) Based on the angles θ_s and ϕ_s and the detection plane positions that have been drawn, it is possible to compute the physical position of the photon beam when it crosses the mask plane.

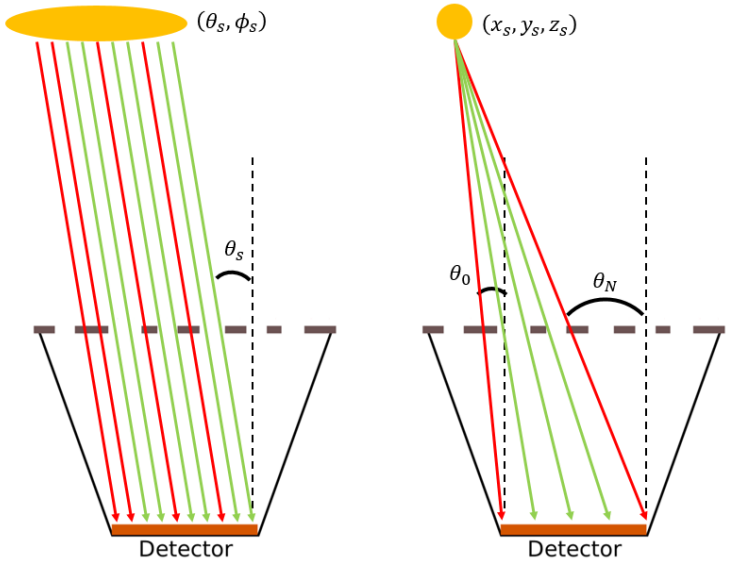

Figure 5.8. Ray-tracing differences between an infinite (left) and finite (right) source

(3) At this location, the algorithm determines whether the photon is crossing a hole in the mask or is stopped by the structure. Photons crossing the masked portion are removed while the others are kept.

An example of shadowgram obtained with the ray-tracing method is presented in Fig. 5.9(a).

Finite distance ray-tracing simulations

Some cases, such as the simulation of a radioactive source during the test campaign, require to apply the ray-tracing at a finite distance. Figure 5.8 illustrates the main difference between the case of a source at a finite and infinite distance. Two modifications from the infinite ray-tracing need to be considered:

(1) The angles θ and ϕ between the detector normal and the source are different, based on the localization of the source and the intersection of the photon path with the detection plane. There is no such relation for an infinite distance source: the photons are all emitted with the exact same θ and ϕ.
(2) The flux intensity is also different since it now depends on the source's localization with respect to the detection plane. While for the infinite distance sources, the position of the photons could be chosen with a 2D-uniform random function, another distribution must be drawn for the finite distance case.

Once the number of photons expected on the surface N has been calculated, M (with $M > N$) detection planelocations are drawn with a 2D-uniform random function. The distance d to the source is computed for each of these locations. For a finite distance source, it can be shown that the flux intensity on the detection plane decreases as $\propto d^{-2}$. Therefore, to obtain a random distribution of detection planelocations that follow this law, each of the

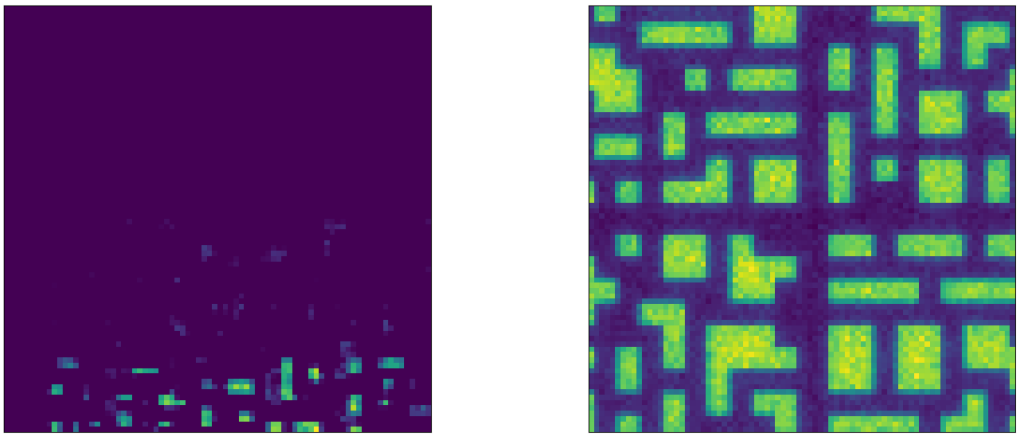

(a) Infinite distance (e.g. GRB) (b) Finite distance (e.g., Americium source)

Figure 5.9. Representation of shadowgrams obtained from on-axis sources located at infinite (a) and finite (b) distance. A shadowgram is a 2D-image of the events received on the 80×80 detection plane within a given time interval and energy range.

M distances is compared to the minimum distance of the detection planeto the source $d_{\min}$. If the ratio $(d_{\min}/d)^2$ is below a random number uniformly drawn between 0 and 1, then the corresponding photon is eliminated from the photon list. Finally, N photons with their corresponding detection planepositions are randomly taken from this corrected list.

For these N detection planepositions, the angles θ_s and ϕ_s between the detection planeposition to the source position and the detector normal are computed. With the individually computed angles and detection planepositions, infinite distance ray-tracing can be used. An example of shadowgram obtained with PIRA is presented in Fig. 5.9(b): the mask pattern is magnified because of the finite distance of the X-ray source.

5.4.2 Application of ECLAIRs response matrices

The output of the ray-tracing is a list of photons, each with a given time of arrival T, incident energy E_{in}, a position XY on the detection plane (in the case of ECLAIRs), and angles θ_s and ϕ_s relatively to the detector normal. Some photons interact with the detectors, leaving a measured energy E_{me}.

As explained in Sec. 3.2, the interaction between the detector and the photons can be simulated thanks to the ARF, RMF, IRF, and energy resolution. The ARF accounts for the instrument surface area available for the detection of photons for a given energy E_{in}, while the RMF describes the way the incident energies of these photos are deposited and measured by ECLAIRs.

The IRF accounts for the variation of the ARF relatively to the direction, which is mainly dominated in the case of ECLAIRs by the coded fraction: for a source located far from ECLAIRs line of sight, some photons are stopped by the shielding. This loss of photons is already taken into account during the ray-tracing, so the IRF is not used in the simulations.

Not using the IRF means we are only using the ARF and RMF computed for an on-axis case. Using the on-axis versions for any θ_s and ϕ_s, we assume that the detection planeefficiency and energy redistribution are the same on-axis and with an incident angle θ_s. For the efficiency, this assumption is slightly pessimistic, as the thickness of the detection plane d seen by a photon incoming with an angle θ_s is equal to $d/\cos\theta_s$, more significant than for an on-axis case: such photons have higher chances to interact with the detection plane.

This assumption remains valid in a first approximation as long as a quantitative estimation of the number of events generated from a photon list must be simulated. For off-axis spectroscopy of a GRB during the *SVOM* mission operations, the ARF with the correct coordinates θ and ϕ will be required.

Application of the ARF

The photons reaching the detection planeeach have a probability of being detected that depends on their incident energy E_{in}. The photons that are successfully depositing at least some of their energy on the detection plane are selected as follows:

(1) The ARF is normalized relative to the detection surface available for an incident on-axis beam of photons so that all its values are between 0 and 1. The detection surface available is the detection plane surface multiplied by the opening fraction of the mask. For the case of the simulations performed by M. Yassine, a surface of 0.397×1296 cm^2 $= 514.5$ cm^2 is considered.
(2) N random values η_i uniformly distributed between 0 and 1 are drawn, corresponding to the N photons that have reached the detection plane.
(3) We compare the η_i with the value of the ARF corresponding to its energy. A photon with an energy $E_{in} \in [E_i, E_{i+1}[$ is compared with the normalized ARF value $A\tilde{R}F([E_i - E_{i+1}[)$.
(4) Photons for which $\eta < A\tilde{R}F([E_i - E_{i+1}])$ are kept, as we consider that they have interacted with the detection plane.

There are now $M < N$ events that have been kept after considering the ARF.

Application of the RMF

The events' energies are redistributed using the RMF matrix. The RMF also accounts for the energy resolution of ECLAIRs. As explained in Sec. 3.6, the value in the line corresponding to the energy bin $[E_i - E_{i+1}]$ shows the probability density function to obtain a measured energy E_{me}. Figure 5.10 illustrates three of these functions, for incident energies E_{in} of 20, 50 and 100 keV. As explained in Sec. 3.3, the shape of the redistribution function depends on the incident energy, as the physical processes differ with the incident energy. Figure 5.10

shows some peaks at energies with no incident photons, primarily caused because of the escape peaks from the Tellure and Cadmium.

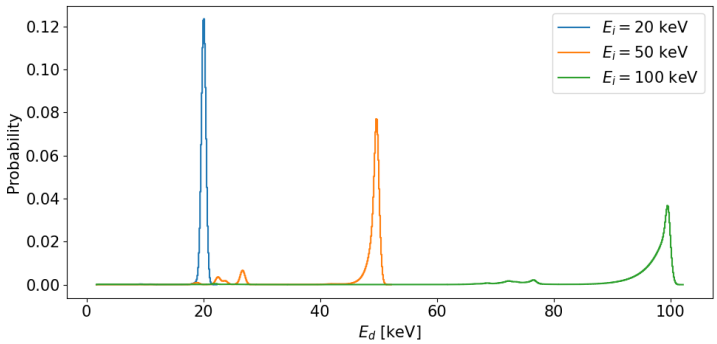

FIGURE 5.10. Illustration of the energies redistribution for 3 different incident energy E_{in}.

The redistribution process works as follows:

(1) A cumulative sum matrix is created from the RMF, so each line of the RMF contains the cumulative sum of all the column values for this given line. The probability density function becomes a cumulative distribution function.
(2) M random values η_i uniformly distributed between 0 and 1 are drawn, corresponding to the M events detected by ECLAIRs.
(3) For each event with incident energy $E_{in} \in [E_i, E_{i+1}]$, the cumulative distribution function is linearly interpolated at the value η_i to obtain the corresponding measured energy E_{me}. For the interpolation function, the probability value given for the measured energy range $[E_m, E_{m+1}]$ should be attributed to the energy E_{m+1}. The first measured energy bin has zero probability, so $E_{m=0} = 0$.

With the RMF applied, the M events now have energies that are redistributed according to the ECLAIRs instrument properties (including the energy resolution).

Application of the energy resolution for `pira-bkg` simulations

The case is slightly different for `pira-bkg` simulations. Since they are based on the GEANT4 database, they do not take into account the redistribution of energy. The energies that are given in the `pira-bkg` output are actually deposited energies E_{de}. However, as for the GEANT4 simulations, they do not incorporate the charge collection processes, so the energy resolution is not considered. For this reason, the energy resolution should be applied for the ECLAIRs and GRM background simulations, which consists in converting the deposited energy E_{de} into a measured energy E_{me}.

For ECLAIRs, the application of the energy resolution is done with a process similar to the RMF application. As the energy resolution does not have a Gaussian shape (see Sec. 5.4), the energy resolution is given as a matrix of dimension $N \times M$, where the vector corresponding to the energy bins $[E_d - E_{d+1}]$ describe the probability density function to

obtain a measured energy E_m. For each of the K events of PIRA, the energy is redistributed as:

- A cumulative sum is created from the resolution matrix so that each line of the resolution matrix represents the cumulative distribution function.
- K random values η_i uniformly distributed between 0 and 1 are drawn, corresponding to the K events that have deposited their energy in the simulation.
- For each event energy $E_{de} \in [E_d, E_{d+1}]$, the cumulative distribution function is interpolated at the value η_i to obtain the corresponding measured energy E_{me}. As is the case for the redistribution in energy, the probability value given for the measured energy range $[E_m, E_{m+1}]$ should be attributed to the energy E_{m+1}. The first measured energy bin has zero probability, so that $E_{m=0} = 0$.

5.4.3 Application of GRM response matrices

In the `eclgrm-data-simulator`, the application of the ARF and RMF is made indifferently for ECLAIRs or the GRM instrument. The Chinese team has developed a GEANT4 model, providing the Detector Response Matrices (DRMs) of the GRD instruments. One DRM (calculated for incidence angles θ_s and ϕ_s) corresponds to the product of the ARF and the RMF matrix. It has a dimension of $M \times N$ with $M = 300$ corresponding to the binning size along the incident energies and $N = 262$ the binning size along the measured energies. Figure 5.11 illustrates one such DRM.

Each response is assumed invariant with the angle ϕ_s and the GRD responses for a given θ_s identical, so that the quantity of DRMs to produce is limited. However, these assumptions are only valid for incidence angle $\theta_s \leq 60°$: above this value, the obstruction of the *SVOM* satellite has to be taken into account.

DRM application

The DRMs provided by the Chinese teams discretized the θ_s space between $\sim 0°$ and 60°. These DRMs can then be applied on a photon list as follow:

(1) For a given photon list incoming on the GRM with an angle θ_s, the corresponding $DRM(\theta_s)$ is constructed by linearly interpolating along $\cos\theta_s$ the available DRMs provided by the Chinese teams.
(2) From $DRM(\theta_s)$, the corresponding $ARF(\theta_s)$ and $RMF(\theta_s)$ can be derived. $ARF(\theta_s)$ is obtained by summing along the measured energy the $DRM(\theta_s)$. $RMF(\theta_s)$ is calculated by normalizing the $DRM(\theta_s)$ matrix so that the sum for a given incident energy of all the measured energy is equal to 1.
(3) The obtained $ARF(\theta_s)$ and $RMF(\theta_s)$ are applied to the photon list with the method above presented for ECLAIRs.

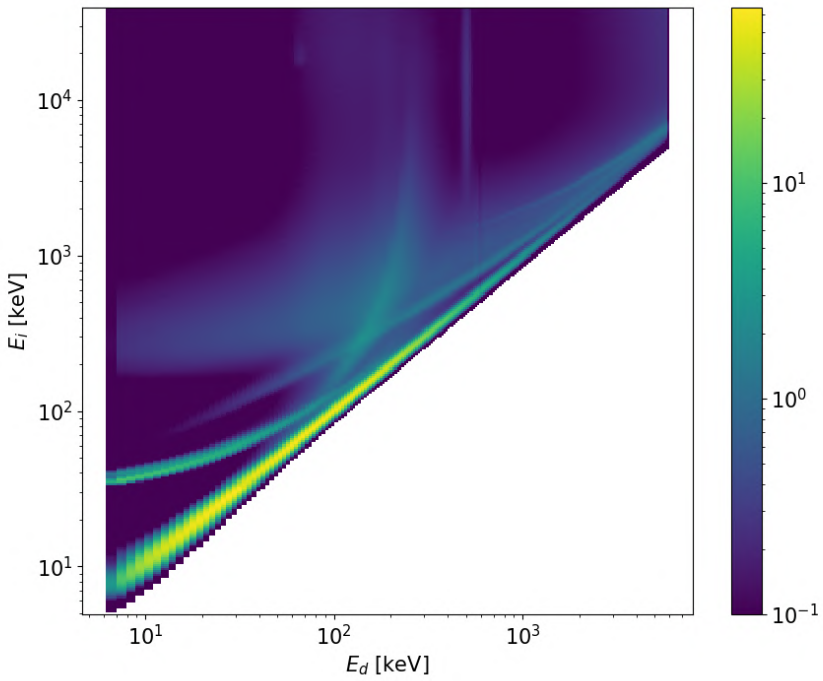

FIGURE 5.11. Example of DRM at $\theta_s \approx 0°$ for GRD1. The color coding represents the surface area available per bin of incident and measured energy.

Energy Resolution

As for ECLAIRs, the `pira-bkg` simulations do not account for the energy resolution for GRM. However,it is applied with a method slightly different from the ECLAIRs method presented above.

For GRM, the energy resolution is assumed to have a Gaussian shape, whose full width at half maximum (FWHM) can be written as:

$$FWHM(E) \ \ [\text{keV}] = \frac{E_{\text{piv}}}{100}\sqrt{p_0^2\,(E/E_{\text{piv}}) + p_1^2\,(E/E_{\text{piv}})^2} \tag{5.1}$$

with $E_{\text{piv}} = 1$ keV and the parameters p_0 (~ 170) and p_1 (~ 5) taking different values depending on the GRD and the energy range considered. The evolution of the $FWHM(E)$ relative to the energy is shown in Fig. 5.12. Using this expression, each event from PIRA-GRM with an energy E has a measured energy randomly drawn according to a Gaussian distribution of parameters $\{\mu = E, \sigma = FWHM(E)/2.35\}$.

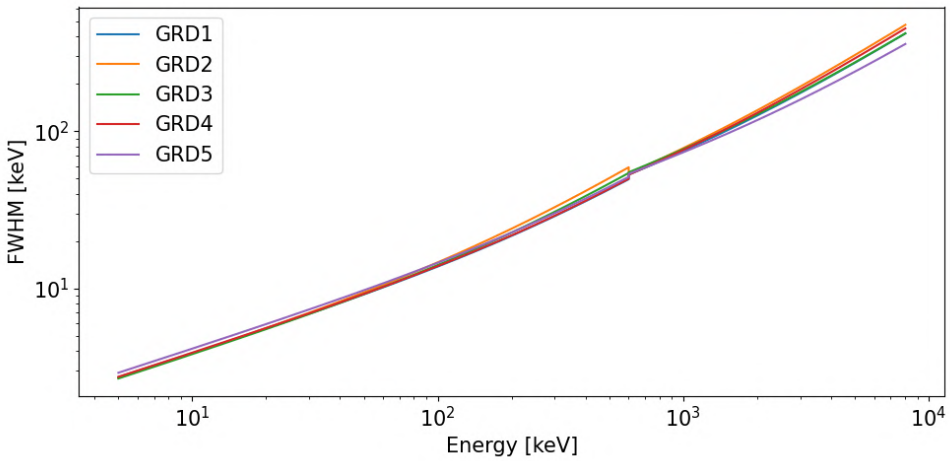

Figure 5.12. Evolution of the GRDs energy resolution as a function of the energy deposited. The 3 first GRDs are that on-board *SVOM*, while the other two are spares.

5.4.4 Comparison with GEANT4 simulations

TBD J'aimerai beaucoup écrire quelques mots sur cette partie. Je pense que c'est important pour valider que la méthode est correcte. Je voudrais seulement mettre une image d'un spectre et d'un shadowgram pour montrer qu'on est proche de la réalité, mais qu'il y a des effets qu'on ne prend pas en compte. Par exemple le vignetting, ou la transparence du masque. Montrer que pour un GRB, le deuxième effet est très négligeable vu que ces photons sont « devant les photons à basse énergie. Mais ce serait bien de le montrer avec 2 ou 3 exemples concrets. (un spectre mou et un spectre dur par exemple). J'attends les simulations de L. Bouchet, qui devraient arriver d'ici la fin de l'été.

It is important to note that the ray-tracing simulations do not consider the fine effects of an accurate GEANT4 simulation. The mask is for example assumed to be completely opaque to photons at all energy, while in practical, there is only a ???% opacity at 80 keV. GRBs have a spectral shape that decreases as $NE(E) \propto E^{-2}$ above $E_{\rm peak}$, so that the photons only represent a few percent of the total number of photons that interact with the ECLAIRs detection plane. Comparison with dedicated GEANT4 simulations has shown that ray-tracing simulations under-estimate by $\sim 10\%$ the number of photons obtained through dedicated GEANT4 simulations.

5.5 The `eclgrm-simulation` package

The `eclgrm-simulation` package gathers all the astrophysical simulation work performed on ECLAIRs at IRAP, IAP, and LUPM. This package has been developed in collaboration with D. Corre from IAP and consists of a wrapper containing all the simulations described above, followed by the detection algorithms and the VHF and X-band pipelines.

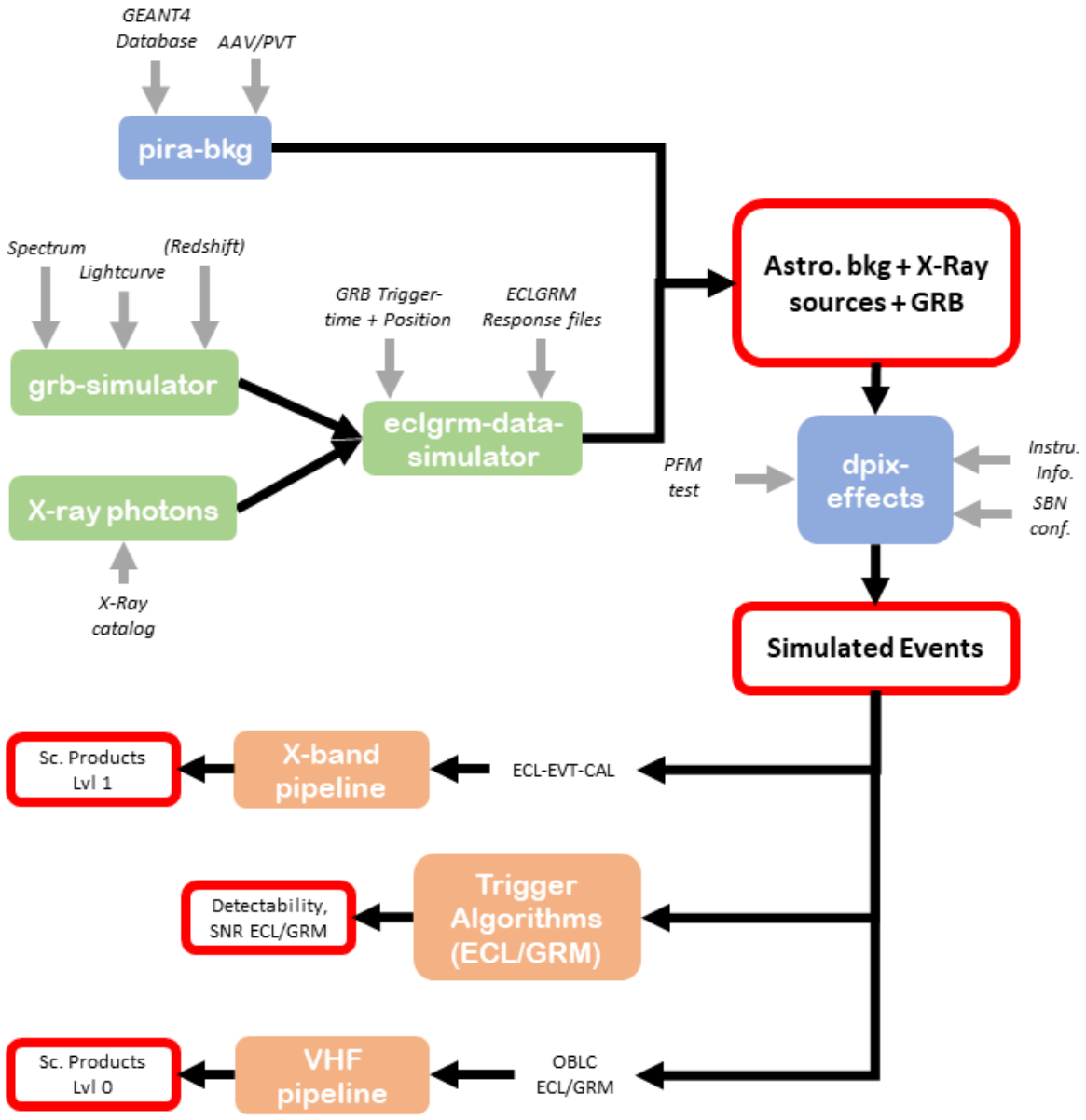

FIGURE 5.13. Schema of the `eclgrm-simulation` workflow. The box circled in red are the products that are obtained from such simulations.

5.5.1 Simulation of GRBs and background

The simulation of GRBs and the background expected in-flight requires several packages working together. A flow chart can be found in Fig. 5.13, and the description of the simulations is as follows:

- `pira-bkg` creates the reference orbit during which the simulation is carried out.

- `eclgrm-data-simulator` finds the quiescent known X-ray sources within the FoV of the instruments for the reference orbit considered.
- The package `eclgrm-simulations.position` generates the positions at which the GRBs will be simulated. The positions can be generated randomly on the orbit, or the trigger time can be chosen and the positions randomized, or the positions and trigger time can be chosen.
- `grb-simulator` simulates the desired GRBs at the desired redshift: it generates a **PhotonDraw.fits** file for each GRB at each redshift for both the ECLAIRs and GRM instruments.
- This file is used by `eclgrm-data-simulator` to simulate the expected events measured by the instruments by applying the instrument responses in the photons from the GRB and/or the X-ray sources.
- `dpix-effects` adds the instrumental noise and instrumental effects such as the non-homogeneity of the detection plane or the SBN configuration impact (see Sec. 3.6). This package only works for ECLAIRs.

The GRB and background events are stored in two different files to save computation time and storage. Then, the GRB and background events are recombined before applying the trigger algorithms or the VHF and X-band pipeline.

5.5.2 Application of the trigger algorithms

Once the events have been simulated, the trigger algorithms are applied. There are several of them corresponding to different implementations of the ECLAIRs algorithms:

- `eclgrm-sim.ecl-count-trigger-theo` is a relatively simple implementation that simulates the count trigger algorithm of ECLAIRs (see Sec. 3.5), without any background estimation involved. Instead of estimating the background from former epochs to compute the SNR at the next epoch, the algorithm simply computes the count SNR by using the origin of the events tagged in the simulations (`procID`). This method therefore assumes a perfect background subtraction. It calculates the count SNR directly from the counts of background and GRB events within a given time interval Δt, zone ΔZ and energy range ΔE, with the modified SNR equation:

$$SNR_{\mathrm{c}}(\Delta E, \Delta t, \Delta Z) = \frac{C_{\mathrm{GRB}}}{\sqrt{C_{\mathrm{bkg}}}}(\Delta E, \Delta t, \Delta Z) \tag{5.2}$$

  The shadowgram created from the optimal interval $(\Delta t, \Delta E)$ found by the counting part and its deconvolution to create the sky image are computed with the same method as the real on-board count trigger algorithm.
- `eclgrm-sim.grm-trigger` reproduces the exact same behavior as the flight algorithm, presented in Sec. 2.2.2.
- There are also some discussions about using the real on-board detection algorithms provided by CEA on the pipeline, using a `Docker` container for more flexibility. However, this solution has not been implemented yet in the frame of the `eclgrm-simulation` package.

5.5.3 Running the VHF and X-band pipelines

The VHF and X-band pipelines are also incorporated into the `eclgrm-simulation` package in their offline version. Starting from the GRB and background events files, the input files used for the pipeline are created by `eclgrm-simulation`: the OBLC_ECL and OBLC_GRM (OBLC standing for On-Board count Light Curves) for the VHF pipeline and the ECL-EVT-CAL for the X-band one (EVT standing for EVenT and CAL for CALibrated).

After that, the pipelines are applied to these simulated data to calculate the resulting scientific products of levels 0 and 1.

5.5.4 Application of `eclgrm-simulation`

This package has many applications, some developed more in detail in the dedicated Sec. 5.6. Here are listed other potential applications:

Optimal on-board trigger configuration and offline trigger performances

With these realistic simulations, it is possible to test the instrument's detection performances on a given population. More important, these performances can be assessed depending on the trigger configuration. This can give clues about the optimal energy range for the trigger algorithms, considering the noise on the detection plane.

Moreover, the possibility of generating hundreds of thousands of GRBs from known catalogs allows testing different trigger algorithms and comparing their performances.

Definition of the hardness ratio energy stripes

By simulating a known population of GRBs, it is possible to define the optimal energy stripes differentiating long and short GRBs (but not only). These simulations use the background and GRB simulation up to the VHF pipeline.

Crude classification of GRBs

Simulating thousands of bursts at different positions for the ECLAIRs and/or GRM instruments and obtaining the lvl 0 scientific products with the VHF pipeline allows training a classifier (probably Random Forest or Support Vector Machine) for a VHF-pipeline module called the CRude CLASSifier (CRCLASS). The CRCLASS tries to infer the nature of the burst (long, short, XRF, SGR, SGR Giant Flare) based on the prompt emission properties of the burst. This work was started under the supervision of Jean-Pascal Dezalay using the tools presented above.

Horizon calculation of a given population

The package offers the possibility to calculate the maximum redshift at which a given burst could be detected. This can be used for many analyses, from the performances of ECLAIRs

detection at high-redshift to the study of the impact of redshift on observed parameters such as T_{90} or the possibility of performing a $N/N_{\max}$ test on the GRBs detected by ECLAIRs (see Chapter 8 for more details on the $N/N_{\max}$ test).

5.6 Astrophysical applications of the simulations

I present below two astrophysical applications of the simulation tools presented in this Chapter.

5.6.1 Validation of the noisy pixels algorithm threshold

During the test campaigns, some pixels displayed erratic behaviors, counting at an abnormally high rate compared to the received photon rate. Some of them have been identified during the test campaign or during the in-flight calibration campaign and will be de-activated. However, some also appear randomly on the detection plane at later epochs during the mission.

These pixels can prevent the system from counting correctly:

(1) They might cause fortuitous coincidence detection: for example, if one pixel of the XRDPIX systematically triggers when another pixel from the module is triggered, all these events will be registered as multiples.
(2) They might also increase the dead-time of ECLAIRs, as each false detection from a noisy pixel induces a dead-time of a few microseconds because of the reading process (explained in Sec. 3.6).
(3) They can also create a domino effect, stimulating other detectors so that they, in turn, become noisy. This has been observed during the tests, referenced as the "column effect," where several detectors belonging to XRDPIX from the same column start becoming noisy because of a noisy pixel.

These pixels need to be detected and de-activated for all these reasons: this is the purpose of the noisy pixels algorithm. The principle of the algorithm is straightforward: every 8 seconds, the UGTS checks if a pixel has more than 200 counts in an 8 second interval (a rate larger than 25 counts/s/pix). If a pixel verifies this condition, the UGTS sets its SBN threshold to 63, so that it is inhibited.

However, it is crucial to verify that during nominal operations (background, GRB, SAA), no pixel has a rate exceeding the 200 counts in the 8 seconds time interval because of statistical fluctuations. We have simulated several nominal scenarios to verify whether some pixels exceed this noisy pixel threshold. For each scenario, we have built a lightcurves per pixel sampled every 8 second. For each time interval of 8 seconds, we extract statistical parameters such as the maximum, mean, median, and standard deviation from the detection plane counts on the 6400 pixels. The maximum curve illustrated in Fig. 5.14 shows the highest count of the 6400 pixels for a given time interval of 8 seconds.

Orbits simulated

The following orbits have been simulated:

- Standard background orbit
- Standard background orbit with GRB 130427A, the most powerful GRB detected during *Swift*/BAT operations
- Standard background orbit with GRB 190114C, the second most powerful GRB detected during *Swift*/BAT operations
- An orbit with SAA core entrance
- An orbit with SAA outer layers entrance

Results

After simulating the orbits with the tools presented in this Chapter, lightcurves with a time resolution of 8 seconds have been built. The expected count for a standard orbit is ~ 3000 counts/s, which translates to ~ 0.5 counts/s/pix or 4 counts/pix in a 8 seconds period. However, because of the statistical fluctuations on the detection plane, some pixels reach 17 counts in an 8 seconds time interval (see Fig. 5.14). As this is way below the 200 count threshold of noisy pixels, a standard background will not generate any noisy pixels.

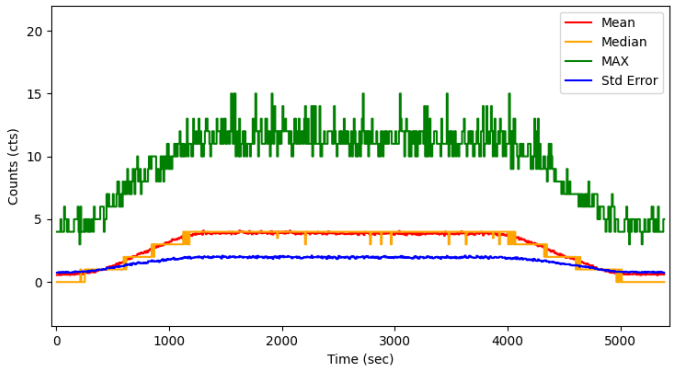

Figure 5.14. Evolution of the statistical parameters for a standard orbit with astrophysical background only.

For cases with GRBs, this is different: assuming that GRB 130427A were to happen in the fully coded portion of the FoV of ECLAIRs, the 8-sec count for some pixels would exceed the 200 counts. However, the noisy pixel algorithm disables only one pixel at a time for each 8 seconds. As the GRB generates such high counts only for a single 8-sec period, *only one pixel per sector would be disabled because of the algorithm.* Moreover, the UGTS algorithm has some options to give a "second chance" to pixels disabled, meaning that these pixels will not be permanently de-activated.

Finally, this GRB was a once-in-a-lifetime event, with 10 times more fluence than the second most fluent GRB detected (whose counts do not exceed the algorithm's threshold). Figure 5.16 shows that for this burst (GRB 190114C), the maximum counts per pixel on the whole detection plane does not exceed the limit of 200 counts. Consequently, there is most likely no GRB that will trigger the noisy pixel algorithm during the *SVOM* mission.

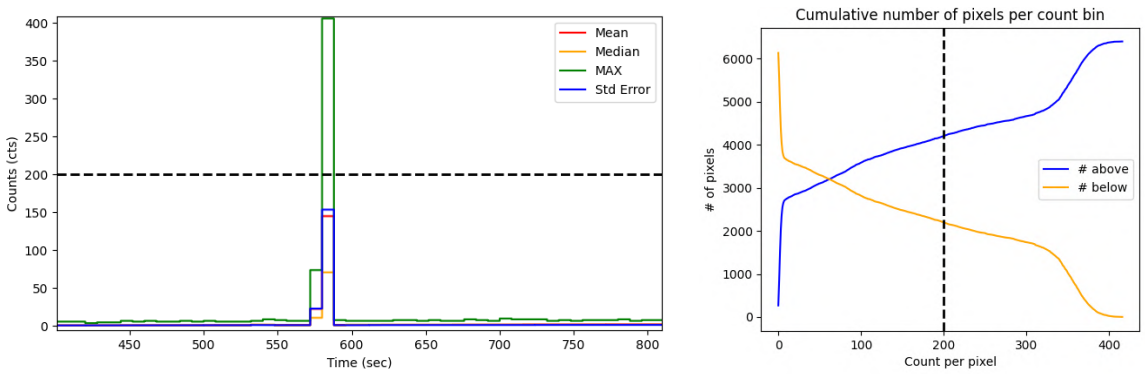

(a) (b)

FIGURE 5.15. Simulation for GRB 130427A for a time interval of 8 seconds. (a) Evolution of statistical parameters during the burst, (b) Cumulative distribution of the individual pixel counts at the GRB peak. The black dashed line represents the threshold of 200 counts on a period of 8 seconds.

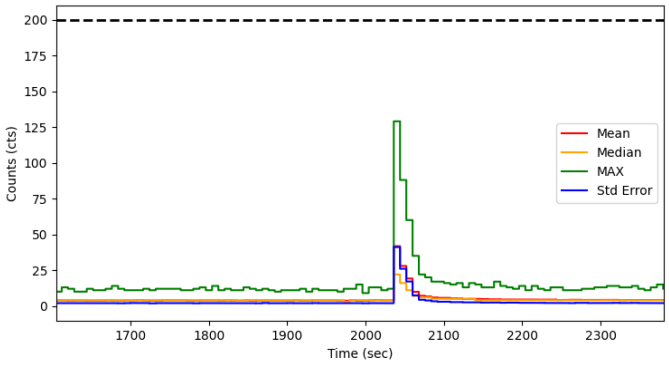

FIGURE 5.16. Evolution of the statistical parameters for a standard orbit with GRB 190114C .

Nevertheless, some events (possibly rarer) called SGR-Giant Flare could have a similar or even more significant impact on the detection plane. A good example is the giant flare from the 27th December 2004, SGR 1806-20, that has a fluence even larger than GRB 130427A. However, these events are typically a few milliseconds long, and they would have, in the worst case, a similar impact as the GRB described before (a single pixel disabled per sector over an 8 seconds time interval).

From the simulations for the SAA entrances, the maximum count per pixel obtained on a 8-sec time interval is around ~ 160 counts when the background noise reaches $\sim 50,000$ counts/s considering the whole camera (see Fig. 5.17). This is $\sim 15\times$ the standard background noise expected during the orbit. At this counts rate, ECLAIRs will have already detected the SAA entrance and disabled the noisy pixel algorithm. *The SAA should not lead to the disablement of noisy pixels.*

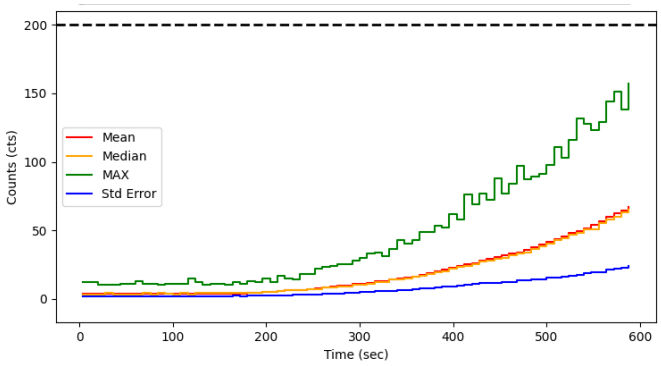

Figure 5.17. Evolution of the statistical parameters for a core SAA entrance.

5.6.2 Actualization of the GRBs detection rate for ECLAIRs and GRM

Estimating the expected number of GRBs detected either by ECLAIRs, GRM or ECLAIRs+GRM is difficult. Antier-Farfar (2016) proposed a first estimation based on the `grbsimulator` tool, simulating the Goldstein catalog (with $\sim$ 2500 BATSE GRBs) and using the log N - log P from Stern et al. (2001). This new estimation uses the same methodology and sample as the one from Antier-Farfar while also considering the latest development for the background and instrument simulations. The tools used are implemented in the package `eclgrm-sim`.

Method

The publication of Stern et al. (2001) presents a log N - log P diagram, indicating the expected number of GRBs per year emitted for the *CGRO*/BATSE FoV for a given peak flux interval. The thorough offline analysis of the BATSE data has allowed them to get a precise estimation of the duty cycle and the sensitivity of the instrument: they reached a peak-flux sensitivity in the $50 - 300$ keV of 0.067 ph cm^{-2} s^{-1}, which is, for example, more than one order of magnitude below the *Swift*/eBAT6 complete GRB sample.

By multiplying the original log N - log P from Stern et al. (2001) by the efficiency of the instruments for each peak flux bin, a new log N - log P relation is obtained. Integrating this relation for all the observable peak fluxes allows us estimate the GRB rate of a given instrument.

The computation of the detection efficiency per peak flux bin relies on the detection efficiency of the instrument considered for the BATSE GRBs in the Goldstein catalog. It can be decomposed into two independent components so that the efficiency per GRB for a given instrument can be computed as:

$$\eta_{\mathrm{GRB,inst}} = \eta_{\mathrm{potTrig,inst}} \times \eta^{\mathrm{potTrig}}_{\mathrm{GRB,inst}} \tag{5.3}$$

The first one is $\eta_{\mathrm{potTrig,inst}}$ and represents the fraction of GRBs from a sample randomly drawn on the sky that falls within the potential trigger condition of the instruments. For

ECLAIRs, the requirement is to fall within the 190×190 inner pixel of the instrument FoV. For GRM, the burst must fall in the FoV of at least two GRDs. Moreover, this fraction also takes into account the instrument duty cycle and the SAA crossing during which the instruments cannot be used. Starting from N positions with random locations (and trigger times), the algorithm selects M positions within the instrument trigger conditions and not masked by the Earth. Moreover, the algorithm also checks that the *SVOM* is not in the SAA and is not under maintenance. This allows to compute $\eta_{\mathrm{potTrig,inst}} = M/N$, equal to $\eta_{\mathrm{potTrig,ECL}} \approx 8.3\%$ for ECLAIRs and $\eta_{\mathrm{potTrig,GRM}} \approx 23.4\%$ for GRM.

The second one is the $\eta^{\mathrm{potTrig}}_{\mathrm{GRB,inst}}$, which is a detection efficiency per GRB and instrument. This efficiency is calculated as the fraction between the number of GRBs randomly drawn in the instrument FoV with a potential trigger and the number of GRBs detected by the instrument. This efficiency depends on the GRB lightcurve and spectral properties. Once the positions are drawn, `grbsimulator` draws for each GRB in the Goldstein catalog the expected photons in the ECLAIRs and GRM energy ranges. Each GRB is then simulated at $K = 100$ positions, and the trigger algorithm is applied to determine the number of positions $L_{\mathrm{GRB,inst}}$ for which the GRB is detected. The detection efficiency is computed as $\eta^{\mathrm{potTrig}}_{\mathrm{GRB,inst}} = L_{\mathrm{GRB,inst}}/K$.

The efficiency of the GRBs is assumed to follow a normal distribution, with a standard deviation equal to the standard deviation of the GRBs within this peak flux bin and the mean value of the GRBs. Each peak flux bin also has incertitudes on the corresponding GRB rate, based on the errorbar provided in the publication of Stern et al. (2001): it is also assumed that the GRB rate for a given peak flux follows a normal distribution, with a standard deviation equal to the error of each peak flux bin. By taking 1 million random sample for the GRB efficiency and the GRB rate of each bins flux, these two errors are propagated to obtain the incertitude on the log N - Log P relation multiplied by the instrument efficiency.

Results

Such a methodology can be applied to calculate the expected GRB yearly rate of ECLAIRs, GRM, or ECLAIRs and GRM together. Figure 5.18(a) below represents the log N – log P from Stern et al. (2001), multiplied by the instruments efficiency.

The estimated rates with this method are as follows:

- ECLAIRs: $47.2^{+9.2}_{-8.6}$ GRB yr^{-1} (lower), $58.0^{+10.4}_{-9.6}$ GRB yr^{-1} (upper)
- GRM: $119.7^{+21.8}_{-20.1}$ GRB yr^{-1} (lower), $137.1^{+27.4}_{-26.4}$ GRB yr^{-1} (upper)
- ECLAIRs + GRM: $43.1^{+7.0}_{-6.7}$ GRB yr^{-1} (lower), $51.6^{+10.0}_{-9.5}$ GRB yr^{-1} (upper)

The results obtained for ECLAIRs with this method are compatible with the ones obtained in Antier-Farfar (2016). Furthermore, based on her thesis work, two additional quantities can be added to the estimated rate:

(1) The "low energy threshold" bonus accounts for the ECLAIRs sensitivity up to 4 keV, while the BATSE trigger algorithm was starting at 15 keV: this represents a

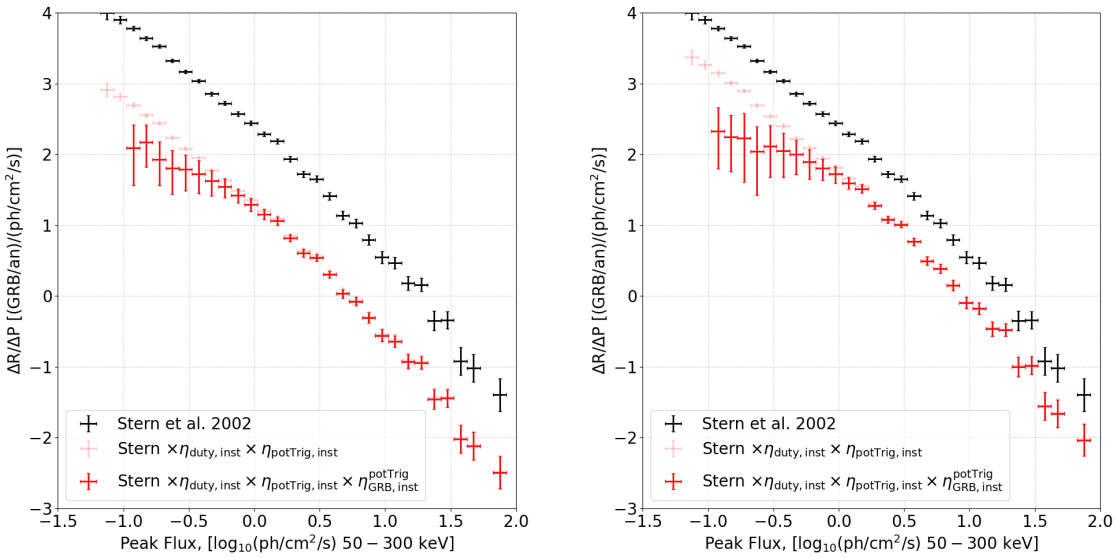

(a) ECLAIRs (b) GRM

Figure 5.18. $\log N - \log P$ plot obtained for (a) ECLAIRs and (b) GRM. The full black line corresponds to the Stern et al. (2001) $\log N - \log P$ normalized to the whole sky (4π), while the fair red and red curves the $\log N - \log P$ multiplied by the global and detection efficiency of the GRBs.

loss on the estimated rate of the instrument. This bonus has been estimated by Antier-Farfar (2016) to be between 9 and 18%.

(2) The "imaging" bonus accounts for the imaging capability of ECLAIRs, increasing its detection efficiency for long and low-peak flux GRBs compared to BATSE. This bonus has been estimated by Antier-Farfar (2016) to be equal to 9%.

All the tools are now available to refine these estimations in the near future. Using the lower limit of the "low energy threshold" bonus, the ECLAIRs rate could be of the order of 56 GRB yr^{-1} for the lower estimation and 68 GRB yr^{-1} for the upper one.

For GRM, the values found are above the $\sim$ 90 GRB yr^{-1} provided in Wei et al. (2016). We have considered in this analysis that the GRD FoV is extended up to an 80° incident angle. However, this analysis used the fact that the GRD responses can be considered invariant for a rotation around their pointing direction. This hypothesis, true for incident angles up to 60°, is not true anymore above this incidence angle, as some satellite components can shield some directions for the GRDs. For this reason, a grid of each GRD response from directions around the satellite is required to get a more precise estimation. The estimation can be seen as an upper value of the actual rate of the satellite.

For ECLAIRs and GRM together, some results are exciting to look at:

(1) Based on the estimation provided, $\sim$ 90% of the GRBs detected by ECLAIRs would also be detected by GRM. However, in reality, this number might be overestimated

because of the low energy threshold and image bonuses discussed above. Taking into account these two bonuses, $\sim 70\%$ of the GRBs detected by ECLAIRs would also be detected by GRM.

(2) There will be ~ 3 GRB yr^{-1} that will be seen only by ECLAIRs or GRM, despite being in the FoV of both instruments. However, taking into account the two bonuses discussed above (and the fact that GRM is not sensitive to such populations), the number of GRBs detected only by ECLAIRs could be increased up to $\sim 10 - 15$ GRB yr^{-1}.

Further analyses are now performed at IRAP to improve the results provided. For example, a more precise estimation of the "low-energy threshold" and "imaging" bonuses could be performed.

- For the effect of the low-energy threshold, a solution would be to used the catalog of Jenke et al. (2016). This catalog contains the GRBs detected by *Fermi*/GBM, not detected on-board but thanks to a ground re-analysis (for which the low-energy threshold is set 8 keV instead of 25 keV). There are 65 GRBs with such conditions identified in the paper, meaning at least 20 GRBs per year. This rate of GRBs detected by GBM can be normalized to an absolute rate, as bright GBM bursts follow the bright part log N – log P from Stern et al. (2001). Using the same methodology as before on this population, it is possible to compute the expected rate of ECLAIRs for them.
- For the "imaging" part, the idea would be to investigate the GRBs detected by *Swift*/BAT, most likely the ones detected thanks to the imaging trigger but missed by the count trigger. However, the rate normalization of such GRBs is difficult to make for *Swift*/BAT, making the estimation complicated to perform.

5.7 Hardware simulation of ECLAIRs

The ECLAIRs events generated by the astrophysical simulation tools described above are processed by the electronic (FPGA from the ELS) before being read by the UGTS. The behavior of the ECLAIRs detection plane electronic is complex: for example, when an ASIC triggers because of an incoming event, it freezes the ASIC of the detection module to its left to prevent a cross-talk effect observed on some pixels. Moreover, the electronic classifies the events with the methodology explained in Sec. 3.4, involving another freezing of the ASIC, during which no event can be detected. These instrumental effects must be considered for testing the ECLAIRs software.

This section describes how this FPGA processing has been simulated with a tool called ELSimulator (the grey box of Fig. 5.19), and how the frames generated by such a method are read by a simulation of the UGTS and *SVOM* platform, the Banc de Validation Système (BVS, the green box of Fig. 5.19). It also describes how some simulations processed by ELSimulator and the BVS have been used to validate the flight software of ECLAIRs.

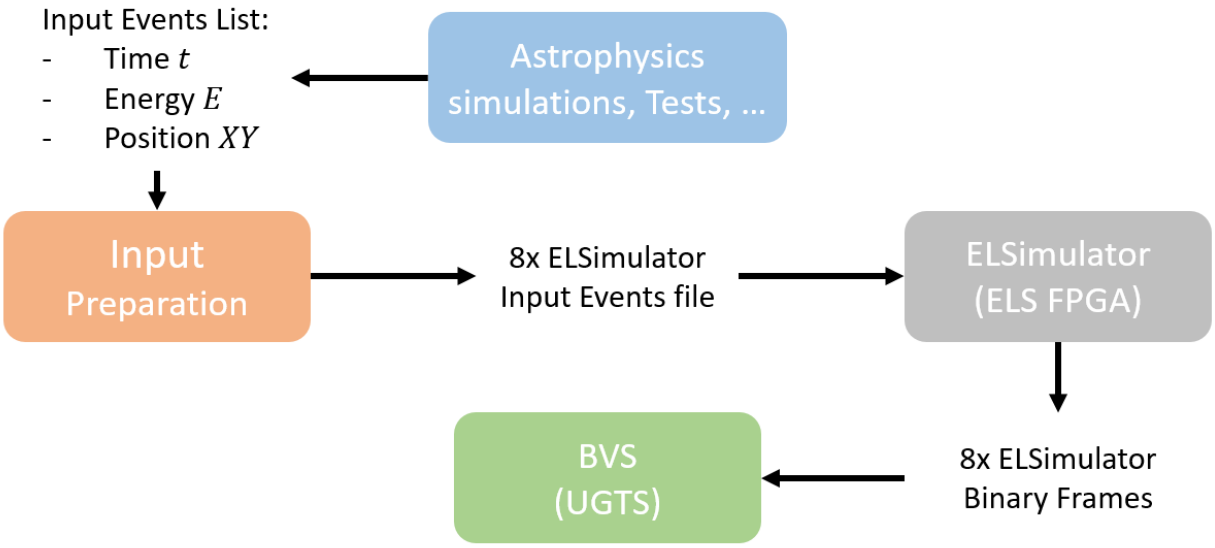

Figure 5.19. Schema of hardware simulation

5.7.1 ELSimulator

ELSimulator has been created by IRAP electronic engineers to simulate the detection planeelectronic behavior and assess its impact on the input events (see Fig. 5.20(b)). It contains a real FPGA, programmed with the same code as the pre-processing card equipping one ELS (see Sec. 3.1). The last version of ELSimulator, ELSimulatorD, simulates the behavior of the 8 ELS at the same time and in real-time. Simulations using this tool are directly controlled by the same software that controls the detection plane during the real tests. As ELSimulatorD contains the same FPGA code as ECLAIRs, it accounts to the dead-time induced by the freezing of the ASICs (see Sec. 3.2) or the classification of the events based on their energies and multiplicities (see Sec. 3.4).

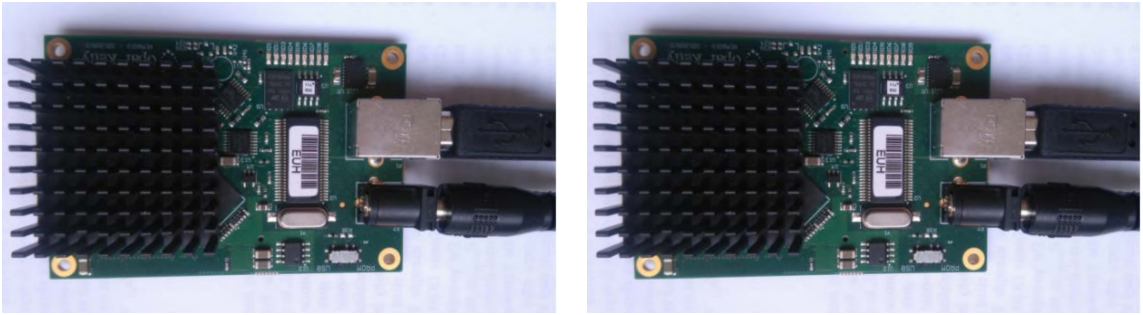

(a) ELSimulator Opal Kelly key (b) ELSimulatorD and the Netpix

Figure 5.20. The hardware used to simulate the ELS electronic of ECLAIRs

Based on an event list obtained from a simulation or a test (output of the blue box from Fig. 5.19), 8 input files are generated with a format that can be read by ELSimulator

(output of the orange box in Fig. 5.19). These files are then processed in real-time by ELSimulator that applies the ELS FPGA algorithms and outputs 8 list of frames with the same format as the output of the real ELS (output of the grey box in Fig. 5.19). These binary frames contain the information communicated between the ELS and the UGTS: the classified events and the TFE.

Creation of ELSimulator inputs

The inputs of ELSimulator are 8 text files (one per ELS) containing simulated events detected by the XRDPIX ASICs and transmitted to the ELS electronic. For this reason, instrumental effects generated by the ASICs, such as the energy thresholds, in-homogeneities of the detection plane, or energy resolution, must be applied before generating this file.

Each line of the 8 *.txt* ELSimulator input files corresponds to one event (which can be either a single event or a multiple on the same ASIC). Each of these events is characterized by the following quantity, corresponding to the column of the input files:

(1) the baseline L_b, which is set equal to 0.
(2) the time interval δt between two events defined above, in units of 10 ns.
(3) the ASIC number on which the event(s) triggered.
(4) a binary representation of the ASIC channel(s) triggered for this event. There are 32 bits, where 1 is set for each channel that has triggered.
(5) the signal S registered on each channel, corresponding the energy of the event measured on the XRDPIX.

An example of such a file format is given in Fig. 5.21.

```
#Els 1  Baseline    DTime(10ns)(>6) AsicNumber  PixelsTrigers   PixelsEnergy
...
0   23000   5   b00000000100000000000000000000000   0    0   0   0   ...   2763   ...
...


#Els 3  Baseline    DTime(10ns)(>6) AsicNumber  PixelsTrigers   PixelsEnergy
...
0   1780    8   b10000000000000000000000100000000   3591    0   0   0   ...   673   ...
0   0       9   b00000000000000000100000000000000   0    0   0   0   ...   1341   ...
...
```

FIGURE 5.21. Example of ELSimulator INPUT for a complex multiple case. The top and bottom paragraphs are supposed to be in two different input files for two different ELS.

As it is explained in the ELSimulator input file format, the time of arrival of the events is encoded differentially: each event is dated relatively to the time of arrival of the previous event (on the same ELS). This is not the case for the simulation files, which are encoded in an absolute way. For ECLAIRs, the synchronization between the ELS is performed by the UGTS. However, the synchronization between the ELS should be done in another way, further developed later.

The FPGA code in ELSimulator is expected to have the exact same information as the real ELS: the energy deposited by each photon is measured by subtracting the baseline value L_b from the signal value S, which will correspond to a given channel $CHAN$. For this reason, the physical energy (in keV) of the events obtained with the simulations should be converted into a signal and a baseline. To perform this conversion, the events energy E is first converted to channels $CHAN(E)$ by applying the linear relation between the event energy and the channel, described in 3.2. Then the baseline following formula is applied to the $CHAN(E)$ to obtain the signal S, with $L_\mathrm{b} = 0$ and $OFFSET = 1433$:

$$S = 2 \times CHAN(E) + L_\mathrm{b} - OFFSET \tag{5.4}$$

Finally, the event position should be referenced in terms of ELS number, ASIC number, and ASIC channel (while for simulations its the X, Y position on the detection plane). Moreover, the ASIC channel that triggers is different from the XRDPIX pixel number attributed according to the IRAP convention. The correspondence can be found in Table 5.1 below.

Table 5.1 . Conversion between the pixel number based on the detection planeconventions and the corresponding channel for a given ASIC.

Pixel	0	1	2	3	4	5	6	7	8	9	10	11	12	13	14	15
ASIC channel	26	22	18	16	14	12	8	4	30	28	24	20	10	6	2	0

Pixel	16	17	18	19	20	21	22	23	24	25	26	27	28	29	30	31
ASIC channel	25	31	29	27	5	1	7	3	23	21	19	17	15	13	11	9

Synchronization of the events between ELS

As stated above, the 8 input file times are based on the relative time difference with the event that preceded them. Thus, the time of all the events from a given ELS input file is relative to its first event. ELSimulator considers that the first events of each ELS input file are synchronous. However, this is not the case in reality: they arrive with a time delay relative to each other. Artificial events happening at the exact same time on each ELS are added at the beginning and end of the input files (called respectively leading and trailing events) to have synchronization between the 8 ELSs. Since all the leading events arrive at the same moment on the 8 ELS, the other events from the input file (whose relative time is based on these leading photons) are synchronized. Moreover, since the time between the leading and trailing events is the same for all ELSs, the simulation time for each ELS will be identical.

Moreover, the synchronization between the ELS relatively to the TFEs is also mandatory for the communication with the UGTS. As explained in Sec. 3.4, these TFE are sent by each ELS every 10 ms and contain the integral count of one of the 800 pixels of the ELS: the first TFE will therefore send the information about pixel 0, then the second about pixel 1, ... pixel 799 and then restart with the pixel 0 after 8 seconds. Therefore, it is crucial for

the UGTS to have synchronized TFE for all the ELS, meaning that the TFE from pixel N should be send at the same moment by all the ELS: ELS4 cannot send a TFE corresponding to pixel 377 while ELS5 sends information about pixel 381. This issue was especially true for the first version of ELSimulator, where the randomness of the initialization time was preventing the TFE synchronization. This has been fixed with the latest version of ELSimulatorD.

Limitations of ELSimulatorD

There are some limitations to the use of ELSimulatorD. This section quickly develops the ones identified.

The first limitation is in the synchronization of the events: although the TFE counters are synchronized between the ELS, this synchronization is actually performed by groups of 4 ELS: from 0 to 3 and from 4 to 7. For this reason, despite the TFE reinitialization, an offset of 1 TFE can be seen between these two groups of ELS. The leading photon will therefore arrive after TFE #134 for ELS 0,1,2,3, while it will arrive after TFE #135 for ELS 4,5,6,7. Overall, the precision for the events synchronization will be limited to 10 ms. This duration corresponds to the smallest timescale for the trigger algorithm, and it could have an impact on simulations with phenomena with very short durations.

The second limitation is the memory available for storing the events. Although this memory has been increased compared to ELSimulator, ELSimulatorD still has a maximum capacity for the number of lines that can be used, limiting the simulation time that can be done in one go. Typically, this limitation is of the order of 5×10^6 lines, corresponding, for example, to 2.5 orbits with background events.

The simulations are performed in real-time, which can become problematic when a large number of simulations need to be done. Moreover, the electronic is used extensively by CNES on its test bench, meaning that access is limited to specific periods.

To overcome these limitations, I developed a Python version of ELSimulatorD. The synchronization, memory, computation time, and availability limitations are removed with such a method. However, the fine effects discussed at the beginning of this section are not taken into account in the code: this Python code only takes care of the classification of the events and the conversion of these events to the proper binary frame format. So although some of the issues with ELSimulatorD are solved with this pythonic version, it is still less representative of the ELS FPGA algorithm than ELSimulatorD.

5.7.2 The BVS for ECLAIRs

As explained above, ELSimulatorD simulates the event frames sent by the ELS to the UGTS. The BVS is a software that CNES has created as a framework to test the flight software globally. A scheme of its architecture can be found in Fig. 5.22.

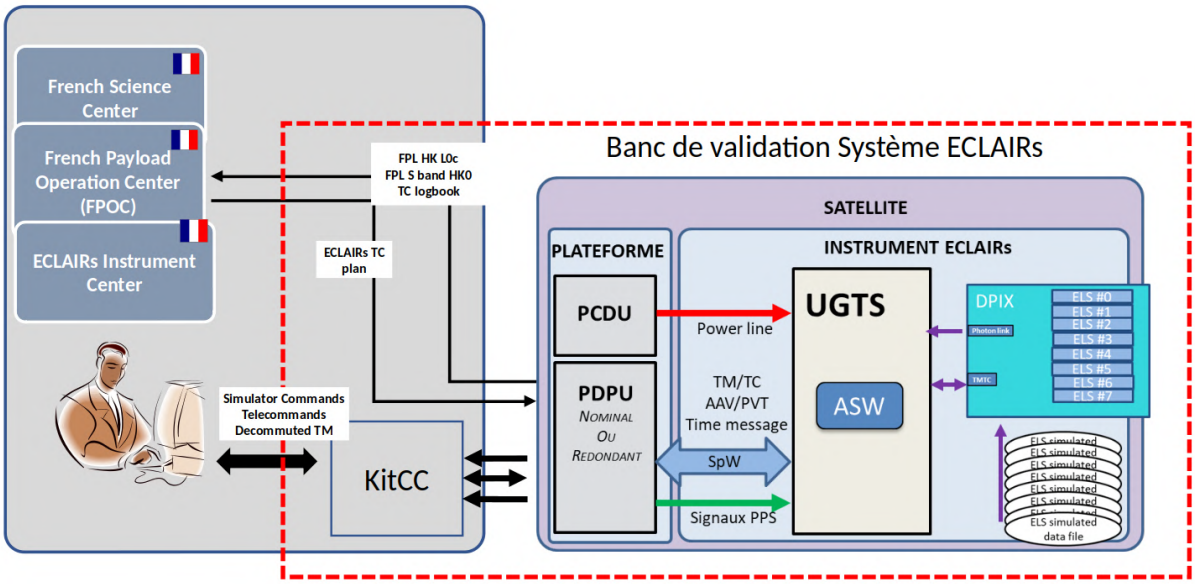

Figure 5.22. Schema of the BVS components and its communication with other sub-systems. Source: CNES - Anne-Marie Janotto

The BVS components

First, the BVS simulates the UGTS: it consists of a real-time simulation of its calculation card, in addition to its FPGA and the communication with the power supply cards. It uses the latest versions of the flight software.

Second, the BVS emulates the *SVOM* platform. It provides the attitude and orbit information (AAV/PVT) sent by *SVOM* to the UGTS. The frames sent by the UGTS to the *SVOM* platform are also processed, packaged, and formatted with the same format as the ones that will be sent by the *SVOM* to the ground. Moreover, the user can send telecommand (TC) at any moment to the UGTS, simulating scenarios such as a change of the detection plane configuration, flight software parameter changes, planned or unexpected SAA entrance, ...

Finally, the BVS also simulates the communication between the UGTS and the detection plane(even simulating the expected voltage and temperatures of the ELS components). In particular, it times the frames generated by ELSimulatorD and sends them in real-time to the UGTS.

Synchronization of events and AAV/PVT

The events generated by ELSimulatorD and the AAV/PVT files (describing the pointing and timing of the platform) are created through entirely different means. Therefore, it is crucial to ensure that they are synchronized, so that the events received by the UGTS correspond to the same situation as the one defined by the AAV/PVT. This is especially important for the X-ray sources catalog matching or the Earth mask applied on the sky image in the trigger algorithms.

In orbit without slew, the synchronization is quite simple. The ELSimulatorD events are pre-loaded into the BVS memory, and the starting time of the events is defined relatively to the ISOT time of the simulation to prevent from the time uncertainties of the initialization procedure,. The ELS frames are sent to the UGTS exactly as when the simulation is supposed to start.

For an orbit with a slew, for instance, *TestRun-TS-USS-05*, the synchronization is a bit more complex. The slew has to start as soon as the slew request from the UGTS has been transmitted to the PDPU. The attitude file for the scenario is then exported by CNES, and another ELSimulatorD simulation is made by IRAP from these attitude files. Finally, the new ELSimulatorD frames are simulated again in the BVS, allowing a synchronization of the event frames and the AAV/PVT.

5.7.3 Pre-validation of the flight software with simulations

The flight software of the ECLAIRs instrument is complex, as it is in charge of the instrument control and the trigger algorithms. Therefore, it was necessary to create realistic scenarios to investigate the instrument's behavior. These scenarios represent a list of events expected from the detection plane, depending on the attitude and position of *SVOM*.

I have created these scenarios with the entire simulation set presented in this Chapter, in addition to the ELSimuatorD presented in Sec. 5.7. Starting from background simulations, X-ray sources and/or GRBs are incorporated, in addition to instrumental effects. These scenarios are then simulated with ELSimulatorD and used as input for the BVS. The scenarios are as follow:

(1) This first scenario *TestRun-TS-USS-01* consists of two standard orbits with the expected background from CXB, Albedo, and Reflection. The impact of the SBN (the detector's energy threshold) has also been incorporated. The purpose of this scenario is to validate the behavior of the system and to test whether the trigger algorithm is stable for standard orbits.
(2) The second scenario *TestRun-TS-USS-02* is identical to *TestRun-TS-USS-01*, except that some SLE noise has been added. It has been used to investigate the impact of the SLE noise on the flight software, particularly on the trigger algorithms.
(3) This third scenario *TestRun-TS-USS-03* incorporates 4 GRBs (GRB 111005A) at various sky locations on top of the second scenario. A lightcurve of this scenario with the decomposition into its several components can be found in Fig. 5.23. This scenario has been created to test the capability of the trigger algorithms to detect and correctly locate GRBs despite the SLE noise.
(4) The fourth scenario *TestRun-TS-USS-04* is a background orbit with several galactic X-ray sources superimposed. The most important one, responsible for 90% of the observed count rate, is Sco-X1. As shown in Fig. 5.24, the scenario starts with an extra-galactic pointing, with a slew around ~ 900 seconds towards the galactic center where most of the strong X-ray sources are located. The X-ray sources then disappears from the counts received by ECLAIRs, as they are obscured by the Earth that is entering the FoV. This scenario aims at testing the flight software with a

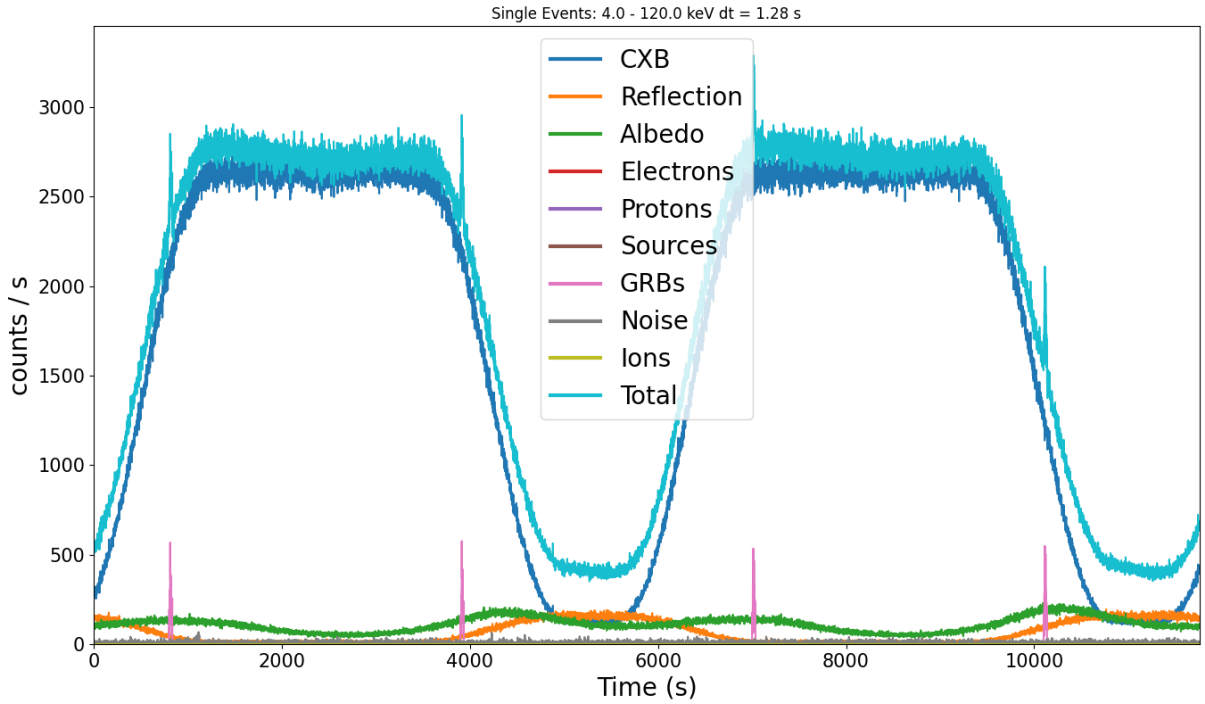

FIGURE 5.23. lightcurve obtained from *TestRun-TS-USS-03* for ECLAIRs, with the various components highlighted.

high count rate coming from known sky X-ray sources, ensuring that these sources do not trigger false alerts. It has also been beneficial to test the synchronization of the ELS frames with the AAV/PVT from the BVS.

(5) The fifth scenario *TestRun-TS-USS-05* consists to a standard background already presented, with a GRB detection followed by a slew towards the target. This scenario is crucial as it validates the behavior of the flight software during the slew. Moreover, it is the opportunity for people working on the data treatment during slews to have a realistic estimation of the X-band data sent by the satellite.

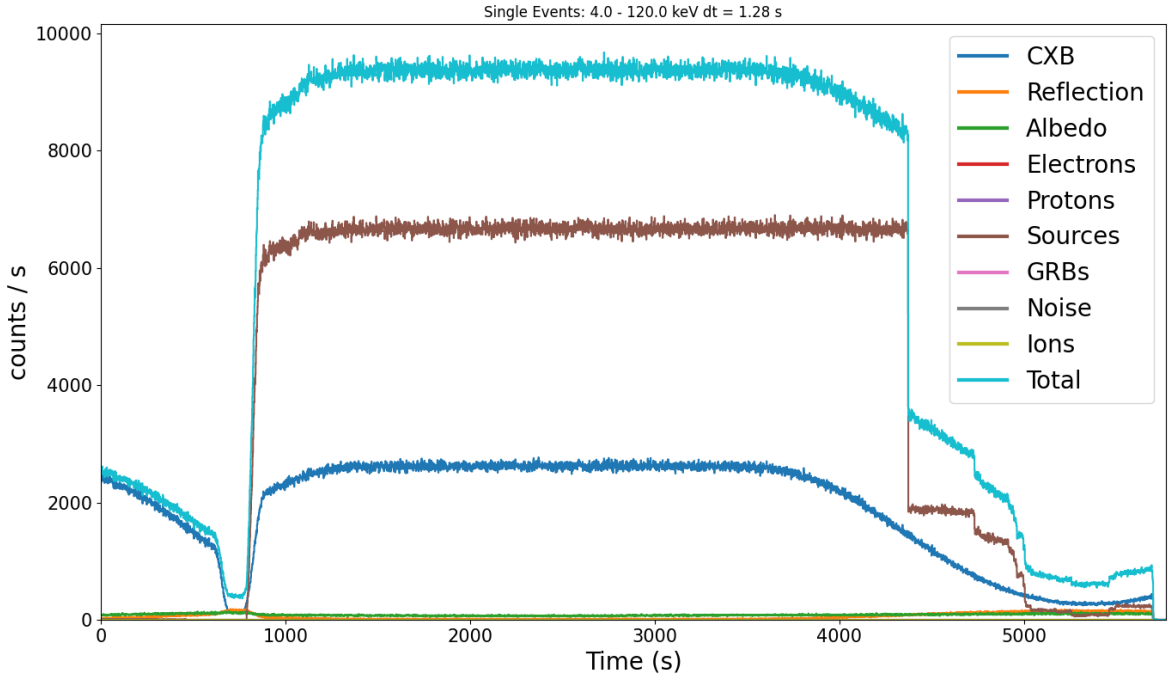

Figure 5.24. lightcurve obtained from *TestRun-TS-USS-04* for ECLAIRs. The slew is visible around $\sim$ 1000 seconds after the beginning of the scenario.

Chapter 6

γ-ray bursts detection using machine learning for ECLAIRs offline trigger

As explained in Sec. 3.5, ECLAIRs will be able to transfer all the events recorded on board to the ground. This allows developing ground detection algorithms freed from the constraints that the on-board detection algorithm ECLAIRs will have. I present in this chapter an innovative approach for such a detection algorithm, using a neural network with semi-supervised learning adapted to time series, to complement the detection performances of the on-board algorithm.

Contents

6.1 Context

GRBs astronomy has entered a new era with the simultaneous detection of a transient signal of gravitational waves GW 170817 and the short high-energy transient GRB 170817A (Abbott et al., 2017a). In addition to the confirmation of the association of short GRBs with neutron stars mergers, this uniquely detected phenomenon had crucial consequences on diverse domains, from the understanding of the prompt emission (Goldstein et al., 2017b), afterglow (D'Avanzo et al., 2018) and kilonova (Tanvir et al., 2017) associated with such events to independent measurements of key cosmological parameters (Baker et al., 2017; Abbott et al., 2017a), and clues on the origin of heavy elements that are not created in normal stars: the scientific community is looking forward for similar detections.

However, GRB 170817A also had the lowest isotropic energy ever recorded for a short GRB (10^{47} erg, Abbott et al. 2017b), with a gamma-ray emission that remained faint compared to most detected GRBs. This event was located at a redshift of $z = 0.0093$: as its fluence was already low, it would not have been possible to detect it at a much higher distance. Arcier et al. (2020) show for example that the on-board trigger of *SVOM*/ECLAIRs could only detect and locate the prompt emission up to $z \sim 0.01$. Therefore, as the horizon redshift for the detection of the GRB prompt emission is low, future conjoint detections of such events will remain rare: Abbott et al. (2017b) estimate the number of *Fermi*/GBM and LIGO/Virgo joint detections between 0.1 and 1.4 per year during the O4 campaign, despite an increase of the NS-NS horizon detection for GW interferometers.

However, *SVOM*/ECLAIRs will be the first γ-ray mission able to transfer the totality of the raw events registered on-board to the ground via X-band telemetry. This allows the re-analysis of the raw data with algorithms working on ground computers, potentially increasing the instrument's sensitivity (discussed more in detail in Sec. 3.5). A similar feature is partially present on the *Swift*/BAT instrument (Tohuvavohu et al., 2020; DeLaunay & Tohuvavohu, 2021), but it requires sending a command to the satellite (linked to the presence of GWs, GRB, or another exciting transient) so that the data can be recorded on-board and quickly sent to the ground for deeper analysis. There is no continuous data stream of *Swift*/BAT data to the ground; only a restrained portion around selected times is received on the ground.

The offline trigger of ECLAIRs will consist of several algorithms that will run in parallel on the raw events sent by the instrument. Several methods are already built or are being built, based on wavelets, improvement of the on-board trigger algorithms with different fitting strategies, or the prediction of the instrument lightcurves with statistical methods. During my Ph.D., I wanted to test another method based on machine learning (ML) and assess its performance for the detecting GRBs on a highly variable background.

The emergence of powerful and affordable Central Processing Units (CPU) and Graphical Processing Units (GPU) with important and fast storage capabilities along with dedicated Python frameworks such as `Tensorflow` or `PyTorch` allow anyone with basic knowledge and material to use the latest results from the field of Artificial Intelligence (AI). Therefore, the advent of *SVOM*/ECLAIRs is a good opportunity to have a Machine Learning (ML)

algorithm implemented as a dedicated offline trigger for high-energy transients detection, which offers exciting possibilities:

- The sensitivity of ECLAIRs could be increased, allowing the detection of events that are not detected by the on-board trigger. As explained in Arcier et al. 2020, *SVOM*/ECLAIRs on-board trigger will struggle to create a sky image for detection on small timescales, which means that some short, high-energy transients such as Soft γ-ray Repeaters (SGR) giant flares or short GRBs could be missed for example.
- The on-board trigger algorithm will not consider sources from the Earth's occulted locations when it makes the sky image. Thus, phenomena such as Terrestrial γ-ray Flashes (TGF, Sarria et al. 2017) will not be detected by the on-board algorithm, while an offline implementation could bypass this limitation and detect such events.
- The algorithm is based on an unsupervised method, meaning that its implementation has been made without any pre-conceived idea of the signature of a GRB. For this reason, it might be sensitive to events that are not expected in orbit.

In this work, we use various acronyms specific to the world of ML. Specifically, we have chosen a semi-supervised Anomaly Detection (AD) approach using a Neural Network (NN) structure called Variational Auto-Encoder (VAE). We refer to this algorithm in the remaining of the chapter as the ML trigger.

Section 6.2 explains our choice of the NN structure and how it is used to detect GRBs. Sections 6.3 and 6.4 show how the NN has been trained and tested, with existing end-to-end simulations of the expected in-flight background. In the following Sec. 6.5, we present how the transient detection is performed by the algorithms, while Sec. 6.6 compares the algorithm's performances with the on-board count trigger algorithm for a sample of GRBs. Finally, Sec. 6.7 discusses the perspectives for the algorithm for its deployment in the offline trigger architecture and future improvements.

6.2 Looking for anomalous events in ECLAIRs with Donut

Machine Learning (ML) is nowadays commonly used in most domains of astrophysics, such as gravitational waves (Morawski et al., 2021), X-ray sources classification (e.g. Arnason et al., 2020), transient detection (Malanchev et al., 2021) or even GRB detection (Abraham et al., 2019) and classification (Jespersen et al., 2020).

The high-energy transients detection with *SVOM*/ECLAIRs fits in a sub-domain of ML, called the Anomaly Detection (AD), consisting of the identification of rare events (the high-energy transients) that have significant differences with a majority of non-anomalous data (the usual background observed by the ECLAIRs instrument). This field has obvious industrial and financial applications: being able to detect an anomalous behavior can save maintenance time (Wang & Wang, 2018), money (Laxhammar et al., 2009), or even lives

(Hundman et al., 2018). Many industrial groups such as Facebook[1], Twitter[2] or LinkedIn[3] have developed time-series anomaly detection programs based on machine learning, and released them in open-source. In this work, instead of building a NN from scratch, we use one of these open-source algorithms called Donut.

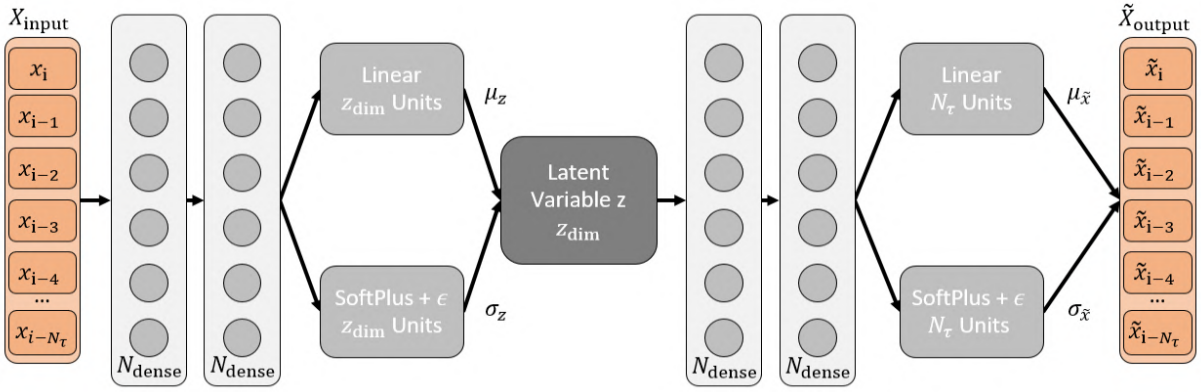

FIGURE 6.1. Architecture of the Donut VAE. The parameters N_{dense}, z_{dim} and N_τ are tunable parameters. μ_z and σ_z are the mean and standard deviation vectors of the latent representation of the input vector, while $\mu_{\tilde{x}}$ and $\sigma_{\tilde{x}}$ are the mean and standard deviation of the reconstructed vector input, $\tilde{X}_{\text{output}}$.

Donut (Xu et al., 2018) is an unsupervised AD algorithm based on a VAE with an open access implementation on Github[4] that outperforms most time series anomaly detection algorithms. Figure 6.1 shows the architecture of a Donut NN.

This NN is based on the autoencoder (AE) architecture, which is a NN architecture that relies on the compression and decompression of the input data. The first half of the algorithm, called the encoder, is a set of layers (light grey layers in Fig. 6.1 with N_{dense} neurons) which compresses the data in a lower dimension space, called the latent space (linear layers with a dimension z_{dim}). From this space, the data go through another set of layers (whose structure is often similar to the encoder structure, again the light grey layers and the linear layers on the right), the decoder, that retrieves the original dimension of the data. The dense layers' parameters of the AE are tuned with training samples to be able to reconstruct an output vector $\tilde{X}_{\text{output}}$ as close as possible to the input one X_{input}. As expected, this type of NN has lots of applications in data compression but also in image recognition, image de-noising, or features extraction.

VAE are a declination of the AE, but with a latent space described by a multivariate random distribution (instead of being deterministic): each feature is described by a normal distribution with a characteristic latent mean and variance (μ_z and σ_z in Fig. 6.1). It has been shown that VAE are actually more efficient than classical AE formulation for AD problems (Zimmerer et al., 2018; Portillo et al., 2020). Moreover, the Donut NN is

[1] https://facebook.github.io/prophet/
[2] https://github.com/twitter/AnomalyDetection
[3] https://github.com/linkedin/luminol
[4] https://github.com/korepwx/donut

a bit different from a classical VAE, as here the means are derived from linear layers (as for regular VAE), but the standard deviations are derived from soft-plus layers (layers of neurons applying the softplus activation function $Y = \log\left(1 + e^X\right)$). The reason is that the values of σ_{x} and σ_{z} might become close to 0 for data with slight local variations, which makes their logarithmic values unbounded. These unbounded values would cause several numerical problems when computing the likelihood of Gaussian variables during the training phase.

VAE (and AE in general) can be used as unsupervised learning methods, meaning that it is not required to put a "nominal" or "anomalous" label on the input data. This approach is used in many failure detection algorithms, where anomalous behaviors are rare compared to the nominal ones. As ECLAIRs will principally observe background noise, the unsupervised approach is ideal for such an instrument. The algorithm is also robust to missing/anomalous data during the training and test phases, making it directly applicable for its utilization on the ground with recorded flight data (see more details in Sec. 6.7).

The VAE Donut is used here to detect GRBs in the *SVOM*/ECLAIRs data: the GRBs data are assimilated to anomalous data compared to the nominal background data received by the instrument. The global approach of the anomaly detection algorithm is shown in Fig. 6.2. The detection of GRBs is based on the temporal analysis of parameters called Key Performance Indicators (KPIs): these indicators are expected to change their behavior during a GRB relatively to a nominal situation. These KPIs are extracted for a given timescale (grey box in Fig. 6.2) from the properties of the raw events (generated from simulations in this analysis but received from X-band telemetry one *SVOM* launched). They can be, for example, the mean energy of the events received within a timescale of 10 seconds or the number of photons on a given energy range received in this same timescale (see Sec. 6.4 for a complete description of the KPIs used in this analysis).

Several (one per KPI) Donut Models (DMs) are trained with the KPIs extracted from dozens of background orbits to detect a change relatively to a nominal situation. The training phase of a DM consists in adjusting the DM parameter to minimize the reconstruction error of the VAE (the input and output of the VAE should be as close as possible) so that the DM becomes sensitive to an anomalous behavior of the corresponding KPI (for which the DM has been trained).

The DM has an implementation that consider the data's time correlation. Indeed, to evaluate the anomalous behavior at the epoch t_{i} from the KPI x_{i}, the algorithm takes into account the KPI previous values $[x_{\mathrm{i-1}}...x_{\mathrm{i-N}_\tau}]$ at epochs $[t_{\mathrm{i-1}}...t_{\mathrm{i-N}_\tau}]$, with N_τ a parameter that can be adjusted to improve the algorithm performances (see Sec. 6.7). Thanks to this implementation, the DMs handle well the seasonality of the KPIs created by the Earth transiting inside the Field of View (FoV, see Section 6.3 for more information).

Once the DMs are trained, we can apply them on orbits for which we want to investigate the presence of a GRB. The test orbits have been generated in this analysis by superimposing simulations of GRBs on top of background orbits (blue box `ecl_data_simulator` of Fig 6.2). In the future, these orbits will directly be recovered from the raw events sent by ECLAIRs to the ground via X-band telemetry. The test KPIs are extracted from these test

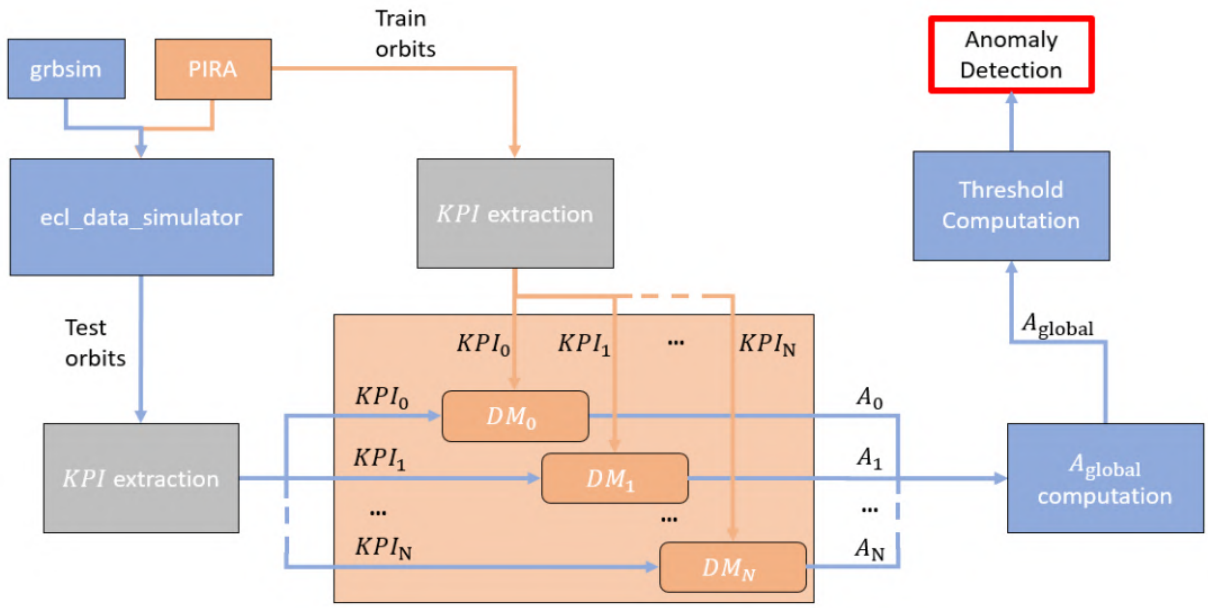

FIGURE 6.2. Architecture of the anomaly detection algorithm created. Blue arrows represent the path of test samples, while orange ones represent the path of training samples. DM_j is the Donut Model trained with the training sample KPI_j so that when the model evaluates the test sample KPI_j, it gives the anomaly score A_j.

orbits using the same method as for the training KPIs. Using the trained DMs on the test KPIs, we obtain an individual anomaly score $A_j(t_i)$ at each epoch t_i for a given $\mathrm{KPI}_j(t_i)$.

This anomaly score is the reconstruction probability of the data at the epoch t_i. It is computed through Monte Carlo integration by taking n samples from the latent space z, propagating them through the decoder part of the DM, and comparing them with the input x. The logarithm of the comparison result is taken, and the mean of these n obtained probabilities defined as the reconstruction probability. The details for calculating this reconstruction probability can be found in Xu et al. (2018). The reconstruction probability is a value between $-\infty$ and 0: the larger the reconstruction probability is for a given epoch t_i, the less likely the KPI point x_i at the same epoch t_i is anomalous. In this study, we will use the opposite of the reconstruction probability vector as the anomaly score since it is closer to intuition: the higher the anomaly score, the more anomalous the data. The individual anomaly score for a given KPI is a vector with the same length as the input KPI vector, giving values between 0 and $+\infty$ that indicate whether the KPI at epochs t_i is anomalous or not.

Donut is a uni-variate NN, meaning that each DM is trained by only one KPI, and able to generate an anomaly score on this KPI only. For each KPI_j used in this analysis, a DM has been trained and used to generate individual anomaly scores A_j. These individual anomaly scores are then combined to get a global anomaly score (see Sec. 6.5). The combination of individual anomaly scores is expected to increase the significance of the excess due to the presence of a GRB: during the GRB emission, all the individual anomaly scores are

expected to increase while they are more or less independent during the remaining of the orbits. On the global anomaly score is applied a threshold-based decision to determine whether the test sample contains an anomaly or not: if the global anomaly score exceeds the defined threshold, an anomaly is detected.

6.3 Simulation of training and test orbit samples

This section describes the methodology used to simulate the training and test orbit samples. This methodology is based on the simulation tools presented in Chapter 5.

6.3.1 Training orbits creation

As explained in Sec. 6.2, the KPIs extracted from the training orbits are used to train the DMs. These KPIs will be used as references for the DMs to grasp the KPIs behavior during a nominal orbit of ECLAIRs. For this reason, the training orbits must be as representative as possible of the flight environment to correctly asses the performances of the ML trigger.

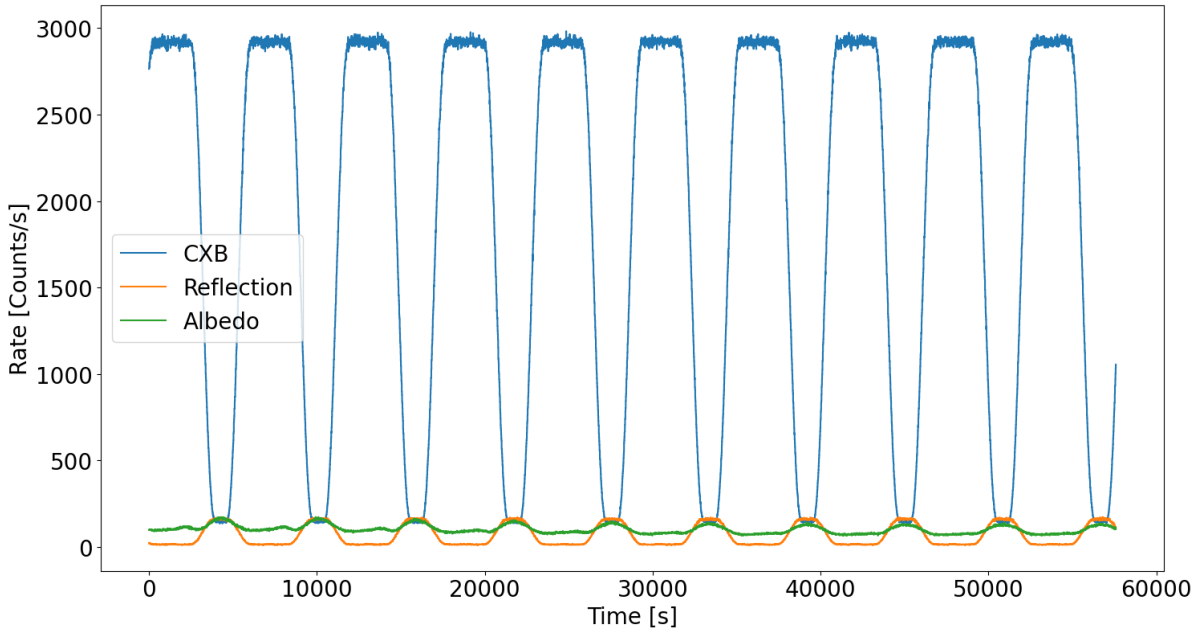

Figure 6.3. Lightcurve with a timescale of 10 seconds in the energy range $4 - 120$ keV of 10 background orbits used for the training sample.

The background events used to compute the training orbits are simulated using PIRA (Mate et al., 2019), a software that relies on a pre-computed database of particle-instrument interactions (see Sec. 5.2). This database is created with Monte-Carlo simulations using the GEANT4 toolkit (Allison et al., 2016) to estimate the dynamical evolution of the background along the orbit. Three components are mostly responsible for the background counts: they are dominated by the cosmic X-ray background CXB (Churazov et al., 2007; Ajello et al., 2008), with additional components from the CXB reflection on the Earth atmosphere

(Churazov et al., 2007) and from the interaction of cosmic rays with the Earth's atmosphere, called albedo (Sazonov et al., 2007; Ajello et al., 2008). The attitude information along the orbit are based on computed orbits generated by CNES, following the B1 attitude pointing law of the *SVOM* mission.

Approximately ~ 100 orbits have been used to train the Donut model, representing $570,000$ sec of simulation or ~ 6.5 days. An example of 10 of these orbits is shown in Fig. 6.3, where we can see the variability of the counts received depending on the Earth's position inside the ECLAIRs FoV (see Sec. 5.2 for more details on this variability).

6.3.2 Test orbits creation

The test sample consists of GRB-generated events superimposed on background events coming from an anomaly-free orbit similar those used in the training sample, which has been similarly used in Arcier et al. (2020) or Dagoneau et al. (2020). The first step of the simulation consists in drawing a list of photons in the ECLAIRs energy range with a tool called *grb-simulator* (see Sec. 5.3) from high-energy transients lightcurves and spectral properties. With this list, the related events can be generated on the ECLAIRs detection plane thanks to a ray-tracing algorithm, taking into account the ECLAIRs instrument response (Sec. 5.4). The events are then superimposed onto a simulated background orbit. The simulated high-energy transients can be placed at any location within the ECLAIRs FoV and happen at random epochs during *SVOM* orbit.

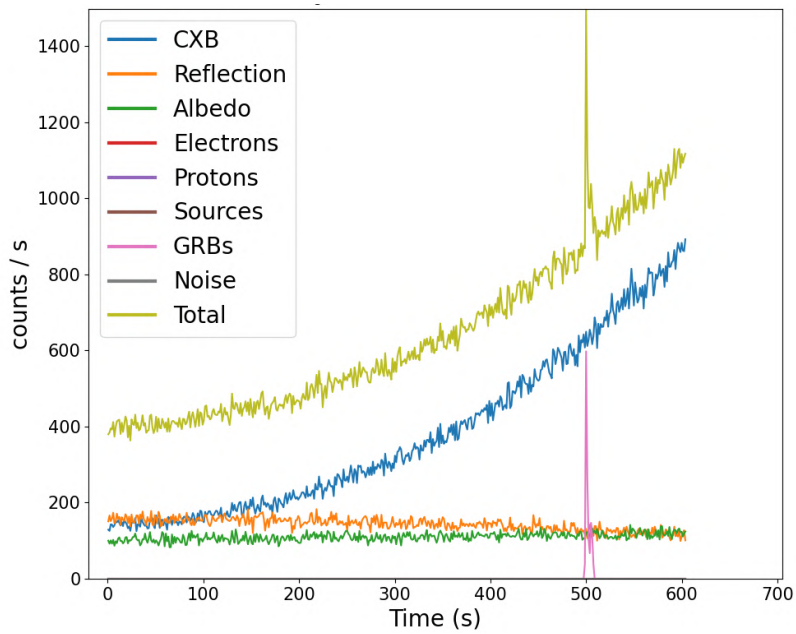

FIGURE 6.4. Lightcurve of an orbit portion used as a test sample, with GRB 191011A superposed. The individual contributions from the background components and the GRB can be seen. The total count represents the sample used during the KPI extraction.

The test orbits have been generated using 676 GRBs from the *Swift*/BAT catalog, using the lightcurves and spectral properties extracted from the BAT catalog (Lien et al., 2016). An example of a test orbit with the individual contributions from the GRB and background can be found in Fig. 6.4.

6.4 Key Performance Indicators

Depending on the origin of the events (GRB, CXB, ...), the distributions of their position (XY), energy (E), and time of arrival (T) are different. For the background, the energy and time distributions of the events change with time, depending on the position of the satellite along the orbit: the background is entirely dominated by the soft spectrum of the CXB when the Earth is outside the FoV, while the Albedo and Reflection contributions are more significant when the Earth enters the FoV. The time of arrival of the events is also much tighter when the Earth is outside the FoV (the count rate is higher). Finally, the positions of such events on the detection plane do not follow the coded mask pattern.

However, events generated by a GRB will be located on positions XY that are distributed according to the projection of the mask pattern on the detection plane. Their energy distribution will follow the GRB spectrum, while the events' arrival will be related to the flux of the burst at a given epoch.

To detect these changes in the parameters distributions, KPIs are extracted from the training and test orbits generated before in Sec. 6.3. These KPIs are extracted at different timescales, ranging for example from $dt = 0.1$ s to $dt = 10$ s. With a timescale of 10 s, a 800 s orbit will be divided into 80 time intervals $\Delta t_\mathrm{i} = [T_\mathrm{i}, T_\mathrm{i} + dt]$ for $\mathrm{i} \in \{0, 79\}$. For each time interval Δt_i, a sub-sample of events whose arrival time is within $[T_\mathrm{i},\ T_{\mathrm{i}+1}]$ is selected. From the properties of the events inside these sub-samples, different KPIs can be extracted. For each timescale dt, sub-samples shifted by half the timescale are also created. In the example before, the additional time intervals considered for these subsamples would be $\Delta t_{\mathrm{i,SHIFT}} = [T_\mathrm{i} + dt/2,\ T_\mathrm{i} + 3dt/2]$ for $\mathrm{i} \in \{0, 79\}$.

The on-board count trigger algorithm also works partly on KPIs, which are integral counts in a given energy range and time interval. By monitoring the evolution of these KPIs along the orbit (using a background estimation thanks to a quadratic fit), it detects their sudden changes due to a GRB, which triggers the remaining of the algorithm (see Sec. 3.5 for more details about the algorithm). The KPIs on which the first phase of the algorithm is based are relatively simple: their choice is mainly driven by the need for a robust algorithm that does not require much processing power.

Therefore, sending all the raw events on the ground offers new possibilities for improving the detection performances of the trigger algorithms. Even if a method similar to the on-board algorithm is used on the ground, the energy bands used to build the lightcurves can be changed to be different and/or more numerous than the ones defined for the on-board trigger algorithms. Having the raw events and their time of arrival, energy and position also allow us to combine them the way we want. For example, to create a shadowgram for any time and/or energy interval desired and to deconvolve it to get the corresponding sky image. This systematic deconvolution is not available on-board, as it requires too much

computing resources: the possibility to perform it for any energy range and time interval is unique to the reception of the raw events. It is also possible to study more in detail the properties of the raw events by analyzing the distribution of the difference in arrival time between one event and the next. The reception of the raw events offers the possibility of constructing more elaborated KPIs than those usually used by the on-board detection algorithms. These KPIs might also be more sensitive to GRBs: using them might improve the detection efficiency of the ML trigger.

KPIs represent a crucial aspect of the ML trigger: they should correctly describe the standard background of the orbit while being sensitive enough to detect a large variety of GRBs. Having multiple independent KPIs might improve the algorithm's sensitivity to some GRBs. However, a higher number of KPIs implies longer KPIs extraction time and training times. Moreover, irrelevant KPIs add noise to the computation of the global anomaly score. It is therefore essential to carefully select the KPIs used in the ML trigger.

In order to find the most relevant KPIs, we have decided to compare their behavior in the presence/absence of a GRB and select only the most relevant (mainly one for each parameter E, T, and XY). We have extracted different KPIs from test orbits for each of these parameters, with and without a GRB. The best KPI for a given parameter has been defined as a KPI that maximizes the ratio between the maximum anomaly score obtained during GRB orbits divided by the standard deviation (obtained from all the anomaly score at each epoch of the orbit) of the same orbits without GRBs. The evolution of these KPIs along a test orbit is shown in Fig. 6.5, the light blue curve being the KPIs with the presence of a GRB and the dark blue curve without the GRB.

6.4.1 Energy KPI: E_{mean}

Because of the GRBs diverse spectra, some energy KPIs can be relevant for some GRBs and irrelevant for others. For example, if a hard GRB explodes while the background is CXB-dominated, GRB photons harder than the CXB ones will be received by the instrument, so the mean energy of the sub-sample will tend to increase compared to a normal situation. Similarly, a soft GRB exploding while the Earth transits in the FoV will decrease the mean energy. However, a GRB with a spectrum similar to the CXB exploding in a CXB-dominated background will not change the KPI value, as the energy will not noticeably be changed.

One energy KPI has been chosen to account for these characteristics, which is the mean energy of the events included in a given sub-sample. Other KPIs based on the quartiles of the energy were giving better results in some cases but not in the majority of tested GRBs. Some tests have also been done using the lowest and highest quartiles, but the results were not as good as using simply the mean energy.

6.4.2 Position KPI: XY_{maxSNR}

The pattern created (for a given time interval and energy range) by the shadow cast from a source or the background on the detection plane is called a shadowgram, which is an 80×80 array. The isotropic background creates a shadowgram that can be fitted with a quadratic

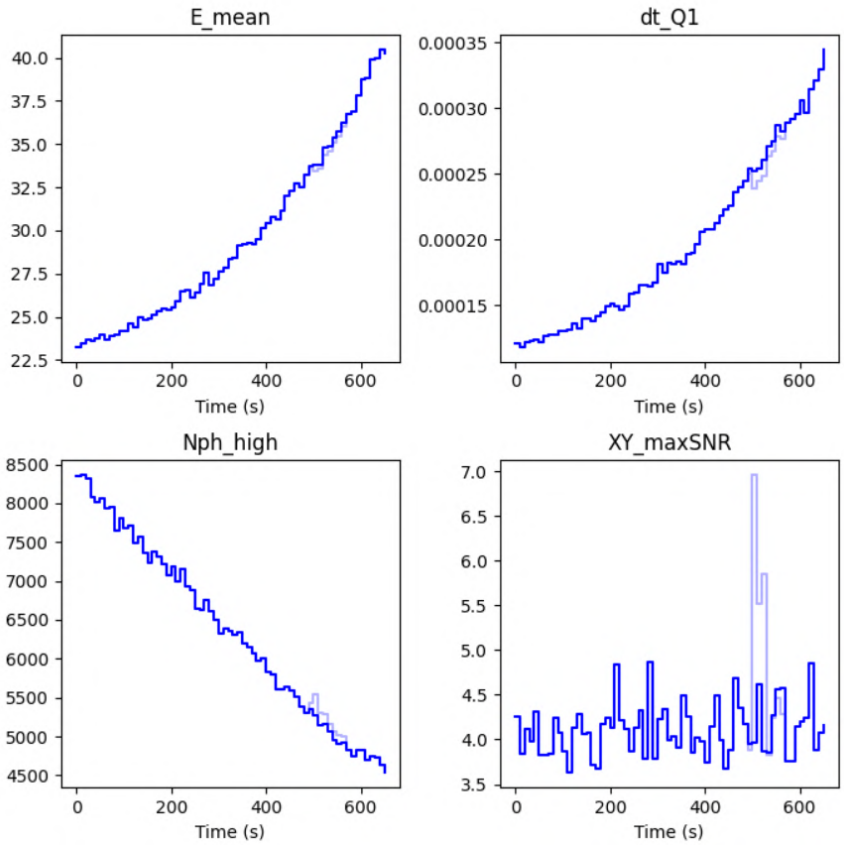

Figure 6.5. KPIs extracted for a 10 s timescale for two test samples. The dark blue curve represents the KPIs evolution of the orbit without the GRB, while the light blue curve is the same orbit but with a GRB. The y-axis labels are: (upper left) E_{mean} [keV], (upper right) dt_{Q1} [s], (lower left) N_{high} [Counts], (lower right) XY_{maxSNR} [SNR].

function or wavelets (Dagoneau et al., 2020), while the shadowgram created by an X-ray source or a GRB encompasses the projection of the coded mask pattern on the detection plane. For example, Fig. 6.6(a) shows a shadowgram for a time interval of 10 seconds for a case of rising Earth, while Fig. 6.6(b) shows another shadowgram for the time interval with a GRB bursting inside the FoV. The pattern of the coded mask can be seen in the latter case. Remember that the GRB is extremely powerful and has been put as an example here.

By making a deconvolution from a cleaned shadowgram (from which the quadratic pattern created by the background has been removed), it is possible to reconstruct a sky image (see Sec. 3.5). This 199×199 image displays the SNR of a source located at a given sky location, based on the counts received on the detection plane. Fig. 6.6(c) and Fig. 6.6(d) show the sky images obtained without and with a GRB inside the instrument FoV: a source is visible in the latter case, while the image is more or less uniform in the former one.

Several KPIs can be extracted from a shadowgram and the reconstructed sky image. The first idea was to use the variance of the shadowgram: during a GRB explosion, some pixels

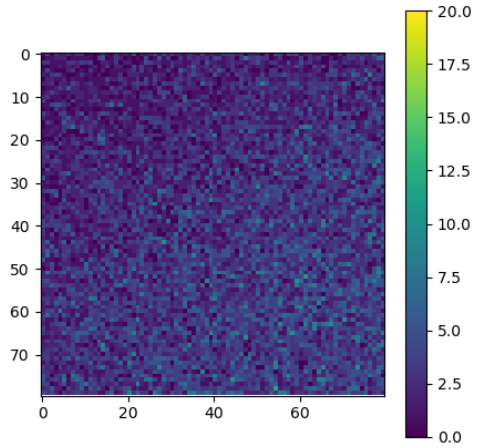

(a) Shadowgram with Earth rising in the FoV

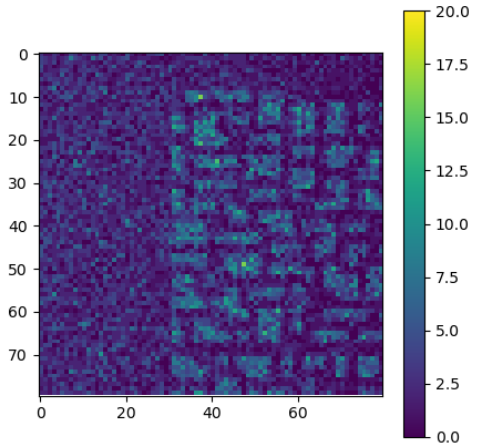

(b) Shadowgram with GRB 031203 in the partially coded part of the FoV.

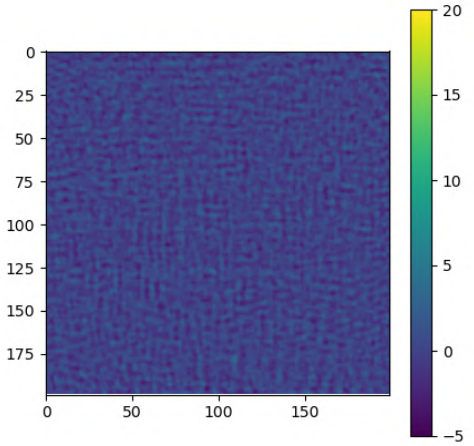

(c) Sky SNR map from a shadowgram without any source

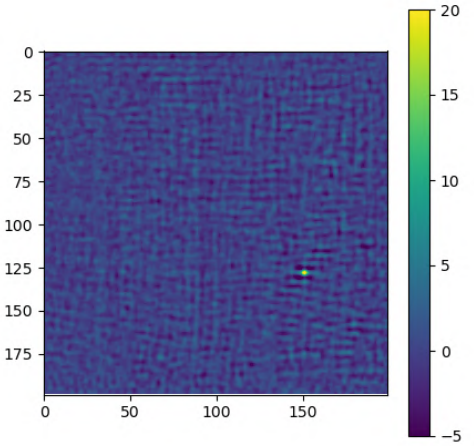

(d) Sky SNR map from a shadowgram with GRB 031203 in the partially coded part of the FoV.

FIGURE 6.6. Shadowgrams and associated sky SNR maps for two situations. Panel (a) shows a more or less homogeneous shadowgram with no source inside the FoV. Panel (c) shows the corresponding sky image. Panel (b) shows the impact of adding a bright GRB, and panel (d) shows the corresponding sky image.

will be more illuminated than others because of the coded mask pattern, which results in an increase in the variance. However, this KPI is not sensitive enough to help detecting faint

GRBs. A similar result is obtained with the variance of the sky image. The maximum of the sky image SNR is the KPI which is the most sensitive to the presence of a GRB. However, this KPI also is more sensitive to noise than the others. Nonetheless, as the purpose of this ML trigger is first to detect the dim GRBs other algorithms might miss, this KPI XY_{maxSNR} has been chosen.

6.4.3 Time KPIs: dt_{Q1}, N_{high}, N_{low}

The last KPIs account for the time information associated with an event. Two types of KPIs have been created using this information: the integral KPIs (N_{high} and N_{low}) and the differential KPI (dt_{Q1}).

The KPIs N_{high} and N_{low} represent the number of events recorded in low- and high-energy bands. When a GRB bursts inside the FoV of ECLAIRs, we expect an increase of photons coming towards the instruments, which means an increase in these two KPIs. Two bands have been chosen in a strategy similar to most trigger algorithms used for GRB detection. As explained for the energy KPI E_{mean}, GRBs have various spectral properties: having KPIs in specific energy bands might help to increase the variations due to the GRBs' presence. The energy range of these bands might be re-defined after the mission launch to accommodate the differences between simulations and in-flight behavior. In this analysis, they have been chosen so that, in a CXB-dominated situation, the number of events in each band is approximately similar. The energy bands are $[5-15]$ keV and $[15-120]$ keV.

The KPI dt_{Q1} is based on the distribution of the differential time of arrival between an event and the next (considering all the events in the energy range $[5-120]$ keV this time). The sudden increase of counts due to a GRB reduces the time interval between the arrival of two events: the distribution of the differential time of arrival will be shifted towards the lower time differences. By taking the first of the 5 quantiles of this distribution, the KPI dt_{Q1} aims at detecting this shift and thus the presence of the GRB. The number of quantiles used has been found through several trials, where 5 quantiles were the optimal value for this KPI.

6.5 GRB detection from individual anomaly scores

As it has been explained in Sec. 6.2, Donut is an uni-variate algorithm. For each of the KPIs defined in Sec. 6.4 (E_{mean}, XY_{maxSNR}, dt_{Q1}, N_{high}, N_{low}), an individual anomaly score A_{j} with $\mathrm{j} \in \{0, ..., n_{KPI}-1\}$ has been computed by a trained Donut VAE. Combining these individual anomaly scores together (see next sub-section) makes it possible to compute a global anomaly score. Furthermore, by applying a threshold to this global anomaly score, it is possible to determine whether the anomalous data in the test sample are detected or not.

6.5.1 Computation of the global Anomaly Score

The individual anomaly scores obtained with the DMs' output do not follow the same statistic. To combine these individual anomaly scores, we first remove their continuous

part. This is performed thanks to a sliding window technique: within a given time interval consisting of K data points $[t_{\mathrm{i}}, t_{\mathrm{i+K}}]$, the mean of the individual anomaly score has been taken and removed from the global anomaly score:

$$\tilde{A}_{\mathrm{j}}(t_{\mathrm{i}}) = A_{\mathrm{j}}(t_{\mathrm{i}}) - \frac{1}{K}\sum_{\mathrm{k=0}}^{\mathrm{K}} A_{\mathrm{j}}(t_{\mathrm{i+k}}) \tag{6.1}$$

Here the sliding window size K has been chosen to be equal to 10 for the timescale of 10 seconds and 100 for the timescale of 1 second. This choice was a trade-off between a sliding window size narrow enough to be adapted to the dynamic evolution of the anomaly score (following the dynamic of the KPIs along the orbit) and a large enough to correctly remove the statistical fluctuations of the anomaly score, and was the one giving the best results.

Once the continuous part is removed, we normalize these anomaly scores so that their distributions have the same standard deviation. To do so, we have computed the individual anomaly scores with trained DMs for orbits that do not contain any GRB. We have calculated the standard deviation for the normalization from the individual anomaly scores distributions obtained for each KPI.

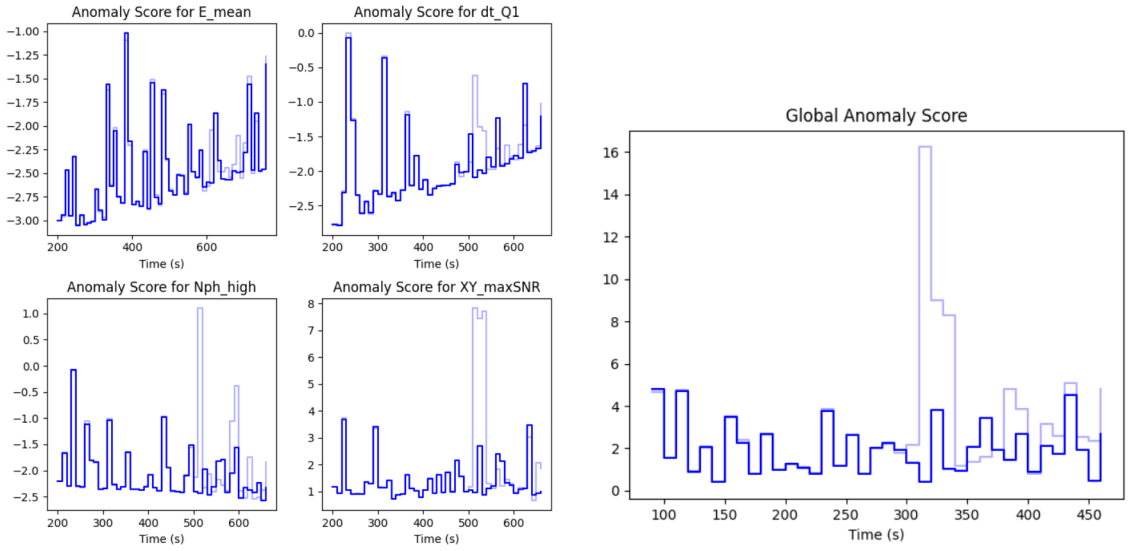

(a) (b)

FIGURE 6.7. Example of anomaly score evolution over time for a faint GRB ($SNR \sim 6.5$). (a) Shows the evolution of the individual anomaly scores, while (b) shows the evolution of the global anomaly score.

From the normalized individual anomaly scores of the KPIs, it is possible to compute the global anomaly score as:

$$A_{\mathrm{global}} = \sum_{\mathrm{j=0}}^{\mathrm{n_{KPI}}-1} \eta_{\mathrm{j}} \tilde{A}_{\mathrm{j}} \tag{6.2}$$

In the frame of this work, the parameters η_j have all been set to 1. However, after the behavior of *SVOM*/ECLAIRs in space will be better characterized, it could be possible to tune these parameters to optimize the detection performances by giving more weight to some KPIs.

The main interest in combining the individual anomaly score is to use the temporal correlation between them. For example, Fig. 6.5.1 shows how the significance of the excess created by the GRB on the anomaly score (light blue curve) is low for the individual KPIs. However, by combining these individual anomaly scores, this excess becomes more significant as it happens at the same epoch.

6.5.2 Threshold calculation

The calculation of the threshold applied to the global anomaly score is a trade-off between a high sensitivity and a low False Alert (FA) rate. The context of the offline trigger is different from the on-board trigger: an alert from the *SVOM*/ECLAIRs on-board algorithm can trigger a slew request, which has critical consequences on the observing program of the satellite. For this reason, the on-board FA rate should be as low as possible. On the other hand, the ML trigger will work in the context of the offline trigger: this algorithm will issue some alerts, which can then be re-treated to decide whether the alert is positive or negative. Therefore, while the FA rate should remain reasonably low, the offline trigger can accept a more significant FA rate.

The threshold calculation presented here uses 100 background test orbits [5] generated with the methods presented in Sec. 6.3 and calculates the global anomaly score obtained with the trained DM on these orbits. A global anomaly score threshold can be derived from the distribution of global anomaly scores obtained during the orbit. Taking a value of FA per orbit (e.g., $\mathrm{FA}_{\mathrm{orbit}} = 1$), the threshold can be adjusted so that the number of epochs with an anomaly score above this threshold is below $\mathrm{FA}_{\mathrm{orbit}}$. This threshold depends on the configuration of the NN used (parameters values, KPIs used) and the recombination process of the individual anomaly scores to obtain the global anomaly score. This threshold will have to be recalculated for each new set of KPIs, recombination method and hyper-parameters of the DMs.

Figure 6.8 shows a histogram of the global anomaly score for the 100 training orbits, the black line representing the threshold chosen: the cumulative counts of the bins at the right end of this threshold is equal to 100, corresponding to 100 FA for the 100 orbits used, or $\mathrm{FA}_{\mathrm{orbit}} = 1$. As expected, this number directly impacts on the number of detected GRBs, which is represented by the orange curve and discussed more in detail in the following Sec. 6.6.

[5] It is highly advised in the ML field not to use the training sample for the exploitation of the results to limit the effects of the NN oversampling. While this effect might be limited for the ML trigger, we have used different background orbits anyway so that we do not have to consider this issue.

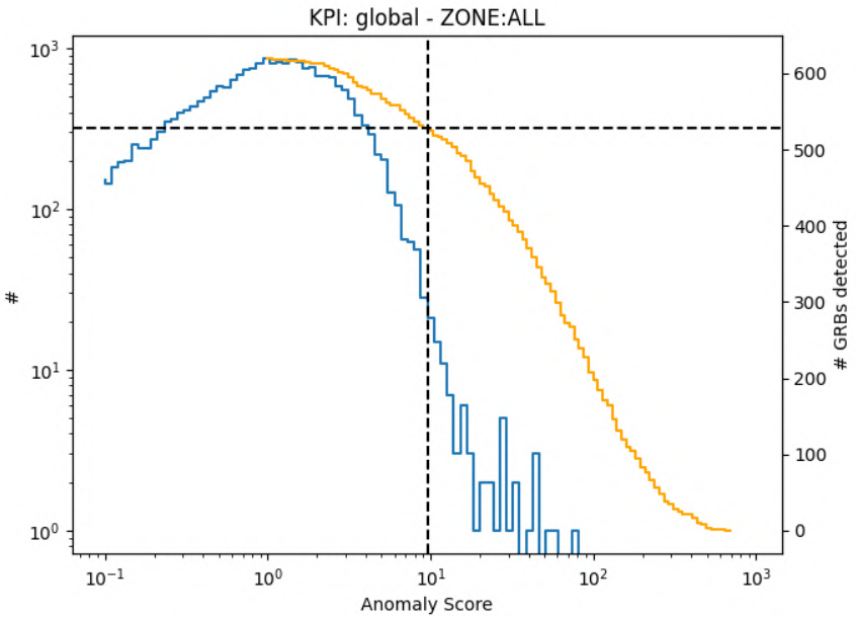

FIGURE 6.8. Histogram of the 100 background orbit global anomaly score. The black dashed line represents the threshold for the anomaly score so that the FA rate remains below one per orbit. The orange curve represents the number of GRBs from the test sample detected for a given threshold.

6.6 Results

Here, we compare the ML trigger with the on-board count trigger algorithm from ECLAIRs. The implementation of the on-board algorithm has been made by CEA and put in a docker container to use the same algorithm as the on-board. The ML trigger algorithm and the on-board count trigger algorithm have been run on the same test sample. On the 676 GRBs from the *Swift*/BAT sample created (see Sec. 6.3), the on-board count trigger successfully detected 573 of them.

For the ML trigger, the number of detected GRBs depends on the threshold of the global anomaly score considered. The orange curve from Fig. 6.8 shows the number of GRBs detected for a given timescale (here 10 seconds) depending on the value of the global anomaly score threshold. For a given global anomaly score threshold of the orange curve, the corresponding number of GRBs detected is obtained as follows:

(1) For each GRB of the 676 GRBs from the test sample, the individual anomaly scores are obtained with the trained DMs.
(2) The individual anomaly scores are combined with the method presented in Sec. 6.5, and the maximum global anomaly score obtained during the test sample is kept.
(3) We compare this maximum to the threshold value: if this maximum is above the threshold, then the associated GRB is considered as detected. The same comparison is applied to the 676 GRBs.

By doing it for different global anomaly score thresholds, the orange curve is built. For example, a threshold value of 100 (illustrated by the black dashed line) allows the detection of $\sim 520/676$ GRBs from the *Swift*/BAT sample. As expected, the higher the threshold, the less the number of GRBs detected: a value of 10 ($\sim$ one FA per day) allows the detection of $\sim 430/676$ GRBs for the 10 seconds timescale.

Figure 6.8 shows that the maximum value of the orange curve is equal to ~ 625 instead of the 676 expected. The ~ 50 missing GRBs are lost during the computation of the maximum global anomaly score for a given orbit: if the maximum of a given test sample happens at an epoch where there are no GRB photons, then this maximum is set to 0 and the GRB considered as undetectable. This strategy was to prevent our test sample from generating FA, which would have made the performance assessment more difficult.

It is interesting to combine the results of different ML trigger algorithms working at different timescales to get an algorithm as sensitive as possible. Here the combination has been made for timescales of 1 and 10 seconds, but we could imagine combining even more timescales, such as intermediate ones (2, 5 seconds, for example) and more extreme ones (0.1 or 100 seconds for example). The combination of the ML trigger at different timescales is simple: if one of the two algorithms has detected a GRB, then we consider that the combination has detected a GRB.

The ML trigger algorithm detected 645 GRBs for a FA rate of 1 per orbit, combining the timescales of 1 and 10 seconds. Although it seems that the ML trigger algorithm outperforms the on-board algorithm, one has to keep in mind that the on-board algorithm has thresholds set so that the FA rate is one per day, while the FA rate used in our analysis is one per orbit.

Nevertheless, the VAE architecture might end up being more sensitive than the count trigger algorithm for several reasons:

(1) it accounts for the temporal dependence of the data, being not only sensitive to the values but also the structural aspect of the KPI evolution.
(2) a sky image is created at each time interval (every 1 or 10 second), while the image creation is triggered on special conditions for the on-board count trigger and made only on large timescales (> 20.48 sec) for the on-board image trigger. The KPI XY_{maxSNR} is most likely the most sensitive KPI employed in the ML trigger method presented in this chapter.
(3) Figure 6.7 shows how the individual anomaly scores correlate in time with the GRB trigger and how the detection significance increases when combined. Using more independent (see Sec. 6.7 after) might increase even more the detection performances.

The test sample that has been used has allowed us to obtain our first results for this algorithm. It could be interesting to test this algorithm on a sample consisting only of faint GRBs that are all hard to detect: the results and the sensitivity differences of different algorithms would be more visible. Creating a representative sample that could be used as a reference for assessing the performances of different algorithms is in progress at IRAP, using the `eclgrm-simulations` package presented before.

6.7 Discussion

While some results have already been provided in Sec. 6.6, this work is still in progress. Many things need to be investigated more in detail to improve the algorithm. Moreover, the algorithm has to be implemented in the offline trigger context, which is more complex than the simple context in which we have performed this analysis.

6.7.1 Perspectives for the algorithm

While the algorithm presented in this chapter already shows acceptable performances, there are many ways this algorithm could be improved.

Hyper-parameters tuning

The Donut NN relies on several hyper-parameters, conditioning the structure of the VAE and the number of input parameters. Optimizing these parameters to the data structure increases the algorithm's performances, but it is not an easy process. Some rules of thumb apply, such having a number of trainable parameters in the VAE that are of the same order as the training samples. Xu et al. (2018) also describe in their paper that the dimension of the latent space (z_{dim}) shall remain low (typically between 2 and 5) depending on the complexity of the input data and that the hidden dense layer shall have a dimension $N_{\text{dense}} \sim 50$. Finally, the number of epochs to consider for the anomaly score calculation (the N_τ discussed in Sec. 6.2) should be high enough to apprehend the structure of the Time Series.

However, after applying these rules of thumb, the choice of a given hyper-parameters configuration can only be obtained by trying various configurations and measuring how well they perform. For example, parameters such as the number of epochs and the batch size for the training phase are difficult to adjust without a method based on trials. After some training and validation for several values of batch size and number of epochs, we have noticed that they do not play a key role in the optimization of the algorithm. The optimization has therefore been focused on N_{dense}, N_τ, and z_{dim}, with the resulting optimal values found being used to obtain the results presented in this chapter.

Nonetheless, it is essential to keep in mind that this optimization depends on the training data's statistical properties. While the background simulations rely on high-level tools, the observed background in space might be different; thus optimizing these hyper-parameters will most likely be needed after the launch to achieve optimal detection results.

Zone segmentation for the KPI calculation

The localization of a GRB in the ECLAIRs FoV impacts the zone of the detection plane illuminated: a GRB exploding in the upper left corner of the FoV will project photons on the lower right corner of the detection plane (see Fig. 6.6(b) and Fig. 6.6(d)). Therefore, we can wonder whether the KPIs used in the anomaly detection should be drawn from the whole pixels of the detection plane or if a strategy similar to the count trigger strategy (Schanne et al., 2019) should be applied.

In the latter case, KPIs such as $[E_{\mathrm{mean}}, dt_{\mathrm{Q1}}, N_{\mathrm{high}}, N_{\mathrm{low}}]$ could be calculated only from events within a zone of the detection plane. By taking only a portion of the detection plane illuminated by the GRB, the ratio between the events generated by the GRB and the ones generated by the background increases, perturbing more the KPIs and thus increasing the global anomaly score during the event. However, as the deconvolution process with the mask pattern requires to use of the whole detection plane, this segmentation would not apply for KPIs involving the sky SNR image, such as XY_{maxSNR}.

This strategy of zone segmentation could potentially increase the sensitivity of the ML trigger for off-axis GRBs.

More elaborated KPIs as input for the algorithm

The method presented here can be applied to any KPIs, as long as they are temporal series. The KPIs for which we have presented the method are rather simple, but the ML trigger could also use more elaborated ones. For example, the Haar wavelet approach has been investigated by a former Ph.D. student S. Mate (Mate, 2021) and by a current Ph.D. student M. Llamas-lanza. Using the wavelet parameters as KPIs might represent a potential gain of sensitivity for the ML trigger. New DMs would be trained with these KPIs, and the resulting individual anomaly scores could then be used to calculate the global anomaly score.

Another idea would be to use data from the other wide field instrument of *SVOM*, GRM. As for ECLAIRs, all the raw events recorded by GRM will be sent to the ground and be available at the FSC. Using the GRM raw events would allow to extract independent KPIs, train other DMs and combine the resulting individual anomaly scores with anomaly scores coming from ECLAIRs KPIs. And as explained in Sec. 6.5, combining independent individual anomaly scores tends to increase the detection sensitivity of the ML trigger.

Forward and backward search

The method that has been presented uses a forward search on the data: the anomaly score $A_{\mathrm{j}}(t_{\mathrm{i}})$ is computed from the previous epochs $[t_{\mathrm{i-1}}, ..., t_{\mathrm{i-N}_\tau}]$. By inverting the training and test vectors, it is also possible to apply the same method but this time computing $A_{\mathrm{j}}(t_{\mathrm{i}})$ from the epochs $[t_{\mathrm{i+1}}, ..., t_{\mathrm{i+N}_\tau}]$. The anomaly scores from the two methods could then be combined to use both the forward and backward approaches. The combination of the two of them might increase the ML trigger's performances, the epochs with the possible GRB presence being the only correlated epochs in the forward and backward anomaly scores.

6.7.2 ML Trigger in the context of the global *SVOM*/ECLAIRs offline trigger

We aim to implement the ML trigger algorithm in the ECLAIRs offline trigger. However, several aspects need to be considered between the simulations-based approach presented in this chapter and the real implementation.

Training and Test time

The GRB science belongs to time-domain astronomy. For example, as explained in Chapter 1, the possibility of observing the afterglow only a few minutes after the detection of the prompt emission is crucial to learn more about GRBs. The characteristics of the *SVOM* orbit (anti-solar pointing, LEO orbit with 30° inclination) have been chosen so that a GRB detection can be almost immediately followed by the observations with ground-based observatories. In this context, the ML trigger must be able to detect the GRBs as soon as possible to transmit the information to the science community. Due to the localization of the X-band stations around Earth, the ECLAIRs raw events will be available every ~ 6 hours: the algorithm should therefore be able to process these 6 hours of data in maximum 6 hours to keep up with the data sent.

The computation time of the ML trigger depends mainly on the timescale considered. For instance, an orbit lasting about 6000 seconds will have only 600 points for a timescale of 10 seconds but $60,000$ for a timescale of 0.1 seconds, multiplying the computation time by a factor $\sim 100\times$. There are three steps in the ML trigger that are time consuming:

(1) The extraction of the KPIs for the raw events is a step that should be performed for both the training and test samples. The slowest part of this process is the deconvolution process of the images to get the XY_{maxSNR} KPI, but a highly optimized code with native parallelization on large multi-core CPUs has allowed to reduce the computation time significantly. Typically, extracting the KPIs from 15 orbits (~ 1 day worth of data) with a timescale of 1 s takes about 15 minutes, including the KPI extraction for the 5 zones of the detection plane (ALL, UP, DOWN, LEFT, RIGHT).
(2) The training phase takes a bit more time (typically one hour for this timescale) but should not be done every time the algorithm is used. In a nominal case, the training phase should only be done once a day or once a week.
(3) The test phase where individual anomaly scores are computed and then combined into the global anomaly score lasts for about 15 minutes for the 1 s timescale, for approximately 15 orbits.

In total, executing an already trained ML trigger on a new batch of 6 hours of ECLAIRs raw data should take about 8 minutes. These times have been recorded on a laptop with an 8 cores CPU i7-8750H at 4.1 Ghz, and a GPU RTX2070-MaxQ for the training and test phase, and a 40 cores CPU Intel Xeon at 2.2 Ghz for the KPIs extraction. Of course, a dedicated computer with equivalent or more powerful GPU/CPU will decrease these computation times. Note that the presence of the GPU is almost mandatory to accelerate the training and testing phase of the ML trigger: a factor $\times 100$ has been noticed between the training time of the laptop and the computer with 40 cores.

The achieved times are more than enough for the algorithm to work in real-time for timescales of 1 and 10 sec, as long as the computer configuration on which the ML trigger will be run is equal to or better than the laptop configuration used. However, adding more and/or more complex parameters might increase the computation time significantly. The same applies when adding more timescales for the KPIs extraction, such as 0.1 seconds. The training

and test time of the algorithm scales linearly with the number of KPIs and the inverse of the timescale.

Good Time Intervals and missing data

Because of maintenance, incoming particles or SAA crossing for example, there are some intervals during which ECLAIRs will record no data. The Good Time Intervals (GTIs) will be provided by the FSC, flagging epochs where the data are available and trustworthy. Therefore, the analysis must be performed considering these GTIs. The ML trigger architecture must therefore be robust to the absence of data. Moreover, that is one of the advantages of using Donut: it can fill the missing/anomalous data with data using novel methods that combine a modified Evidence Lower BOund (M-ELBO) for the training phase and Missing Data Injection (more details can be found in Xu et al. 2018). Thus, dealing with GTIs should not be a problem for the ML trigger.

The quiescent X-ray sources

The quiescent X-ray sources in the FoV can induce a sudden change on the KPIs that can be interpreted as an anomaly by the ML trigger. For example, the Crabe entering in the FoV will at least increase the anomaly score of the KPIs XY_{maxSNR} and N_{low}. Therfore, the ML trigger will probably flag this time interval as a possible GRB detection. To limit the FA rate, a post-treatment of the ML trigger alert will be necessary, with, for example, the creation of a sky image that allows locating the source potentially responsible for the alert. As for the count trigger, if this detected source is at the localization of a known quiescent source, the detection will be considered a false alert.

Pointing strategy

In the method presented here, 100 orbits have been used to train the DM. However, the pointing strategy of *SVOM* will never have such a long exposure in one direction. In practice, the pointing of the satellite will be changed every ~ 10 orbits. Therefore, the evolution of the KPIs will be slightly modified, as the Earth will not enter the FoV the same way. For this reason, it might be challenging to find enough consecutive orbits to train a DM properly. Moreover, depending on the importance of those evolution changes, the DM might need to be re-trained. The same applies to the observations during slews: as the DM has not been trained for slews, the anomaly score will increase even in the absence of an anomaly.

This limitation might restrain the use of some KPIs sensitive to the pointing of the satellite relative to Earth (e.g., the mean energy or the number of photons received). A dedicated analysis needs to be done with the simulated and flight data to see how a DM trained on a given pointing can be used to assess the anomaly scores from data from a different pointing. On the other hand, the DM is not as sensitive to the periodicity as some statistical models, such as ARMA (AutoRegressive Moving-Average) models, so the changes in pointing might not impact significantly the test performances of the model. Moreover, other KPIs such as the ones based on the sky image could still be used: once the shadowgram is cleaned and

the background is removed, the evolution of the sky SNR along the orbit is expected to remain constant, no matter the pointing of the instrument.

6.8 Conclusion

In this chapter, I have demonstrated the feasibility and the performances of the ML trigger for ideal cases created with the simulations presented in Chapter 5. I have shown in this Chapter the main advantages of such a method, but also its limitations. Nevertheless, the results obtained show that there is a certain interest in carrying on this type of study for the *SVOM*/ECLAIRs offline trigger. However, the choice of KPIs remains a crucial aspect, on which a dedicated analysis needs to be performed with the real data once available.

Chapter 7

Detection of short high-energy transients in the local universe with SVOM ECLAIRs

This Chapter presents an article written and published during the first year of my Ph.D. I have performed an extensive literature survey in Sec. 7.2 to characterize the properties of the 41 HE transients composing the sample. Using these properties, I have simulated in Sec. 7.4 these HE transients within the ECLAIRs FoV. This study has also been the opportunity to discuss the potential synergies of ECLAIRs with the other *SVOM* instruments and other observatories, as in Sec. 7.5.

Contents

Context

The local high-energy transients and their understanding are one of the main scientific goals of the *SVOM* mission (Wei et al., 2016). Therefore, it was crucial to release a paper that assesses the detection performances of the on-board algorithm on these phenomena and how the *SVOM* synergy could help shed some light on their mysteries.

The *SVOM*/ECLAIRs collaboration has created several tools (presented in Chap. 5) for the simulation of the instrument. PIRA (Mate et al., 2019) has been created by a former Ph.D. student S. Mate, and so does the `grbsimulator` (Antier-Farfar, 2016). However, these tools had never been brought together: the IAP has been working on a large database of simulated GRBs with the `grbsimulator`, but the background that was superposed was created through ray-tracing algorithms and was therefore not as representative as the one created by the algorithm from Mate et al. (2019). A paper from Dagoneau et al. (2020) on a sub-sample of LGRBs, called the ultra-long GRBs, was released a few months before and focused on the detection performances of the ECLAIRs image trigger. However, the background used was similar to the one used by IAP, and the focus was on a small sub-sample of the global population.

Therefore, my new article was the opportunity to link several existing works and gather them into an individual paper. It was also the opportunity to become familiar with the *SVOM*/ECLAIRs scientific team and the tools that have been created. Moreover, this work has also been the opportunity to become familiar with the high-energy transients detection field. The sub-sample of high-energy transients from the local Universe has been finely characterized using publications and GCNs. Not only this paper presents a characterization of ECLAIRs performances for this population, but it also provides a list of the high-energy transients observable in the local Universe. Finally, the paper has discussed the consequences of detecting such transients in the context of *SVOM*.

Contribution

For several months, my supervisor and I have selected the HE transients that fit into our local sample by discarding some with inconsistent properties (spectral information, uncertainties on redshift, ...) and retrieving some that were not correctly mentioned in the literature. The presented properties from this sample ($E_{\rm iso}$, ...) have been computed by myself, allowing me to generate the tables that can be found in the appendix. The simulations of the ECLAIRs instrument have been performed by myself, with guidance from former Ph.D. students working on the project, such as S. Mate, N. Dagonneau, and M. Bocquier. They have mainly been performed by multi-threading on a dedicated computer of ECLAIRs, called *flash*. My tutor and I started the article's discussion (especially the part about the giant flares in Virgo, the SN-less long GRBs, and the nature of XRFs), but the co-authors of the paper contributed to enriching it. They have also provided extremely interesting feedback for the global paper, allowing it to be accepted in the *Astrophysics and Space Science* journal in December 2020.

Detection of short high-energy transients in the local universe with SVOM ECLAIRs

B. Arcier[1], JL. Atteia[1], O. Godet[1], S. Mate[1], S. Guillot[1], N. Dagoneau[2], J. Rodriguez[2], D. Gotz[2], S. Schanne[2], M.G. Bernardini[3,4]

[1]Institut de Recherche en Astrophysique et Planétologie, Université de Toulouse, UPS/CNRS/CNES, 9 Avenue du Colonel Roche, BP44346, F-31028 Toulouse Cedex 4, France.
[2]Lab AIM, CEA/CNRS/Universite Paris-Saclay, Universite de Paris, F-91191 Gif-sur-Yvette, France
[3]INAF – Osservatorio Astronomico di Brera, via Bianchi 46, 23807 Merate (LC), Italy
[4]LUPM – Laboratoire Univers et Particules Montpellier, Place Eugene Bataillon, 34090 Montpellier, France

Corresponding author: Benjamin.Arcier@irap.omp.eu
Published in Astrophysics and Space Science in December 2020.
https://ui.adsabs.harvard.edu/abs/2020Ap%26SS.365..185A

Abstract

The coincidental detection of the gravitational wave event GW 170817 and the gamma-ray burst GRB 170817A marked the advent of multi-messenger astronomy and represented a milestone in the study of GRBs. Significant progress in this field is expected in the coming years with the increased sensitivity of gravitational waves detectors and the launch of new facilities for the high-energy survey of the sky. In this context, the launch of *SVOM* in mid-2022, with its two wide-field high-energy instruments ECLAIRs and GRM, will foster the possibilities of coincidental transient detection with gravitational waves and gamma-rays events. The purpose of this paper is to assess the ability of *SVOM*/ECLAIRs to detect and quickly characterize high-energy transients in the local Universe ($z \leq 0.3$), and to discuss the contribution of this instrument to multi-messenger astronomy and to gamma-ray burst (GRB) astrophysics in the 2020's. A list of local HE transients, along with their main characteristics, is constructed through an extensive literature survey. This list includes 41 transients: 24 long GRBs, 10 short GRBs and 7 SGR Giant Flares. The detectability of these transients with ECLAIRs is assessed with detailed simulations using tools developed for the *SVOM* mission, including a GEANT4 simulation of the energy response and a simulated trigger algorithm representative of the onboard trigger algorithm. *SVOM*/ECLAIRs would have been able to detect 88% of the short high-energy transients in our list: 22 out of 24 long GRBs, 8 out of 10 short GRBs and 6 out of 7 SGR Giant Flares. The SNR for almost all detections will be sufficiently high to allow the on-board ECLAIRs trigger algorithm to derive the localisation of the transient, transmitting it to the *SVOM* satellite and ground-based instruments. Coupled with

the anti-solar pointing strategy of *SVOM*, this will enable an optimal follow-up of the events, allowing the observation of their afterglows, supernovae/kilonovae counterparts, and host galaxies. We conclude the paper with a discussion of the unique contribution expected from *SVOM* and of the possibility of simultaneous GW detection for each type of transient in our sample.

7.1 Introduction

High-energy transients in the local universe are privileged targets for the *Space-based multi-band astronomical Variable Objects Monitor* (*SVOM*) especially in the nascent multi-messenger astrophysics context. The potential of this new field has been beautifully illustrated by the coincidental detection of GRB 170817A and GW 170817, which confirmed the link between short gamma-ray bursts and neutron star mergers (Abbott et al., 2017), and the subsequent detection of the kilonova AT 2017gfo (Tanvir et al., 2017), whose optical spectrum evidenced the production of r-process elements (Pian et al., 2017).

The launch of *SVOM* in mid-2022 will add new resources for multi-messenger astrophysics as described by Wei et al. (2016). We discuss here the performance of ECLAIRs, the hard X-ray imager of *SVOM* (Godet et al., 2014), for the detection and near real-time identification of various types of short high-energy transients in the local universe: short GRBs (SGRBs), long GRBs (LGRBs) and soft gamma-ray repeaters giant flares (SGR GFs), in the perspective of studying their multi-messenger emission. The motivation for this study is twofold: first, to verify the capability of ECLAIRs to detect these events and second, to check whether ECLAIRs data are sufficient to recognize the various types of events, especially their likelihood to be associated with transient Gravitational Wave (GW) signals. Being able to detect and quickly follow-up these events could shed some light on some important GRBs topics, such as the nature of long GRBs without a supernova (SN) (Gehrels et al., 2006; Yang et al., 2015), the rate of SGR GFs in our local Universe (Hurley, 2011a), the differences between short GRBs with and without extended emission (Barthelmy et al., 2005c; Jin et al., 2016) and the connection between X-Ray Flashes (XRFs) and classical long GRBs (Sakamoto et al., 2005; Sakamoto et al., 2008). Our study encompasses 41 short extra-galactic transients closer than $z = 0.3$, a volume chosen to contain a sufficient number of events of each type. While we have tried to compile the most complete list of high-energy transients in the local universe, we cannot guarantee that we have not missed some of them. This is, however, not a problem in the context of this paper, since we seek to get a representative sample of events to study their appearance and detectability by ECLAIRs, and not a complete sample.

The construction of the sample is discussed in Sect. 7.2. The ECLAIRs instrument is presented in Sect. 7.3, while its performance for the detection and classification of events in the local universe is discussed in Sect. 7.4. Section 7.5 places these results in their astrophysical context.

This work relies on a complete simulation package involving realistic response matrices, the detailed simulation of the instrument background (Mate et al., 2019), and a computation of high-energy transients Signal-to-Noise Ratio (SNR) taking into account the main features

of the on-board trigger algorithm. In all this paper, we use the cosmological parameters measured by the Planck collaboration: $H_0 = 67.4$ km s^{-1} Mpc^{-1} and $\Omega_m = 0.315$ (Planck Collaboration et al., 2018). The errors quoted in this paper are given at the 1σ confidence level.

7.2 The local GRB sample

7.2.1 Construction of the sample

The construction of our local GRB sample starts with the selection of 33 GRBs with a redshift smaller than $z = 0.3$ in the public GRB table made available by J. Greiner[1] (up to the end of 2019). The redshift $z = 0.3$ has been chosen so that the number of short GRBs included in the sample is approximately 10, giving a statistically meaningful sample of local events. We limited ourselves to GRBs with a secured redshift measured either on their host galaxy or with the GRB afterglow spectroscopy.[2] After a rapid survey of the literature, we have added GRB 040701 at $z = 0.2146$ (Kelson et al., 2004; Soderberg et al., 2005), reaching a sample with 34 GRBs. We note that this GRB sample is by no means exhaustive.

The sample has been divided into 24 long GRBs (LGRBs) and 10 short GRBs (SGRBs). The list of events in each class can be found in Tables 7.1 (for LGRBs) and 7.4 (for SGRBs). It is important to note that the short/long classification of GRBs is based on the literature, and not only on their duration and spectral hardness.

To this list we have added 3 GFs from SGRs located in our galaxy or the Large Magellanic Cloud, and 3 giant flare candidates located in nearby galaxies, all taken from Hurley (2011b), and another candidate GF 200415A that has been recently discovered (Svinkin et al., 2020). They are listed in Table 7.7 . Confirmed giant flares are associated with a magnetar detected before the giant flare (GF 790305, GF 980827, GF 041227), the other events are considered as candidate giant flares. Giant flares from soft gamma repeaters typically consist of a short hard pulse followed by an oscillating tail several orders of magnitude weaker (Mazets et al., 2005; Tanaka et al., 2007). In all cases, we consider only the properties of first short pulse here, as this is the only component that can be seen at distances greater than a few hundreds of kiloparsecs.

GRBs will be referred by GRB YYMMDD in the remaining of this paper, while giant flares will be designated with the same date-based denomination preceded by GF, irrespective of their classification as secure or candidate giant flares. For example, the giant flare from SGR 1806-20 will be designated as GF 041227. The correspondence between the SGR origin of the giant flares and the date-based denomination can be found in Table 7.9 .

Within these categories, some sub-categories have been created to emphasize specific characteristics for some of the bursts.

Some long GRBs such as GRB 100316D or GRB 060218 have their high-energy emission recorded for thousands of seconds and they have therefore been placed in the ultra-long

[1] http://www.mpe.mpg.de/~jcg/grbgen.html

[2] GRB 150424A, whose redshift is not secure (Tanvir et al., 2015), has been excluded

GRBs group (ulGRB) (Campana et al., 2006; Starling et al., 2011; Gendre et al., 2013; Levan et al., 2014; Sakamoto et al., 2015; Dagoneau et al., 2020). Some other GRBs are classified as XRFs because of their soft prompt emission, such as GRB 020903 (Sakamoto et al., 2005) and GRB 040701 (Barraud et al., 2004; Pélangeon et al., 2008). GRB 031203 is also sometimes referred to as an XRF (Watson et al., 2004). However, since its soft X-ray emission cannot be unambiguously associated with the prompt emission (Watson et al., 2006) and its peak energy measured with INTEGRAL is > 100 keV (Sazonov et al., 2004; Ulanov et al., 2005), we stay conservative and do not include it in our list of XRFs. GRB 060218 and GRB 100316D are also sometimes referred as XRFs (Soderberg et al., 2006b; Cano et al., 2011). However, we consider here that their main characteristic is their duration, and not the softness of their spectrum, and we class them in the ulGRB category. Finally, for some GRBs, the short/long paradigm based on the duration does not exactly apply, and they have been classified according to the consensus found in the literature:

- GRB 050709 displays a short hard spike followed by a softer extended emission, so that $T_{90} = 160$ s (Villasenor et al., 2005),[3] an unusually long duration for a short GRB. However, as the spectral properties of the first spike are typical of short GRBs, and since GRB 050709 was not associated with a surpernova (Fox et al., 2005), but with a possible kilonova (Jin et al., 2016), we classify it as a short GRB. In this paper, it will be considered as a representative member of the sub-category of "short GRBs with extended emission" (eeSGRB).
- GRB 050724 has also been assigned to the eeSGRBs sub-category, because of its extended emission. This is further justified by the fact that the fluence of the tail represents only 10% of the total burst fluence (Barthelmy et al., 2005c), explaining why the T_{90} remains equal to ≈ 3 s.
- GRB 060614 can be considered as a long-duration burst with $T_{90} \approx 109$ s and a first peak lasting ~ 5 s, but it has a temporal lag and peak flux close to those of short GRBs, in addition to the lack of associated supernova (Zhang et al., 2006). While a collapsar origin has been strongly questioned (Kann et al., 2011; Xu et al., 2009; Gal-Yam et al., 2006; Gehrels et al., 2006) and a kilonova has been tentatively detected (Yang et al., 2015; Jin et al., 2015), it will be considered as a long GRB in the rest of this paper: this classification does not change our analysis of the detectability of this object.While its origin remains uncertain , it will be considered as a long GRB in the rest of this paper.

Beyond the classification in duration, a clear demarcation in energy is visible in Fig. 7.1(a), where three low-energy GRBs are detected at distances that are typically ten times closer than the bulk of the "classical" population. With isotropic energies $E_{\rm iso}$ below 10^{48} erg, GRB 170817A (short), GRB 980425 (long) and GRB 111005A (long) are much fainter than the bulk of the long or short GRB population. Although the criterion is based on the energetic rather than luminosity of the bursts, they have been placed in a "low-luminosity" group (llSGRBs and llLGRBs) to remain consistent with the literature appellation. In summary, three groups of high-energy transients have been considered in the local Universe, which are the long GRBs, the short GRBs and the SGR giant flares. The long GRBs

[3]According to Lien et al. (2016), T_{90} refers to the duration of the burst over which 90% of its photon fluence has been emitted.

are divided into 4 sub-categories: 17 classical long GRBs (LGRBs), 3 ultra-long GRBs (ulGRBs), 2 X-Ray Flashes (XRFs) and 2 low-luminosity long GRBs (llLGRBS). Similarly, the short GRBs are divided into 3 categories: 7 classical short GRBs (SGRBs), 2 short GRBs with an extended emission (eeSGRBs) and 1 low-luminosity short GRBs (llSGRBs). This classification into long GRBs, short GRBs and giant flares will be used throughout the article.

7.2.2 A deeper look into the local sample

The main detected features of the 41 transients in our sample are summarized in Tables 7.1 , 7.4 and 7.7 (in appendices A, B, C), for the long GRBs, short GRBs and SGR giant flares respectively. For each event, the tables indicate the satellite(s) that have detected it, the event sub-category, the presence/absence of an afterglow or supernova and references for the host galaxy and the burst duration. Overall 30 of the 41 GRBs of our sample have been detected by *Swift*/BAT (Barthelmy et al., 2005d), 15 by *Wind*/KONUS (Aptekar et al., 1995), 8 by *Fermi*/GBM (Meegan et al., 2009b), 7 by *INTEGRAL* (Winkler et al., 2003), 4 by *HETE-2* (Atteia et al., 2003; Shirasaki et al., 2003), 3 by *CGRO*/BATSE, and 1 by either *BeppoSAX* (Boella et al., 1997b), *RHESSI* (Lin et al., 2002) or *MAXI* (Matsuoka et al., 2009).

The time scale for which the peak flux has been given depends on the category of transient: long GRBs have their peak flux measured over a 1s duration, whereas the peak flux of short GRBs and SGR giant flares is measured over a duration of 64ms. The rationale for this choice lies in the fact that the peak flux of short GRBs and SGR giant flares is underestimated by taking a one-second interval, their total duration being usually below one second.

For *Swift*/BAT, the peak flux was only available in the 1s timescale in the *Swift*/BAT catalog (Lien et al., 2016). Unless specified, the 64ms peak flux used in Table 7.5 has been calculated from the 64ms light curves, normalized to recover the 1s peak flux on the 1s timescale.

A dedicated column $P_{\mathrm{flux,norm}}$ has been created in Tables 7.2 , 7.5 and 7.8 , containing the peak flux information in the common 15–150 keV energy range, to compare the high-energy transients in Fig. 7.3. This peak flux is computed from the other peak flux column and the corresponding transient spectrum from Tables 7.2 , 7.5 and 7.8 .

GRB 050709, GRB 060614, GRB 180728A and
GRB 190829A exhibit a clear decomposition into two distinct parts, with distinct spectral models. The variability in their spectrum is so significant that fitting a spectral model for the total duration of the burst (time-integrated spectrum) gives poor results compared to a time-resolved fit. Thus, for these GRBs, the spectral properties of each of the two parts is given separately.

The peak energy E_{peak} presented in Tables 7.2 , 7.5 and 7.8 comes from the best spectral model of the time-integrated spectrum, which can be the Band function (Band et al., 1993), a cutoff power law (CPL, sometimes also called Comptonized model) or in the case of SGR

GF an optically-thin thermal bremsstrahlung (OTTB) model. Few particular cases need to be noted:

- For GRB 191019A, the *Swift*/BAT time-integrated spectral model extracted from the catalog has no peak energy $E_{\rm peak}$. However, the peak flux spectral model has one, this value of $E_{\rm peak}$ has been considerFed instead.
- The case is similar for GRB 150101B, the *Fermi*/GBM catalog does not contain any model with a peak energy. However, the work of Burns et al. (2018) indicates that the first 16 ms of the burst can be fitted by Comptonized spectral model with a peak energy $E_{\rm peak} = 550 \pm 190$ keV. Because the burst has a short duration ($T_{90} = 0.23$ s) and the tail only represents 10% of the global fluence (Burns et al., 2018), the peak flux spectrum and the time-integrated spectrum should be rather similar. The peak energy of the time-integrated spectrum of the burst has therefore been chosen to be $E_{\rm peak} = 550 \pm 190$ keV, equal to the peak energy of the peak flux spectrum.
- For GRB 031203, the spectral model used is a power law but the work of Sazonov et al. (2004) identifies a lower limit for the peak energy. The peak energy lower limit has been kept, even if the spectral model indicated in the table remains a power law.
- GRB 120422A, GRB 040701 and GRB 020903 only have upper limits on their peak energies. Their time-integrated spectral models remain power-laws, but the upper limit on $E_{\rm peak}$ is indicated in the spectral properties.

Tables 7.3 , 7.6 and 7.9 summarize the intrinsic properties of the local transients. The intrinsic peak energy $E_{\rm peak,i}$ is computed from the peak energy and the redshift, with the classical formula $E_{\rm peak,i} = E_{\rm peak} \times (1+z)$. The isotropic energy $E_{\rm iso}$ is directly taken from the literature. However, when the information was not available or when the assumptions taken in the paper implied the use of a different time-integrated spectral model than the one mentioned in Tables 7.2 , 7.5 and 7.8 , the isotropic energy has been calculated with the following equations.

$$E_{\rm iso} = S_{\rm bol} \times \frac{4\pi\ D_{\rm l}(z)^2}{1+z} \tag{7.1}$$

$$\text{with } S_{\rm bol} = S_{E_{\rm min}\rightarrow E_{\rm max}} \times \frac{\int_{\frac{1}{1+z}}^{\frac{10^4}{1+z}} E\ N(E)\ dE}{\int_{E_{min}}^{E_{max}} E\ N(E)\ dE} \tag{7.2}$$

Equ. 7.1 gives the isotropic energy that has been emitted by the transient in its reference frame, from an initial fluence $S_{E_{\rm min}\rightarrow E_{\rm max}}$ measured in the energy range $[E_{\rm min};\ E_{\rm max}]$, a spectral model N(E) and a redshift measurement z giving a luminosity distance $D_{\rm l}(z)$. In this equation, the term $S_{\rm bol}$ represents the fluence extrapolated to a common energy range from 1 keV to 10 MeV in the source frame. The term $1+z$ below each energy appears because the spectral model $N(E)$ is defined in the observer frame, so a redshift correction has to be taken into account for the energy released in the transient reference frame.

When there is no peak energy in the spectral model used for the calculation (power-law model), the isotropic energy calculated with this formula tends to overestimate the low- and/or high-energy contributions, these cases are discussed below.

- For GRB 031203, a power-law spectrum is given with a lower limit on the peak energy. To calculate the isotropic energy given in Table 7.3 , a CPL with $\alpha = -1.63$ and $E_{\rm peak} = 300$ keV has been used, giving $E_{\rm iso} = 1.4 \times 10^{50}$ erg. Assuming the same model but with $E_{\rm peak} = 200$ keV and 500 keV, the isotropic energy becomes $E_{\rm iso} = 1.3 \times 10^{50}$ erg and $E_{\rm iso} = 1.7 \times 10^{50}$ erg, respectively. Therefore the value of $E_{\rm peak}$ has little impact on the calculated isotropic energy.
- For transients with a power-law index $\Gamma > -1.6$, $E_{\rm iso}$ has not been calculated. Without any peak energy, a unique power-law with such an index will overestimate high- energy contributions, jeopardising the isotropic energy calculation. GRB 150518A ($\Gamma = -1.3$), GRB 080905A ($\Gamma = -1.33$), GRB 060502B ($\Gamma = -0.98$), GRB 050826 ($\Gamma = -1.16$) and GRB 050509B ($\Gamma = -1.57$) are also included.
- For transients with a power-law index $\Gamma \leq -1.6$, $E_{\rm iso}$ has been calculated. We consider that the high-energy contribution is not overestimated with such an index. It includes GRB 191019A ($\Gamma = -2.25$), GRB 130702A ($\Gamma = -2.44$); GRB 111225A ($\Gamma = -1.7$), GRB 051109B ($\Gamma = -1.97$), GF 050906 ($\Gamma = -1.66$) and GRB 050724 ($\Gamma = -1.89$).

Figures 7.1(a) and 7.1(b) display selected parameters of Tables 7.3 , 7.6 and 7.9 . Two figures are needed to ensure the readability while covering the full distance range of local transients. On Fig. 7.1(a), low-luminosity events such as GRB 170817A stand clearly apart. Indeed, except for GF 050906 (which is not a GRB), no GRB has been measured from a co-moving volume ranging from 10^{-3} to $\sim 5 \times 10^{-2}$ Gpc^3. We also note that the most energetic events in our sample have $E_{\rm iso} \sim 10^{52}$ erg, well below the maximum isotropic energy measured for GRBs at redshifts $z \geq 1$, $E_{\rm iso} \sim 3 \times 10^{54}$ erg (Atteia et al., 2017).

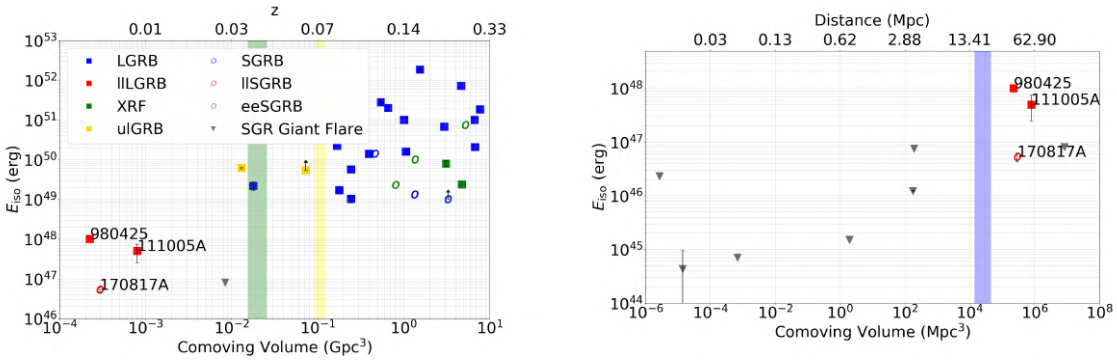

(a) (b)

Figure 7.1. Intrinsic properties of GRBs in our sample: $E_{\rm iso}$ as a function of the co-moving volume for high-energy transients. The symbols represent the three main categories of GRBs: full squares for long GRBs, empty circles for short GRBs and triangles for SGR giant flares. The colors describe the sub-categories defined in Table 7.1 and Table 7.4 . (a) GRBs with $z < 0.3$. The green and yellow bands represent the O4 LIGO sensitivity limits for respectively a NS-NS and a BH-NS merger. (b) SGR giant flares and low-luminosity GRBs. The blue band represents the approximate distance of the Virgo Cluster.

Figure 7.2 represents the GRB distribution in the $E_{\rm peak}$–$E_{\rm iso}$ plane for GRBs with measured peak energy. Some GRBs such as GRB 060218 and GRB 030329 follow the Amati relation (Amati, 2006) down to low values of $E_{\rm iso}$. However, other long GRBs such as GRB 98042, GRB 161219B or GRB 171205A are outliers of this relation. At z < 0.3, it is possible to detect much fainter GRBs, allowing the observation of a population with more variety than at higher redshift. This diversity includes GRBs with lower luminosities that are outliers of the Amati relation, in agreement with the work of Heussaff et al. (2013). SGR GFs seem to follow a relation between $E_{\rm iso}$and $E_{\rm peak,i}$ reminiscent of the Amati relationship (see Zhang et al. (2020a) for a discussion about the possible origin of such correlation).

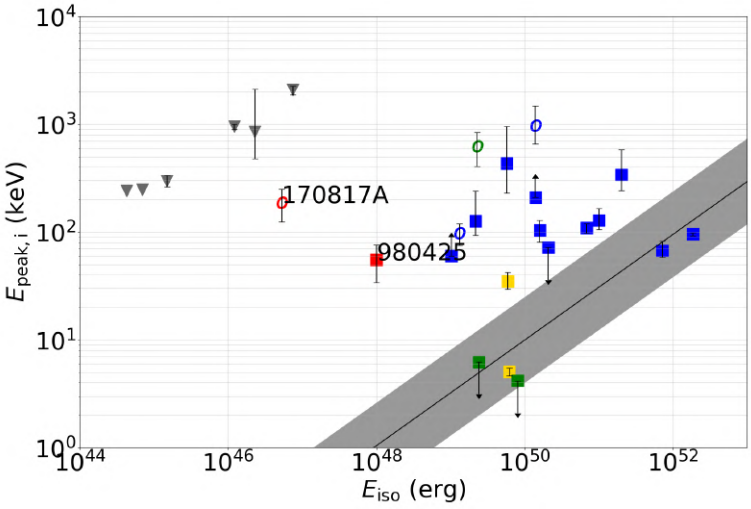

Figure 7.2. Intrinsic properties of GRBs in our sample: the Amati relation. The black line has been plotted according to Amati (2006), the grey area representing a vertical logarithmic deviation of 0.4 compared to the best-fitting power law values for the Amati relation $E_{\rm peak,i} = 95 \times E_{\rm iso}^{0.49}$. Color-coding and shape-coding are the same as in Fig. 7.1(a).

In Fig. 7.3, the usual bi-modal population of long/short GRBs is less clear, as most of the T_{90}-values come from the *Swift*/BAT instrument. Indeed, by extending its flux sensitivity as well as its low-energy threshold, BAT can see parts of the prompt emission that would have been buried into the noise for BATSE and previous GRB missions. With its low energy threshold, ECLAIRs might also be able to observe longer prompt emission for short GRBs.

7.3 The *SVOM*/ECLAIRs instrument

The *SVOM* mission is a Sino-French mission dedicated to the observation of GRBs and other high-energy transients, which will be launched in mid-2022. It will operate on a LEO orbit (625 km, an orbital period of 96 min) with a 30 degree inclination and quasi anti-solar pointing strategy. The *SVOM* spacecraft will be operated in a similar manner as *Swift*, encompassing two wide-field gamma-ray detectors: ECLAIRs (Godet et al., 2014) and the

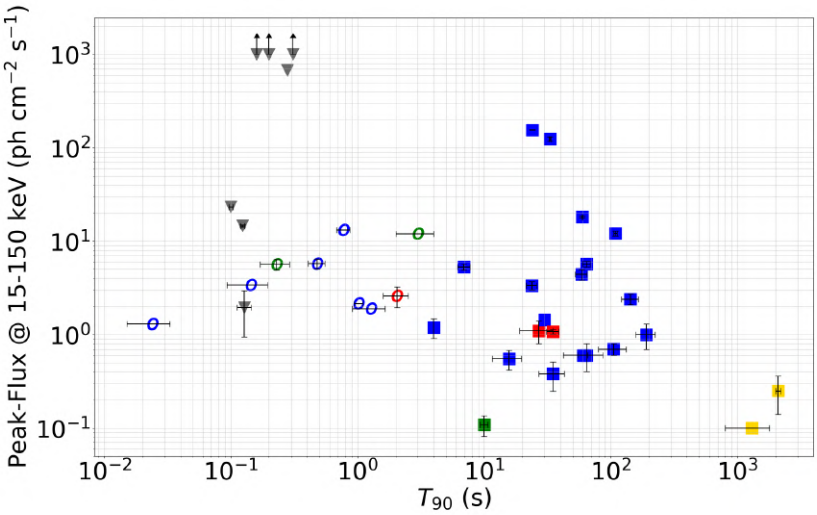

FIGURE 7.3. Observed properties of GRBs in our sample: T_{90} at 15–350 keV vs Peak Flux (15–150 keV). The SGR Giant Flare peak flux and the short GRBs peak flux are measured on a 64ms long time interval and the long GRBs one on a 1s long time interval. The transients whose peak flux has not been measured in the 15–150 keV energy band have been translated thanks to the fluence model provided in Tables 7.2 , 7.5 and 7.8 . Color-coding and shape-coding are the same as in Fig. 7.1(a).

Gamma-Ray Burst Monitor GRM (Zhao et al., 2012), and two narrow-field instruments: the Microchannel X-ray Telescope MXT (Götz et al., 2014) and the Visible Telescope VT (Wu et al., 2012), for the rapid follow-up of GRBs. In addition to the satellite, the mission will benefit from a dedicated ground segment with the Ground-based Wide Angle Camera GWAC (Turpin et al., 2020b), the COLIBRI telescope (Catching OpticaL and Infrared BRIght transients, Fuentes-Fernández et al. 2020) and the Chinese-Ground Follow-up Telescope C-GFT.

ECLAIRs is the wide-field hard X-ray imager of *SVOM*, in charge of the autonomous detection and localisation of GRB prompt emission in near real-time. It can be considered as a smaller analog of the *Swift*/BAT (Burst Alert Telescope, Barthelmy et al. 2005d). The main features of the instrument and its performances have been described in Godet et al. (2014); Schanne et al. (2019); Mate et al. (2019); Dagoneau et al. (2020), and they are summarized in Table 7.10 . In a few words, ECLAIRs encompasses a $\sim$ 1000 cm^2 detection plane with its readout electronics, which looks at the sky through a coded-mask (see Fig. 7.4). Its energy range extends from 4 to 150 keV, and the instrument is operated in photon counting mode. A passive lateral Pb/Al/Cu shield blocks the hard X-ray radiation originating from outside the 2 sr field of view and provides fluorescence lines useful to monitor the energy scale of the detectors. A digital processing unit (UGTS)[4] controls the

[4]UGTS is a French acronym for the ECLAIRs data processing unit: “Unité de Gestion et de Traitement Scientifique”.

detection plane and analyses in near real-time the detected events to look for high-energy transients.

The detection plane is made of 6400 pixels of CdTe (4×4 mm^2 and 1 mm thick, Remoué et al. 2010). It is located 46 cm below a 54×54 cm^2 coded mask, made of 4 quadrants with 23×23 elements each, of which 40% are open. This geometry guarantees a point spread function with a full width at half maximum (FWHM) of 52 arcminutes and a point source localization error (PSLE) better than 13 arcminute (90% confidence level) for sources at the detection limit ($SNR \sim 7\sigma$). ECLAIRs is thus a compact instrument, which has been optimized considering the limited resources (mass, power, volume) available on the *SVOM* spacecraft.

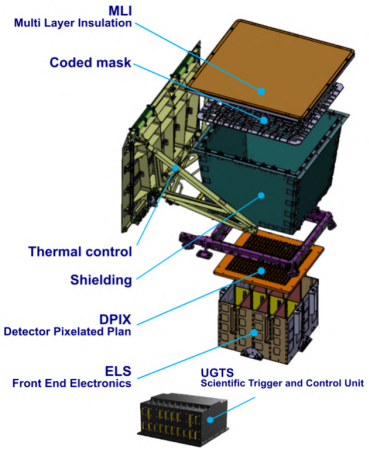

Figure 7.4. Schematic view of the ECLAIRs instrument.

The UGTS configures the instrument and searches for new transient sources within reconstructed sky images of the field of view (FoV). When a new source is detected, it alerts immediately the satellite about its location. The position is then sent to the ground through the VHF antenna network to alert the community that a transient has been detected and to start the follow-up. Hard X-ray transients are identified as count-rate excesses detected on the full detection plane or just a fraction of it. Count-rate excesses are monitored in 4 energy bands on time scales ranging from 10 ms to 20 s, the whole process aiming at detecting short transients. When a count-rate excess is detected, a sky image is constructed in the same time and energy intervals, and the trigger is validated if a significant excess is found in the sky image. Longer transients are directly searched in sky images constructed cyclically on time scales ranging from 20 s to 20 minutes. A detailed description of the ECLAIRs trigger can be found in Schanne et al. (2019). Finally, all recorded events are sent to the ground, allowing delayed data analysis on the ground for the accurate calibration of the detectors and offline searches of faint transient sources undetected on-board.

Two major challenges of the instrument are the 4 keV energy threshold and the on-board detection of transients on top of a strongly varying background modulated by the transit of Earth in the field of view. The 4 keV energy threshold is imposed by the requirement to be sensitive to X-Ray Flashes and highly redshifted GRBs. This requirement puts significant

constraints on the coded mask structure, whose transparent elements must be fully open, and on the detectors, which must have very low intrinsic noise. The mask requirements have been solved with a sandwich structure made of a punched plate of tantalum inserted between two complex titanium pieces. For the detectors, ECLAIRs uses Schottky CdTe detectors with intrinsically low leakage current operated at $-20°$ C, which are powered and read out by a low noise ASIC (Gevin et al., 2009; Lacombe et al., 2018). The detection of GRBs on top of a highly variable background is based on the use of timing and image information as described in Schanne et al. (2019). Detailed simulations based on realistic instrument background and performance including both the real trigger software and several GRB catalogs predict the detection of about 60 GRB yr^{-1} (Wei et al., 2016), several non-GRB extra-galactic transients, dozens of AGNs and hundreds of galactic X-ray transients and persistent sources (this last number is strongly dependent on the pointing strategy because X-ray transients are concentrated in the galactic plane).

7.4 Signal-to-noise ratio computation with *SVOM*/ECLAIRs

The purpose of this section is to assess the detectability by *SVOM*/ECLAIRs of each high-energy transient in our local sample, by computing its count and image SNRs for a detection in the fully-coded FoV, hereafter called "best SNRs". The fully coded FoV represents the fraction of the sky in which a source will be able to completely illuminate the detection plane of ECLAIRs, maximising the number of photons received by the instrument. On *SVOM*/ECLAIRs, the fully-coded FoV is a square with a side of 22 deg. In addition to the best SNR, the fraction of the ECLAIRs FoV in which the GRBs is detectable with a SNR ≥ 6.5 has also been computed.

7.4.1 Methodology of the SNR calculation

The SNR calculation proceeds along the following steps:

- First, the expected background in space is estimated with simulations based on to the Particle Interaction Recycling Approach PIRA (Mate et al., 2019).
- Then the photon events are simulated using the transient spectral properties given in Tables 7.2 , 7.5 and 7.8 .
- The SNR is then computed, taking into account the event counts on the detector and the background generated in the previous steps.
- A sky image is created in the energy range and time interval for which the count SNR has the maximum value. The SNR of the transient source in this image is then computed, giving the image SNR of the transient.

This operation can be performed for transients placed at different locations in the ECLAIRS FoV, allowing us to estimate in which fraction of the FoV the high-energy transient will be detected.

Background simulation

The sensitivity of ECLAIRs is limited by the background counts, which are dominated by the cosmic X-ray background CXB (Churazov et al., 2007; Ajello et al., 2008), with additional components from the CXB reflection on the Earth atmosphere (Churazov et al., 2007) and from the interaction of cosmic rays with the Earth's atmosphere, called albedo (Sazonov et al., 2007; Ajello et al., 2008). These background events are all simulated using PIRA (Mate et al., 2019), a software that relies on a pre-computed database of particle-instrument interactions simulated using the GEANT4 toolkit (Allison et al., 2016) to estimate the dynamical evolution of the background along the orbit. In the following, the high-energy transient is placed in the portion of the orbit when the Earth is completely out of the FoV, thus maximizing the number of events generated by the CXB. An example of generated orbit can be seen in Fig. 5.2.

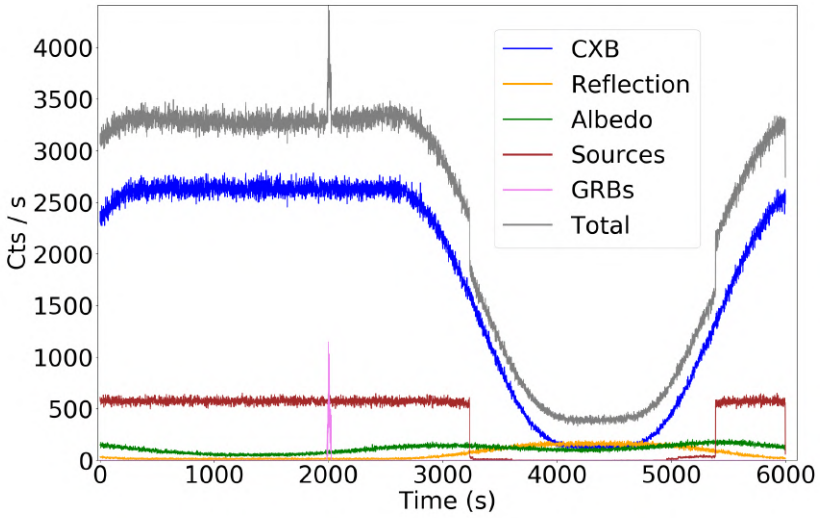

Figure 7.5. Example of PIRA background light curve (grey curve), with GRB 111005A (pink curve) superimposed on it. The total background is the addition of several components: the Cosmic X-ray Background, which is modulated by Earth transits in the FoV (blue curve); Albedo and reflection (yellow and green curves), which are also modulated by Earth transits, and the Crab nebula, which is hiding and rising behind the Earth (brown curve).

Other X-ray/gamma-ray sources

Once the background is generated, it is possible to add photons coming from known X-ray sources (Dagoneau, 2020) by using ray-tracing algorithms. Some X-ray sources have a significant contribution, reaching for example $\sim$ 600 cts/s in the 4–150 keV energy range for the Crab pulsar and its nebula. The simulation conditions chosen here represent a standard orbit with an extra-galactic pointing law (Wei et al., 2016), which means that the instrument will avoid observing the Galactic plane throughout this orbit. In these conditions, there is

no strong X-ray source in the field of view of ECLAIRs. The performance could be different for transients located close to some bright galactic sources such as the Crab or Sco-X1.

High-energy transient photon list generation

The first step of the transient simulation consists in translating the source spectrum from its observed energy bands into *SVOM*/ECLAIRs energy bands. The tool used, called *movegrb* (Antier-Farfar, 2016), allows to generate a list of photons in the ECLAIRs energy range, from a transient with a known spectrum and light curve. The spectral properties of the HE transients come from Tables 7.2 , 7.5 and 7.8 . For the light curves, there are several sources:

- To keep the consistency of the light curve morphology with respect to the morphology that would be observed by *SVOM*/ECLAIRs, we preferentially use the light curves measured by *Swift*/BAT, which has an energy range similar to ECLAIRs. The light curves are taken from the *Swift*/BAT light curve catalog (Lien et al., 2016), using the interactive BAT light curves[5] available over 1 s and 64 ms timescales. Transients with T_{90} larger than 10 s have been sampled with 1 s bins, while the transients with shorter durations have been sampled with 64 ms bins. Exceptions are made for GRB 150101B and GRB 160821B whose morphology was much better sampled at 16 ms because of their small duration.
- The light curves from transients that have not been seen by *Swift*/BAT are extracted from the instrument which displays a well-sampled light curve. For GRB 130702A the *Fermi*/GBM light curve has been taken directly from `https://heasarc.gsfc.nasa.gov/FTP/Fermi/data/gbm/bursts/`.
- For some transients, the light curves have been directly extracted from the associated paper: GRB 980827 (Tanaka et al., 2007), GRB 980425 (Pian et al., 2000), GRB 020903 (Sakamoto et al., 2004), GRB 031203 (Sazonov et al., 2004), GRB 040701 (Barraud et al., 2004), GRB 041227 (Mazets et al., 2005) and also GRB 050709 (Villasenor et al., 2005), GF 051103 (Hurley et al., 2010), GF 070201 (Mazets et al., 2008), GRB 170817A (Goldstein et al., 2017a) and GF 200415A (Frederiks et al., 2020).

The lightcurves used can be found in the appendix in Fig. 7.7.6.1. Light curves in counts are normalized by the *movegrb* simulator to recover the fluence measured in the ECLAIRs energy range. The second step is then to superimpose the simulated HE transients onto the generated orbit, with the same method as for X-ray sources. An example of a long GRB, a short GRB and a SGR GF superimposed on the background can be found in Fig. 7.6.

Computation of the Signal-to-Noise ratio and the FoV detectability fraction

The count and image SNRs are finally computed by applying a simulated *SVOM*/ECLAIRs count trigger algorithm (Schanne et al., 2019) to the data. As it is the case for the flight algorithm, the trigger simulation computes the SNR in 4 energy bands (a possible configuration is 4–120, 4–25, 15–50 and 25–120 keV), 12 timescales (logarithmically spaced

[5]BATlightcurves, Sakamoto T., Barthelmy S., see `https://swift.gsfc.nasa.gov/results/batgrbcat/`

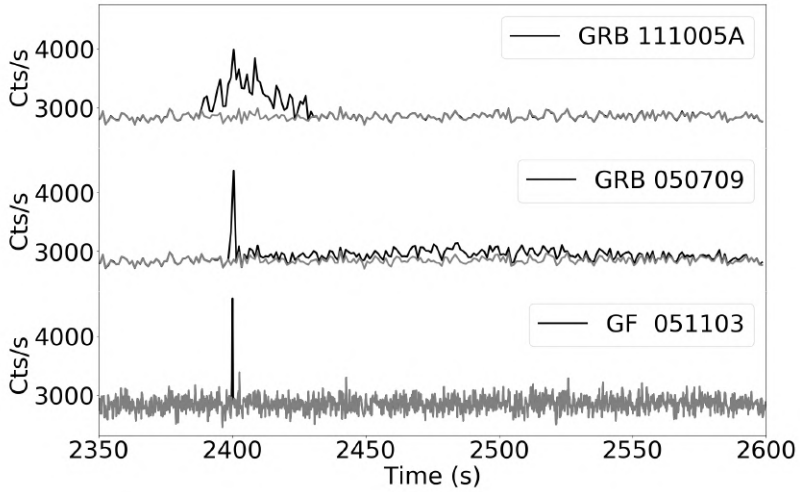

Figure 7.6. Lightcurves of GRB 111005A, GRB 050709 and GF 051103 obtained with the *movegrb* algorithm. The top and middle curves have a bin timescale of 1 s, while the bottom one has a bin timescale of 0.2 s. The grey lightcurves represent the background simulated without the GRB.

from 10 ms to 20.48 s) and 9 zones on the detection plane. The count SNR is computed as $SNR = C_{\rm GRB}/\sqrt{C_{\rm other}}$, where $C_{\rm GRB}$ is the number of events generated by the GRB, and $C_{\rm other}$ is the number of background events (including the X-ray sources inside the FoV). The difference with the on-board count-rate trigger algorithm is that there is no background estimation involved for this work. As the origin of the events created on the detection plane is tracked, the background is computed by selecting the appropriate events. The SNRs calculated here can thus be considered as best case SNRs. However, since the background count-rate is flat on the portion of the orbit where the transient is placed (the Earth is completely out of the FoV), the background estimation used by the on-board count trigger (based on the fit of a 1D quadratic function) is close to $C_{\rm other}$.

When the count rate SNR exceeds a count threshold η_c, a sky image of the excess (characterized by its energy band, timescale and zone) is reconstructed with a deconvolution algorithm (Caroli et al., 1987). If this image displays an unknown source with a significance exceeding a preset image threshold η_i, the GRB is considered as detected and localized by ECLAIRs, which will send a slew request to the satellite. The count and image SNR obtained are listed in Tables 7.11 , 7.12 and 7.13 . In the present work, the count and image thresholds have been set to the same value: $\eta_c = 6.5$ and $\eta_i = 6.5$.

The fraction of the FoV in which a transient is detectable has also been evaluated by measuring the count and image SNRs at different sky locations. The FoV of ECLAIRs is divided into 199×199 sky pixels: as the ECLAIRs FoV is a square projected on the sky, pixels on the edge have a larger angular size than pixels in the center. For practical reasons and to save computation time, the SNR has been computed on a 19×19 pixels grid (at pixel locations $-99, -88, ...0...88, 99$) and has been interpolated to get an estimation of the

SNR for each pixel. For each pixel location, the high-energy transient is simulated and the count SNR estimated. The image SNR is then obtained by creating an image whose parameters (energy band, timescale) maximize the count SNR.

7.4.2 Results

The SNRs obtained for all the high-energy transients can be found in Tables 7.11 , 7.12 and 7.13 . As can be seen, most of the transients that have been detected in the local Universe by previous gamma-ray instruments will be detectable by ECLAIRs.

The count and image SNRs given in the tables represent the median value of the SNR calculated for the sky pixels in the fully coded field of view. The energy range and timescale given represent the configuration for which these count and image SNRs are obtained. The fraction of the FoV represents the portion of the 2.0 sr ECLAIRs FoV where both the count SNR and image SNR are larger than 6.5, triggering a slew request from ECLAIRs to the platform of the *SVOM* satellite. These SNRs have also been plotted for each transient relatively to the co-moving volume in Fig. 7.7(a) and 7.7(b).

For LGRBs, 21/24 (88%) have both a count SNR and the resulting image SNR above 6.5. For SGRBs, 8/10 (82%) and for SGR giant flares 6/7 (86%). It can be noticed that the image SNR is systematically lower than the count SNR for SGRBs and Giant Flares (except for GRB 050709-p2, the extended emission of GRB 050709). The reason is that the timescale on which the detection has been made is minute, and therefore only a small number of events are available to reconstruct the sky image. This degrades significantly the performance of the reconstruction. It is always possible that by looking at longer timescales, more photons would be collected (both from the transient and the background) that could increase the image SNR and consequently the fraction of the FoV in which a slew request could be made. This possibility is not considered here, in order to stay as close as possible to the on-board trigger behavior.

Similarly, for LGRBs whose maximum count SNR is detected over timescales of several seconds and not limited by the number of photons, the image SNR can be significantly lower than the count-rate SNR for very high values of the count-rate SNR (GRB 030329 and GRB 180728A for example). This effect results from the difference in calculation between the count SNR and image SNR. The count SNR divides the signal counts by a background estimation, so that the count SNR scales as the signal counts. Whereas the image SNR is obtained through deconvolution of the shadowgram, which mixes signal and background counts. As a consequence, both the signal and the background contribute to the noise on the image and when the signal dominates over the background, the image SNR scales as the square root of the signal.

It can be noticed that GRB 020903, an XRF detected by HETE-2, would probably not be detected by ECLAIRs. This is because this XRF has a peak energy that is below 6 keV, making its detection difficult even for instruments with low energy threshold such as ECLAIRs.

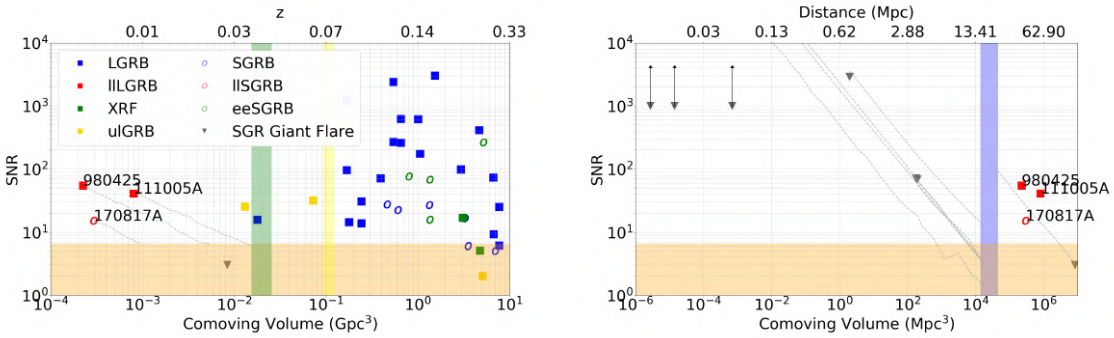

(a) (b)

Figure 7.7. ECLAIRs on-axis count SNR for transients in our sample. The orange horizontal band represents the detection limit of ECLAIRs at SNR = 6.5. (a) Local GRBs. The green and yellow bands represent the O4 LIGO distance sensitivity limits for NS-NS and BH-NS mergers respectively. The light grey trails represent the evolution of the on-axis count SNR with the redshift. (b) SGR Giant Flares. The blue band represents the approximate distance from the Virgo Cluster. GF 790205, GF 980827 and GF 041227 on the top left have SNR over 10^4 and would most likely saturate the instrument, we show them with arrows to improve the readability of the graph.

7.4.3 Events identification with ECLAIRs

Once a high-energy event is detected by *SVOM*/ECLAIRs and/or GRM, it is important to rapidly infer its nature. At first, the only data available relate to the prompt emission measured by the gamma-ray instruments. The simulation results in Sect. 7.4.1 can be used to find some criteria for assessing the source type/nature. Fig. 7.8 shows that the three classes of events in our sample are relatively well separated in a plane showing the hardness of the transients as a function of their "flatness". The hardness is defined as the ratio of the counts in the energy range $25 - 120$ keV to the counts in the energy range $4 - 25$ keV. The flatness is defined by the ratio of the total counts over the peak counts (on the 64ms timescale), both measured in the $4 - 120$ keV energy range. As shown in Fig. 7.8, these two parameters enable to separate the three classes of transients in our sample. This classification cleanly separates the long GRBs from the short GRBs and SGR Giant Flares classes. The ultra-long category also seems to be easily identified in this graph. The lightcurve shape might be used to separate eeSGRBs (with a first short peak followed by an extended emission) from classical long GRBs.

The ECLAIRs instrument covers an energy band extending from 4 keV to 120 keV that is small compared to other instruments such as *Fermi*/GBM (from $\sim$ 8 keV to $\sim$ 40 MeV, Meegan et al. 2009b). The problem of spectral identification with ECLAIRS only is thus similar to *Swift*/BAT, whose narrow energy band often prevents the measure of the peak energy. Nonetheless, *SVOM* has another gamma-ray instrument called GRM, which operates in the 15 keV – 5 MeV energy range. Since GRM covers a field of view that encompasses

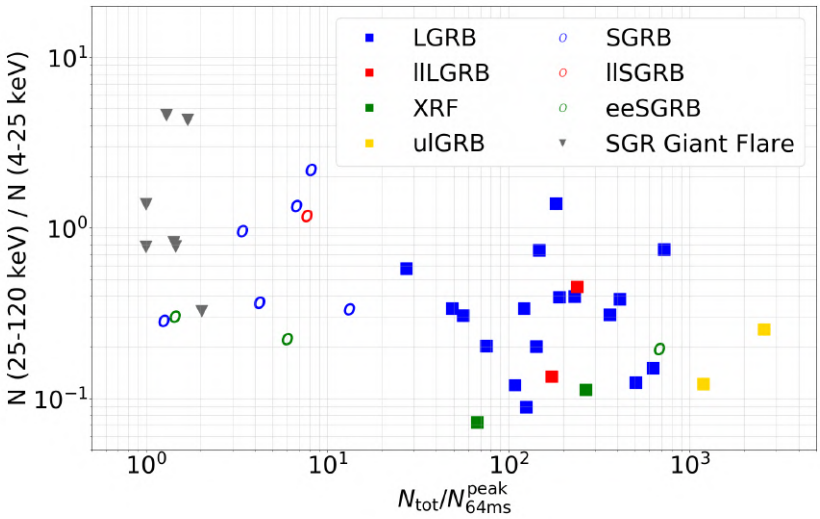

FIGURE 7.8. Hardness ratio N(25–120 keV)/N(4–25 keV) as a function of the ratio N_{tot}/N_{64ms}^{peak} in the 4–120 keV energy range.

the ECLAIRs one, most ECLAIRS transients, except the softest ones, will also be detected by the GRM, offering a joint energy range of 4 keV – 5 MeV for spectral analysis. In this range, *SVOM* will provide spectral information on the prompt emission with an accuracy comparable to that of *Fermi*/GBM (Bernardini et al., 2017). This will help identifying more precisely the nature of the high-energy transients detected by *SVOM*, with the measure of their peak energy and broadband spectral model.

7.5 Discussion

7.5.1 Long GRBs with and without supernova

After the first detection of GRB 980425 (Soffitta et al., 1998), a long GRB associated with a supernova SN1998bw (Tinney et al., 1998; Galama et al., 1998), the origin of long GRBs seemed intrinsically linked to the core-collapse of massive stars (so-called collapsars). In this way, a supernova is expected to rise few days after the detection of nearby long GRBs ($z \leq 0.1$), although the collapsar model does not systematically predict its appearance (Tominaga et al., 2007). However, detecting the supernova associated with a long GRB requires an active follow-up with sensitive instruments, explaining in some cases why several nearby long GRBs have not been associated with supernova despite their proximity:

- GRB 050219A ($z = 0.211$) had no optical observations sufficiently deep to detect a supernova (de Ugarte Postigo et al., 2005; Berger & Gonzalez, 2005). A SN was not searched because the redshift of the host galaxy was measured several years after the GRB (Rossi et al., 2014).
- For GRB 050826 ($z = 0.297$), no optical searches for an optical transient have been performed. The redshift has been measured in 2014 by Rossi et al. (2014).

- For GRB 051109B (z = 0.080), no observations have been performed to find a supernova. The redshift has been measured in July 2006 by Perley et al. (2006).
- GRB 080517 (z = 0.089) was satisfying the possible high-z criteria from Ukwatta et al. (2008), which might explain why no SN search has been performed.
- For GRB 111225A (z = 0.297), the GRB redshift has been discovered more than 3 years after the GRB (Thoene & de Ugarte Postigo, 2014), which explains why no supernova search has been conducted.
- For GRB 191019A (z = 0.248), an optical source thought to be the afterglow has been found, but no further search has been documented for the moment.

These examples show the importance of having a fast redshift determination that will trigger deeper and longer follow-ups of nearby GRBs in order to seek for a potential supernova association. However, there are also some GRBs where deep searches for an associated supernova have been made, and no evidence of such a signal has been found. The limiting magnitude of the observations has been compared to well-known supernovae associated with long GRBs such as SN 2003dh / GRB 030329 (Stanek et al., 2003; Hjorth et al., 2003) or SN 1998bw / GRB 980425 (Tinney et al., 1998).

- The absence of supernova for GRB 060614 and GRB 060505 has been demonstrated down to limits hundreds of times fainter than typical LGRB/SN associations (Fynbo et al., 2006).
- Using Hubble Space Telescope observations, Soderberg et al. (2005) have demonstrated with high confidence that GRB 040701 lacked an associated supernova, even if one takes into account a possible high extinction coming from its host.
- For the low-luminosity GRB 111005A (Michałowski et al., 2018), the near infrared and mid-infrared threshold was ∼20 times fainter than usual SNe associated with GRBs, which leads to the conclusion that the origin might be different from the usual collapsar model (Tanga et al., 2018).

For this reason, in Table 7.1 the long GRBs in the first category do not have a flag for the presence or absence of supernova, whereas GRBs in the second category have been flagged with **NO** supernova associated.

The systematic follow-up of *SVOM*/ECLAIRs GRBs with the VT (with R-band limiting magnitudes $m_{\rm R} \sim 22.5$ for SNR ≥ 5 in a 300 s long exposure, and $m_{\rm R} \sim 24$ for a 4,800 s long exposure) and/or with the GFTs (with an R-band limiting magnitude $m_{\rm R} \sim 22.8$ for SNR ≥ 5 in a 300 s long exposure) will permit detecting the appearance of the associated supernova. Figure 7.9 illustrates how powerful could be the VT to detect Type Ic supernovae within the local Universe ($z \leq 0.3$). The Fig. 7.9 also shows that within the range of the O4 BNS detection limit ($z \sim 0.038$), the red component of a kilonova similar to AT2017gfo would be easily detectable by the VT. In fact, such kilonova would be detectable up to a redshift of 0.15. The detection of an associated kilonova in debated cases would solve the issue of classification for SN-less GRBs.

Therefore having the VT optical telescope on-board *SVOM* (more powerful than the *Swift*/UVOT) will enable to put stringent constraints on the presence or absence of a supernova associated to long GRBs. The possibility to reliably identify long GRBs with and

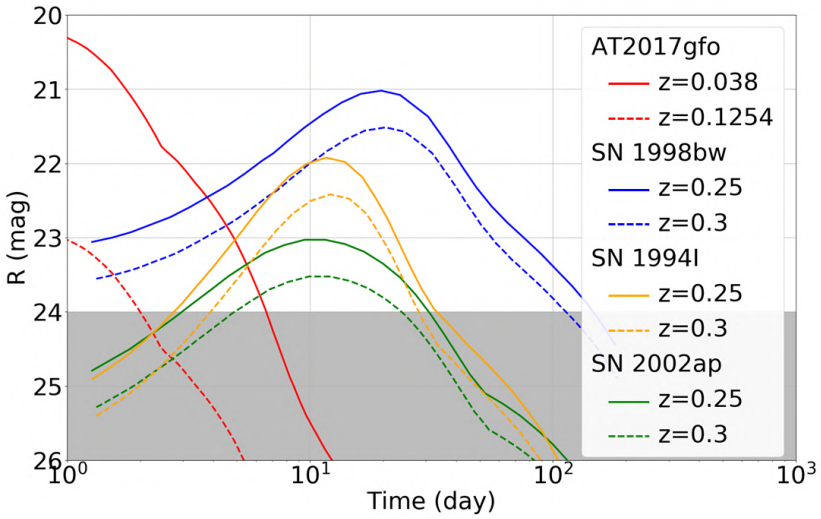

FIGURE 7.9. Expected lightcurves in the R-band from three Type Ic supernovae and the kilonova AT2017gfo compared to the VT limiting magnitude. Lightcurves at $z = 0.25$ are from Soderberg et al. (2005). The kilonova lightcurve is extracted from Cowperthwaite et al. (2017), originally at the GRB 170817A redshift ($z = 0.0093$). The grey band represents the V-band limiting magnitude of VT for an exposure time of 4,800 s, corresponding to ~ 2 orbits of *SVOM*.

without a supernova will allow to better characterize the prompt emission and afterglow of both types of GRBs, using the full instrument suite of *SVOM*. This will lead to a better understanding of the origin of long GRBs without SN whose nature is still debated (Gehrels et al., 2006; Yang et al., 2015).

7.5.2 Events with gravitational waves counterparts

The coincidental detection of GW 170817, a transient signal of gravitational waves and GRB 170817A, a short gamma-ray burst (Abbott et al., 2017b; Abbott et al., 2017; Goldstein et al., 2017a; Savchenko et al., 2017) marked an essential milestone in our understanding of GRB physics, confirming the link between short GRBs and binary neutron star (BNS) mergers. Based on the results presented in Table 7.12 , GRB 170817A would have been detected in 63% of the ECLAIRs FoV with a maximum $\mathrm{SNR}_0 \approx 16.4$ in the centre of the FoV (see also the internal *SVOM* study on GRB 170817A by S. Schane[6]). The ECLAIRs detection would have triggered an automatic slew of the satellite, allowing the Visible Telescope VT and ground-based telescopes associated with *SVOM* (the French/Mexican telescope COLIBRI and the Chinese telescope C-GFT) to observe the kilonova associated with GW 170817.

[6] http://www.svom.fr/en/portfolio/svom-in-the-era-of-gravitational-waves/ The results are summarized in Fig. 2, which also shows that GRB 170817A would have been detected by ECLAIRs up to 35 deg off-axis and by GRM up to an off-axis angle of ~ 50 deg.

The larger horizon of the O4 campaign of LIGO/Virgo and the advent of the Kamioka Gravitational Wave Detector KAGRA (Somiya, 2012; Aso et al., 2013) in 2022-2023 (Abbott et al., 2018b) will increase to 160–190 Mpc the distance up to which gravitational waves from BNS mergers could be detected, expanding by a factor three the explored volume compared to the O3 campaign. However, even if the increase in sensitivity of GW detectors for O4 run will likely result in a larger number of BNS detections, it is not clear if this will enhance the detection of coincidental EM high-energy counterparts. For example, While 6 BNS merger candidates have been Searched for EM counterparts during the O3 run of LIGO/Virgo, none has been found. This shows how challenging is the search for EM counterpart. Indeed, since the GRB jet axis is in general likely to be pointed away from Earth, the GRB luminosity drops very quickly with the off-axis angle. This is clearly illustrated in the case of the off-axis GRB 170817A since the prompt emission from this source would be hardly detectable by ECLAIRs if located at a distance larger than 50 Mpc (see Fig. 7.7(a)). On the other hand, on-axis GRBs are too rare to be detected at distances smaller than 480 Mpc ($z = 0.1$), too far for the detection of gravitational waves from BNS mergers (but not for the third generation of GW detectors, Punturo et al. 2010; Reitze et al. 2019).

NS-BH mergers may also produce GRBs (Ciolfi, 2018) associated with strong GW signals. The eeSGRBs sub-population could be associated with NS-BH merger progenitors according to Troja et al. (2008) and Gompertz et al. (2020). According to Abbott et al. (2018b), the volume sampled by O4 for NS-BH detection, reaching a distance limit of 330 Mpc (~ 0.1 Gpc^3), might permit the detection of few (1^{+91}_{-1} yr^{-1}) NS-BH mergers. The joint detection of a GW signal and a GRB from 200 Mpc to 330 Mpc would probably be the manifestation of such an event. Long GRBs without SN could represent a possible third source of transient GWs. While the origin of these events remains mysterious, their lack of SN would be naturally explained if they are due to mergers. Our sample contains four events of this type (XRF 040701, GRB 060505, GRB 060614 and GRB 111005A) at redshifts ranging from z = 0.013 to z = 0.215. In this context, GRB 111005A at a distance of only 57 Mpc appears especially interesting, because the horizon for its detection with ECLAIRs (170 Mpc) is comparable to the horizon of GW detectors for BNS detection in the O4 run (Fig. 7.7(a)). The detection of an event like GRB 111005A within 170 Mpc with ECLAIRs during the LVC O4 run would thus permit confirming or discarding a merger origin for GRBs without SN. This method has already been used in the past to strengthen a SGR origin for SGR 070201 in M31. A SGR origin was favored considering that a merger would have produced a burst of gravitational waves, which was not observed by LIGO at that time (Abbott et al., 2008).

Even if the coincidental detection of a short GRB and a BNS merger during O4 remains speculative, they are not the only candidates for coincidental GRB and GW emission. Considering the youth of the field, it will be crucial to systematically look for coincidental transient signals detected by ECLAIRs and the GW detectors during O4, in order to assess their origin. This is also true for the GRM, which has a larger field of view than ECLAIRs for the detection of short GRBs (nearly 6 sr), albeit with much lower localization accuracy.

7.5.3 The nature of X-ray flashes

XRFs are high-energy transients whose emission is dominated by low energy photons, with most of their fluence below 30 keV. Their origin is still highly debated.

According to Barraud et al. (2005), XRFs could be less energetic events with a contrast of Lorentz factor between internal shells (between 1 and 2) which is smaller than that of classical GRBs. This low contrast could lead to smaller energy dissipation inside the jet, leading to the characteristic XRF spectral energy distribution peaking between few keV and few tens of keV, with little or no emission above 50 keV (Heise et al., 2001; Kippen et al., 2003; Barraud et al., 2003).

Other explanations invoke extrinsic parameters, like different viewing angles, XRFs being GRBs seen from the side (Yamazaki et al., 2004; Lamb et al., 2005). However, according to Sakamoto et al. (2008) XRFs and classical GRBs have different X-ray afterglow light-curves, which cannot be explained only by the jet orientation.

The quasi absence of high-energy photons (Kippen et al., 2003) in these events requires an instrument particularly sensitive to low energies, for their detection. From February 2001 to September 2003, HETE-2 has detected 16 XRFs and 19 XRRs (X-Ray Rich GRBs) (Sakamoto et al., 2005), mostly thanks to the low low-energy threshold of two of its instruments:

- The Wield-field X-ray Monitor WXM (Shirasaki et al., 2003) sensitive in the $2-25$ keV energy range, with an effective area of 85.4 cm^2 at 8.3 keV.
- The FREnch GAmma TElescope FREGATE (Atteia et al., 2003) sensitive in the $6-400$ keV energy range, with an effective area larger than 120 cm^2 in the range $6-200$ keV.

Thanks to its low energy threshold (4 keV) and its effective area of ~ 400 cm^2 at 20 keV, *SVOM*/ECLAIRs should be able to detect at least as many XRFs as HETE-2, providing the unique opportunity to test the nature of their differences with classical GRBs. This will take place through the detailed study of their X-ray and visible afterglows, host galaxies and associated supernovae, if any. The ability of *SVOM* to slew towards ECLAIRs detected XRFs in few minutes will improve our knowledge of their optical and X-ray afterglow emission. Coupled with the prompt emission characteristics such as $E_{\rm peak}^{\rm obs}$, it will allow to put further constraints on the geometrical jet models discussed before (Zhang et al., 2004; Yamazaki et al., 2004; Lamb et al., 2005), but also to derive the jet structure and micro-physics. Finally, this new XRF sample will also provide better constraints on the XRF and GRB luminosity functions.

7.5.4 The nature of ultra-long GRBs

The potentialities brought by *SVOM*/ECLAIRs in this field have been presented in a dedicated paper by Dagoneau et al. (2020), and will not be discussed here. Their main conclusion is that ECLAIRs may detect ulGRBs at a rate comparable to *Swift*/BAT, taking into account the differences in sensitivity, duty cycle and field of view of both

instruments. The longer duration of *SVOM* pointings (up to 20 hours) combined with the capability to send all the counts recorded to the ground could also allow the ground-based detection of these GRBs. These observations will shed new light on the nature of the ulGRB phenomenon. Finally, we note that the ulGRB class is heterogeneous, including genuine ultra-long GRBs, like GRB 111209A (at z=0.677) and nearby low-energy transients, which have been attributed to SN shock breakout, like GRB 060218 or GRB 100316D. Considering their small distances, the detection of such events with ECLAIRs will permit to constrain their gravitational wave emission with GW interferometers during the O4 run, and confirm their nature.

7.5.5 Detection of SGR Giant Flares in the Virgo cluster

SGR Giants Flares are much more luminous than classical SGR bursts, and can be detected up to a few Mpc (GRB 200415A and GF 051103, for example, have been detected respectively at distances of 3.5 and 3.6 Mpc), and even up to 130 Mpc for GF 050906 (but see below for a discussion on the nature of this event). Based on the work of Cline et al. (1982); Crider (2006); Levan et al. (2007); Hurley et al. (2010); Ofek et al. (2008); Svinkin et al. (2020), most of the detected Giant Flares seem to come from our direct neighborhood.

Figure 7.7(b) shows with light grey trails the expected SNR for Giant Flares as a function of distance. Only GF 070201 and GF 050906 seem to be sufficiently luminous so that their count SNR is above 6.5 at the distance of the Virgo Cluster (∼16.5 Mpc), with the flare in the fully coded FoV. The cluster spans a radius of approximately 8 deg on the sky, which means that the whole cluster would fit inside the *SVOM*/ECLAIRs fully coded field of view (a square of about $22 \times 22\,\mathrm{deg}^2$). Our simulations show that GF 070201 would have $\mathrm{SNR}_0 = 8$ on the 10 ms timescale (SNR_0 representing the SNR obtained in the fully coded FoV). This corresponds to ~ 45 photons on the detector, which is not enough to produce a sky image with a SNR greater than 6.5 (SNR$\sim 5.9\sigma$, using only the photons from the Giant Flare). This giant flare will therefore not be localized in real time by *SVOM*, which means that there will be no follow-up of such an event. However, since *SVOM* transmits all detected photons to the ground, it will be possible to look for short spikes when ECLAIRs points at the Virgo cluster, during pre-planned large programs (for instance, the search for relativistic Tidal Disruption Events in the Virgo Cluster with MXT, see Wei et al. 2016). Such analyses may lead to the detection of an excess of very short transients due to giant flares in the Virgo Cluster. Depending on the luminosity function of giant flares, the brightest of them could lead to rapid Target of Opportunity observations with *SVOM* or other space/ground facilities, that may allow their detailed follow-up.

M31, the putative host of GF 070201, has an estimated star formation rate (SFR) of ~ 0.7 $\mathrm{M}_\odot\ \mathrm{yr}^{-1}$ (Lewis et al., 2015). This SFR can be compared to the star formation rate of all the galaxies in the Virgo Cluster which amounts to $50 - 100\ \mathrm{M}_\odot\mathrm{yr}^{-1}$ (Boselli et al., 2016). Assuming that the rate of SGR giant flares is directly correlated to neutron stars creation and therefore to the massive star formation rate, the event rate from the Virgo Cluster could be up to two orders of magnitude greater than for large spiral galaxies like M31 or the Milky Way.

The second giant flare candidate that could be detectable in the Virgo Cluster is GF 050906 (SGR 0331-1439), detected by *Swift*/BAT (Parsons et al., 2005; Levan et al., 2007). This event is however significantly different from the other giant flares in our sample. First, it is associated with a local galaxy IC328 at distance of ≈ 130 Mpc, more than twenty times further away than GF 970110, the second most distant giant flare, detected in NGC6946 at a distance of 5.9 Mpc (Crider, 2006). Second, the spectrum of this flare is much softer than other giant flares (GRB 200415A, GF 051103), while having approximately the same energy as GF 051103 ($E_{\rm iso} \sim 7.5 \times 10^{46}$ erg, see Table 7.9). This softness results in a much larger number of photons, making it easily detectable in the Virgo cluster with a count SNR value of ~ 150 in the fully coded FoV.

The significant differences between GF 050906 and the other SGR giant flares (spectrum and volumetric rate) questions the nature of this event. A recent work by Dichiara et al. (2020) shows that this event might instead belong to a category of low-luminosity short GRBs with typical energies around 10^{46-47} erg, close to the energy of GRB 170817A.

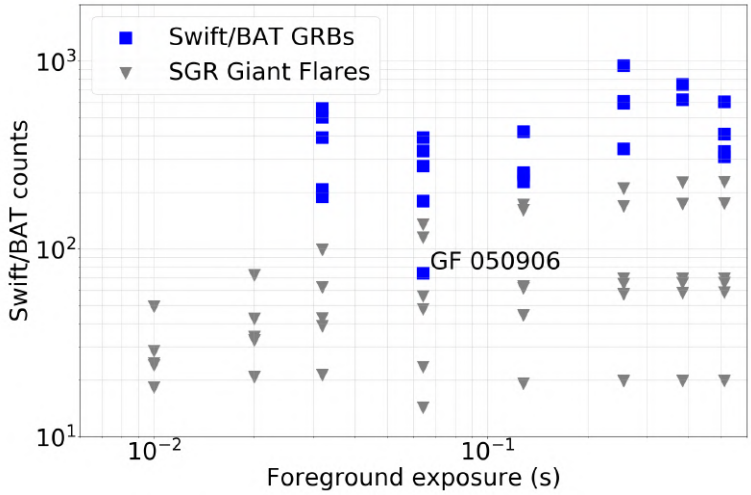

Figure 7.10. Comparison between the faintest *Swift*/BAT GRBs (blue squares) and SGR Giant Flares simulated in the Virgo Cluster (grey triangles), showing that SGR Giant Flares in the Virgo Cluster are fainter than the faintest GRBs detected with *Swift*/BAT. GF 050906 is the faintest event detected by *Swift*/BAT.

We have made a comparison between the dimmest GRBs observed by *Swift*/BAT and simulated Giant Flares in the Virgo Cluster seen by this same instrument in Fig. 7.10. This comparison has been made on the smallest timescales for which *Swift*/BAT has triggered (32 ms, 64 ms, 128 ms, 384 ms, 512 ms), using the recorded GRB counts from the GCN. For all timescales, the only event from *Swift*/BAT dimmer than some of the Giant Flares is GF 050906. It has been detected on a 64 ms with a count-level ~ 5 times lower than the second faintest detection by *Swift*/BAT on this timescale. Nonetheless, the other faint events with a number of counts similar to GF 050906 such as GRB 070406, GRB 080702B and

GRB 100216A have been detected or confirmed only with the help of ground analysis. The in-flight detection of GF 050906 seems to be a "once in the *Swift*/BAT lifetime" opportunity. To conclude, the fact that *Swift*/BAT has not detected any Giant Flare when pointing towards the Virgo cluster seems to be acceptable.

Additional simulations have been performed to determine the count SNR registered by GRM for Giant Flare events in the Virgo Cluster. Thanks to the wide energy range and the sensitivity to high-energy photons, GRM will also be able to detect these events, allowing coincident searches between the two *SVOM* gamma-ray instruments.

7.6 Conclusion

We have shown that *SVOM*/ECLAIRs will be able to detect the large diversity of short high-energy transients known in the local Universe. Once an event is detected, *SVOM* will be able to obtain unique diagnostics thanks to its slewing capability, the on-board narrow field instruments and the follow-up by ground telescopes. Furthermore, the photons recorded by ECLAIRs are entirely sent to the ground: exotic transients not detected by the on-board trigger could be found by the offline trigger on ground and later-on followed. Finally, ECLAIRs low-energy threshold of 4 keV will be an asset to detect soft transients in the hard X-ray range, and its combination with GRM might allow an even better spectral characterization at low energies than what is currently achieved by *Fermi*/GBM.

Various local high-energy transients are also within the range of the GW detectors LIGO and VIRGO, which permitted for example detecting the well-known GRB 170817A coincident with GW 170817 at $z = 0.0093$. The multi-messenger astronomy and the detection or lack of gravitational waves could shed crucial light on the origin of long GRBs without SN such as GRB 111005A and GRB 060614. The VT, C-GFT and Colibri telescopes and their systematic follow-up strategy of long GRBs will put strong constraints on associated supernovae, if the redshift is measured sufficiently early to allow the adequate follow-up of selected nearby GRBs. GW observations might also put strict limits on the GW energy liberated by the SGR Giant Flares progenitors, an opportunity to derive rates for the existence of such objects.

However, one condition for this success is a long lasting lifetime of *SVOM*/ECLAIRs, as it is the case for *Fermi*/GBM and *Swift*/BAT for example. Low-z high-energy transients are scarcely detected, even if all the instruments detections are added: the 24 long GRBs and 10 short GRBs detected and listed in this paper span over two decades, from May 1998 to November 2019 (~ 1.7 yr^{-1}). The SGR Giant Flares are even rarer, only 7 of them have been detected from March 1979 to April 2020 (~ 0.2 yr^{-1}). *SVOM* will have all the assets to detect and characterise these events, their progenitors and their hosts, if they happen in the lifespan of the mission...

Acknowledgements

ECLAIRs is a cooperation between CNES, CEA and CNRS, with CNES acting as prime contractor. This work is supported by CNES and the Paul Sabatier University. Jérôme Rodriguez acknowledges partial funding from the French Space Agency (CNES) and the

French Programme National des Hautes-Energies (PNHE). We would like to thank Frédéric Daigne and Maxime Bocquier from IAP, Paris, for providing the tools to transport GRB light curves to different redshifts, developed during the thesis of Sarah Antier at CEA Paris-Saclay. This article made use of the GRB table maintained by J. Greiner (see footnote 1 of Sect. 7.2.1).

7.7 Appendix

7.7.1 Long GRBs

This section discusses the properties of the 24 long GRBs in our sample, starting with some comments about peculiar GRBs.

- GRB 150518A has only been detected by MAXI/GSC located on the ISS (Sakamoto et al., 2015) and partially by Konus-Wind (Golenetskii et al., 2015a). Its energy has not been measured by Konus-Wind because of a data gap during the main emitting episode. The light curve has been partially recorded by MAXI/GSC, but Konus-Wind observations seem to indicate that this burst was already emitting $\sim$ 250 s before MAXI/GSC observations, implying that the light curve and the GRB properties recovered by MAXI/GSC are only a fraction of an ultra-long GRB. For this reason, the simulations that have been made on this burst are incomplete and only account for the part visible by MAXI/GSC.
- GRB 190829A has two distinct peaks separated by $\sim$ 45 s, with completely different spectra. The case is similar for GRB 180728A, with a precursor and then the main emission of the burst. Thus, the emission properties of those two GRBs have been divided into two parts.

Tables 7.1 , Table 7.2 and Table 7.3 summarize the features detected for the long GRBs.

The population observed is diverse in terms of observed characteristics:

- Concerning the fluence, the minimum fluence observed is 1.0×10^{-8} erg cm^{-2} for GRB 150818A while the maximum one is 1.63×10^{-4} erg cm^{-2} for GRB 030329, with the median equal to 3.55×10^{-6} erg cm^{-2}.
- For the 1s peak flux, the minimum is $0.1^{+0.06}_{-0.03}$ ph cm^{-2} s^{-1} for GRB 100316D and the maximum is 451^{+25}_{-25} ph cm^{-2} s^{-1} for GRB 030329, with the median equal to 2.65 ± 0.63 ph cm^{-2} s^{-1} for GRB 060505.
- For the peak energy of the fluence spectrum, 13 out of the 30 long GRBs do not have any peak energy information. This is mainly because they have been observed with instruments such as *Swift*/BAT whose energy band is often too narrow to measure properly the spectrum peak energy. GRB 020903, GRB 120422A and GRB 040701 only have a lower estimation. For the remaining 14 long GRBs with peak energy, the minimum $E_{\rm peak}$ for long GRBs is equal to 4.9 ± 0.4 keV for GRB 060218 and the maximum equal to 302^{+214}_{-85} keV for the first part of GRB 060614, with a median of 68 keV from GRB 030329.

- For T_{90} -values, the minimum value is 4.0 s for GRB 060505, the maximum 2100 ± 100 s for GRB 060218 and the median is 34 s.

There are also some differences in the intrinsic properties:

- The closest long GRB that has been detected is GRB 980425, at a redshift of 0.0085 ($\approx$ 38 Mpc). The furthest one in our local GRB sample is at a redshift of z = 0.297 ($\approx$ 1590 Mpc), GRB 111225A. the median redshift of the sample is z = 0.135 ($\approx$ 660 Mpc).
- The minimum isotropic energy detected in the long GRB sample is $E_{\rm iso} = 5 \times 10^{47}$ erg for GRB 111005A (Tanga et al., 2018), while the maximum isotropic energy is equal to 1.86×10^{52} erg for GRB 030329. The median value for the long GRBs is $E_{\rm iso} = 1.65 \times 10^{50}$ erg, significantly lower than the median $E_{\rm iso}$ of classical long GRBs observed at larger distances.

Based on the observations on Fig. 7.3, the 1s peak flux in the energy range 15–150 keV for the 2 closest long GRBs (GRB 980425 and GRB 111005A) is of the order of 1 ph cm^{-2} s^{-1}, which is slightly lower than for classical GRBs (the 1s peak flux median in the *Swift*/BAT catalog is $\sim$ 1.4 ph cm^{-2} s^{-1}, see Lien et al. 2016), while these low-energy GRBs are one order of magnitude closer. This suggests that these two GRBs are the tip of the iceberg of a much larger population (Soderberg et al., 2004a). Two long GRBs of the sample, GRB 040701 and GRB 150518A, have no peak flux mentioned in the literature and therefore do not appear in Fig. 7.3.

Table 7.1 . Detected features for Long GRBs

Name	Instrument(s)[a]	Class	Afterglow[b]	SN/KN	Host	T_{90} (s)[c]
980425	C B	llLGRB	X(O)R [1]	SN1998bw [2]	[3]	$34.9^{+3.8}_{-3.8}$ [4]
020903	H	XRF [5]	OR [6,7]	SN [6]	[6]	$10.0^{+0.7}_{-0.7}$ [5]
030329	K H	LGRB	XOR [8,9,10]	SN2003dh [11,12]	[13]	$33.1^{+0.5}_{-0.5}$ [5]
031203	I	LGRB [14]	XOR [15,16,17]	SN2003lw [18]	[19]	30.0 [20]
040701	H	XRF [21]	X [21]	NO [21]	[22]	$11.7^{+5.7}_{-5.7}$ [23]
050219A	S	LGRB	X [24,25,26]	...	[27]	$23.8^{+2.3}_{-2.3}$
050826	S	LGRB	XO [28,29]	...	[29]	$35.0^{+8.0}_{-8.0}$ [30]
051109B	S	LGRB	X [31,32]	...	[33]	$15.7^{+4.1}_{-4.1}$
060218	S	ulGRB [34]	XOR [35,36]	SN2006aj [37]	[34]	2100^{+100}_{-100} [34]
060505	S SUZ	LGRB	XO [38,39]	NO [40]	[41]	4
060614	S K	LGRB	XO [42]	NO [43,44,45]	[44,45]	$109.1^{+3.4}_{-3.4}$
080517	S	LGRB	X [46]	...	[46]	$64.5^{+22.3}_{-22.3}$
100316D	S	ulGRB	XO [47,48]	SN2010bh [49]	[50]	1300^{+500}_{-500} [51]
111005A	S	llLGRB	R [52]	NO [53,54]	[55]	$27.0^{+8.0}_{-8.0}$ [56]
111225A	S	LGRB	XO [57]	-	[58]	$105.7^{+26.2}_{-26.2}$
120422A	S	LGRB	XO(R) [59,60]	SN2012bz [61]	[62]	$60.4^{+5.7}_{-5.7}$
130702A	F K	LGRB	XOR [63,64,65]	SN2013dx [66]	[67]	$58.9^{+6.2}_{-6.2}$
150518A	K M	ulGRB [68]	XOR [69,70,71]	SN [72]	[70]	1000.0 [68]
150818A	S K	LGRB [73]	XO [74,75]	SN [76]	[77]	$143.3^{+21.8}_{-21.8}$
161219B	S K	LGRB	XOR [78,79,80]	SN2016jca [81]	[82]	$6.9^{+0.8}_{-0.8}$
171205A	S K	LGRB	XOR [83,84,85]	SN2017iuk [86]	[87]	$190.5^{+33.9}_{-33.9}$
180728A	S F K AS	LGRB [88]	XO [89,90]	SN2018flp [91]	[92]	24.0 [88]
190829A	S F K A	LGRB	HXOR [93,94]	SN2010bh [95]	[93]	$59.4^{+0.6}_{-0.6}$ [96]
191019A	S	LGRB	XO [97,98,99]	...	[99,98]	$64.3^{+4.5}_{-4.5}$

Notes. [(a)] A for AGILE/GRID and/or AGILE/SA, AS for Astrosat/CZTI, B for BeppoSax/WFC, C for CGRO/BATSE, F for *Fermi*/GBM, H for HETE-2/FREGATE and/or WXM, I for INTEGRAL/IBIS and/or INTEGRAL/SPI, K for Wind/KONUS, M for MAXI/GSC, S for *Swift*/BAT, SUZ for *Suzaku*/WAM [(b)] The letters X, O and R stands respectively for X-ray, Optical and Radio afterglow. H represents the High-Energy detection by H.E.S.S. [(c)] Unless quoted differently, T_{90}-values are measured by the *Swift*/BAT instrument in the $15 - 350$ keV band

References. (1) Pian et al. (1998); (2) Tinney et al. (1998); (3) Galama et al. (1998); (4) Soffitta et al. (1998); (5) Sakamoto et al. (2005); (6) Soderberg et al. (2002); (7) Soderberg et al. (2004b); (8) Marshall et al. (2003); (9) Peterson & Price (2003); (10) van der Horst et al. (2006); (11) Stanek et al. (2003); (12) Hjorth et al. (2003); (13) Greiner et al. (2003); (14) Watson et al. (2004); (15) Santos-Lleo et al. (2003); (16) Reichart (2003); (17) Frail (2003); (18) Bersier et al. (2004); (19) Prochaska et al. (2003); (20) Mereghetti & Gotz (2003); (21) Soderberg et al. (2005); (22) Kelson et al. (2004); (23) Pélangeon et al. (2008); (24) Romano et al. (2005); (25) Berger & Gonzalez (2005); (26) de Ugarte Postigo et al. (2005); (27) Rossi et al. (2014); (28) Mangano et al. (2005); (29) Halpern et al. (2006); (30) Markwardt et al. (2005); (31) Campana et al. (2005); (32) de Pasquale et al. (2005); (33) Perley et al. (2006); (34) Campana et al. (2006); (35) Cusumano et al. (2006); (36) Soderberg & Frail (2006); (37) Masetti et al. (2006); (38) Conciatore et al. (2006); (39) Ofek et al. (2006); (40) Xu et al. (2009); (41) Thoene et al. (2006); (42) Parsons et al. (2006); (43) Fynbo et al. (2006); (44) Gal-Yam et al. (2006); (45) Valle et al. (2006); (46) Parsons et al. (2008); (47) Stamatikos et al. (2010); (48) Wieringa et al. (2010); (49) Wiersema et al. (2010); (50) Vergani et al. (2010); (51) Starling et al. (2011); (52) Xu et al. (2011); (53) Levan et al. (2011); (54) Michałowski et al. (2018); (55) Malesani et al. (2011); (56) Tanga et al. (2018); (57) Siegel et al. (2011); (58) Thoene & de Ugarte Postigo (2014); (59) Beardmore et al. (2012); (60) Kuin & Troja (2012); (61) Malesani et al. (2012); (62) Tanvir et al. (2012); (63) D'Avanzo et al. (2013); (64) Guidorzi & Virgili (2013); (65) van der Horst (2013); (66) Schulze et al. (2013); (67) Singer et al. (2013); (68) Sakamoto et al. (2015); (69) Sbarufatti et al. (2015); (70) Xu et al. (2015); (71) Kamble (2015); (72) Pozanenko et al. (2015); (73) Palmer et al. (2015); (74) D'Elia et al. (2015); (75) Marshall & D'Elia (2015); (76) Mazaeva et al. (2015); (77) Sanchez-Ramirez et al. (2015); (78) Beardmore et al. (2016); (79) D'Ai et al. (2016); (80) Alexander et al. (2016); (81) de Ugarte Postigo et al. (2016); (82) Kruehler et al. (2016); (83) Kennea et al. (2017); (84) Osborne et al. (2017); (85) Chandra et al. (2017); (86) de Ugarte Postigo et al. (2017); (87) Izzo et al. (2017); (88) Wang et al. (2019); (89) Perri et al. (2018); (90) Laporte & Starling (2018); (91) Izzo et al. (2018); (92) Rossi et al. (2018); (93) Dichiara et al. (2019); (94) Rhodes et al. (2020); (95) Perley & Cockeram (2019); (96) Narayana Bhat et al. (2016); (97) Sbarufatti et al. (2019); (98) Reva et al. (2019); (99) Perley et al. (2019);

Table 7.2 . Spectral properties of Long GRBs

Name	Fluence (10^{-6} erg cm^{-2})	1-s P.-flux (ph cm^{-2} s^{-1})	Energy Band[a] (keV - Inst.)	P.-flux (norm)[b] (ph cm^{-2} s^{-1})	E_{peak} (keV)	Spectral Model[c]
980425	$4.0^{+0.74}_{-0.74}$ (1)	$1.0^{+0.05}_{-0.05}$ (1)	20 - 2000 - C	$1.1^{+0.1}_{-0.1}$	55^{+21}_{-21} (1)	BAND: 55, -1.00, -2.10 (1)
020903	$0.10^{+0.06}_{-0.06}$ (2)	$2.8^{+0.7}_{-0.7}$ (2)	2 - 400 - H	$0.1^{+0.0}_{-0.0}$	< 5 (2)	PL: -2.60 (2)
030329	186 (3)	451^{+25}_{-25} (2)	2 - 400 - H	$124.5^{+6.9}_{-6.9}$	82^{+3}_{-3} (3)	BAND: 70, -1.32, -2.44 (3)
031203	$2.0^{+0.4}_{-0.4}$ (4)	1.2 (5)	20 - 200 - I	1.4	> 190 (4)	PL: -1.63 (4)
040701	$0.54^{+0.05}_{-0.05}$ (6)	...	2 - 30 - H	...	< 3 (6)	PL: -2.30 (6)
050219A	$5.2^{+0.4}_{-0.4}$ (7)	$3.5^{+0.3}_{-0.3}$	15 - 350 - S	$3.3^{+0.3}_{-0.3}$	90^{+9}_{-9} (7)	CPL: 90, -0.75 (7)
050826	$0.41^{+0.07}_{-0.07}$	$0.4^{+0.1}_{-0.1}$	15 - 150 - S	$0.4^{+0.1}_{-0.1}$	...	PL: -1.23
051109B	$0.27^{+0.04}_{-0.04}$	$0.6^{+0.1}_{-0.1}$	15 - 150 - S	$0.6^{+0.1}_{-0.1}$	...	PL: -1.98
060218	$1.57^{+0.15}_{-0.15}$	$0.2^{+0.1}_{-0.1}$	15 - 150 - S	$0.2^{+0.1}_{-0.1}$	5^{+0}_{-0} (8)	PL: -2.26
060505	$2.30^{+1.08}_{-1.08}$ (9)	$2.6^{+0.6}_{-0.6}$	15 - 2000 - S	$1.2^{+0.3}_{-0.3}$	397^{+485}_{-485} (9)	BAND: 397, -1.19, -2.39 (9)
060614-p1	$8.19^{+0.56}_{-0.56}$ (10)	$11.5^{+0.7}_{-0.7}$	20 - 2000 - K*	$11.5^{+0.7}_{-0.7}$	302^{+214}_{-214} (10)	CPL: 302, -1.57 (10)
060614-p2	$32.7^{+1.7}_{-1.7}$ (10)	...	20 - 2000 - K	...	...	PL: -2.13 (10)
080517	$0.56^{+0.12}_{-0.12}$	$0.6^{+0.2}_{-0.2}$	15 - 150 - S	$0.6^{+0.2}_{-0.2}$	> 55 (11)	PL: -1.54
100316D	$5.10^{+0.39}_{-0.39}$ (12)	0.1	15 - 150 - S	0.1	33^{+7}_{-7} (12)	CPL: 33, -1.33 (12)
111005A	0.48 (13)	$1.1^{+0.3}_{-0.3}$	15 - 150 - S	$1.1^{+0.3}_{-0.3}$	...	PL: -2.40 (13)
111225A	$1.30^{+0.12}_{-0.12}$	$0.7^{+0.1}_{-0.1}$	15 - 150 - S	$0.7^{+0.1}_{-0.1}$	...	PL: -1.70
120422A	0.23	0.6	15 - 150 - S	0.6	< 56 (14)	PL: -1.91 (14)
130702A	$5.72^{+0.12}_{-0.12}$	$7.0^{+0.9}_{-0.9}$	10 - 1000 - F	$4.4^{+0.5}_{-0.5}$	...	PL: -2.44
150518A	$0.01^{+0.003}_{-0.003}$ (15)	...	2 - 20 - M	...	...	PL: -1.30 (15)
150818A	$5.3^{+0.7}_{-0.7}$ (16)	$2.4^{+0.3}_{-0.3}$ (16)	20 - 1000 - K*	$2.4^{+0.3}_{-0.3}$	100^{+29}_{-29} (16)	CPL: 100, -1.40 (16)
161219B	$3.1^{+0.8}_{-0.8}$ (17)	$5.3^{+0.4}_{-0.4}$	20 - 1000 - K*	$5.3^{+0.4}_{-0.4}$	91^{+21}_{-21} (17)	CPL: 91, -1.59 (17)
171205A	$6.0^{+1.8}_{-1.8}$ (18)	$1.0^{+0.3}_{-0.3}$	15 - 1500 - K*	$1.0^{+0.3}_{-0.3}$	122^{+111}_{-111} (18)	CPL: 122, -0.85 (18)
180728A-p1	1.59	...	10 - 1000 - F	...	...	PL: -2.31 (19)
180728A-p2	54.3	$231.0^{+1.2}_{-1.2}$	10 - 1000 - F	$155.3^{+0.8}_{-0.8}$	129 (19)	BAND: 129, -1.55, -3.48 (19)
190829A-p1	$2.4^{+0.7}_{-0.7}$ (20)	...	10 - 1000 - F	...	130^{+20}_{-20} (20)	CPL: 130, -1.40 (20)
190829A-p2	$13.8^{+0.4}_{-0.4}$ (20)	$33.5^{+0.5}_{-0.5}$	10 - 1000 - F	$18.2^{+0.3}_{-0.3}$	11^{+1}_{-1} (20)	BAND: 11, -0.92, -2.51 (20)
191019A	$10.40^{+0.26}_{-0.26}$	$5.7^{+0.4}_{-0.4}$	15 - 150 - S	$5.7^{+0.4}_{-0.4}$	54^{+12}_{-12}	PL: -2.26

Notes. For the *Swift*/BAT and *Fermi*/GBM instruments, unless specified, properties are respectively from the *Swift*/BAT (Lien et al., 2016) and the *Fermi*/GBM (Narayana Bhat et al., 2016) catalogs. (a) Energy range and Instrument (abbreviation from Table 7.1) used to obtain the fluence, peak flux and spectral model determination. (b) Peak Flux translated in the $15-150$ keV band, used with T_{90} to plot Fig. 7.3. Units are in ph cm^{-2} s^{-1} (c) Parameters for the spectral model: BAND: $E_{\rm peak}$ (keV), α, β ; CPL: $E_{\rm peak}$ (keV), α ; PL: Γ (*) Fluence and Spectral Model are from Wind/Konus, Peak-Flux is from *Swift*/BAT in the $15-150$ keV energy range.

References. (1) Yamazaki et al. (2003); (2) Sakamoto et al. (2005); (3) Vanderspek et al. (2004); (4) Sazonov et al. (2004); (5) Gotz et al. (2003); (6) Pélangeon et al. (2008); (7) Tagliaferri et al. (2005); (8) Campana et al. (2006); (9) Krimm et al. (2009); (10) Golenetskii et al. (2006a); (11) Stanway et al. (2015); (12) Starling et al. (2011); (13) Tanga et al. (2018); (14) Melandri et al. (2012); (15) Sakamoto et al. (2015); (16) Golenetskii et al. (2015b); (17) Frederiks et al. (2016); (18) D'Elia et al. (2018); (19) Wang et al. (2019); (20) Chand et al. (2020);

Table 7.3 . Intrinsic properties of Long GRBs

Name	Redshift	$E_{\rm peak,i}$ (keV)	$E_{\rm iso}{}^{a}$ ($\times 10^{50}$ erg)
980425	0.0085 [1]	55^{+21}_{-21} [2]	0.01
020903	0.25 [3]	< 6 [4]	0.24 [5]
030329	0.168 [6]	96^{+3}_{-3} [7]	186 [7]
031203	0.105 [8]	> 210 [9]	1.4
040701	0.215 [10]	< 4 [11]	0.8 [11]
050219A	0.211 [12]	109^{+11}_{-11} [13]	6.8
050826	0.297 [14]	...	...
051109B	0.080 [16]	...	0.17
060218	0.033 [18]	5^{+0}_{-0} [19]	0.62 [19]
060505	0.089 [21]	432^{+528}_{-528} [22]	0.57
060614	0.125 [26]	340^{+241}_{-241} [27]	20.13
080517	0.089 [29]	> 60 [29]	0.10 [29]
100316D	0.059 [30]	35^{+7}_{-7} [30]	> 0.59 [30]
111005A	0.013 [31]	...	0.005 [32]
111225A	0.297 [33]	...	18.5
120422A	0.283 [34,35]	< 72 [36]	2.1
130702A	0.145 [37]	...	10.0
150518A	0.256 [39]	...	...
150818A	0.282 [40]	128^{+37}_{-37} [41]	10 [41]
161219B	0.147 [43]	104^{+24}_{-24} [44]	1.6 [44]
171205A	0.037 [46]	126^{+115}_{-115} [45]	0.22 [45]
180728A	0.117 [48]	...	28.1 [47]
190829A	0.079 [49]	...	2.22 [50]
191019A	0.248 [51]	67^{+15}_{-15}	72.1

Notes. [a] (erg) Isotropic energy released between 1 keV and 10 MeV. The values given are either extracted from the literature if mentioned or calculated with the corresponding spectrum and fluence that can be found in Table 7.2

References. (1) Tinney et al. (1998); (2) Yamazaki et al. (2003); (3) Soderberg et al. (2002); (4) Sakamoto et al. (2005); (5) Sakamoto et al. (2004); (6) Greiner et al. (2003); (7) Vanderspek et al. (2004); (8) Prochaska et al. (2003); (9) Sazonov et al. (2004); (10) Kelson et al. (2004); (11) Pélangeon et al. (2008); (12) Rossi et al. (2014); (13) Tagliaferri et al. (2005); (14) Halpern et al. (2006); (15) Mirabal et al. (2007); (16) Perley et al. (2006); (17) Bromberg et al. (2011); (18) Mirabal et al. (2006); (19) Campana et al. (2006); (20) Fynbo et al. (2006); (21) Thoene et al. (2006); (22) Krimm et al. (2009); (23) Ofek et al. (2007); (24) Gal-Yam et al. (2006); (25) Fynbo et al. (2006); (26) Price et al. (2006); (27) Golenetskii et al. (2006a); (28) Zhang et al. (2006); (29) Stanway et al. (2015); (30) Starling et al. (2011); (31) Levan et al. (2011); (32) Tanga et al. (2018); (33) Thoene & de Ugarte Postigo (2014); (34) Schulze et al. (2012); (35) Tanvir et al. (2012); (36) Melandri et al. (2012); (37) Leloudas et al. (2013); (38) Toy et al. (2016); (39) Xu et al. (2015); (40) Sanchez-Ramirez et al. (2015); (41) Golenetskii et al. (2015b); (42) Cano et al. (2017); (43) Tanvir et al. (2016); (44) Frederiks et al. (2016); (45) D'Elia et al. (2018); (46) Izzo et al. (2017); (47) Wang et al. (2019); (48) Rossi et al. (2018); (49) Valeev et al. (2019); (50) Chand et al. (2020); (51) Fynbo et al. (2019);

7.7.2 Short GRBs

Tables 7.4 , 7.5 and 7.6 summarize the information regarding the 10 short GRBs in our sample.

The detection of the kilonova AT2017gfo associated with GRB 170817A (Tanvir et al., 2017) was the first and only detection of a kilonova in real-time. However, by looking into the archive data, some short GRBs have been tentatively associated with a kilonova.

- GRB 050709 has an optical and infrared signal at t > 2.5 days after the trigger, which could be dominated by a kilonova (Jin et al., 2016).
- For GRB 070809, Jin et al. (2020) has found a possible optical kilonova at t $\sim$ 0.47 d after the trigger.
- The work of Lamb et al. (2019) has enabled to find for GRB 160821B the best-sampled kilonova light curve, without having a gravitational wave trigger.
- Troja et al. (2018) associate GRB 150101B to an off-axis short GRB with a kilonova, similar to the well-known GRB 170817A.

The short GRBs in our sample have diverse prompt emission properties:

- Concerning the fluence, the minimum fluence observed is 9×10^{-9} erg cm^{-2} for GRB 050509B while the maximum one is 5.33×10^{-6} erg cm^{-2} for GRB 061201, with the median equal to 3.6×10^{-7} erg cm^{-2}.
- For the 64ms peak flux, the minimum is 3.21 ph cm^{-2} s^{-1} for GRB 070809 and the maximum is 92.1 ph cm^{-2} s^{-1} for GRB 050709, with the median equal to 7.74 ph cm^{-2} s^{-1}.
- For the peak energy of the fluence spectrum, 6 out of the 10 short GRBs do not have any peak energy information. GRB 050709 only has a peak energy for the first part of the GRB, the second part of the burst being best fitted by a power-law (Villasenor et al., 2005). For the remaining 4 short GRBs with a peak energy, the minimum $E_{\rm peak}$ is equal to 84 ± 19 keV for GRB 160821B and the maximum equal to 302^{+214}_{-85} keV for the first part of GRB 060614, with a median of 68 keV from GRB 030329.
- For T_{90} -values, the minimum value is 0.024 s for GRB 050509B, the maximum 160 s for GRB 050709 and the median is 0.90 s.

There are also some differences in the intrinsic properties:

- The closest short GRB that has been detected is GRB 170817A, at a redshift of 0.0093 ($\approx$ 42 Mpc). The furthest one in our local GRB sample is at a redshift of z = 0.287 ($\approx$ 1530 Mpc), GRB 050724. the median redshift of the sample is z = 0.160 ($\approx$ 790 Mpc).
- The minimum isotropic energy detected in the short GRB sample is $E_{\rm iso} = 4 \pm 1 \times 10^{46}$ erg for GRB 170817A (Abbott et al., 2017), while the maximum isotropic energy is equal to 7.65×10^{50} erg for GRB 050724. The median value for the short GRBs is $E_{\rm iso} = 8.6 \times 10^{49}$ erg: there are two orders of magnitude between GRB 170817A and the second dimmest short GRB, GRB 050509B.

Table 7.4 . Detected features for Short GRBs

Name	Instrument(s)[a]	Class	Afterglow[b]	SN/KN	Host	T_{90} (s)[c]
050509B	S	SGRB	X [1]	...	[2]	$0.024^{+0.0089}_{-0.0089}$
050709	H	eeSGRB	XO [3,4]	(KN) [5]	[4]	160 [6]
050724	S	eeSGRB [7]	XOR [8,9]	...	[9]	3^{+1}_{-1} [8]
060502B	S	SGRB	X [10,11]	...	[12]	$0.14^{+0.05}_{-0.05}$
061201	S K	SGRB	XO [13,14]	...	[14]	$0.78^{+0.10}_{-0.10}$
070809	S	SGRB	XO [15]	(KN) [16]	[15]	$1.28^{+0.37}_{-0.37}$
080905A	S F I SUZ	SGRB	XO [17,18]	...	[19,20,18]	$1.02^{+0.08}_{-0.08}$
150101B	S F I	eeSGRB [21]	XO [22]	(KN) [23]	[22]	$0.23^{+0.06}_{-0.06}$
160821B	S F	SGRB	XOR [24,25,26]	(KN) [27,28]	[25]	$0.48^{+0.07}_{-0.07}$
170817A	F K I	llSGRB	XOR [29,30]	KNAT2017gfo [31]		$2.05^{+0.47}_{-0.47}$ [32]

Notes. [a] F for *Fermi*/GBM, H for HETE-2/FREGATE and/or WXM, I for INTEGRAL/IBIS and/or INTEGRAL/SPI, K for Wind/KONUS, S for *Swift*/BAT, SUZ for *Suzaku*/WAM [b] The letters X, O and R stands respectively for X-ray, Optical and Radio afterglow. [c] Unless quoted differently, the T_{90} are measured by the *Swift*/BAT instrument in the $15 - 350$ keV band

References. (1) Gehrels et al. (2005); (2) Prochaska et al. (2005a); (3) Fox et al. (2005); (4) Hjorth et al. (2005); (5) Jin et al. (2016); (6) Villasenor et al. (2005); (7) Barthelmy et al. (2005c); (8) Berger et al. (2005); (9) Prochaska et al. (2005b); (10) Troja et al. (2006); (11) Poole & Troja (2006); (12) Bloom et al. (2006a); (13) Marshall et al. (2006); (14) Holland & Marshall (2006); (15) Perley et al. (2008); (16) Jin et al. (2020); (17) Pagani et al. (2008); (18) Rowlinson et al. (2010); (19) Malesani et al. (2008); (20) de Ugarte Postigo et al. (2008); (21) Burns et al. (2018); (22) Fong et al. (2016b); (23) Troja et al. (2018); (24) Levan et al. (2016); (25) Xu et al. (2016); (26) Fong et al. (2016a); (27) Troja et al. (2019); (28) Lamb et al. (2019); (29) Troja et al. (2017); (30) Hallinan et al. (2017); (31) Tanvir et al. (2017); (32) Narayana Bhat et al. (2016);

Table 7.5 . Spectral properties of Short GRBs

Name	Fluence (10^{-6} erg cm^{-2})	64-ms P.-flux (ph cm^{-2} s^{-1})	Energy Band[a] (keV - Inst.)	P.-flux (norm)[b] (ph cm^{-2} s^{-1})	E_{peak} (keV)	Spectral Model[c]
050509B	$0.007^{+0.002}_{-0.002}$ (1)	1.3 (1)	15 - 150 - S	1.3	...	PL: -1.57
050709-p1	$0.40^{+0.04}_{-0.04}$ (2)	$92.1^{+7.6}_{-7.6}$ (2)	2 - 400 - H	$50.9^{+4.2}_{-4.2}$	84^{+11}_{-11} (2)	CPL: 84, -0.53 (2)
050709-p2	$1.10^{+0.14}_{-0.14}$ (2)	$2.72^{+0.47}_{-0.47}$ (2)	2 - 25 - H	$0.37^{+0.06}_{-0.06}$	...	PL: -1.98 (2)
050724	$1.01^{+0.12}_{-0.12}$	12.05	15 - 150 - S	12.05	...	PL: -1.93
060502B	$0.05^{+0.01}_{-0.01}$	3.4 (1)	15 - 150 - S	3.4	...	PL: -0.99
061201	5.33 (3)	13.2	20 - 3000 - K*	13.2	873^{+458}_{-458} (3)	CPL: 873, -0.36 (3)
070809	$0.102^{+0.015}_{-0.015}$	1.9 (1)	15 - 150 - S	1.9	...	PL: -1.66
080905A	$0.85^{+0.05}_{-0.05}$	3.7 (1)	10 - 1000 - F	2.2	...	PL: -1.33
150101B	$0.238^{+0.015}_{-0.015}$	$10.48^{+1.35}_{-1.35}$	10 - 1000 - F	$5.66^{+0.73}_{-0.73}$	550^{+190}_{-190} (4)	PL: -1.76
160821B	0.168 (5)	$9.16^{+1.19}_{-1.19}$ (5)	10 - 1000 - F	$5.75^{+0.75}_{-0.75}$	84^{+19}_{-19} (5)	CPL: 84, -1.37 (5)
170817A	$0.31^{+0.07}_{-0.07}$ (6)	$3.73^{+0.93}_{-0.93}$	10 - 1000 - F	$2.60^{+0.65}_{-0.65}$	185^{+62}_{-62} (6)	CPL: 185, -0.62 (6)

Notes. For the *Swift*/BAT and *Fermi*/GBM instruments, unless specified, properties are respectively from the *Swift*/BAT (Lien et al., 2016) and the *Fermi*/GBM (Narayana Bhat et al., 2016) catalogs. [(a)] Energy range and Instrument (abbreviation from Table 7.4) used to obtain the fluence, peak flux and spectral model determination. [(b)] Peak Flux translated in the $15 - 150$keV band, used with T_{90} to plot Fig. 7.3 [(c)] Parameters for the spectral model: BAND: E_{peak} (keV), α, β ; CPL: E_{peak} (keV), α ; PL: Γ [(*)] Fluence and Spectral Model are from Wind/Konus, Peak-Flux is from *Swift*/BAT in the $15 - 150$ keV energy range.

References. (1) D'Avanzo et al. (2014); (2) Villasenor et al. (2005); (3) Golenetskii et al. (2006b); (4) Burns et al. (2018); (5) Stanbro & Meegan (2016); (6) Goldstein et al. (2017a);

Table 7.6 . Intrinsic properties of Short GRBs

Name	Redshift	$E_{\rm peak,i}$ (keV)	$E_{\rm iso}{}^{a}$ ($\times 10^{50}$ erg)
050509B	0.225 (1)	...	...
050709	0.161 (3)	...	1 (4)
050724	0.258 (5)	...	7.41
060502B	0.287 (6)	...	...
061201	0.111 (7)	970^{+509}_{-509} (8)	1.4 (9)
070809	0.219 (11)	...	> 0.1 (10)
080905A	0.122 (12)	...	...
150101B	0.134 (14)	624^{+215}_{-215} (15)	0.23 (16)
160821B	0.160 (18)	97^{+22}_{-22} (19)	0.13
170817A	0.0093	187^{+63}_{-63} (22)	0.00053 (16)

Notes. (a) (erg) Isotropic energy released between 1 keV and 10 MeV. The values given are either extracted from the literature if mentioned or calculated with the corresponding spectrum and fluence that can be found in Table 7.5

References. (1) Bloom et al. (2006b); (2) Jin et al. (2016); (3) Price et al. (2005); (4) Villasenor et al. (2005); (5) Prochaska et al. (2005b); (6) Bloom et al. (2006a); (7) Berger et al. (2006); (8) Golenetskii et al. (2006b); (9) Stratta et al. (2007); (10) Jin et al. (2020); (11) Perley et al. (2008); (12) Rowlinson et al. (2010); (13) Troja et al. (2018); (14) Levan et al. (2015); (15) Burns et al. (2018); (16) Abbott et al. (2017); (17) Lamb et al. (2019); (18) Levan et al. (2016); (19) Stanbro & Meegan (2016); (20) Lü et al. (2017); (21) Abbott et al. (2017b); (22) Goldstein et al. (2017a);

7.7.3 SGR Giant-Flares

Tables 7.7 , 7.8 and 7.9 summarize the information detected for the SGR giant flares.

- Concerning the fluence, the minimum fluence observed is 5.6×10^{-9} erg cm^{-2} for GF 050906 while the maximum one is 0.61 erg cm^{-2} for GF 041227, with the median equal to 2.7×10^{-5} erg cm^{-2}.
- For the 64ms peak flux, the minimum is 1.95 ph cm^{-2} s^{-1} for GF 050906 and the maximum is 11.9×10^{6} ph cm^{-2} s^{-1} for GF 041227, with the median equal to 990 ph cm^{-2} s^{-1} for GF 070201.
- For the peak energy of the fluence spectrum, 6 out of the 7 SGR giant flares have spectra showing a peak energy. This is the consequence of the extremely high-luminosity of such events, in addition to the large diversity of instruments that have observed some of them (see Table 7.7). GF 050906 has a fluence model that is best fitted by a power law, mainly because it was a faint burst (5.6×10^{-9} erg cm^{-2}) only detected by *Swift*/BAT. The minimum $E_{\rm peak}$-value is equal to 240 keV for GF 980827 with an OTTB spectrum, the maximum equal to 2080 keV for GF 051103 with a Band spectrum, with a median of 548 keV.
- For T_{90} -values, the minimum value is 0.1 s for GF 051103, the maximum 0.310 s for GF 980827 and the median is 0.2 s for GF 200415A.

There are also some differences in the intrinsic properties:

- The closest Giant Flare detected is GF 041227. At an assumed distance of 8.7 kpc, it comes from one of the two galactic SGRs that have emitted a giant flare (the other being GF 980827). GF 050906 is the furthest one at a distance of 130 Mpc. The median distance of the sample is 0.780 Mpc.
- The minimum isotropic energy detected for the giant flares is $E_{\rm iso} = 4.3 \pm 1 \times 10^{44}$ erg for GF 980827, while the maximum isotropic energy is equal to 8.0×10^{46} erg for GF 050906. The median value is $E_{\rm iso} = 1.2 \times 10^{46}$ erg for GF 041227.

As it can be seen in Table 7.9 , GF 050906 is an outlier among the giant flares, being detected at a distance that is forty times larger than the second most distant Giant Flare GF 051103. This will be discussed further in Section 7.7.3.

Table 7.7 . Detected features for SGR Giant Flares

Name	Instrument(s)[a]	Host	T_{90} (s)	Pulsating Tail
790305	K ICE HEL IS V P	(1)	0.2 (2)	Yes
980827	K B U	(3)	0.31 (4)	Yes
041227	S K I R COR SOP	(5)	0.16 (5)	Yes
050906	S	(6)	$0.13^{+0.02}_{-0.02}$ (7)	No
051103	S	(10)	$0.1^{+0.004}_{-0.004}$ (10)	No
070201	S K I	(11)	0.28 (11)	No
200415A	S F K I	(12)	$0.124^{+0.005}_{-0.005}$ (13)	No

Notes. [(a)] B for BeppoSax/WFC, C for CGRO/BATSE, COR for CORONAS-F, F for *Fermi*/GBM, H for HETE-2/FREGATE and/or WXM, HEL for Helios B, I for INTEGRAL/IBIS and/or INTEGRAL/SPI, ICE for ICE, IS for ISEE 3, K for Wind/KONUS, P for PVO and Prognoz 7, R for RHESSI, S for *Swift*/BAT, SOP for SOPA, U for Ulysses, V for Vela 5A 5B 6A and Venera 11 12

References. (1) Evans et al. (1980); (2) Fenimore et al. (1996); (3) Vrba et al. (2000); (4) Tanaka (2007); (5) Mazets et al. (2005); (6) Levan et al. (2007); (7) Parsons et al. (2005); (8) Lipunov et al. (2005); (9) Cameron & Frail (2005); (10) Hurley et al. (2010); (11) Ofek et al. (2008); (12) Svinkin et al. (2020); (13) Minaev & Pozanenko (2020);

Table 7.8 . Spectral properties of SGR Giant Flare

Name	Fluence (10^{-6} erg cm^{-2})	64-ms P.-flux (ph cm^{-2} s^{-1})	Energy Band[a] (keV - Inst.)	P.-flux (norm)[b] (ph cm^{-2} s^{-1})	E_{peak}/kT (keV)	Spectral Model[c]
790305	4.5×10^2 (1)	1.8×10^4 (1)	30 - 2000 - K	2.0×10^4	246 (1)	OTTB: 246 (1)
980827	$1.6^{+2.0}_{-2.0} \times 10^4$ (2)	5.5×10^5 (2)	15 - 20000 - C	4.4×10^5	240 (3)	OTTB: 240 (3)
041227	$6.1^{+3.5}_{-3.5} \times 10^5$ (4)	11.9×10^6 (4)	20 - 10000 - COR	6.5×10^6	850^{+1259}_{-1259} (5)	CPL: 800, -0.70 (4)
050906	$5.6^{+2.4}_{-2.4} \times 10^{-3}$	$2.0^{+1.0}_{-1.0}$ (6)	15 - 150 - S	$2.0^{+1.0}_{-1.0}$	...	PL: -1.66
051103	$33.3^{+2.1}_{-2.1}$ (7)	245.7 (7)	20 - 10000 - K	23.3	2080^{+180}_{-180} (7)	BAND: 2080, 0.13, -2.78 (7)
070201	$20^{+1}_{-2.6}$ (8)	990.0 (8)	20 - 1200 - K	674.2	296^{+38}_{-38} (8)	CPL: 296, -0.98 (8)
200415A	$5.2^{+0.1}_{-0.1}$ (9)	$74.0^{+2.0}_{-2.0}$ (10)	20 - 10000 - K	$14.6^{+0.4}_{-0.4}$	950^{+50}_{-50} (9)	CPL: 950, 0.07 (9)

Notes. For the *Swift*/BAT and *Fermi*/GBM instruments, unless specified, properties are respectively from the *Swift*/BAT (Lien et al., 2016) and the *Fermi*/GBM (Narayana Bhat et al., 2016) catalogs. [(a)] Energy range and Instrument (abbreviation from Table 7.7) used to obtain the fluence, peak flux and spectral model determination. [(b)] Peak Flux translated in the $15 - 150$keV band, used with T_{90} to plot Fig. 7.3 [(c)] Parameters for the spectral model: BAND: E_{peak} (keV), α, β ; CPL: E_{peak} (keV), α ; PL: Γ ; OTTB: kT (keV) [(*)] Fluence and Spectral Model are from Wind/Konus, Peak-Flux is from *Swift*/BAT in the $15 - 150$ keV energy range.

References. (1) Fenimore et al. (1996); (2) Tanaka (2007); (3) Hurley et al. (1999); (4) Mazets et al. (2005); (5) Frederiks et al. (2007); (6) Parsons et al. (2005); (7) Hurley et al. (2010); (8) Mazets et al. (2008); (9) Bissaldi et al. (2020); (10) Frederiks et al. (2020);

Table 7.9 . Intrinsic properties of SGR Giant Flares

Name	Origin	Distance (kpc)	$E_{\rm peak,i}$ (keV)	$E_{\rm iso}{}^{a}$ ($\times 10^{45}$ erg)
790305*	SGR 0526-66	55 (1)	246 (2)	0.7 (1)
980827	SGR 1900+14	15 (3)	240 (4)	0.43 (5)
041227	SGR 1806-20	8.7 (6)	850^{+1259}_{-1259} (7)	23 (7)
050906	SGR 0331-1439	130000 (8)	...	80
051103	SGR 0952+69	3600 (9)	2082^{+180}_{-180} (9)	75 (9)
070201	SGR 0044+42	780 (10)	296^{+38}_{-38} (1)	1.5 (1)
200415A	...	3500 (11)	951^{+50}_{-50} (12)	12.2 (12)

Notes. (a) Isotropic energy released between 1 keV and 10 MeV. The values given are either extracted from the literature if mentioned or calculated with the corresponding spectrum and fluence that can be found in 7.8 (*) The fluence and spectral properties from Fenimore et al. (1996) given in Table 7.8 have a different dead time correction than the $E_{\rm iso}$ value calculated by Mazets et al. (2008).

References. (1) Mazets et al. (2008); (2) Fenimore et al. (1996); (3) Vrba et al. (2000); (4) Hurley et al. (1999); (5) Tanaka (2007); (6) Hurley et al. (2005); (7) Frederiks et al. (2007); (8) Levan et al. (2007); (9) Hurley et al. (2010); (10) Ofek et al. (2008); (11) Svinkin et al. (2020); (12) Bissaldi et al. (2020);

7.7.4 Summary of *SVOM*/ECLAIRs characteristics

Table 7.10 . Main characteristics and expected performance of *SVOM*/ECLAIRs

Measured property	Value
Energy range	4 – 150 keV
Mode of operation	Photon counting
Time resolution	20 μs
Detecting area	~ 1000 cm^2
Detectors	CdTe
Number of detectors	6400
Size of detectors	4 mm $\times$ 4 mm $\times$ 1 mm
Energy resolution (median)	< 1.6 keV @ 60 keV
Field of view (half-coded / full)	0.9 / 2.0 sr
Coded mask dimensions	54 cm $\times$ 54 cm
Coded mask open fraction	40 %
Coded mask element size	10.4 mm
Detector-Mask distance	46 cm
Telescope PSF	52 arcminute FWHM
Expected performance	**Value**
Effective area at 20 keV	~ 400 cm^2
Background level (empty sky)	~ 4000 cts s^{-1}
Point source localization (90% confidence)	13 arcminute @ SNR = 7
Limiting flux for a 20 s long on-axis GRB	1.5×10^{-8} erg cm^{-2} s^{-1}
Dead time	$\leq 5\%$ for 10^5 cts s^{-1}

7.7.5 Signal-to-Noise Ratio for local high-energy transients

Table 7.11 . SVOM/ECLAIRs Signal To Noise Ratio for Long GRBs

Name	Energy Range (keV)	Time Scale (s)	Count SNR	Image SNR	Fraction FoV
980425	4 - 120	20.48	53.7	52.0	0.86
020903	...	...	< 6.5	< 6.5	...
030329	4 - 120	20.48	2943.0	722.3	0.99
031203	4 - 120	20.48	67.9	63.9	0.89
040701	4 - 25	20.48	17.3	18.3	0.63
050219A	4 - 120	20.48	98.6	86.1	0.92
050826	4 - 120	20.48	< 6.5	7.6	...
051109B	4 - 120	20.48	14.5	16.0	0.56
060218	4 - 25	20.48	13.4	13.8	0.52
060505	4 - 120	5.12	29.9	28.4	0.78
060614-p1	4 - 120	5.12	253.2	134.9	0.97
060614-p2	4 - 120	20.48	613.7	304.7	0.98
080517	4 - 120	20.48	14.1	15.6	0.53
100316D	4 - 120	20.48	14.0	15.8	0.51
111005A	4 - 25	20.48	40.2	39.9	0.83
111225A	4 - 120	20.48	24.8	25.7	0.74
120422A	4 - 120	10.24	9.4	10.4	0.25
130702A	4 - 25	10.24	600.6	246.2	0.98
150518A	...	...	< 6.5	< 6.5	...
150818A	4 - 120	20.48	73.6	68.2	0.90
161219B	4 - 120	5.12	168.0	104.2	0.95
171205A	4 - 120	20.48	15.7	16.6	0.61
180728A-p1	4 - 25	2.56	265.7	115.6	0.97
180728A-p2	4 - 120	5.12	2414.1	470.0	0.98
190829A-p1	4 - 120	5.12	98.2	71.4	0.91
190829A-p2	4 - 25	10.24	1171.6	356.3	0.98
191019A	4 - 25	20.48	402.2	222.6	0.98

Table 7.12 . SVOM/ECLAIRs Signal To Noise Ratio for Short GRBs

Name	Energy Range (keV)	Time Scale (s)	Count SNR	Image SNR	Fraction FoV
050509B	...	...	< 6.5	< 6.5	...
050709-p1	15 - 50	0.01	70.0	8.5	0.35
050709-p2	4 - 120	20.48	15.4	15.9	0.60
050724	4 - 120	0.16	282.3	66.8	0.96
060502B	...	...	< 6.5	< 6.5	...
061201	25 - 120	0.64	26.4	17.1	0.72
070809	4 - 120	1.28	15.9	14.9	0.63
080905A	4 - 120	1.28	20.5	18.9	0.69
150101B	4 - 120	0.04	79.2	24.1	0.85
160821B	4 - 120	0.08	26.7	15.0	0.70
170817A	25 - 120	0.32	13.2	9.5	0.43

Table 7.13 . SVOM/ECLAIRs Signal To Noise Ratio for SGR Giant Flares

Name	Energy Range (keV)	Time Scale (s)	Count SNR	Image SNR	Fraction FoV
790305	25 - 120	0.02	> 10000	337.9	0.31
980827	25 - 120	0.01	> 10000	647.6	0.19
041227	25 - 120	0.01	> 10000	705.7	0.19
050906	...	...	< 6.5	< 6.5	...
051103	25 - 120	0.01	77.0	9.6	0.45
070201	15 - 50	0.01	3113.1	63.3	0.95
200415A	25 - 120	0.01	74.0	9.8	0.44

Notes. The energy range and the timescale given in Tables 7.11 , 7.12 and 7.13 are the configurations for which the best Signal to Noise Ratio displayed in those tables is obtained. The Fraction FoV is the fraction in which both the count SNR and the resulting image SNR are above the SNR limit 6.5.

7.7.6 Light curves used in the simulations

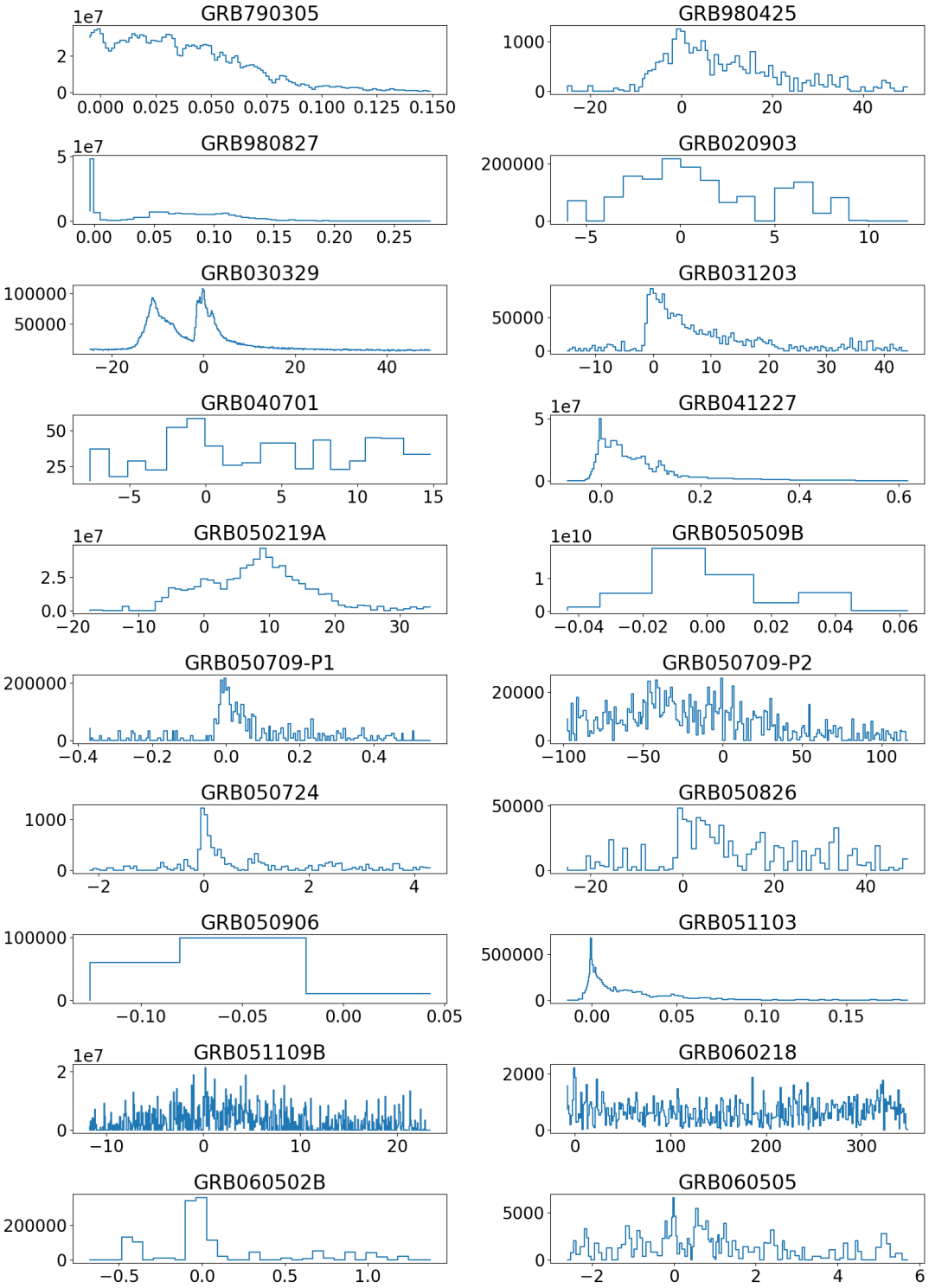

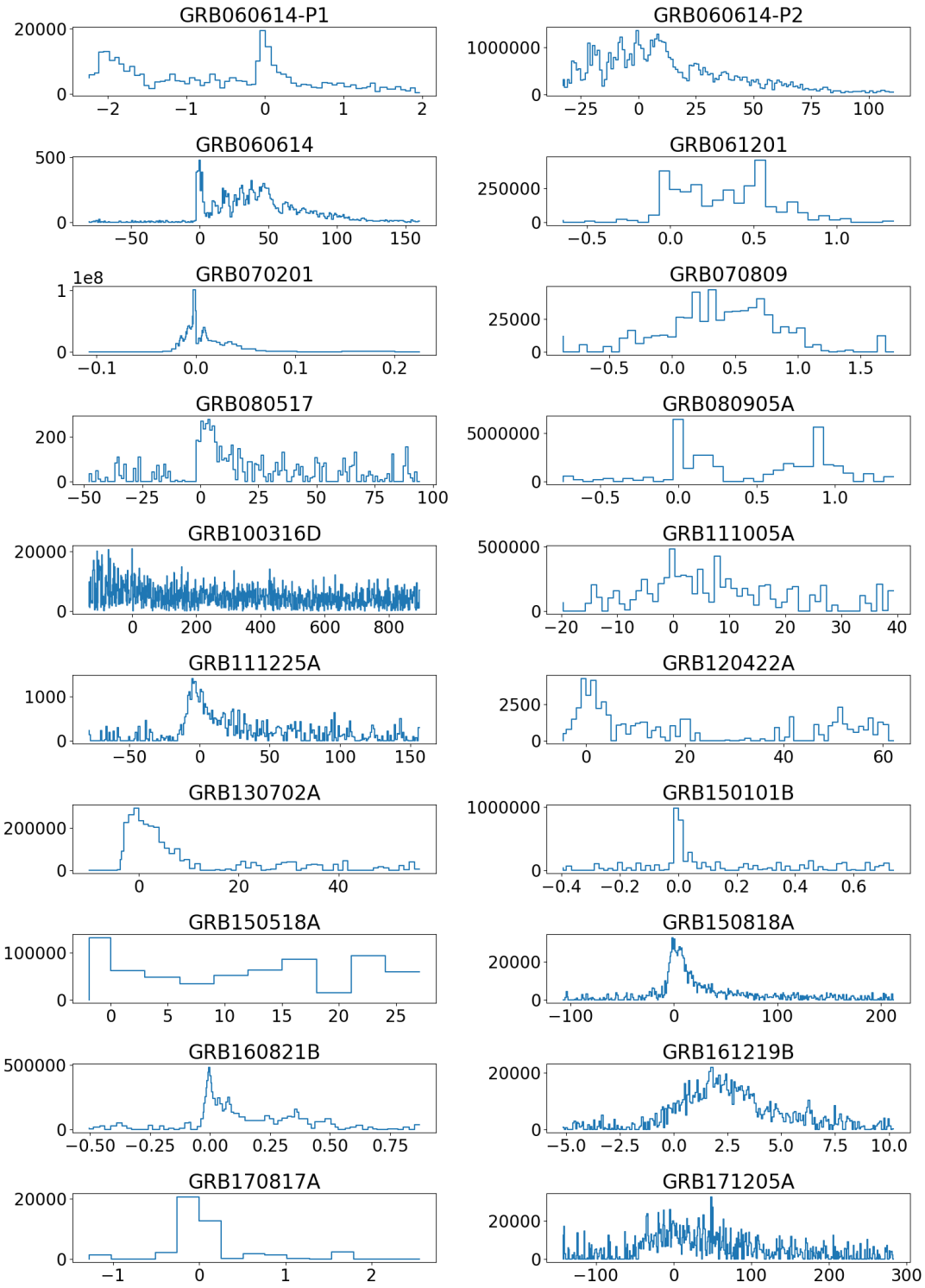
GRB060614-P1
GRB060614-P2
GRB060614
GRB061201
GRB070201
1e8
GRB070809
GRB080517
GRB080905A
GRB100316D
GRB111005A
GRB111225A
GRB120422A
GRB130702A
GRB150101B
GRB150518A
GRB150818A
GRB160821B
GRB161219B
GRB170817A
GRB171205A

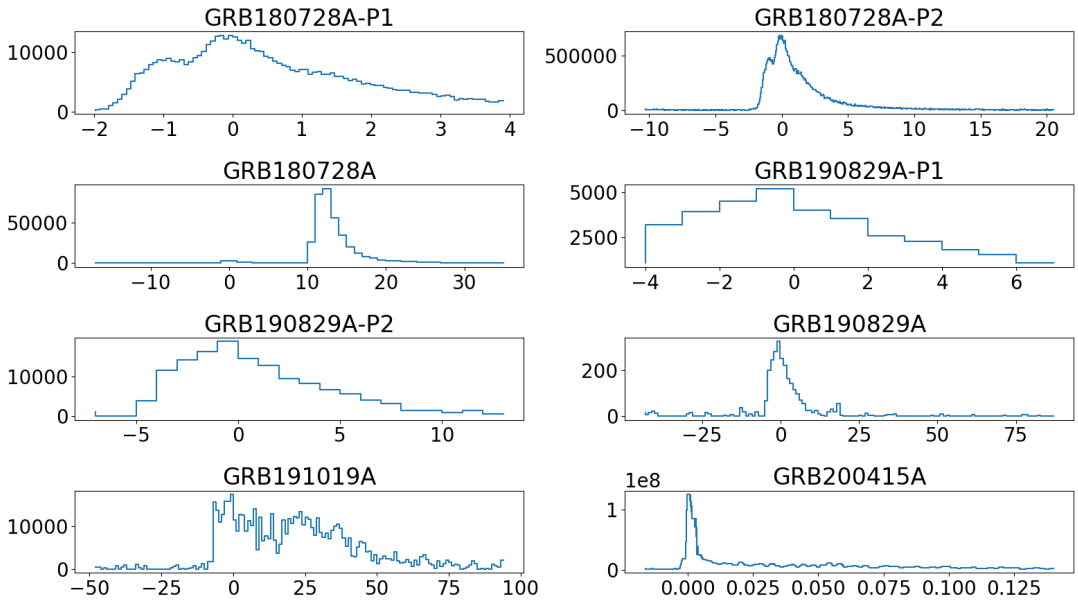

Figure 7.11. light curves used to simulate the photon counts from GRBs in the *movegrb-simulator* program. The x-axis is in s while the y-axis is the expected cnt/ s per bin.

Chapter 8

Are BBH mergers and long GRBs drawn from the same BH population?

This Chapter presents an article written and published during the third year of my Ph.D. It deals with a study exploring the possible connections between two BH populations: the BHs produced during long GRBs and the mergers of binary black holes observed through GW emissions. Section 8.2 presents a method to compare their redshift evolution relative to time, while Sec. 8.3 compares the estimated local rate of these two populations. Finally, these results and their implications are discussed in Sec. 8.4.

Contents

Context

Since the first gravitational wave was detected in 2015 from the coalescence of black holes, $\sim$ 100 events have been detected thanks to LIGO/Virgo interferometers (Abbott et al., 2019, 2020; The LIGO Scientific Collaboration et al., 2021b). The population of BHs observed through the emission of gravitational waves has some intriguing characteristics. For example, some black holes with very high masses are difficult to explain within the current stellar physics, as pair instabilities should emerge in the core of the progenitor star and prevent the creation of such high mass objects (De Luca et al., 2021a; Volonteri et al., 2021). Another intriguing finding is that most black holes detected do not seem to have high angular momentum (The LIGO Scientific Collaboration et al., 2021a), indicating an efficient angular momentum transport within the stellar envelope.

On the other hand, the long GRBs also trace a sub-population of black holes and their progenitors. Moreover, long GRBs require a high angular momentum to form, and binarity is one potential key to fulfilling this condition (Piran & Piran, 2020; Belczynski et al., 2020; Marchant et al., 2021). Therefore, it is natural to investigate to which extent the populations of long GRBs progenitors and binary black hole mergers are linked (e.g. Bavera et al., 2021).

This paper is an extension of the ideas from Atteia et al. (2018), which was focused on the BBHs mergers local rate observed during O1 and O2 and the observed rate of long GRBs. The work uses the additional events recorded during the O3 campaign, meaning that the sample size went from 10 events to 79 events. In addition to better constraints on the local density rate of BBH merger events, this higher number enables us to analyze the redshift distribution of such events.

Contribution

This article was written in collaboration with my supervisor, based on his ideas from his first article (Atteia et al., 2018). The code used to compute the BBH merger rate from an existing population distribution has been written by me, based on the equations from (Atteia et al., 2018). However, these equations have been slightly modified to calculate the GRB delayed density rate at any redshift.

Are binary black hole mergers and long γ-ray bursts drawn from the same BH population?

B. Arcier[1], JL. Atteia[1]

[1]Institut de Recherche en Astrophysique et Planétologie, Université de Toulouse, UPS/CNRS/CNES, 9 Avenue du Colonel Roche, BP44346, F-31028 Toulouse Cedex 4, France.

Corresponding author: Benjamin.Arcier@irap.omp.eu
Published in The Astrophysical Journal in 2022.
https://ui.adsabs.harvard.edu/abs/2022ApJ...933...17A/abstract

Abstract

Since the detection of the first binary black hole (BBH) merger in 2015, $\sim$ 50 gravitational waves (GW) events have been detected, enabling unique measurements of the population of BBH mergers. Similarly, the detection of hundreds of long gamma-ray bursts (LGRBs) with a redshift shows another facet of the population of stellar mass black holes (BHs), since LGRBs are believed to be emitted during the collapse of a massive stellar core leading to the birth of a new BH. This paper compares the population of BBH mergers observed by LIGO/Virgo with selected GRB world models convolved with a delay function. The comparison involves the redshift distribution and the fraction of GRBs required to produce the local rate of BBH mergers measured in the gravitational-wave transient catalogs GWTC-1 and GWTC-2. The comparison of redshift distributions is performed thanks to an N/N_{max} test. For a given model and a merger at redshift z, the ratio N/N_{max} is the number of BBH mergers closer than redshift z divided by the number of BBH mergers within the volume of detection. If the model is correct, the observed BBH merger is randomly chosen among all detectable mergers and N/N_{max} follows a uniform distribution $\mathcal{U}(0,1)$. The distribution of N/N_{max} obtained for BBH mergers from GWTC-1-2 is tested against the expected $\mathcal{U}(0,1)$ distribution with a Kolmogorov-Smirnov test, leading to measure the delay that makes GRB models compatible with the observed population of BBH mergers. We find that BBH mergers and GRBs can be drawn from the same BH population if the bulk of the GRB population observed at redshift $z \approx 2-3$ produces BBHs that are detected by current GW interferometers ($z \leq 0.7-0.8$), implying a delay of at least 6 Gyr between the peak of GRBs formation and the peak of BBH mergers. All our acceptable models predict a rate of mergers that decreases beyond redshift $z \sim 0.8$. Furthermore, we show that few percent of the GRB population is needed to supply all BBH mergers with one or two GRB ancestors. These results will be testable with the run O4.

8.1 Introduction

Black hole (BH) astrophysics is a rapidly evolving field, especially thanks to the discovery of dozens of binary black hole mergers by the LIGO Scientific Collaboration and Virgo Collaboration (LVC). Despite the apparent simplicity of black holes as astrophysical objects, a global vision of their origin and evolution is still missing as well as a full understanding of their role in the evolution of the universe and in the formation of its structures. In such a situation, the comparison of the properties of various BH populations may shed light on their common or diverse origins. We focus here on two populations of stellar mass black holes, which are observed in different contexts: long gamma-ray bursts (long GRBs or LGRBs) and the mergers of stellar mass black holes (BBH mergers).

Long GRBs are the brightest explosions detectable in the electromagnetic domain (e.g. Vedrenne & Atteia, 2009; Atteia et al., 2017). They occur when the core of a massive star collapses into a black hole or an hypermassive magnetar, subsequently ejecting a transient relativistic jet in our direction. The association of LGRBs with stellar collapse is confirmed by the detection of broad-line core-collapse supernovae of type Ibc following several nearby LGRBs ($z \leq 0.3$) after a few days (Galama et al., 1998; Tagliaferri et al., 2006). However, only a small fraction of core collapse supernovae produce LGRBs.

This fraction has been evaluated by Soderberg et al. (2006c), based on volumetric rates of about 9000 $\mathrm{Gpc}^{-3}\,\mathrm{yr}^{-1}$ for supernovae Ibc and $f_\mathrm{b} \times 1$ $\mathrm{Gpc}^{-3}\mathrm{yr}^{-1}$ for classical LGRBs (e.g. Wanderman & Piran, 2010; Palmerio & Daigne, 2021), where f_b is the GRB beaming factor. It is difficult to evaluate the true rate of GRBs, due to large uncertainties on the measurements of the beaming angle of GRB jets (thus on f_b). With typical values of f_b in the range $75 - 250$ (corresponding to jet opening angle in the range $5°-9°$), the classical LGRBs represent from 1 to 3% of SNIbc. This is compatible with another study of Soderberg et al. (2006a), which shows that less than 10% of SNIbc are associated with a successful GRB, based on the radio followup of 68 local supernovae of Type Ibc. We note that this fraction concerns only classical LGRBs, excluding low-luminosity GRBs, which have also been shown to be associated with SNIbc, or choked GRBs, whose jet does not pierce the star's envelope. The rate of low-luminosity GRBs is estimated to be $\sim 100 - 1000$ Gpc^{-3} yr^{-1} (Soderberg et al., 2006c; Liang et al., 2007), comparable or a few times higher than the rate of classical LGRBs. The rate of choked GRBs has not been measured.

The conditions for GRB production by dying massive stars is far from being fully elucidated. MacFadyen & Woosley (1999) emphasized the key role of the angular momentum of the stellar core, which has to be sufficiently large to permit the survival of a massive accretion disk when the BH forms. Before the discovery of BBH mergers with low effective spins by the LVC, it was commonly assumed that GRB progenitors could be single stars with low metallicity, whose weak stellar winds carry away a small fraction of the star angular momentum or stars in binary systems, which are sufficiently close to be tidally locked and keep a high angular momentum (e.g. Woosley & Bloom, 2006; Levan et al., 2016; Chrimes et al., 2020). Except for a few events with an associated supernova, we have only indirect information about the progenitors of LGRBs, because the information is mediated by the

relativistic jet, whose properties are not directly connected with the nature of the progenitor. The population of long GRB progenitors can nevertheless be constrained via statistical studies relying on redshift measurements and the nature of their host galaxies. This has led to the construction of long GRB world models, which describe the history of long GRB formation and are compatible with their observed redshift distribution. (Salvaterra et al., 2012a; Lien et al., 2014; Palmerio & Daigne, 2021)

Contrary to LGRBs, BBH mergers are mostly silent in the electromagnetic domain (see however Farris et al. 2010; Bartos et al. 2017; McKernan et al. 2020 for discussions about the possible emission of electromagnetic transients by BBHs lying in a dense gaseous environment). These cataclysmic events, which have been discovered by the LVC in 2015 (Abbott et al., 2016), release most of their energy in gravitational waves (GW). The origin of these BBH mergers is highly debated, and the variety of systems discovered by the LVC probably calls for multiple populations (Zevin et al., 2021; Wang et al., 2021), however see Bavera et al. 2020. There is nevertheless a broad consensus that most of the mergers detected by the LVC are of astrophysical origin, even if a marginal contribution from primordial black holes remains possible (De Luca et al., 2021b). BBH mergers of astrophysical origin result from the evolution of massive stars, which can be in isolated binary systems or in a dense environment prone to dynamical interactions.

Considering the different biases affecting the detection of BBH mergers and LGRBs, the comparison of these two populations is likely to shed new light on the origin and evolution of stellar mass black holes of astrophysical origin.

In this article, we compare basic statistics concerning these two populations. First a V/V_{max} test is used to compare the redshift distribution of BBH mergers with various delayed long GRB models, where long GRB models are used as proxies for the formation history of stellar mass black holes. This comparison, which takes into account the shape of the redshift evolution independent of the normalization of the two populations, leads us to identify several models compatible which can reproduce the redshift distribution of BBH mergers detected by LVC. In a second step, we compare the rate of BBH mergers measured by LVC with the rate of long GRB. This comparison makes no assumption of a physical connection between the two populations, it only uses the rate of long GRBs as a useful reference for the comparison of populations with different redshift evolution. We find that the progenitors of BBH mergers are rare compared with GRBs. For these two studies the BBH mergers are considered as a single population.
These findings are then briefly discussed in the context of models developed to explain the BBH mergers and the GRBs. Emphasizing the potential role of tidal spin-up for both types of sources, we show that present data allow the existence of a minority of fast-spinning BBH mergers that quickly follow the production of a LGRBs.

This study has been made possible by the publication of the GWTC-2 and GWTC-3 catalogs obtained with the O3 observing run (Abbott et al., 2020; The LIGO Scientific Collaboration et al., 2021b). These catalogs contain 79 BBH mergers with redshifts ranging from $z = 0.05$ to $z = 0.82$ with a median of $z = 0.3$), enabling the comparison of the redshift distributions of BBH mergers with GRBs over the last 7 Gyrs. It follows a first work from Atteia et al.

(2018), based on the GWTC-1 catalog (Abbott et al., 2019) and thus limited to the rates comparison of BBHs and LGRBs.

This paper is organized as follows: in the next two sections we compare the redshift distribution (Sect. 8.2) and the volumetric rate (Sect. 8.3) of BBH mergers and LGRBs. Then, in Sect. 8.4, we briefly discuss the implication of these results in the context of stellar evolution models developed to explain LGRBs and BBH mergers.

In all this paper, we use a flat ΛCDM cosmological model with the parameters measured by the Planck Collaboration: $H_0 = 67.4$ km s^{-1} Mpc^{-1} and $\Omega_m = 0.315$ (Planck Collaboration et al., 2018).

8.2 Redshift distribution

The fast growing number of BBH mergers detected by the LVC provides some indications on their redshift distribution, as discussed in Abbott et al. (2021) and The LIGO Scientific Collaboration et al. (2021a). Using a generalization of the V/V_{max} test developed by Schmidt (1968), we compare here the redshift distribution of 79 BBH mergers detected with high confidence by the LVC with three recent models of classical LGRBs and one star formation history (SFH) model.

8.2.1 Methodology

We use a test called N/N_{max}, which is a variant of the V/V_{max} test developed by Schmidt (1968). These tests are used to assess the compatibility of the volumetric distribution of observed sources with a model. In the V/V_{max} test, the model is used to compute, for each source, the ratio of the volume enclosed by the source to the maximum volume of detection for this source. If the model is correct, the source is randomly chosen among all visible sources and the ratio V/V_{max} follows a uniform distribution $\mathcal{U}(0,1)$. In its simplest form, the V/V_{max} test considers sources without cosmological evolution. For sources with cosmological evolution, the test can be adapted by considering the ratio of the predicted number of sources within the volume enclosed by a source to the number of sources within the maximum volume of detection for this source. When the model is completely defined and the volume of detection is correctly calculated, the V/V_{max} and N/N_{max} tests are hardly affected by selection effects, because each source is placed within its own volume of detection.

The volume of detection of each BBH merger is computed via the determination of its *horizon* $z_{h,i}$, which is the maximum redshift at which this merger could be detected (see below). Knowing the merger event redshift z_i and its horizon redshift $z_{h,i}$, we can compute N_i, the number of sources closer than z_i, and $N_{max,i}$, the number of sources closer than the horizon $z_{h,i}$, for various source models. A model is acceptable if the ratio $N_i/N_{max,i}$ follows a uniform distribution $\mathcal{U}(0,1)$. The agreement of the distribution of $N_i/N_{max,i}$ with $\mathcal{U}(0,1)$ is evaluated with a Kolmogorov-Smirnov test (hereafter, KS test). This comparison does not take into account the normalization of the GRB and BBH merger rates, which is discussed in Sect. 8.3.

The method used to determine the horizon redshift is based on the horizon calculation method proposed in Chen et al. (2021) and the open-source code available at `https://github.com/hsinyuc/distancetool`. The equation to compute the SNR evolution with the redshift is taken from Chen et al. (2021):

$$\mathrm{SNR}_{\mathrm{Ch21}} = \sqrt{4 \int_{f_{\min}}^{f_{\max}} \frac{|h^{+}(f)|^2}{S_{\mathrm{h}}(f)} \mathrm{d}f} \tag{8.1}$$

where $h^{+}(f)$ is the plus polarization of the gravitational-wave merger and $S_{\mathrm{h}}(f)$ is the power spectral density of the interferometer. The calculation of $h^{+}(f)$ depends on the binary properties and its distance relatively to the observer, in addition to the masses m_1 and m_2 of the BBH merger components. This plus polarization is obtained using the `lalsimulation` Python package with the waveform *IMRPhenomD* (as for the online calculator provided by Chen et al. 2021, since m_1 or $m_2 \geq 3$ $\mathrm{M}_{\odot}$). For the term $S_{\mathrm{h}}(f)$, we took the same strain noise curve for LIGO Handford and LIGO Livingston, for a given observing run, already included in the Github repository from Chen et al. (2021).

Contrary to Chen et al. (2021), who define the horizon as the highest redshift at which a BBH merger could be detected with the best antenna pattern (considering that the BBH system is optimally oriented relative to the GW detectors and located in a portion of the sky where the interferometers performances are maximum), we define the horizon as the maximum redshift at which a BBH merger would be detected, *under the conditions of its detection*. Since the antenna pattern does not depend upon distance and cosmology, it is possible to normalize the SNR dependence on redshift with the actual signal-to-noise ratio SNR_0 obtained for a given merger detected at redshift z_0. We obtain the SNR dependence on redshift corrected by the antenna pattern, allowing to compute the horizon redshift for each detected merger.

$$\mathrm{SNR}(z, m_1, m_2) = \frac{\mathrm{SNR}_{\mathrm{Ch21}}(z, m_1, m_2)}{\mathrm{SNR}_{\mathrm{Ch21}}(z_0, m_1, m_2)} \times \mathrm{SNR}_0 \tag{8.2}$$

Taking a threshold $\mathrm{SNR}_{\mathrm{lim}}$, the horizon redshift is the variable $z_{\mathrm{h,i}}$ solving the equation:

$$\mathrm{SNR}(z_{\mathrm{h,i}}, m_1, m_2) = \mathrm{SNR}_{\mathrm{lim}} \tag{8.3}$$

The SNR, mass and detected redshift are taken from the Gravitational Wave Open Science Center (GWOSC) event list[1], created from the GWTC catalogs (Abbott et al., 2019, 2020; The LIGO Scientific Collaboration et al., 2021c,b). In the following, we consider $\mathrm{SNR}_{\mathrm{lim}} = 8$ in agreement with the smallest SNR observed for BBHs mergers (Abbott et al., 2019, 2020), and with the theoretical sensitivities of LIGO/Virgo (Abbott et al., 2018a). Recent merger observations from the deep extended catalog from O3a (The LIGO Scientific Collaboration et al., 2021c) and from GWTC-3 (The LIGO Scientific Collaboration et al., 2021b) have however detected events with a network matched filter SNR below this limit. These events

[1] `https://www.gw-openscience.org/eventapi/html/GWTC/`

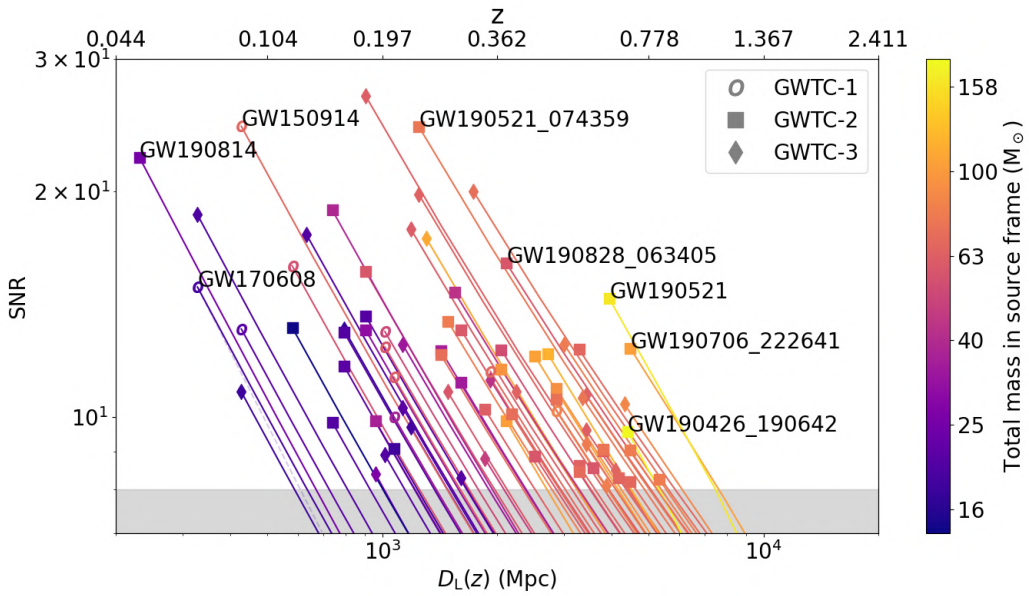

FIGURE 8.1. SNR dependence on redshift for the BBH mergers observed during O1, O2, O3a and O3b. The color coding represents the total mass of the binary in the observer frame, while the marker style represents the catalog in where the events are listed. The dashed line for GW 170608 illustrates a SNR dependency inversely proportional to the luminosity distance.

are not considered in this study. Events with mass m_1 and/or m_2 below 2.4 $M_\odot$ have also been removed, to prevent the contamination from NS-NS or NS-BH merger events.

Table 8.2 gives the horizons of the 79 events used in this article, computed with this method. Figure 8.1 illustrates the redshift dependence and the impact of the shape of the aLIGO power-spectral density (which is not exactly flat), which causes the departure from the inverse luminosity distance law (shown with a faint dashed line for GW 170608). Mergers in GWTC-1, GWTC-2 and GWTC-3 have a broad range of horizons, from z = 0.12 to z = 1.10 with a median z = 0.50. This is the reflection of their mass range, which spans over 1 decade. This broad range of horizons implies very different detection volumes for massive ($\sim 160\ M_\odot$) and less massive BBH mergers ($\leq 20\ M_\odot$), and a mass distribution of detected mergers which is strongly biased in favor of massive BBHs. By construction the N/N_{max} test takes into account this bias by considering the individual contribution of each BBH merger within its own volume of detection.

The N/N_{max} test requires computing N_i, the number of mergers expected up to redshift z_i and $N_{max,i}$, the number of mergers expected up to redshift $z_{h,i}$. This is based on a world model of source population that specifies $\rho(z)$, the evolution of the source density rate with redshift. N_i is computed as follows:

$$N_i = \int_0^{z_i} \rho(z)\ \frac{dV(z)}{dz}\ \frac{1}{1+z}\ dz \tag{8.4}$$

Where $\rho(z)$ is the BBHs merger density rate (in $\mathrm{Gpc}^{-3}\ \mathrm{yr}^{-1}$), $\mathrm{d}V(z)$ is the differential co-moving volume, and the term $1/(1+z)$ accounts for the impact of time dilation when we measure a *rate* of events (Mao & Paczynski, 1992).

We compare here the observed distribution of BBH mergers with several density rate models: a constant rate model, a model of SFH and three GRB world models which all reproduce the observed properties of GRBs detected by the *Swift* and *Fermi* missions. These three models and the SFH are illustrated in Fig. 8.2a.

The first GRB model is proposed by Salvaterra et al. (2012a):

$$\mathcal{R}^{\mathrm{S}}_{\mathrm{GRB}}(z) = \mathcal{R}^{\mathrm{S}}_{0}\ (1+z)^{\delta_{\mathrm{n}}}\ \Sigma^{\mathrm{Li}}_{\mathrm{SFH}}(z) \tag{8.5}$$

based on the cosmic SFH rate from Li (2008):

$$\Sigma^{\mathrm{Li}}_{\mathrm{SFH}}(z) = \frac{a+bz}{1+(z/c)^{d}} \tag{8.6}$$

with $\mathcal{R}^{\mathrm{S}}_{0} = 0.24\ \mathrm{Gpc}^{-3}\ \mathrm{yr}^{-1}$, $\delta_n = 1.7$, $a = 0.0158$, $b = 0.118$, $c = 3.23$ and $d = 4.66$.

The second is proposed by Lien et al. (2014):

$$\mathcal{R}^{\mathrm{L}}_{\mathrm{GRB}}(z) = \mathcal{R}^{\mathrm{S}}_{0} \begin{cases} (1+z)^{\mathrm{n}_1} & \text{if } z < \mathrm{z}_1 \\ (1+\mathrm{z}_1)^{(\mathrm{n}_1-\mathrm{n}_2)}(1+z)^{\mathrm{n}_2} & \text{if } z \geq \mathrm{z}_1 \end{cases} \tag{8.7}$$

with $\mathcal{R}^{\mathrm{L}}_{0} = 0.42\ \mathrm{Gpc}^{-3}\ \mathrm{yr}^{-1}$, $n_1 = 2.07$, $n_2 = -0.7$ and $\mathrm{z}_1 = 3.6$.

The third is proposed by Palmerio & Daigne (2021):

$$\mathcal{R}^{\mathrm{P}}_{\mathrm{GRB}}(z) = \mathcal{R}^{\mathrm{P}}_{0} \begin{cases} e^{az} & \text{if } z < \mathrm{z}_{\mathrm{m}} \\ e^{(a-b)\mathrm{z}_{\mathrm{m}}} e^{bz} & \text{if } z \geq \mathrm{z}_{\mathrm{m}} \end{cases} \tag{8.8}$$

with $\mathcal{R}^{\mathrm{P}}_{0} = 1.0\ \mathrm{Gpc}^{-3}\ \mathrm{yr}^{-1}$, $a = 1.1$, $b = -0.57$ and $\mathrm{z}_{\mathrm{m}} = 1.9$.

Since the population of BBHs mergers is probably not directly tracing the GRB population, we also consider delayed models with a delay function between the GRB emission (when the BH is created) and the transient GW emission (when the BH merges with its companion). This approach is similar to the studies that compare the rates of binary neutron star mergers and short GRBs (Nakar, 2007; Wanderman & Piran, 2015). Considering a time delay probability density function $f(\tau)$ and integrating over all possible time delays, the calculation of the BBH merger rate at redshift z_0 becomes:

$$\rho(z_0) \propto \int_{z_0}^{\infty} \mathcal{R}_{\mathrm{GRB}}(z)\ f(T_c(z) - T_c(z_0))\ \frac{\mathrm{d}T_c}{\mathrm{d}z}\ \mathrm{d}z \tag{8.9}$$

where $T_c(z)$ is the lookback time at redshift z, and $\tau = T_c(z) - T_c(z_0)$ is the time delay in Gyr between a GRB at redshift z and a merger produced at redshift $z_0 < z$. In practice, a limiting redshift $z_{\mathrm{lim}} = 20$ has been chosen for the calculation of the integral, and we have

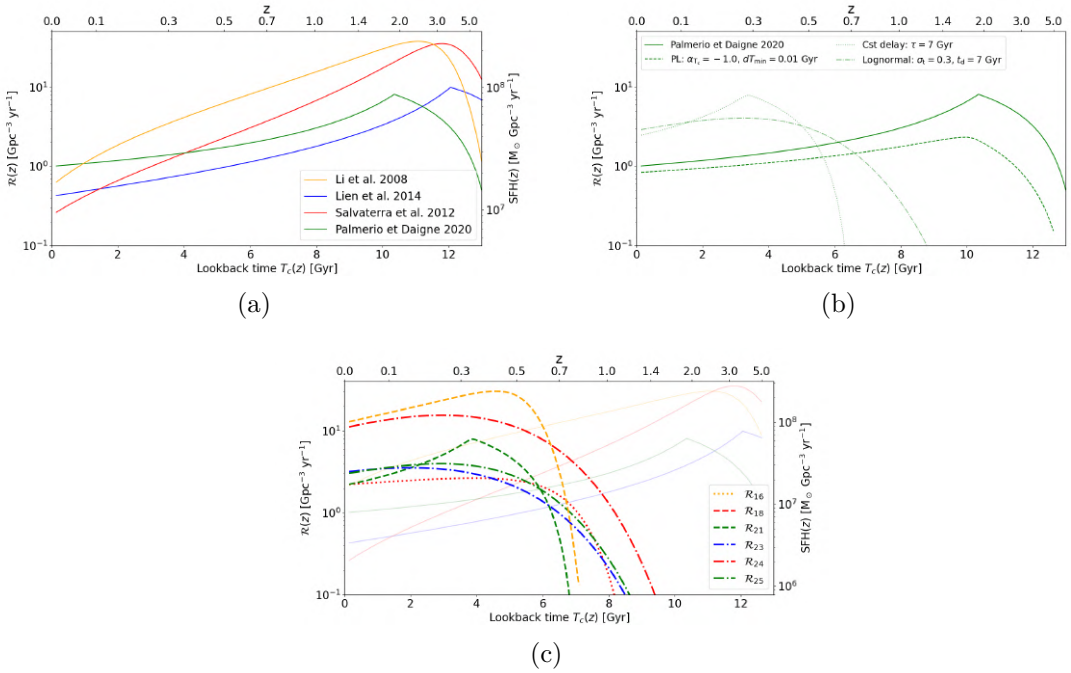

(a) (b)

(c)

FIGURE 8.2. (a) GRB density rate for the three GRB world models (blue, red and green) and the SFH (orange). (b) GRB density rate obtained from Palmerio & Daigne convolved with three shapes of the delay function: dotted for the power-law shape, dashed for the constant delay shape and dash-dotted for a lognormal shape. (c) (c) Some models with a p-value above 0.1 (dotted and dashed lines). The corresponding models can be found in Table 8.1 . The faint full line plots are the GRB/SFH models before the delay function convolution.

verified that changing this value from 20 to 100 has no significant impact on the results. The delay function $f(\tau)$ can have several shapes, and in the following we consider three of them: a power-law, a lognormal distribution, and a constant delay.

The power-law has two parameters: a negative slope α (for example $\alpha = -1$ in Belczynski et al. 2016) and a minimum merging time $dT_{\rm min}$. It is described by:

$$f(\tau) = \begin{cases} 0 & \tau \leq dT_{\rm min} \\ \tau^{\alpha} & \tau > dT_{\rm min} \end{cases} \tag{8.10}$$

The lognormal distribution of width $\sigma_{\rm t}$ centered around a time delay $t_{\rm d}$ is described by:

$$f(\tau) = \frac{1}{\tau\sigma_{\rm t}\sqrt{2\pi}} \exp\left(-\frac{\ln(\tau/t_{\rm d})^2}{2\sigma_{\rm t}^2}\right) \tag{8.11}$$

The constant delay is modeled by setting a small dispersion of the lognormal distribution (typically $\sigma_t = 0.01$). This is how the constant delay GRB density rate presented on Fig. 8.2b has been created. From the GWTC-1, GWTC-2 and GWTC-3 catalogs, the maximum redshift observed for a BBHs merger is $z = 0.71$, which represents a lookback time of ~ 6.5 Gyr, with the cosmology used in this paper. For this reason, we have not considered constant delay models with a delay greater than 7 Gyr, which would lead to produce the most distant BBH mergers before the Big Bang. The differential of the lookback time at redshift z is calculated using the definition of the lookback time in Condon & Matthews 2018:

$$\frac{\mathrm{d}T_c}{\mathrm{d}z}(z) = \frac{1}{H(z)(1+z)} \tag{8.12}$$

Fig. 8.2b illustrates the impact of these different delay functions on the GRB model of Palmerio & Daigne 2021.

8.2.2 Results

Using the $\mathrm{N/N_{max}}$ test defined in the previous section, we now compare the redshift distribution of BBH mergers in the GWTC catalogs with various delayed GRB models. A model is considered acceptable if the KS test gives a p-value larger than 1% and favored if the p-value exceeds 10%. This is illustrated in Fig. 8.3, which compares the cumulative $\mathrm{N/N_{max}}$ distributions of various models with the data. The light grey zone indicates the 99% confidence region, while the dark grey zone the 90% confidence interval: a model is accepted at a given confidence level if its $\mathrm{N/N_{max}}$ cumulative distribution function lies entirely inside the grey zone.

The values of $\langle \mathrm{N/N_{max}} \rangle$, the mean of the $\mathrm{N/N_{max}}$ distribution, and the p-values of the KS test are given in Table 8.1 for selected models. The first 5 models are a constant density rate evolution in addition to the SFH and the three GRB models presented in the methodology section, without any delay. They are followed by 12 models with a power-law delay function, with two values of the power-law index, $\alpha = -2$, and $\alpha = -1$, and two values of dT_{min}, 0.01 and 5 Gyr. The first value of dT_{min} is standard for such models, while larger values of this parameter have been used to explore its impact on the rate density distributions. Finally, we also consider 12 models with a lognormal delay function, with three values of the dispersion: $\sigma_t = 0.01$, 0.3 and 1.0, and for each of them we indicate the delay t_d that gives the largest p-value. As explained before, the model with $\sigma_t = 0.01$ is equivalent to a constant delay model.

According to Table 8.1 , ten models have p-values larger than 10% (favored models), while 11 models have a p-value between 1 and 10%. All favored models are delayed models, with a significant delay between the GRB and the merger event:

- The SFH model and the GRB models of Salvaterra et al., Lien et al. and Palmerio & Daigne convolved with a power-law delay function with $\alpha = -1$ and $dT_{\mathrm{min}} = 5$ Gyr ($\mathcal{R}_{14}$, $\mathcal{R}_{15}$, $\mathcal{R}_{16}$, $\mathcal{R}_{17}$).

Table 8.1 . Results of the Kolmogorov-Smirnov test for various population models (see text). The p-values of favored models are indicated in boldface.

#	Population model	Delay parameters	p-value	$\langle N/N_{max} \rangle$	Fig.
$\mathcal{R}_1$	Constant	...	*0.035*	0.452	8.3
$\mathcal{R}_2$	SFH: Li (2008)	...	0.001	0.389	8.2(a), 8.3
$\mathcal{R}_3$	GRB: Lien et al. (2014)	...	0.005	0.406	8.2(a)
$\mathcal{R}_4$	GRB: Salvaterra et al. (2012a)	...	0.000	0.356	8.2(a)
$\mathcal{R}_5$	GRB: Palmerio & Daigne (2021)	...	*0.014*	0.417	8.2(a), 8.2(b)
$\mathcal{R}_6$	SFH: Li (2008)	PL, $dT_{min} = 0.01$ Gyr, $\alpha = -1.0$	0.006	0.412	...
$\mathcal{R}_7$	GRB: Lien et al. (2014)	PL, $dT_{min} = 0.01$ Gyr, $\alpha = -1.0$	*0.012*	0.419	8.3
$\mathcal{R}_8$	GRB: Salvaterra et al. (2012a)	PL, $dT_{min} = 0.01$ Gyr, $\alpha = -1.0$	0.003	0.401	...
$\mathcal{R}_9$	GRB: Palmerio & Daigne (2021)	PL, $dT_{min} = 0.01$ Gyr, $\alpha = -1.0$	*0.017*	0.425	8.2(b)
$\mathcal{R}_{10}$	SFH: Li (2008)	PL, $dT_{min} = 0.01$ Gyr, $\alpha = -2.0$	0.001	0.390	...
$\mathcal{R}_{11}$	GRB: Lien et al. (2014)	PL, $dT_{min} = 0.01$ Gyr, $\alpha = -2.0$	0.005	0.406	...
$\mathcal{R}_{12}$	GRB: Salvaterra et al. (2012a)	PL, $dT_{min} = 0.01$ Gyr, $\alpha = -2.0$	0.000	0.357	...
$\mathcal{R}_{13}$	GRB: Palmerio & Daigne (2021)	PL, $dT_{min} = 0.01$ Gyr, $\alpha = -2.0$	*0.014*	0.417	...
$\mathcal{R}_{14}$	SFH: Li (2008)	PL, $dT_{min} = 5.0$ Gyr, $\alpha = -1.0$	**0.799**	0.517	...
$\mathcal{R}_{15}$	GRB: Lien et al. (2014)	PL, $dT_{min} = 5.0$ Gyr, $\alpha = -1.0$	**0.144**	0.463	8.2(c)
$\mathcal{R}_{16}$	GRB: Salvaterra et al. (2012a)	PL, $dT_{min} = 5.0$ Gyr, $\alpha = -1.0$	**0.325**	0.476	...
$\mathcal{R}_{17}$	GRB: Palmerio & Daigne (2021)	PL, $dT_{min} = 5.0$ Gyr, $\alpha = -1.0$	**0.676**	0.524	...
$\mathcal{R}_{18}$	SFH: Li (2008)	Cst Delay, $\tau = 6.5$ Gyr	**0.533**	0.494	8.3
$\mathcal{R}_{19}$	GRB: Lien et al. (2014)	Cst Delay, $\tau = 7.0$ Gyr	*0.014*	0.422	...
$\mathcal{R}_{20}$	GRB: Salvaterra et al. (2012a)	Cst Delay, $\tau = 7.0$ Gyr	*0.035*	0.458	8.2(c)
$\mathcal{R}_{21}$	GRB: Palmerio & Daigne (2021)	Cst Delay, $\tau = 6.5$ Gyr	**0.255**	0.502	8.2(b), 8.2(c)
$\mathcal{R}_{22}$	SFH: Li (2008)	logNorm, $t_d = 7.3$ Gyr, $\sigma_t = 0.3$	**0.966**	0.499	...
$\mathcal{R}_{23}$	GRB: Lien et al. (2014)	logNorm, $t_d = 10.0$ Gyr, $\sigma_t = 0.3$	**0.892**	0.519	8.2(c)
$\mathcal{R}_{24}$	GRB: Salvaterra et al. (2012a)	logNorm, $t_d = 8.6$ Gyr, $\sigma_t = 0.3$	**0.990**	0.498	...
$\mathcal{R}_{25}$	GRB: Palmerio & Daigne (2021)	logNorm, $t_d = 7.3$ Gyr, $\sigma_t = 0.3$	**0.986**	0.504	8.2(b), 8.2(c), 8.3
$\mathcal{R}_{26}$	SFH: Li (2008)	logNorm, $t_d = 5.0$ Gyr, $\sigma_t = 1.0$	*0.023*	0.437	...
$\mathcal{R}_{27}$	GRB: Lien et al. (2014)	logNorm, $t_d = 5.0$ Gyr, $\sigma_t = 1.0$	*0.012*	0.424	...
$\mathcal{R}_{28}$	GRB: Salvaterra et al. (2012a)	logNorm, $t_d = 5.0$ Gyr, $\sigma_t = 1.0$	0.007	0.416	...
$\mathcal{R}_{29}$	GRB: Palmerio & Daigne (2021)	logNorm, $t_d = 5.0$ Gyr, $\sigma_t = 1.0$	*0.017*	0.436	...

- The SFH model and the GRB model of Palmerio & Daigne convolved with a constant delay function of 7 Gyr ($\mathcal{R}_{18}$, $\mathcal{R}_{21}$).
- The SFH model and the GRB models of Lien et al., Salvaterra et al. and Palmerio & Daigne convolved with a lognormal delay function with $\sigma_t = 0.1$ or 0.3 and optimal t_d values ($\mathcal{R}_{22}$, $\mathcal{R}_{23}$, $\mathcal{R}_{24}$, $\mathcal{R}_{25}$).

Some favored models are shown in Fig. 8.2c, for instance the model of Lien et al. with a delay $t_d = 10$ Gyr and a dispersion $\sigma_t = 0.3$ ($\mathcal{R}_{23}$). A common feature of these models is the decreasing density of mergers beyond $z \approx 0.8$. This is due to the fact that the temporal delay between the GRB and the merger transforms the peak of GRB production (at $z \approx 2 - 3$) into a peak of merger production at $z \approx 0.5$.

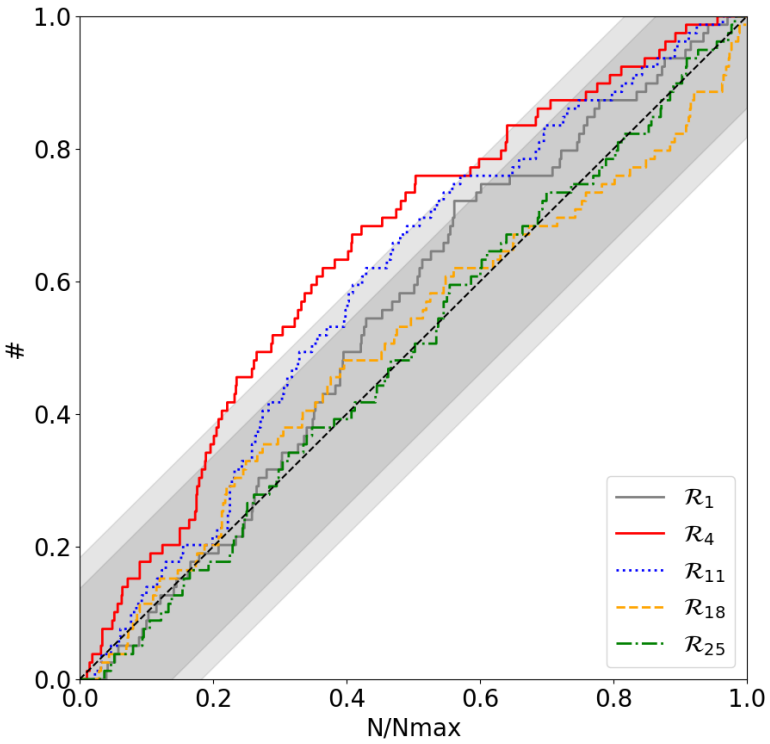

FIGURE 8.3. Comparison of N/N_{max} cumulative distributions with the expected $\mathcal{U}(0,1)$ distribution. The shaded areas represent the 1% and 10% acceptance regions for the KS test. $\mathcal{R}_1$ represents the constant model, $\mathcal{R}_4$ the GRB model from Salvaterra et al. (2012a), $\mathcal{R}_{11}$ the GRB model from Lien et al. (2014) convolved with a PL delay function (with $\alpha = -2$ and $dT_{min} = 0.01$ Gyr), $\mathcal{R}_{18}$ the SFH from Li (2008) with a constant delay of 6.5 Gyr and $\mathcal{R}_{25}$ the GRB model from Palmerio & Daigne (2021) convolved with a lognormal delay function (with $t_d = 7.3$ Gyr and $\sigma_t = 0.3$).

Regarding models which are not-favored (rejected or simply acceptable), they all have values of $< N/N_{max} >$ below 0.5, indicating that they predict too many distant BBH mergers, compared with GW observations. This is well illustrated by the cumulative distribution function of N/N_{max} for models $\mathcal{R}_4$ or $\mathcal{R}_{11}$ in Fig. 8.3.

Figure 8.4 provides an insight into the impact of the delay for the three delay functions studied here, it emphasizes some trends: (*i*) SFH or GRB populations with no or short delay are not favored; (*ii*) When a delay is included, the three delay functions can reproduce the observed distribution if the delay is sufficiently large: larger than ~ 6 Gyr for the constant and lognormal delay functions, and dT_{min} larger than ~ 4 Gyr for the power-law delay function; (*iii*) Delays with a broad distribution (e.g. a lognormal distribution with $\sigma_t = 1$ or a power-law distribution with dT_{min} smaller than 4 Gyr) are not favored, and finally, (*iv*)

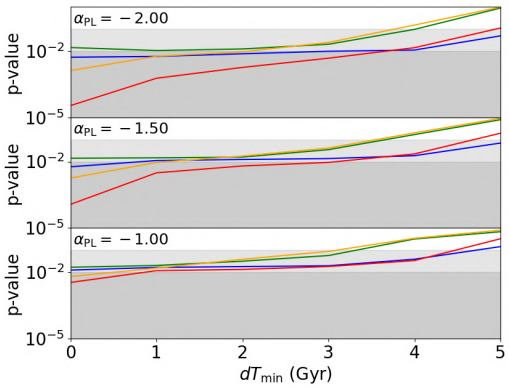

(a) Power-Law delay function

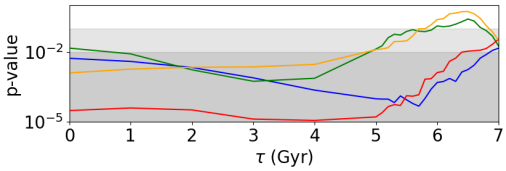

(b) Constant delay function

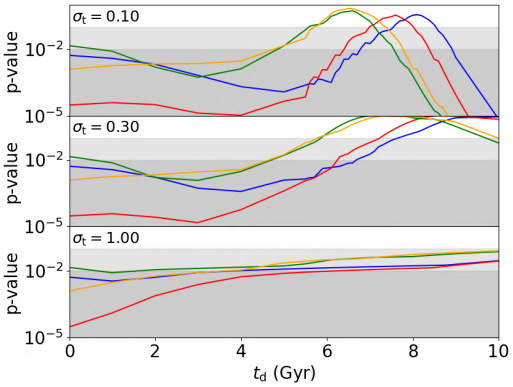

(c) Lognormal delay function

FIGURE 8.4. Evolution of the p-value with the delay, for various delay functions applied to the three GRB world models considered in the paper (blue, red and green for respectively Lien et al. 2014, Salvaterra et al. 2012a and Palmerio & Daigne 2021) and the SFH from Li (2008) in orange. The shaded light-grey and dark-grey areas represent the thresholds p-values for the accepted and favored models, respectively set to 1% and 10%.

the crucial parameter for the power-law distribution is $dT_{\rm min}$, the slope playing a marginal role.

8.2.3 Impact of systematics

These conclusions rely on the accuracy of the redshift measurement by LVC and on the calculation of the merger horizon.

The effect of redshift uncertainties on the p-values has been investigated using the redshift limits given in GWTC-1, GWTC-2 and GWTC-3. The redshifts of BBH mergers are poorly constrained in these catalogs, with a relative median redshift uncertainty of 39%. We have

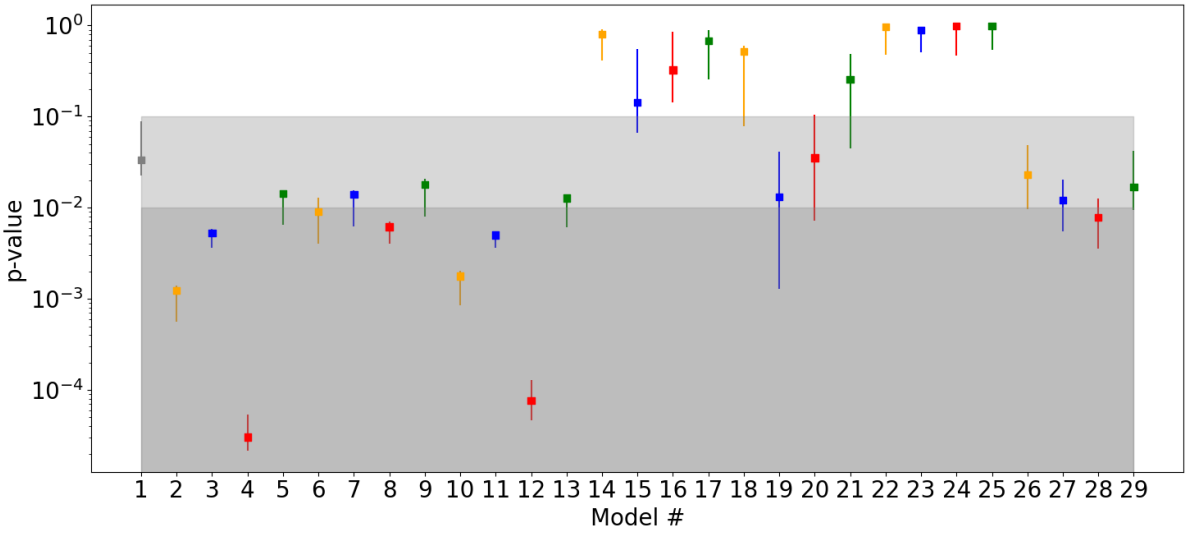

Figure 8.5. Effect of the redshift uncertainties on the p-values obtained for the selected models. The range displayed is the 90% confidence interval on the p-value. The shaded grey area represents the threshold below which models are rejected, set to 1%

randomized the redshift values given in the catalog (assuming that the incertitude on the redshift could be modeled by two half-Gaussian distributions whose standard deviations are equal to the 90% confidence interval divided by 1.65) and tested 10,000 times the p-value obtained for each model. Figure 8.5 shows the 90% confidence interval obtained for the p-values of a given model. When the redshift uncertainty is taken into account, the accepted models $\mathcal{R}_5$ $\mathcal{R}_7$, $\mathcal{R}_9$, $\mathcal{R}_{13}$, $\mathcal{R}_{19}$, $\mathcal{R}_{20}$, $\mathcal{R}_{27}$ and $\mathcal{R}_{29}$ can be rejected for some cases of redshift, while models $\mathcal{R}_6$ and $\mathcal{R}_{28}$ become acceptable. These models are referred as marginally acceptable in the remaining of the paper. The list of favored models does not change, except for model $\mathcal{R}_{15}$, $\mathcal{R}_{18}$ and $\mathcal{R}_{21}$ that becomes only acceptable for some cases. These models are referred as marginally favored in the remaining of the paper.

We conclude that our study is marginally sensitive to statistical uncertainties on the measured merger redshifts. The findings of this article, discussed in the next section, are mainly limited by the number of BBH mergers detected until now.

8.3 The rate of BBHs

In this section, we evaluate the rate density of BBH merger progenitors necessary to produce the BBH mergers density rate observed by LVC, considering favored and marginally favored models identified in Sec. 8.2 (with a p-value larger than 10%). This density rate will be expressed in terms of the LGRBs density rate, the models using the SFH density rate evolution are therefore not considered here. Using the LGRB density rate as a reference does not imply a connection between LGRBs and BBH mergers, this is just a convenient

way of specifying the density rate. We defer to section 8.4 the discussion of the possible connections between the two populations.

8.3.1 Methodology

Following the approach of Equ. 8.9, we write the expected rate of BBHs mergers $\rho(z_0)$ as a function of their birth rate $\mathcal{R}_{\rm BBHs}(z)$ and the normalized delay distribution $f(z, z_0)$:

$$\rho(z_0) = \int_{z_0}^{\infty} \mathcal{R}_{\rm BBHs}(z)\ f(z, z_0) \frac{{\rm d}T_c}{{\rm d}z} {\rm d}z \tag{8.13}$$

The best measurement of the BBH merger rate density in GWTC-3 (The LIGO Scientific Collaboration et al., 2021a) occurs at $z = 0.2$. For this reason, the equation above will be computed at $z_0 = 0.2$ to get an estimation of the fraction as precise as possible. Using the LGRB rate as a reference, the BBH birth rate $\mathcal{R}_{\rm BBHs}(z)$ can be linked to the observed LGRBs rate using two factors, $f_{\rm b}$ and η_0:

$$\mathcal{R}_{\rm BBHs}(z) = \eta_0 \times f_{\rm b} \times \mathcal{R}_{\rm GRB}(z) \tag{8.14}$$

The beaming factor $f_{\rm b}$ represents the ratio of total number of LGRBs to the number of *detected* LGRBs pointing towards us. It is sometimes expressed relatively to the jet opening angle θ, as $f_{\rm b} = (1 - \cos\theta)^{-1}$. It is assumed to be independent of redshift.

The parameter η_0 is a normalization factor to be applied to LGRBs density rate to reproduce the observed rate of BBH mergers. η_0 is the number that we aim to constrain in this section, as it permits to compare the relative rates of BBH mergers and LGRBs. η_0 has been assumed constant and independent of redshift in this analysis. However, it is also possible to assume a difference in evolution between massive BBHs and GRBs, favoring or disfavoring the production of BBH systems relatively to the LGRBs. This evolution can follow a simple parametrization of the density population (e.g. $\eta(z) = \eta_0(1+z)^{0.6}$, similarly as in Salvaterra et al. 2012a). It can also be assumed that the BBHs production is favored at low metallicity, meaning that the evolution of $\eta(z)$ is inversely proportional to the metallicity evolution ($\eta(z) = \eta_0 10^{0.15z}$, using the metallicity evolution from Li 2008). In both models, this factor boosts the BBHs density evolution by a factor $\times 2$ at $z = 2$ compared to LGRBs.

Given the two equations above, it is possible to compute the fraction η_0 as:

$$\eta_0 = \frac{\rho(z_0)}{f_{\rm b}} \times \left(\int_{z_0}^{\infty} \mathcal{R}_{\rm GRB}(z)\ f(z, z_0) \frac{{\rm d}T_c}{{\rm d}z} {\rm d}z \right)^{-1} \tag{8.15}$$

8.3.2 Results

Figure 8.6 shows the values of η_0 calculated for the 7 favored models in the previous section, for two values of the GRB beaming factor, $f_{\rm b} = 250$ and $f_{\rm b} = 70$, respectively corresponding

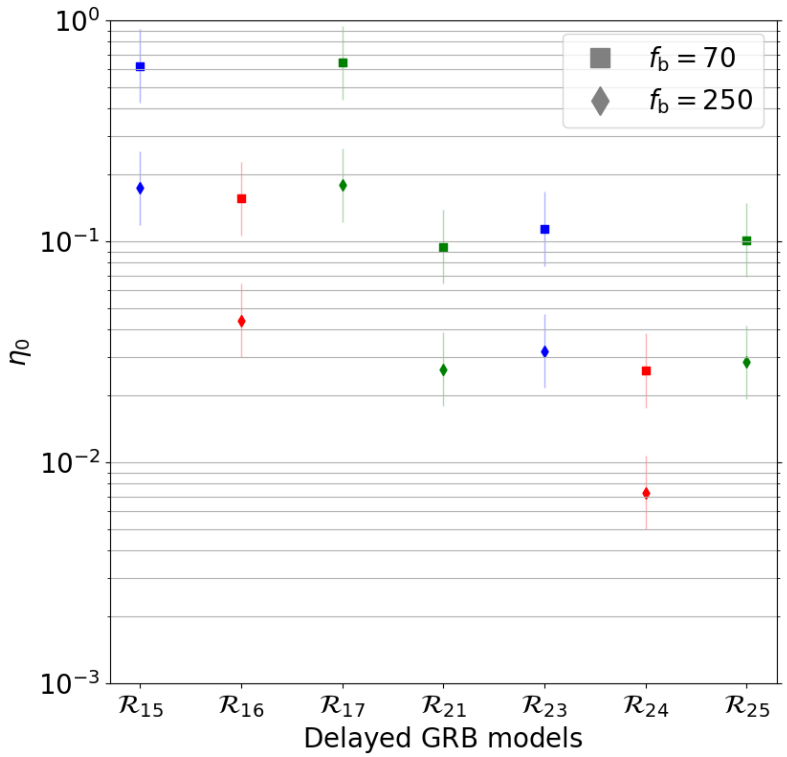

Figure 8.6. The rate of BBH mergers in units of the LGRB rate, for the 7 favored GRB models. The error reflects the incertitude on the value of $\rho(z_0 = 0.2)$. The marker shapes represent combinations of beaming factors ($f_b = 70, 250$).

to jet opening angles of about 5 and 9 degrees. In the rest of the discussion, we consider $f_b = 250$ as a typical value (Goldstein et al., 2016; Tsvetkova et al., 2017; Lamb et al., 2021), while $f_b = 70$ is to be considered as a lower bound to the beaming factor. For the BBH mergers rate $\rho(z_0)$, we adopt the value given in the GWTC-3 catalog (The LIGO Scientific Collaboration et al., 2021a), $\rho(z_0 = 0.2) = 19 - 41$ Gpc^{-3} yr^{-1}. Taking into account the uncertainties on LVC BBH mergers local density rate, equation 8.15 gives a large range of predictions for η_0, ranging from ~ 0.01 to ~ 1 (see Fig. 8.6). Considering the beaming factor $f_b = 250$, the value of η_0 is typically of few percents for models $\mathcal{R}_{16}$, $\mathcal{R}_{21}$, $\mathcal{R}_{23}$ and $\mathcal{R}_{25}$, going up to ten percents for models $\mathcal{R}_{15}$ and $\mathcal{R}_{17}$ and as low as few tenths of a percent for model $\mathcal{R}_{24}$. The values for a beaming factor $f_b = 70$ are about three times larger. We note that for models $\mathcal{R}_{15}$, $\mathcal{R}_{16}$ and $\mathcal{R}_{17}$, the delay between the GRB and the merger follows a power-law with DTmin = 5 Gyr, meaning that there is no merger during 5 Gyr after a LGRB. These models, while acceptable from a statistical point of view, seem little realistic from an astrophysical point of view.

Figure 8.6 also shows that this ratio is below 1 for all acceptable models and f_b larger than 70. If BBH mergers and LGRBs come from the same BH population, BBH mergers must

be rarer than LGRBs. Considering $f_b = 250$ as previously justified, BHs in BBH mergers may represent at most a few percent of those produced in LGRBs. The vast majority of BHs produced in LGRBs do not end their lives in BBH mergers.

8.4 Discussion

8.4.1 Constraints on the BBH merger population

Section 8.2 shows that BBH mergers and LGRBs cannot have the same formation history, unless BBH mergers have a long coalescence time of several Gyr. We briefly discuss this assumption here. Since the LGRB formation rate peaks about 2-3 Gyr after the big bang, models that consider a delay of t_d Gyr between the GRB and the merger predict a peak of mergers at 3+t_d Gyr after the big bang. For values of t_d smaller than 5 Gyr, this peak occurs beyond the horizon of GW interferometers, leading to a rate of BBHs that steadily increases with the redshift in the range of current GW interferometers ; such models are not compatible with the data. On the other hand, models with a longer delay ($t_d \approx 5 - 6$ Gyr), which lead to a peak of BBH mergers formation at redshift $z \approx 0.5 - 0.6$, appear favored by the data. These models imply a decrease of the BBH mergers beyond the peak (Fig. 8.2c), providing a direct mean to test the assumption that BBH mergers and LGRBs have progenitors with the same formation history.
Most evolutionary models of BBH mergers, however, predict a delay function following a power-law with steep index α and low $dT_{\rm min}$, with a mean delay time close to ~ 1 Gyr (e.g. Dominik et al., 2012), even if other studies suggest that a delay time of several Gyr might also be possible for BH-BH systems (Peters, 1964; Abbott et al., 2016; Broekgaarden et al., 2021). Since coalescence times of several Gyr are hardly credible, we conclude that BBH mergers and LGRBs do not have the same formation history. This conclusion needs, of course, to be confirmed with larger BBH merger samples, which will become available in a near future, with runs O4 and O5.

In Sec. 8.3, we compare the rate of BBH mergers measured by the LVC collaboration with the rate of LGRBs. Assuming again that BBH mergers and LGRBs have the same formation history, we show that BBH mergers are rarer than LGRBs: taking for example the model $\mathcal{R}_{25}$ and a standard value for the beaming factor $f_b = 250$, the normalization factor η_0 is between 2 and 4%. If the two populations share the same formation history, several percent of the LGRBs suffice to explain the measured rate of BBH mergers, and if not, this is an indication of a lack of connection between LGRBs and BBH mergers. In both cases, the large majority of the BHs born in LGRBs do not end their lives in BBH mergers. Taken together these two studies suggest that BBH mergers and LGRBs have distinct progenitors, and that LGRBs are more frequent than BBH mergers.

8.4.2 The nature of LGRB progenitors

One of the surprises of LVC detections was the dominance of BHs with a low spin. This tells us that the cores of massive stars have lost most of their angular momentum when they collapse into a BH. The core angular momentum has been transferred to the stellar envelope

which has been ejected. This is the indication of an efficient transport of angular momentum in the progenitors of BBH mergers and possibly in most massive stars (Olejak & Belczynski, 2021; Bavera et al., 2021; Fuller & Lu, 2022). If this scenario is correct, LGRBs, which require stellar cores with a large angular momentum at BH creation, cannot be emitted by single massive stars, nor by massive stars in wide binary systems. According to Kushnir et al. (2017); Piran & Piran (2020); Bavera et al. (2020); Belczynski et al. (2020); Marchant et al. (2021) the best way for a massive stellar core to keep a large angular momentum until it becomes a BH is through tidal spin-up in a compact system, which is bound to merge after some time. In this model, the population of LGRBs and BBHs (or at least a sub-sample of the latter) would therefore share common progenitors.

Bavera et al. (2021) have recently published a study using binary stellar evolution and population synthesis calculations to explain the sub-population of spinning merging BBHs and the emission of LGRBs at the BH formation. They reach the conclusion that the progenitors of fast-spinning BBH mergers, formed via isolated binary evolution, are likely a major contribution to the observed rate of luminous LGRBs.

This conclusion differs from the results obtained in this paper, as we propose different origins for BBH mergers and LGRBs. This tension can be explained as follow:

- The population of BH progenitors generated by Bavera et al. (2021) for the production of LGRBs is based on a value close to the upper limit of the local rate measured by LVC, $\rho(z_0 = 0) = 38.3\ \mathrm{Gpc}^{-3}\ \mathrm{yr}^{-1}$. We have taken the logarithmic mean of the upper- and lower- limits ($\rho(z_0 = 0.2) = 28\ \mathrm{Gpc}^{-3}\ \mathrm{yr}^{-1}$), which is smaller.
- The SHOALS survey used as a reference for the LGRBs distribution in Bavera et al. (2021) gives a local rate of observed GRBs $\sim 0.2\ \mathrm{Gpc}^{-3}\ \mathrm{yr}^{-1}$, while the ones used in this papers are larger, and closer to $1\ \mathrm{Gpc}^{-3}\ \mathrm{yr}^{-1}$.
- Bavera et al. (2021) use a beaming fraction of 0.05 (corresponding to a beaming factor of $f_\mathrm{b} = 20$ or a jet opening angle of $\theta_\mathrm{j} \sim 18°$), while we consider a larger beaming factor, by a factor $\sim 3 - 12$. Goldstein et al. (2016) show that the distribution of jet opening angles derived from the prompt emission of 638 GBM GRBs peaks at $\sim 6°$ or $f_\mathrm{b} = 180$, and Tsvetkova et al. (2017) find a median opening angle of $\theta_\mathrm{j} \sim 4°$ ($f_\mathrm{b} = 400$), based on breaks in the afterglows of 43 bright GRBs detected by KONUS. Independent measurements obtained by Lamb et al. (2021) on long GRB afterglows also seem to point towards a jet opening angle around $\sim 5°$ ($f_\mathrm{b} = 260$). As the beaming factor is directly connected to the true GRB rate, the different values taken by Bavera et al. (2021) and us explain our different results.

These three factors, which all go in the same direction, lead to a ratio of ~ 100 between the long GRB rate used by Bavera et al. (2021) and the one we use. This explains why we find that at most a small fraction of LGRBs could be associated to BBH mergers, while Bavera et al. (2021) propose to associate all long GRBs with the sub-population of BBH mergers with non-zero spin. In the rest of this discussion we consider that our LGRB models (including the beaming factor) are realistic, and we discuss our findings in this context.

If the majority of LGRBs do not end their lives in BBH mergers, they cannot be produced in compact binary systems and must be emitted by single stars (e.g. Aguilera-Dena et al.,

2020) or in binary systems that do not merge. It may be natural to associate them with systems like the X-ray Binaries (LMXBs, HMXBs) found in the galaxy, such as Cygnus X-1 (Krawczynski & Beheshtipour, 2022; Zhao et al., 2021), GRS 1915+105 (Shreeram & Ingram, 2020) or EXO 1846-031 (Draghis et al., 2020) which are rapidly spinning and could be the descendants of LGRBs (although Belczynski et al. (2021a) show that BH spins determination can be subject to systematic effects). The detection of such systems, especially HMXBs for which accretion spin-up is limited by the lifetime of the secondary star (e.g. Wong et al., 2012), requires the birth of highly spinning BHs (Qin et al., 2019; Miller-Jones et al., 2021), an expected characteristics of LGRB descendants. Nonetheless, it is also possible that LGRB descendants are partitioned in several populations, X-ray binaries being only a subset of them.

8.4.3 Short-lived LGRB descendants in the BBH merger population ?

While our analysis suggests that the majority of BBH mergers have no direct connection with LGRBs, it does not preclude the existence of a small fraction of GRB descendants, with non-zero spin and short merging times, among BBH mergers. Such systems could be produced during a phase of tidal spin-up in a compact system of two massive stars (or a BH and a massive star) as proposed by Bavera et al. (2021). We show here that the addition of a minority fraction of short-lived GRB descendants to a favored model does not change its acceptability.
For illustration we have constructed a mixed model, made of 85% of sources following model $\mathcal{R}_{25}$ and 15% of sources following the GRB distribution of Palmerio & Daigne (2021) (model $\mathcal{R}_5$). The fraction used roughly corresponds to the fraction of BBH mergers in our sample with a $\chi_{\rm eff}$ consistent with being positive. This mixed model, shown in Figure 8.7, is acceptable for the $N/N_{\rm max}$ test ($p = 0.90$). It requires the following fractions of the GRB population to explain the two components of the model: 3% for sources following the $\mathcal{R}_{25}$ distribution and 2% for sources following the Palmerio & Daigne (2021) distribution ($\mathcal{R}_5$).

The addition of a sub-population of GRB descendants with short merging times has an interesting consequence: this population becomes dominant beyond a certain redshift ($z \approx 0.7$ in Fig. 8.7). This is the consequence of the weak evolution of BBH mergers (cf. Sec. 8.2) compared with the strong evolution of GRBs. This provides a test of the existence of a fraction of direct GRB descendants with short merging times among BBH mergers. If this population exists, it may become dominant at intermediate redshifts and start to be detectable in runs O4 and O5.

Another prediction of having GRBs exploding in compact binary systems is the possibility of precessing black holes and precessing GRB jets, that may leave an imprint on the prompt emission or the afterglow of some LGRBs. This possibility has been discussed by various authors, in different contexts (Blackman et al., 1996; Fargion & Grossi, 2006; Huang & Liu, 2021).

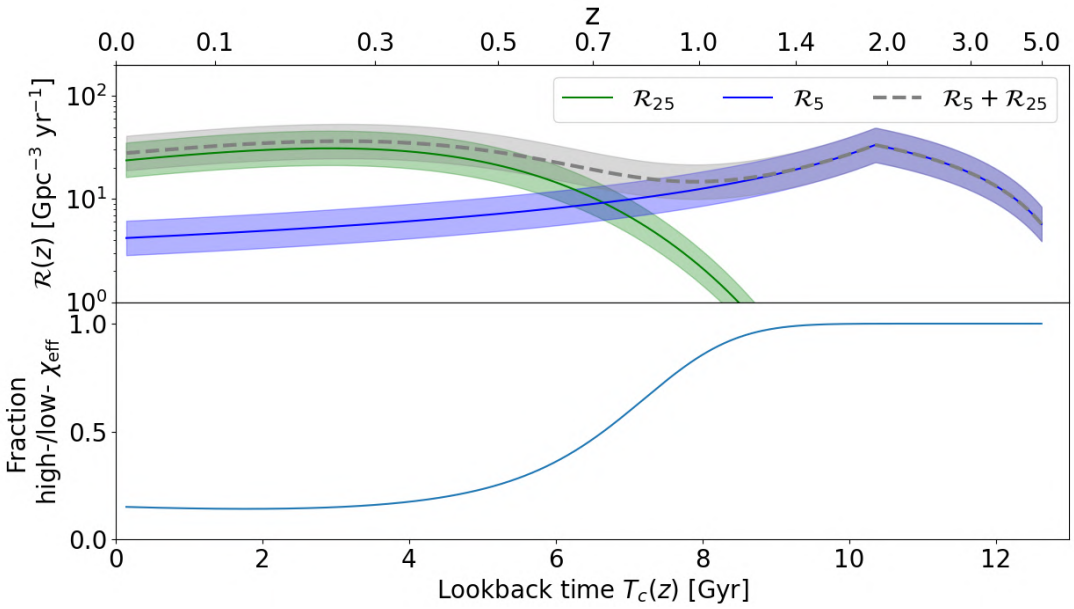

FIGURE 8.7. Illustration of the potential two-population: the rate density presented on top is composed at 85% by a high-delay (low-spin) population and 15% by a low-delay (high-spin) population, the sum of the two illustrated by the dashed grey line. The bottom panel illustrates the evolution of the high-spin fraction of BBHs mergers relatively to redshift.

8.5 Conclusion and perspectives

With the increasing number of stellar mass BH detections, population studies become effective for the comparison of their various sub-classes. Section 8.2 shows the comparison between the BBH merger population and a BH population traced by LGRBs, showing that their redshift distributions are compatible only if we consider a delay of several Gyr between the occurrence of the LGRB and the BBH merger. Section 8.3 shows that for most of the compatible models, the BBH merger progenitors rate density represents less than 10% of the LGRBs rate density. These two results are interpreted in Sec. 8.4.1 as an indication that BBH mergers and LGRBs have distinct progenitors, with the proposal that the descendants of LGRBs could resemble more BHs found in galactic X-ray binaries than those of BBH mergers (Sec. 8.4.2).

After the publication of GWTC-2, various authors have underlined the fact that BBH mergers may not be a single population (e.g. Bouffanais et al., 2021; Hütsi et al., 2021; Zevin et al., 2021), but a mix of BH populations originating from isolated stellar binaries, dynamic mergers, and possibly primordial BHs. This claim, however, has been challenged by other authors (e.g. Belczynski et al., 2021b; Broekgaarden et al., 2021). The same is true for LGRBs, which can have different "engines", a black hole or a fast rotating magnetar (e.g. Bernardini, 2015), and which encompass various sub-classes like X-ray Flashes, low-luminosity GRBs, choked GRBs, ultra-LGRBs or LGRBs with a plateau in their afterglow. Future samples of BBH mergers with better statistics will permit to sort

out these sub-populations, which are expected to have different mass, spin and redshift distributions. It will then be possible to correlate GRBs with theoretically or empirically defined BBH merger sub-classes (e.g. BBH mergers with non-zero effective spin, within a given mass range), getting more insight into the physical connections between these phenomena.

In this context, larger samples of BBH mergers and GRBs with a redshift originating from various sub-classes will permit population studies of these sub-classes, providing insight into the zoo of astrophysical BHs. Section 8.4.3 has shown for example a test for the existence of a sub-population of BBH mergers that would be descendants from LGRBs. Larger samples of BBH mergers are expected with the increasing sensitivity of GW interferometers (Abbott et al., 2018a), and larger samples of GRBs with a redshift will be provided by current and future GRB missions doing fast localizations like *Swift* (Gehrels et al., 2004b; Barthelmy et al., 2005d), *Fermi* (Meegan et al., 2009c), *INTEGRAL* (Winkler et al., 2003; Lebrun et al., 2003; Mereghetti et al., 2003), *GECAM* (Lv et al., 2018) or the coming *SVOM* (Wei et al., 2016; Godet et al., 2014; Arcier et al., 2020).

In parallel with these studies, it is essential to develop models of stellar evolution designed to follow the evolution of massive stars up to the production of BHs and their manifestations like GRBs, and BBH mergers (see for instance Bavera et al., 2021). Only with such models guiding us, we will be able to get all the knowledge that can be extracted from the diversity of BH manifestations that are being revealed by present day instruments.

Acknowledgements

The authors thank the referee for helpful comments on the evolution of binary systems of massive stars that contributed to improve this paper. The authors are grateful to N. Leroy for helpful discussions regarding the operations of the LIGO and Virgo GW detectors. This work is supported by CNES and the Paul Sabatier University. NumPy (van der Walt et al., 2011), SciPy (Virtanen et al., 2020), Matplotlib (Hunter, 2007), Astropy (Astropy Collaboration et al., 2013), LALSuite (LIGO Scientific Collaboration, 2018)

8.6 Horizon redshift calculation

Table 8.2 . BBHs mergers used in this paper from Abbott et al. (2019, 2020); The LIGO Scientific Collaboration et al. (2021b), with the original SNR and the calculated horizon redshift $z_{\rm h}$ thanks to Equation 8.3. Errors are given at the 90% confidence interval. GW events with $^{\rm O}$, ■ and ♦ are respectively from GWTC-1, GWTC-2 and GWTC-3.

Name	$m_1\,(\mathrm{M}_\odot)$	$m_2\,(\mathrm{M}_\odot)$	SNR	z	$z_{\rm h}$	$V_{\rm max}/V$
GW200316_215756♦	13.1	7.8	10.3	$0.22^{+0.08}_{-0.08}$	$0.28^{+0.10}_{-0.10}$	2.05
GW200311_115853♦	34.2	27.7	17.8	$0.23^{+0.05}_{-0.07}$	$0.53^{+0.12}_{-0.17}$	9.59
GW200302_015811♦	37.8	20.0	10.8	$0.28^{+0.16}_{-0.12}$	$0.38^{+0.22}_{-0.17}$	2.33
GW200225_060421♦	19.3	14.0	12.5	$0.22^{+0.09}_{-0.10}$	$0.35^{+0.15}_{-0.16}$	3.55
GW200224_222234♦	40.0	32.5	20.0	$0.32^{+0.08}_{-0.11}$	$0.86^{+0.24}_{-0.33}$	12.34
GW200220_124850♦	38.9	27.9	8.5	$0.66^{+0.36}_{-0.31}$	$0.71^{+0.39}_{-0.33}$	1.18
GW200219_094415♦	37.5	27.9	10.7	$0.57^{+0.22}_{-0.22}$	$0.79^{+0.32}_{-0.32}$	2.19
GW200216_220804♦	51.0	30.0	8.1	$0.63^{+0.37}_{-0.29}$	$0.64^{+0.37}_{-0.29}$	1.03
GW200210_092254♦	24.1	2.8	8.4	$0.19^{+0.08}_{-0.06}$	$0.20^{+0.08}_{-0.06}$	1.14
GW200209_085452♦	35.6	27.1	9.6	$0.57^{+0.25}_{-0.26}$	$0.70^{+0.32}_{-0.33}$	1.64
GW200208_130117♦	37.8	27.4	10.8	$0.40^{+0.15}_{-0.14}$	$0.55^{+0.21}_{-0.20}$	2.30
GW200202_154313♦	10.1	7.3	10.8	$0.09^{+0.03}_{-0.03}$	$0.12^{+0.04}_{-0.04}$	2.41
GW200129_065458♦	34.5	28.9	26.8	$0.18^{+0.05}_{-0.07}$	$0.64^{+0.20}_{-0.28}$	30.53
GW200128_022011♦	42.2	32.6	10.6	$0.56^{+0.28}_{-0.28}$	$0.76^{+0.39}_{-0.39}$	2.13
GW200112_155838♦	35.6	28.3	19.8	$0.24^{+0.07}_{-0.08}$	$0.62^{+0.20}_{-0.23}$	12.76
GW191230_180458♦	49.4	37.0	10.4	$0.69^{+0.26}_{-0.27}$	$0.92^{+0.35}_{-0.36}$	1.95
GW191222_033537♦	45.1	34.7	12.5	$0.51^{+0.23}_{-0.26}$	$0.83^{+0.39}_{-0.44}$	3.28
GW191216_213338♦	12.1	7.7	18.6	$0.07^{+0.02}_{-0.03}$	$0.16^{+0.05}_{-0.07}$	11.78
GW191215_223052♦	24.9	18.1	11.2	$0.35^{+0.13}_{-0.14}$	$0.50^{+0.19}_{-0.21}$	2.56
GW191204_171526♦	11.9	8.2	17.5	$0.13^{+0.04}_{-0.05}$	$0.29^{+0.09}_{-0.11}$	9.48
GW191204_110529♦	27.3	19.3	8.8	$0.34^{+0.25}_{-0.18}$	$0.38^{+0.28}_{-0.20}$	1.31
GW191129_134029♦	10.7	6.7	13.1	$0.16^{+0.05}_{-0.06}$	$0.26^{+0.08}_{-0.10}$	4.11
GW191127_050227♦	53.0	24.0	9.2	$0.57^{+0.40}_{-0.29}$	$0.66^{+0.47}_{-0.34}$	1.45
GW191126_115259♦	12.1	8.3	8.3	$0.30^{+0.12}_{-0.13}$	$0.31^{+0.13}_{-0.14}$	1.11
GW191109_010717♦	65.0	47.0	17.3	$0.25^{+0.18}_{-0.12}$	$0.55^{+0.39}_{-0.26}$	8.22
GW191105_143521♦	10.7	7.7	9.7	$0.23^{+0.07}_{-0.09}$	$0.28^{+0.09}_{-0.11}$	1.73
GW191103_012549♦	11.8	7.9	8.9	$0.20^{+0.09}_{-0.09}$	$0.22^{+0.10}_{-0.10}$	1.36

Table 8.3 . Continued.

Name	$m_1\,(\mathrm{M}_\odot)$	$m_2\,(\mathrm{M}_\odot)$	SNR	z	z_h	V_max/V
GW190930_133541■	12.3	7.8	9.8	$0.15^{+0.06}_{-0.06}$	$0.18^{+0.07}_{-0.07}$	1.82
GW190929_012149■	80.8	24.1	9.9	$0.38^{+0.49}_{-0.17}$	$0.47^{+0.59}_{-0.21}$	1.74
GW190926_050336■	39.8	23.2	9.0	$0.62^{+0.40}_{-0.29}$	$0.71^{+0.47}_{-0.34}$	1.37
GW190925_232845■	21.2	15.6	9.9	$0.19^{+0.07}_{-0.07}$	$0.24^{+0.09}_{-0.09}$	1.83
GW190924_021846■	8.9	5.0	13.2	$0.12^{+0.04}_{-0.04}$	$0.20^{+0.07}_{-0.07}$	4.23
GW190916_200658■	44.3	23.9	8.2	$0.71^{+0.46}_{-0.36}$	$0.73^{+0.47}_{-0.37}$	1.07
GW190915_235702■	35.3	24.4	13.1	$0.30^{+0.11}_{-0.10}$	$0.50^{+0.19}_{-0.18}$	3.96
GW190910_112807■	43.9	35.6	13.4	$0.28^{+0.16}_{-0.10}$	$0.48^{+0.29}_{-0.18}$	4.27
GW190909_114149■	45.8	28.3	9.0	$0.62^{+0.41}_{-0.33}$	$0.71^{+0.47}_{-0.38}$	1.39
GW190828_065509■	24.1	10.2	11.1	$0.30^{+0.10}_{-0.10}$	$0.42^{+0.14}_{-0.14}$	2.50
GW190828_063405■	32.1	26.2	16.0	$0.38^{+0.10}_{-0.15}$	$0.81^{+0.24}_{-0.36}$	6.76
GW190814■	23.2	2.6	22.2	$0.05^{+0.01}_{-0.01}$	$0.14^{+0.02}_{-0.03}$	19.29
GW190805_211137■	48.2	32.0	8.3	$0.82^{+0.48}_{-0.40}$	$0.85^{+0.50}_{-0.41}$	1.08
GW190803_022701■	37.3	27.3	8.6	$0.55^{+0.26}_{-0.24}$	$0.60^{+0.29}_{-0.26}$	1.22
GW190731_140936■	41.5	28.8	8.5	$0.55^{+0.31}_{-0.26}$	$0.58^{+0.33}_{-0.28}$	1.16
GW190728_064510■	12.3	8.1	13.6	$0.18^{+0.05}_{-0.07}$	$0.31^{+0.09}_{-0.12}$	4.58
GW190727_060333■	38.0	29.4	12.3	$0.55^{+0.21}_{-0.22}$	$0.89^{+0.36}_{-0.38}$	3.16
GW190725_174728■	11.5	6.4	9.1	$0.21^{+0.10}_{-0.09}$	$0.24^{+0.11}_{-0.10}$	1.43
GW190720_000836■	13.4	7.8	11.7	$0.16^{+0.12}_{-0.06}$	$0.23^{+0.18}_{-0.09}$	2.97
GW190708_232457■	17.6	13.2	13.1	$0.18^{+0.06}_{-0.07}$	$0.30^{+0.10}_{-0.12}$	4.07
GW190707_093326■	11.6	8.4	13.0	$0.16^{+0.07}_{-0.07}$	$0.26^{+0.12}_{-0.12}$	4.00
GW190706_222641■	67.0	38.2	12.3	$0.71^{+0.32}_{-0.27}$	$1.10^{+0.45}_{-0.38}$	2.70
GW190701_203306■	53.9	40.8	11.6	$0.37^{+0.11}_{-0.12}$	$0.54^{+0.16}_{-0.18}$	2.75
GW190630_185205■	35.1	23.7	15.6	$0.18^{+0.10}_{-0.07}$	$0.36^{+0.21}_{-0.15}$	6.81
GW190620_030421■	57.1	35.5	10.9	$0.49^{+0.23}_{-0.20}$	$0.68^{+0.32}_{-0.28}$	2.28
GW190602_175927■	69.1	47.8	12.1	$0.47^{+0.25}_{-0.17}$	$0.71^{+0.36}_{-0.25}$	2.86
GW190527_092055■	36.5	22.6	8.9	$0.44^{+0.34}_{-0.20}$	$0.49^{+0.39}_{-0.23}$	1.33
GW190521_074359■	42.2	32.8	24.4	$0.24^{+0.07}_{-0.10}$	$0.78^{+0.25}_{-0.36}$	22.02
GW190521■	95.3	69.0	14.4	$0.64^{+0.28}_{-0.28}$	$1.08^{+0.40}_{-0.40}$	3.36
GW190519_153544■	66.0	40.5	12.0	$0.44^{+0.25}_{-0.14}$	$0.67^{+0.37}_{-0.21}$	2.90
GW190517_055101■	37.4	25.3	10.2	$0.34^{+0.24}_{-0.14}$	$0.44^{+0.32}_{-0.19}$	2.00
GW190514_065416■	39.0	28.4	8.3	$0.67^{+0.33}_{-0.31}$	$0.70^{+0.35}_{-0.33}$	1.10
GW190513_205428■	35.7	18.0	12.3	$0.37^{+0.13}_{-0.13}$	$0.58^{+0.22}_{-0.22}$	3.25
GW190512_180714■	23.3	12.6	12.3	$0.27^{+0.09}_{-0.10}$	$0.42^{+0.14}_{-0.16}$	3.31

Table 8.4 . Continued.

Name	$m_1\,(\mathrm{M}_\odot)$	$m_2\,(\mathrm{M}_\odot)$	SNR	z	z_h	V_max/V
GW190503_185404■	43.3	28.4	12.1	$0.27^{+0.11}_{-0.11}$	$0.41^{+0.17}_{-0.17}$	3.21
GW190426_190642■	106.9	76.6	9.6	$0.70^{+0.41}_{-0.30}$	$0.82^{+0.46}_{-0.34}$	1.45
GW190424_180648■	40.5	31.8	10.1	$0.39^{+0.23}_{-0.19}$	$0.50^{+0.30}_{-0.25}$	1.91
GW190421_213856■	41.3	31.9	10.6	$0.49^{+0.19}_{-0.21}$	$0.66^{+0.27}_{-0.29}$	2.12
GW190413_134308■	47.5	31.8	9.0	$0.71^{+0.31}_{-0.30}$	$0.81^{+0.36}_{-0.34}$	1.37
GW190413_052954■	34.7	23.7	8.6	$0.59^{+0.29}_{-0.24}$	$0.63^{+0.32}_{-0.26}$	1.20
GW190412■	30.1	8.3	18.9	$0.15^{+0.03}_{-0.03}$	$0.35^{+0.07}_{-0.07}$	11.12
GW190408_181802■	24.6	18.4	14.7	$0.29^{+0.06}_{-0.10}$	$0.55^{+0.12}_{-0.20}$	5.48
GW170823$^\mathbf{O}$	39.5	29.0	11.5	$0.35^{+0.15}_{-0.15}$	$0.51^{+0.23}_{-0.23}$	2.75
GW170818$^\mathbf{O}$	35.4	26.7	11.3	$0.21^{+0.07}_{-0.07}$	$0.30^{+0.10}_{-0.10}$	2.69
GW170814$^\mathbf{O}$	30.6	25.2	15.9	$0.12^{+0.03}_{-0.04}$	$0.24^{+0.06}_{-0.08}$	7.36
GW170809$^\mathbf{O}$	35.0	23.8	12.4	$0.20^{+0.05}_{-0.07}$	$0.31^{+0.08}_{-0.11}$	3.51
GW170729$^\mathbf{O}$	50.2	34.0	10.2	$0.49^{+0.19}_{-0.21}$	$0.63^{+0.25}_{-0.28}$	1.92
GW170608$^\mathbf{O}$	11.0	7.6	14.9	$0.07^{+0.02}_{-0.02}$	$0.13^{+0.04}_{-0.04}$	6.20
GW170104$^\mathbf{O}$	30.8	20.0	13.0	$0.20^{+0.08}_{-0.08}$	$0.33^{+0.14}_{-0.14}$	4.01
GW151226$^\mathbf{O}$	13.7	7.7	13.1	$0.09^{+0.04}_{-0.04}$	$0.15^{+0.07}_{-0.07}$	4.22
GW151012$^\mathbf{O}$	23.2	13.6	10.0	$0.21^{+0.09}_{-0.09}$	$0.26^{+0.11}_{-0.11}$	1.89
GW150914$^\mathbf{O}$	35.6	30.6	24.4	$0.09^{+0.03}_{-0.03}$	$0.28^{+0.10}_{-0.10}$	25.65

Conclusion et Perspectives

Les phénomènes de sursauts gamma présentés dans le chapitre 1 sont complexes et nécessitent des observations multi-longueurs d'onde et multi-messagers pour en apprendre davantage sur leurs mécanismes et leur origine. La mission *SVOM* (Chapitre 2), qui sera lancée en 2023, vise à détecter, localiser et caractériser les émissions promptes et rémanentes des GRBs. ECLAIRs (Chapitre 3) est l'instrument clé de la mission *SVOM* : ce télescope à rayons X durs à large FoV détectera et localisera l'émission prompte du GRB, permettant ainsi le suivi avec les instruments à champ étroit de la mission *SVOM*.

Ma thèse s'est déroulée pendant l'assemblage et le test du modèle de vol de ECLAIRs. Ceci m'a amené à contribuer à la caractérisation de l'instrument, comme le montre le Chapitre 4. Tout d'abord, j'ai développé un programme pour valider le modèle de ECLAIRs utilisé par L. Bouchet pour les simulations GEANT4, en utilisant les résultats de la campagne de test du modèle de vol de ECLAIRs. Ce programme applique des effets instrumentaux (seuils SBN, résolution en énergie) sur les simulations GEANT4 et les normalise pour les rendre comparables aux données des tests réels. En utilisant les principales raies d'émission de plusieurs sources radioactives (Am-241, Ba-133, Co-57, Fe-55 ou Zn-65), j'ai montré que les simulations GEANT4 et les tests concordent bien ($\pm 10\%$), ce qui indique que le modèle de ECLAIRs utilisé par L. Bouchet est bien représentatif de la réalité.
Deuxièmement, j'ai étudié l'origine d'une raie spectrale à 20 keV non prédite par les modèles GEANT4. Avec un programme similaire à celui utilisé pour la calibration, j'ai montré que l'intensité de la raie est proportionnelle à l'intensité du continuum, ce qui suggère qu'elle provient de la fluorescence d'un élément. De plus, l'intensité de la raie est uniformément distribuée sur le plan de détection et ne dépend pas de la configuration instrumentale : l'élément responsable de son émission serait situé sous le plan de détection. Le rhodium est le candidat idéal, ayant une raie de fluorescence autour de 20 keV : les simulations GEANT4 réalisées par L. Bouchet montrent que 5% de rhodium situé dans l'ASIC des XRDPIX excité par des muons sont suffisants pour expliquer cette raie de 20 keV. La prochaine étape serait de confirmer avec le fabricant des XRDPIX qu'un tel pourcentage de rhodium à l'intérieur des matériaux est possible. Néanmoins, cette ligne n'est pas assez forte pour contribuer de manière significative au bruit de fond, de sorte que sa présence n'est pas gênante pour ECLAIRs.
Enfin, j'ai étudié le "bruit caloducs" découvert lors des campagnes de test. Corrélé à l'activité des caloducs, ce bruit pourrait être problématique pour les algorithmes de déclenchement embarqués. Pour cette raison, j'ai caractérisé ses propriétés temporelles, spectrales et spatiales. Le but de cette analyse était de mieux comprendre son origine et de développer une méthode pour atténuer son impact pour l'analyse à bord et au sol. La caractérisation du "bruit caloducs" a montré sa présence à basse énergie (inférieure à 10 keV pour les événements

SE), préférentiellement sur les coins de XRDPIX et avec des différences temporelles courtes (< 1 ms) avec les autres événements. L'étape suivante consisterait à simuler des données de fond et à les combiner avec des mesures de "bruit caloducs" pour voir comment notre méthode d'atténuation développée se comporte sur des cas plus réalistes. Cependant, des tests récents suggèrent que le "bruit caloducs" pourrait ne pas être présent en vol. Durant ces tests, le plan de détection est en configuration horizontale, alors qu'il était en configuration verticale lors de la campagne de test des modèles de vol. Cette configuration est plus représentative de l'environnement de vol des caloducs, la gravité ayant moins d'impact sur leur comportement. Il est fort probable que ce bruit ne soit pas présent en vol, ou du moins très diminué.

La simulation des performances en vol d'ECLAIRs présentée dans le chapitre 5 a représenté le cœur de ma thèse. J'ai rassemblé des simulations astrophysiques du fond attendu (Mate et al., 2019), des sources de rayons X (Dagoneau, 2020) et des GRBs (Antier-Farfar, 2016) ainsi qu'une implémentation de la réponse ECLAIRs et des effets instrumentaux pour créer des scénarios réalistes du comportement de l'instrument dans l'espace. Cependant, un effet important n'a pas encore été implémenté : l'activation due au passage de la SAA. Observée sur toutes les missions en orbite basse (par exemple Biltzinger et al., 2020), cet effet devrait augmenter le taux de comptage de fond reçu par ECLAIRs. Sa modélisation représente l'étape finale pour rendre les simulations ECLAIRs aussi réalistes que possible.
Ma thèse a également été l'occasion d'étendre les outils développés pour ECLAIRs à l'instrument GRM, en partenariat avec des laboratoires externes comme le LUPM, l'IAP ou l'IHEP. Des simulations GEANT4 du GRM ont été réalisées par A. Maiolo et L. Bouchet, tandis que j'ai adapté `pira-bkg` pour le cas du GRM. J'ai également modélisé la réponse de l'instrument GRM, en utilisant les fichiers de réponse fournis par l'IHEP. Toutes les simulations ECLAIRs et GRM ont été rassemblées dans un module Python appelé `eclgrm-simulations`, les rendant facilement accessibles à l'ensemble de la communauté *SVOM*. Ces simulations, couplées à une implémentation des algorithmes de détection embarqués, ont permis de mettre à jour les estimations de taux de GRBs de ECLAIRs (Antier-Farfar, 2016) et du GRM (Wei et al., 2016). Elles serviront également de support au choix des bandes d'énergie d'ECLAIRs pour l'algorithme de détection embarqué, à la définition des bandes d'énergie GRM/ECLAIRs pour les rapports de dureté utilisés dans le pipeline VHF ou encore à la génération d'un échantillon d'entraînement pour l'algorithme de classification des GRBs.
Ces simulations ECLAIRs ont également été couplées à des simulateurs matériels, ELSimulatorD étant utilisé pour simuler le programme FPGA ELS et le BVS pour le comportement en temps réel de l'UGTS. J'ai développé des scripts pour convertir les résultats des simulations astrophysiques au bon format, afin qu'ils puissent être lus par ELSimulatorD, dont les résultats peuvent à leur tour être utilisés par le BVS. Pris ensemble, les simulations, ELSimulatorD et le BVS reproduisent toute la chaîne de détection des ECLAIRs pour des événements générés par diverses situations. Ce travail a permis de créer des scénarios réalistes en vol (traversée de la SAA, GRB détecté, demande d'orientation pour le ToO) afin de valider le logiciel de vol de l'instrument. De plus, les sorties BVS peuvent être utilisées comme entrées pour tester le pipeline VHF et bande X. La perspective de ce travail serait d'utiliser cette méthode pour générer le scénario du Data Challenge 3.

Ces simulations réalistes ont également été utilisées comme cadre pour le développement de nouveaux algorithmes de détection. Comme expliqué dans le chapitre 3, ECLAIRs sera capables de transférer au sol tous les événements enregistrés à bord. Cela permet la création d'algorithmes de déclenchement au sol qui auront accès aux mêmes informations que les algorithmes embarqués. Pour ECLAIRs, le principal défi était de développer un algorithme robuste à la variabilité des comptages le long de l'orbite (à cause du transit terrestre) qui soit capable de détecter les transitoires de haute énergie. Pour ce faire, j'ai développé ce qui pourrait devenir un module du déclencheur au sol, une nouvelle approche basée sur l'apprentissage automatique présentée dans le chapitre 6. J'ai utilisé une architecture de réseau de neurones appelée auto-encodeur variationnel, spécialement conçue pour la détection d'anomalies dans les séries temporelles (Xu et al., 2018). Cette approche est semi-supervisée : le réseau de neurones est entraîné par des données simulées ne contenant que du bruit de fond. Cette architecture de réseau neuronal est bien adaptée au déclenchement hors ligne, car ECLAIRs observera l'émission de fond pendant la grande majorité de son temps. De plus, elle ne fait aucune hypothèse sur les propriétés de l'anomalie (les GRBs) à détecter : l'algorithme apprend par lui-même ce qui peut être considéré comme une anomalie. Cette méthode complétera les systèmes actuels de déclenchement à bord, en donnant un point de vue différent sur les données reçues par ECLAIRs. J'ai montré dans le chapitre 6 que cet algorithme a des performances comparables à l'algorithme de déclenchement embarqué. Le principal défi est maintenant d'implémenter cette méthode sur l'architecture de déclenchement au sol du Centre Scientifique Français, en proposant une version capable de traiter le flux de données réel (gestion des bons intervalles de temps, franchissement de SAA, re-pointages, sources de rayons X). Enfin, certaines informations provenant de l'autre instrument γ de *SVOM*, GRM, ou des indicateurs plus complexes tels que les paramètres d'ondelettes pourraient également être utilisés comme entrées pour cette méthode.
D'autres algorithmes pour le déclenchement hors ligne sont en cours de développement. J'ai par exemple co-supervisé un stagiaire travaillant sur une approche différente : l'utilisation de modèles ARMA (AutoRegressive-Moving-Average) sur des courbes de lumière ECLAIRs. Cette méthode utilise les orbites de fond pour entraîner le modèle ARMA et prédire ensuite le comportement de la courbe de lumière pour les orbites suivantes. Enfin, Miguel Llamas Lanza, un étudiant en doctorat de L. Bouchet, travaille sur une approche basée sur les ondelettes. Son doctorat vise également à incorporer les informations provenant du broker FINK (Möller et al., 2021) du télescope Vera Rubin. Tous ces développements sont basés sur les simulations présentées dans le chapitre 5.

J'ai également appliqué ces simulations sur une population spécifique, les évènements transitoires HE courts de l'Univers local ($z < 0.3$, Arcier et al. 2020). J'ai effectué une étude approfondie de la littérature pour caractériser les propriétés des 41 évènements transitoires HE composant l'échantillon : leur modèle spectral, la détermination du décalage vers le rouge, la rémanence et la détection de supernova/kilonova. À l'aide de ces informations, j'ai simulé ces phénomènes transitoires HE dans le champ de vision de ECLAIRs et j'ai montré que la grande majorité d'entre eux seront détectables par l'algorithme de déclenchement de comptage embarqué de ECLAIRs. Cette étude a également été l'occasion de discuter des synergies potentielles de ECLAIRs avec les autres instruments *SVOM* et d'autres observatoires. Par exemple, certains phénomènes transitoires HE locaux sont suffisamment

proches pour être détectés par les interféromètres LIGO/Virgo : l'augmentation de la sensibilité apportée par O4 et O5 va étendre l'horizon NS-BH et BH-BH à une distance où des GRBs sur l'axe pourraient être détectés. Ceci indique des synergies multi-messagers potentielles dans un futur proche avec *SVOM*. L'échantillon local contient également quelques longs GRBs sans supernovae associée : j'ai montré que, pour la majorité d'entre eux, l'absence de SN peut être expliquée par un manque ou un suivi tardif. Cependant, il y a encore quelques longs GRBs comme GRB 111005A ou GRB 060614 qui n'ont pas eu de détection de SN jusqu'à des limites strictes. Grâce à la stratégie *SVOM*, des limites supérieures seront dérivées quasi-systématiquement pour les SN associés aux longs GRBs, permettant d'ajouter plus de contraintes sur les longs GRBs sans SN, élucidant finalement leur nature (comme des collapsars ou des fusions d'étoiles à neutron). Enfin, l'article aborde également la possibilité de détecter les éruptions géantes de SGRs de l'amas de la Vierge, où le *SVOM* pointera pendant de longues périodes pour le *Programme général*, augmentant potentiellement la taille de l'échantillon de ces objets.
En utilisant la même méthodologie que celle développée dans ce travail, une étude des GRBs à haut décalage vers le rouge est actuellement réalisée par Miguel Llamas Lanza avec moi-même, O. Godet et M. Yassine. En plus des performances de ECLAIRs pour la détection d'une telle population, ce travail vise à étudier la dépendance des durées des GRBs avec le redshift pour les GRBs détectés par ECLAIRs.

Enfin, j'ai réalisé une étude indépendante qui explore les connexions possibles entre deux populations de BHs : les BHs produits pendant les longs GRBs et les fusions de trous noirs binaires observées par les émissions GW. Cette étude (Arcier & Atteia, 2022) a été motivée par la publication du dernier catalogue GW GWTC-3, contenant 79 fusions de BBHs : l'échantillon était suffisamment étendu pour effectuer une comparaison de l'évolution du redshift entre les deux populations. Nous avons montré que l'évolution du taux de densité des GRBs longs est compatible avec la distribution en redshift des fusions de BBHs seulement si un délai important est introduit entre la naissance du BBH et le moment où il fusionne. De plus, une analyse des taux attendus de tels événements suggère que le taux de densité local des fusions de BBHs est de l'ordre de 1% de celui des longs GRBs. Ces deux résultats laissent à penser que ces deux populations sont très probablement distinctes : la plupart des GRBs longs ne terminent pas leur vie dans une fusion BBH. Cette étude a également fait quelques prédictions concernant les populations de BBHs et de GRB longs que les observations futures pourraient être en mesure de vérifier ou de contredire.

En conclusion, ma thèse a fourni un ensemble complet d'outils de simulation pour ECLAIRs avec des applications concrètes telles que le test du logiciel de vol et les pipelines *SVOM*. J'ai démontré que ECLAIRs sera capable de détecter et de localiser des populations uniques de GRBs et d'autres transitoires courts de haute énergie, permettant leur caractérisation multi-longueurs d'onde et multi-messagers par *SVOM* et les observatoires astronomiques mondiaux.

Conclusion and Perspectives

The GRB phenomena introduced in Chapter 1 are complex, requiring multi-wavelength and multi-messenger observations to shed some light on their mechanisms and origin. The *SVOM* mission (chapter 2), to be launched in 2023, aims at detecting, localizing, and characterizing the GRB prompt and afterglow emissions. ECLAIRs (chapter 3) is the key instrument of *SVOM*: this wide FoV hard X-ray telescope will detect and localize the GRB prompt emission, enabling the follow-up with *SVOM* narrow field instruments.

My thesis has taken place during the assembly and testing of the ECLAIRs flight model. This led to contributing to the characterization of the instrument, as shown in Chapter 4. First of all, I developed a program to validate the ECLAIRs model used for GEANT4 simulations performed by L. Bouchet, using the results from the test campaign of ECLAIRs flight model. This program applies instrumental effects (SBN thresholds, energy resolution) on the GEANT4 simulations and normalizes them to make them comparable with real test data. Using the main emission lines of several radioactive X-ray sources (Am-241, Ba-133, Co-57, Fe-55, or Zn-65), I have shown that the GEANT4 simulations and the test agree well ($\pm 10\%$), indicating that the ECLAIRs model used by L. Bouchet is well representative of the reality.
Second, I have investigated the origin of a spectral line at 20 keV not predicted by the GEANT4 models. With a program similar to the one used for the calibration, I have shown that the line intensity scales with the continuum intensity, suggesting that it originates from the fluorescence of an element. Moreover, the line intensity is uniformly distributed on the detection plane and does not depend on the instrumental configuration: the element responsible for its emission would be located below the detection plane. The rhodium is the ideal candidate, having a fluorescence line around 20 keV: GEANT4 simulations performed by L. Bouchet show that 5% of rhodium located in the XRDPIX ASIC excited by a muon background are enough to explain this 20 keV line. The next step would be to confirm with the manufacturer that such a percentage of rhodium inside the materials is possible. Nonetheless, this line is not strong enough to significantly contribute to the background noise, so its presence is not troublesome for ECLAIRs.
Finally, I have investigated the so-called "heat-pipes noise" discovered during the test campaigns. Correlated to the activity of the heat-pipes, this noise could be problematic for the on-board trigger algorithms. For this reason, I have characterized its specific temporal, spectral, and spatial properties. This analysis aimed to understand its origin better and to develop a method to mitigate its impact for the on-board and offline analysis. The characterization of the "heatpipes noise" has shown its presence at low-energy (below 10 keV for SE events), preferentially on the corners of XRDPIX, and with short temporal time differences (< 1 ms) with other events. The next step would be to simulate background

data and combine them with "heatpipes noise" measurements to see how well our mitigation method performs in more realistic cases. However, recent tests suggest that the "heatpipes noise" might not be present in-flight. Here the detection plane is in the horizontal configuration, while it was in the vertical configuration during the flight model test campaign. This configuration is more representative of the flight environment for the heatpipes, as the gravity has less impact on their behavior. Therefore, it is highly likely that this noise will not be present during flight, or only at least significantly diminished.

The simulation of the in-flight ECLAIRs performances presented in Chapter 5 has represented the core of my thesis. I have gathered astrophysical simulations of the expected background (Mate et al., 2019), X-ray sources (Dagoneau, 2020) and GRBs (Antier-Farfar, 2016) along with an implementation of the ECLAIRs response and instrumental effects to create realistic scenarios of the instrument behavior in space. However, a significant effect has not been implemented yet: the activation due to the SAA crossing. Observed on all the low-Earth orbit missions (e.g. Biltzinger et al., 2020), this effect is expected to increase the background count rate received by ECLAIRs. Its modeling represents the final step to make ECLAIRs simulations as realistic as possible.
My thesis has also been the opportunity to extend the tools developed for ECLAIRs to the GRM instrument in partnership with external labs such as LUPM, IAP, or IHEP. GEANT4 simulations of GRM have been made by A. Maiolo and L. Bouchet, while I have adapted `pira-bkg` for the GRM case. I have also modeled the GRM instrument response using the response files provided by IHEP. All the ECLAIRs and GRM simulations have been gathered in a Python module called `eclgrm-simulations`, making them easily accessible to the whole *SVOM* community. These simulations, coupled with an implementation of the on-board trigger algorithms, offered the opportunity to update the GRB rate estimations of ECLAIRs (Antier-Farfar, 2016) and GRM (Wei et al., 2016). They will also be used as a support for the choice of the energy bands of ECLAIRs for the on-board trigger, the definition of the GRM/ECLAIRs energy bands for the hardness ratios used in the VHF pipeline, or the generation of a training sample for the crude classification algorithm.
These ECLAIRs simulations have also been coupled with hardware simulators, ELSimulatorD being used for simulating the ELS FPGA program and the BVS for the UGTS real-time behavior. Furthermore, I developed scripts to convert the astrophysical simulation results to the correct format so that they can be read by ELSimulatorD, whose results can, in turn, be used by the BVS. Taken together, the simulations, ELSimulatorD, and BVS reproduce the whole detection chain of ECLAIRs for events generated from various situations. This work has allowed to create realistic in-flight scenarios (SAA crossing, GRB detected, slew request for ToO) to validate the flight software of the instrument. Moreover, the BVS outputs can be used as inputs for testing the VHF and X-band pipeline. The perspective of this work would be to use this method for generating the scenario of the Data Challenge 3.

These realistic simulations have also been used as a framework for developing new detection algorithms. As explained in Chapter 3, ECLAIRs will be able to transfer to the ground all the events recorded on-board. This enables the creation of ground trigger algorithms that will access the same information as the on-board algorithms. For ECLAIRs, the main challenge was to develop an algorithm robust to the variability of the counts along the orbit (because of the Earth transit) that can detect the high-energy transients. To do so, I have

developed what could become a module of the offline trigger, a new approach based on machine learning presented in Chapter 6. I have used a neural-network architecture called variational auto-encoder, specially tuned for detecting anomalies in time series (Xu et al., 2018). This approach is semi-supervised: the neural network is trained by simulated data containing only background noise. This neural-network architecture is well suited for the offline trigger, as ECLAIRs will observe background emissions most of the time. Moreover, it makes no assumption on the anomaly (the GRBs) properties to be detected: the algorithm learns what can be considered an anomaly by itself. This method will complement the current on-board trigger systems, giving a different point of view on the data received from ECLAIRs. I have shown in Chapter 6 that this algorithm has performances comparable to the on-board trigger algorithm. The main challenge now is to implement this method on the ground trigger architecture at the French Science Center, by proposing a version able to deal with the real data stream (management of the good time intervals, SAA crossing, slews, X-ray sources). Finally, some information from the other *SVOM* γ instrument GRM or more complex indicators such as wavelet parameters could also be used as inputs for this method.
Other algorithms for the offline trigger are being developed. I have, for example, co-supervised an intern working on a different approach: the use of AutoRegressive-Moving-Average (ARMA) models of ECLAIRs lightcurves. This method uses background orbits to train the ARMA model and then predicts the lightcurve behavior for the next orbits. Finally, Miguel Llamas Lanza, a Ph.D. student of L. Bouchet, is working on a wavelets-based approach. His Ph.D. also aims at incorporating the information from the Vera Rubin telescope broker FINK (Möller et al., 2021). These developments are all based on the simulations presented in Chapter 5.

I have also applied the simulations of ECLAIRs to a specific population, the short HE transients from the local Universe ($z < 0.3$, Arcier et al. 2020). I have performed an extensive literature survey first to characterize the properties of the 41 HE transients composing the sample: their spectral model, redshift determination, afterglow, and supernova/kilonova detection. Using these information, I have simulated these HE transients within the ECLAIRs FoV and shown that the large majority of them will be detectable by the ECLAIRs on-board count trigger algorithm.
This study also allowed to discuss the potential synergies of ECLAIRs with the other *SVOM* instruments and other observatories. For instance, some local HE transients are, for example, close enough to be detected by the LIGO/Virgo interferometers: the increase of sensitivity brought by O4 and O5 will extend the NS-BH and the BH-BH horizon at a distance where the on-axis GRBs could be detected. This indicates some potential multi-messenger synergies in the near future with *SVOM*. The local HE transients sample also contains some long GRBs without associated supernovae: I have shown that the absence of SN can be explained by a lack or a late follow-up for most of them. However, there are still some long GRBs such as GRB 111005A or GRB 060614 that had no detection of SN up to stringent limits. Thanks to the *SVOM* strategy, upper limits will be quasi-systematically derived for SN associated with long GRBs, allowing to add more constraints on SN-less long GRBs, ultimately elucidating their nature (as collapsars or mergers). Finally, the paper also discusses the possibility of detecting SGR Giant Flares from the Virgo cluster, where

SVOM will point for extensive periods for the *General Program*, potentially increasing the sample size of such objects.
Using the same methodology as the one developed in this work, a study of high-redshift GRBs is currently made by Miguel Llamas Lanza with myself, O. Godet, and M. Yassine. In addition to the ECLAIRs' performances for detecting such a population, this study investigates the GRB durations dependency with redshift for GRBs detected by ECLAIRs.

Finally, I have done an independent study that explores the possible connections between two BH populations: the BHs produced during long GRBs and the mergers of binary black holes observed through GW emissions. This study (Arcier & Atteia, 2022) was motivated by the release of the latest GW catalog GWTC-3, containing 79 BH mergers: the sample was extensive enough to compare the redshift evolution between the two populations. We have shown that the density rate evolution of long GRBs is compatible with the BBH mergers redshift distribution only if a high delay is introduced between the birth of the BH and the moment it merges. Moreover, an analysis of the expected rates of such events suggests that the local density rate of BBH mergers is in the order of 1% of the long GRBs one. These two results suggest that these two populations are most likely distinct: most of the long GRBs do not end their lives in a BBH merger. This study also made some predictions concerning the BBH and long GRB populations that future observations might be able to verify or contradict.

In conclusion, my thesis has provided a complete set of simulation tools for ECLAIRs with concrete applications, such as testing the flight software and the SVOM pipelines. I have shown that ECLAIRs can detect and localize unique populations of GRBs and other short high-energy transients, enabling their multi-wavelength and multi-messenger characterization by SVOM and worldwide astronomical observatories.

Bibliography

Aartsen, M. G., Ackermann, M., Adams, J., et al. 2014, Phys. Rev. Lett., 113, 101101, doi: 10.1103/PhysRevLett.113.101101

—. 2015, ApJ, 805, L5, doi: 10.1088/2041-8205/805/1/L5

Abbasi, R., Abdou, Y., Abu-Zayyad, T., et al. 2011, Phys. Rev. Lett., 106, 141101, doi: 10.1103/PhysRevLett.106.141101

Abbott, B., Abbott, R., Adhikari, R., et al. 2008, ApJ, 681, 1419, doi: 10.1086/587954

Abbott, B. P., Abbott, R., Abbott, T. D., et al. 2016, Phys. Rev. Lett., 116, 061102, doi: 10.1103/PhysRevLett.116.061102

—. 2017a, ApJ, 848, L12, doi: 10.3847/2041-8213/aa91c9

—. 2017b, ApJ, 848, L12, doi: 10.3847/2041-8213/aa91c9

Abbott, B. P., Abbott, R., Abbott, T. D., et al. 2017, ApJ, 848, L13, doi: 10.3847/2041-8213/aa920c

Abbott, B. P., Abbott, R., Abbott, T. D., et al. 2017a, Nature, 551, 85, doi: 10.1038/nature24471

—. 2017b, ApJ, 848, L13, doi: 10.3847/2041-8213/aa920c

—. 2018a, Living Reviews in Relativity, 21, 3, doi: 10.1007/s41114-018-0012-9

—. 2018b, Living Reviews in Relativity, 21, 3, doi: 10.1007/s41114-018-0012-9

—. 2019, Physical Review X, 9, 031040, doi: 10.1103/PhysRevX.9.031040

Abbott, R., Abbott, T. D., Abraham, S., et al. 2020, arXiv e-prints, arXiv:2010.14527. https://arxiv.org/abs/2010.14527

—. 2021, ApJ, 913, L7, doi: 10.3847/2041-8213/abe949

Abdalla, H., Adam, R., Aharonian, F., et al. 2019, Nature, 575, 464, doi: 10.1038/s41586-019-1743-9

Abraham, J., Aglietta, M., Aguirre, I. C., et al. 2004, Nuclear Instruments and Methods in Physics Research A, 523, 50, doi: 10.1016/j.nima.2003.12.012

Abraham, S., Mukund, N., Vibhute, A., et al. 2019, arXiv e-prints, arXiv:1906.09670. https://arxiv.org/abs/1906.09670

Acernese, F., Agathos, M., Agatsuma, K., et al. 2015, Classical and Quantum Gravity, 32, 024001, doi: 10.1088/0264-9381/32/2/024001

Ackermann, M., Asano, K., Atwood, W. B., et al. 2010, ApJ, 716, 1178, doi: 10.1088/0004-637X/716/2/1178

Adrián-Martínez, S., Albert, A., Samarai, I. A., et al. 2013, A&A, 559, A9, doi: 10.1051/0004-6361/201322169

Adrián-Martínez, S., Ageron, M., Aharonian, F., et al. 2016, Journal of Physics G Nuclear Physics, 43, 084001, doi: 10.1088/0954-3899/43/8/084001

Aguilera-Dena, D. R., Langer, N., Antoniadis, J., & Müller, B. 2020, ApJ, 901, 114, doi: 10.3847/1538-4357/abb138

Ahumada, T., Singer, L. P., Anand, S., et al. 2021, Nature Astronomy, 5, 917, doi: 10.1038/s41550-021-01428-7
Ajello, M., Greiner, J., Sato, G., et al. 2008, ApJ, 689, 666, doi: 10.1086/592595
Albert, A., André, M., Anghinolfi, M., et al. 2017, ApJ, 850, L35, doi: 10.3847/2041-8213/aa9aed
Albert, A., Alfaro, R., Alvarez, C., et al. 2020, ApJ, 905, 76, doi: 10.3847/1538-4357/abc2d8
Alexander, K. D., Laskar, T., & Berger, E. 2016, GRB Coordinates Network, 20313, 1
Allison, J., Amako, K., Apostolakis, J., et al. 2016, Nuclear Instruments and Methods in Physics Research A, 835, 186, doi: 10.1016/j.nima.2016.06.125
Amati, L. 2006, MNRAS, 372, 233, doi: 10.1111/j.1365-2966.2006.10840.x
Amati, L., O'Brien, P., Götz, D., et al. 2018, Advances in Space Research, 62, 191, doi: 10.1016/j.asr.2018.03.010
Antier-Farfar, S. 2016, PhD thesis, CEA-Saclay. http://www.theses.fr/2016SACLS467
Aptekar, R. L., Frederiks, D. D., Golenetskii, S. V., et al. 1995, Space Sci. Rev., 71, 265, doi: 10.1007/BF00751332
Arcier, B. 2022, Conventions used in PIRA, Internal Report, IRAP
Arcier, B., & Atteia, J.-L. 2022, arXiv e-prints, arXiv:2204.05013. https://arxiv.org/abs/2204.05013
Arcier, B., Atteia, J. L., Godet, O., et al. 2020, Ap&SS, 365, 185, doi: 10.1007/s10509-020-03898-z
Arnason, R. M., Barmby, P., & Vulic, N. 2020, MNRAS, 492, 5075, doi: 10.1093/mnras/staa207
Arnaud, K. A. 1996, in Astronomical Society of the Pacific Conference Series, Vol. 101, Astronomical Data Analysis Software and Systems V, ed. G. H. Jacoby & J. Barnes, 17
Aso, Y., Michimura, Y., Somiya, K., et al. 2013, Phys. Rev. D, 88, 043007, doi: 10.1103/PhysRevD.88.043007
Astropy Collaboration, Robitaille, T. P., Tollerud, E. J., et al. 2013, A&A, 558, A33, doi: 10.1051/0004-6361/201322068
Atteia, J. L. 2022, GRB Coordinates Network, 31365, 1
Atteia, J. L., Dezalay, J. P., Godet, O., et al. 2018, A&A, 610, A58, doi: 10.1051/0004-6361/201731875
Atteia, J. L., Barat, C., Hurley, K., et al. 1987, ApJS, 64, 305, doi: 10.1086/191198
Atteia, J. L., Boer, M., Cotin, F., et al. 2003, in American Institute of Physics Conference Series, Vol. 662, Gamma-Ray Burst and Afterglow Astronomy 2001: A Workshop Celebrating the First Year of the HETE Mission, ed. G. R. Ricker & R. K. Vanderspek, 17–24, doi: 10.1063/1.1579292
Atteia, J. L., Heussaff, V., Dezalay, J. P., et al. 2017, ApJ, 837, 119, doi: 10.3847/1538-4357/aa5ffa
Atwood, W. B., Abdo, A. A., Ackermann, M., et al. 2009, ApJ, 697, 1071, doi: 10.1088/0004-637X/697/2/1071
Bajat, A. 2018, PhD thesis, IRAP. http://www.theses.fr/2018TOU30151
Bajat, A., Godet, O., & Atteia, J. L. 2018a, in Society of Photo-Optical Instrumentation Engineers (SPIE) Conference Series, Vol. 10699, Space Telescopes and Instrumentation 2018: Ultraviolet to Gamma Ray, ed. J.-W. A. den Herder, S. Nikzad, & K. Nakazawa,

106995J, doi: 10.1117/12.2311429
Bajat, A., Godet, O., Atteia, J. L., et al. 2018b, Experimental Astronomy, 46, 337, doi: 10.1007/s10686-018-9606-1
Baker, T., Bellini, E., Ferreira, P. G., et al. 2017, Phys. Rev. Lett., 119, 251301, doi: 10.1103/PhysRevLett.119.251301
Band, D., Matteson, J., Ford, L., et al. 1993, ApJ, 413, 281, doi: 10.1086/172995
Band, D. L., & Preece, R. D. 2005, ApJ, 627, 319, doi: 10.1086/430402
Barraud, C., Daigne, F., Mochkovitch, R., & Atteia, J.-L. 2005, A&A, 440, 809, doi: 10.1051/0004-6361:20041572
Barraud, C., Olive, J. F., Lestrade, J. P., et al. 2003, A&A, 400, 1021, doi: 10.1051/0004-6361:20030074
Barraud, C., Ricker, G., Atteia, J. L., et al. 2004, GRB Coordinates Network, 2620, 1. https://ui.adsabs.harvard.edu/abs/2004GCN..2620....1B
Barthelmy, S. D., Barbier, L. M., Cummings, J. R., et al. 2005a, Space Sci. Rev., 120, 143, doi: 10.1007/s11214-005-5096-3
Barthelmy, S. D., Cannizzo, J. K., Gehrels, N., et al. 2005b, ApJ, 635, L133, doi: 10.1086/499432
Barthelmy, S. D., Chincarini, G., Burrows, D. N., et al. 2005c, Nature, 438, 994, doi: 10.1038/nature04392
Barthelmy, S. D., Barbier, L. M., Cummings, J. R., et al. 2005d, Space Sci. Rev., 120, 143, doi: 10.1007/s11214-005-5096-3
Bartos, I., Kocsis, B., Haiman, Z., & Márka, S. 2017, ApJ, 835, 165, doi: 10.3847/1538-4357/835/2/165
Bavera, S. S., Fragos, T., Qin, Y., et al. 2020, A&A, 635, A97, doi: 10.1051/0004-6361/201936204
Bavera, S. S., Fragos, T., Zapartas, E., et al. 2021, arXiv e-prints, arXiv:2106.15841. https://arxiv.org/abs/2106.15841
Beardmore, A. P., Evans, P. A., Goad, M. R., & Osborne, J. P. 2012, GRB Coordinates Network, 13247, 1
—. 2016, GRB Coordinates Network, 20297, 1
Beardmore, A. P., Barthelmy, S. D., Marshall, F. E., et al. 2021, GRB Coordinates Network, 31316, 1
Belczynski, K., Done, C., & Lasota, J. P. 2021a, arXiv e-prints, arXiv:2111.09401. https://arxiv.org/abs/2111.09401
Belczynski, K., Holz, D. E., Bulik, T., & O'Shaughnessy, R. 2016, Nature, 534, 512, doi: 10.1038/nature18322
Belczynski, K., Perna, R., Bulik, T., et al. 2006, ApJ, 648, 1110, doi: 10.1086/505169
Belczynski, K., Klencki, J., Fields, C. E., et al. 2020, A&A, 636, A104, doi: 10.1051/0004-6361/201936528
Belczynski, K., Romagnolo, A., Olejak, A., et al. 2021b, arXiv e-prints, arXiv:2108.10885. https://arxiv.org/abs/2108.10885
Bellm, E. C., Kulkarni, S. R., Graham, M. J., et al. 2019, PASP, 131, 018002, doi: 10.1088/1538-3873/aaecbe
Beloborodov, A. M. 2017, ApJ, 838, 125, doi: 10.3847/1538-4357/aa5c8c
Beniamini, P., & Giannios, D. 2017, MNRAS, 468, 3202, doi: 10.1093/mnras/stx717

Berger, E. 2014, ARA&A, 52, 43, doi: 10.1146/annurev-astro-081913-035926
Berger, E., Berger, & E. 2006, GCN, 5952, 1
Berger, E., & Gonzalez, S. 2005, GRB Coordinates Network, 3048, 1
Berger, E., Price, P. A., Cenko, S. B., et al. 2005, Nature, 438, 988, doi: 10.1038/nature04238
Bernardini, M. G. 2015, Journal of High Energy Astrophysics, 7, 64, doi: 10.1016/j.jheap.2015.05.003
Bernardini, M. G., Xie, F., Sizun, P., et al. 2017, Experimental Astronomy, 44, 113, doi: 10.1007/s10686-017-9551-4
Bernstein, R., Dressler, A., Apai, D., et al. 2018, Giant Magellan Telescope Science Book 2018 (GMT Science Advisory Committee, GMT Project Office)
Bersier, D., Rhoads, J., Fruchter, A., et al. 2004, GRB Coordinates Network, 2544, 1
Bhalerao, V., Bhattacharya, D., Vibhute, A., et al. 2017, Journal of Astrophysics and Astronomy, 38, 31, doi: 10.1007/s12036-017-9447-8
Biltzinger, B., Kunzweiler, F., Greiner, J., Toelge, K., & Burgess, J. M. 2020, A&A, 640, A8, doi: 10.1051/0004-6361/201937347
Bissaldi, E., Briggs, M., Burns, E., et al. 2020, GRB Coordinates Network, 27587, 1. https://ui.adsabs.harvard.edu/abs/2020GCN.27587....1B
Blackman, E. G., Yi, I., & Field, G. B. 1996, ApJ, 473, L79, doi: 10.1086/310403
Bloom, J. S., Perley, D., Kocevski, D., et al. 2006a, GRB Coordinates Network, 5238, 1
Bloom, J. S., Prochaska, J. X., Pooley, D., et al. 2006b, Astrophys. J., 638, 354, doi: 10.1086/498107
Boella, G., Butler, R. C., Perola, G. C., et al. 1997a, A&AS, 122, 299, doi: 10.1051/aas:1997136
—. 1997b, A&AS, 122, 299, doi: 10.1051/aas:1997136
Boselli, A., Boissier, S., Voyer, E., et al. 2016, A&A, 585, A2, doi: 10.1051/0004-6361/201526915
Bouchet, L., & Atteia, J.-L. 2016, Offline Trigger description and justification, EIC, IRAP
Bouffanais, Y., Mapelli, M., Santoliquido, F., et al. 2021, arXiv e-prints, arXiv:2102.12495. https://arxiv.org/abs/2102.12495
Broekgaarden, F. S., Berger, E., Stevenson, S., et al. 2021, arXiv e-prints, arXiv:2112.05763. https://arxiv.org/abs/2112.05763
Bromberg, O., Nakar, E., & Piran, T. 2011, ApJ, 739, L55, doi: 10.1088/2041-8205/739/2/L55
Burns, E., Veres, P., Connaughton, V., et al. 2018, ApJ, 863, L34, doi: 10.3847/2041-8213/aad813
Burrows, D. N., Hill, J. E., Nousek, J. A., et al. 2005, Space Sci. Rev., 120, 165, doi: 10.1007/s11214-005-5097-2
Cameron, P. B., & Frail, D. A. 2005, GRB Coordinates Network, 4266, 1
Camp, J., & Transient Astrophysics Probe Team. 2018, in American Astronomical Society Meeting Abstracts, Vol. 231, American Astronomical Society Meeting Abstracts #231, 121.05
Campana, S., Mineo, T., Romano, P., Tagliaferri, G., & Burrows, D. N. 2005, GRB Coordinates Network, 4226, 1

Campana, S., Mangano, V., Blustin, A. J., et al. 2006, Nature, 442, 1008, doi: 10.1038/nature04892
Cano, Z., Bersier, D., Guidorzi, C., et al. 2011, ApJ, 740, 41, doi: 10.1088/0004-637X/740/1/41
Cano, Z., Izzo, L., de Ugarte Postigo, A., et al. 2017, A&A, 605, A107, doi: 10.1051/0004-6361/201731005
Caroli, E., Stephen, J. B., Di Cocco, G., Natalucci, L., & Spizzichino, A. 1987, Space Sci. Rev., 45, 349, doi: 10.1007/BF00171998
Cenko, B. 2022, GRB Coordinates Network, 31547, 1
Chand, V., Banerjee, A., Gupta, R., et al. 2020, arXiv e-prints, arXiv:2001.00648
Chandra, P., Nayana, A. J., Bhattacharya, D., Cenko, S. B., & Corsi, A. 2017, GRB Coordinates Network, 22264, 1
Chattopadhyay, T., Vadawale, S. V., Aarthy, E., et al. 2019, ApJ, 884, 123, doi: 10.3847/1538-4357/ab40b7
Chen, H.-Y., Holz, D. E., Miller, J., et al. 2021, Classical and Quantum Gravity, 38, 055010, doi: 10.1088/1361-6382/abd594
Chen, Y., Cui, W., Han, D., et al. 2020, in Society of Photo-Optical Instrumentation Engineers (SPIE) Conference Series, Vol. 11444, Society of Photo-Optical Instrumentation Engineers (SPIE) Conference Series, 114445B, doi: 10.1117/12.2562311
Cherenkov Telescope Array Consortium, Acharya, B. S., Agudo, I., et al. 2019, Science with the Cherenkov Telescope Array (Astrophysical Journal Supplement), doi: 10.1142/10986
CHIME/FRB Collaboration, Amiri, M., Bandura, K., et al. 2018, ApJ, 863, 48, doi: 10.3847/1538-4357/aad188
Chrimes, A. A., Stanway, E. R., & Eldridge, J. J. 2020, MNRAS, 491, 3479, doi: 10.1093/mnras/stz3246
Churazov, E., Sunyaev, R., Revnivtsev, M., et al. 2007, A&A, 467, 529, doi: 10.1051/0004-6361:20066230
Ciolfi, R. 2018, International Journal of Modern Physics D, 27, 1842004, doi: 10.1142/S021827181842004X
Cline, T. L., Desai, U. D., Teegarden, B. J., et al. 1982, ApJ, 255, L45, doi: 10.1086/183766
Collazzi, A. C., Schaefer, B. E., Goldstein, A., & Preece, R. D. 2012, ApJ, 747, 39, doi: 10.1088/0004-637X/747/1/39
Conciatore, M. L., Capalbi, M., Vetere, L., Palmer, D., & Burrows, D. 2006, GRB Coordinates Network, 5078, 1
Condon, J. J., & Matthews, A. M. 2018, PASP, 130, 073001, doi: 10.1088/1538-3873/aac1b2
Cowperthwaite, P. S., Berger, E., Villar, V. A., et al. 2017, ApJ, 848, L17, doi: 10.3847/2041-8213/aa8fc7
Crider, A. 2006, in A Magnetar Flare in the BATSE Catalog?, ed. S. S. Holt, N. Gehrels, & J. A. Nousek, Vol. 836, 64–67, doi: 10.1063/1.2207859
Cusumano, G., Moretti, A., Tagliaferri, G., Kennea, J., & Burrows, D. 2006, GRB Coordinates Network, 4781, 1
Dagoneau, N. 2020, PhD thesis, Université Paris-Saclay. http://www.theses.fr/2020UPASP040
Dagoneau, N. 2020, A&A

Dagoneau, N., Schanne, S., Atteia, J.-L., Götz, D., & Cordier, B. 2020, arXiv e-prints, arXiv:2005.12560. https://arxiv.org/abs/2005.12560
D'Ai, A., Kennea, J. A., Krimm, H. A., et al. 2016, GRB Coordinates Network, 20296, 1
Daigne, F., & Mochkovitch, R. 1998, MNRAS, 296, 275, doi: 10.1046/j.1365-8711.1998.01305.x
D'Avanzo, P., Porterfield, B., Burrows, D. N., et al. 2013, GRB Coordinates Network, 14973, 1
D'Avanzo, P., Salvaterra, R., Bernardini, M. G., et al. 2014, MNRAS, 442, 2342, doi: 10.1093/mnras/stu994
D'Avanzo, P., Campana, S., Salafia, O. S., et al. 2018, A&A, 613, L1, doi: 10.1051/0004-6361/201832664
De Luca, V., Franciolini, G., Pani, P., & Riotto, A. 2021a, J. Cosmology Astropart. Phys., 2021, 003, doi: 10.1088/1475-7516/2021/05/003
—. 2021b, J. Cosmology Astropart. Phys., 2021, 003, doi: 10.1088/1475-7516/2021/05/003
de Naurois, M. 2019, The Astronomer's Telegram, 13052, 1
de Pasquale, M., Tagliaferri, G., Blustin, A. J., et al. 2005, GRB Coordinates Network, 4233, 1
de Ugarte Postigo, A., Eguchi, S., Gorosabel, J., Yock, P., & Castro-Tirado, A. J. 2005, GRB Coordinates Network, 3041, 1
de Ugarte Postigo, A., Izzo, L., Kann, D. A., et al. 2017, The Astronomer's Telegram, 11038, 1
de Ugarte Postigo, A., Malesani, D., Levan, A. J., Hjorth, J., & Tanvir, N. R. 2008, GRB Coordinates Network, 8195, 1
de Ugarte Postigo, A., Cano, Z., Izzo, L., et al. 2016, GRB Coordinates Network, 20342, 1
DeLaunay, J., & Tohuvavohu, A. 2021, arXiv e-prints, arXiv:2111.01769. https://arxiv.org/abs/2111.01769
D'Elia, V., Breeveld, A. A., Evans, P. A., et al. 2015, GRB Coordinates Network, 18152, 1. https://ui.adsabs.harvard.edu/abs/2015GCN.18152....1D
D'Elia, V., Campana, S., D'A\'\i, A., et al. 2018, \aap, 619, A66, doi: 10.1051/0004-6361/201833847
Dezalay, J. P., Barat, C., Talon, R., et al. 1992, in American Institute of Physics Conference Series, Vol. 265, American Institute of Physics Conference Series, ed. W. S. Paciesas & G. J. Fishman, 304
Dezalay, J. P., Lestrade, J. P., Barat, C., et al. 1996, ApJ, 471, L27, doi: 10.1086/310321
di Sciascio, G., & Lhaaso Collaboration. 2016, Nuclear and Particle Physics Proceedings, 279-281, 166, doi: 10.1016/j.nuclphysbps.2016.10.024
Dichiara, S., Troja, E., O'Connor, B., et al. 2020, MNRAS, 492, 5011, doi: 10.1093/mnras/staa124
Dichiara, S., Bernardini, M. G., Burrows, D. N., et al. 2019, GRB Coordinates Network, 25552, 1
Dominik, M., Belczynski, K., Fryer, C., et al. 2012, ApJ, 759, 52, doi: 10.1088/0004-637X/759/1/52
Draghis, P. A., Miller, J. M., Cackett, E. M., et al. 2020, ApJ, 900, 78, doi: 10.3847/1538-4357/aba2ec

Duque, R., Beniamini, P., Daigne, F., & Mochkovitch, R. 2021, arXiv e-prints, arXiv:2112.02917. https://arxiv.org/abs/2112.02917
Evans, W. D., Klebesadel, R. W., Laros, J. G., et al. 1980, ApJ, 237, L7, doi: 10.1086/183222
Fan, X., Zou, G., Wei, J., et al. 2020, in Society of Photo-Optical Instrumentation Engineers (SPIE) Conference Series, Vol. 11443, Society of Photo-Optical Instrumentation Engineers (SPIE) Conference Series, 114430Q, doi: 10.1117/12.2561854
Fargion, D., & Grossi, M. 2006, Chinese Journal of Astronomy and Astrophysics Supplement, 6, 342, doi: 10.1088/1009-9271/6/S1/44
Farris, B. D., Liu, Y. T., & Shapiro, S. L. 2010, Phys. Rev. D, 81, 084008, doi: 10.1103/PhysRevD.81.084008
Fenimore, E. E., Klebesadel, R. W., & Laros, J. G. 1996, ApJ, 460, 964, doi: 10.1086/177024
Fishbach, M., & Kalogera, V. 2021, arXiv e-prints, arXiv:2111.02935. https://arxiv.org/abs/2111.02935
Fishman, G. J., Meegan, C. A., Wilson, R. B., et al. 1989, in Bulletin of the American Astronomical Society, Vol. 21, 860
Fishman, G. J., Meegan, C. A., Wilson, R. B., et al. 1994, ApJS, 92, 229, doi: 10.1086/191968
Fong, W., Alexander, K. D., & Laskar, T. 2016a, GRB Coordinates Network, 19854, 1
Fong, W., Margutti, R., Chornock, R., et al. 2016b, ApJ, 833, 151, doi: 10.3847/1538-4357/833/2/151
Fox, D. B., Frail, D. A., Price, P. A., et al. 2005, Nature, 437, 845, doi: 10.1038/nature04189
Frail, D. A. 2003, GRB Coordinates Network, 2473, 1
Frail, D. A., Waxman, E., & Kulkarni, S. R. 2000, ApJ, 537, 191, doi: 10.1086/309024
Frail, D. A., Kulkarni, S. R., Sari, R., et al. 2001, ApJ, 562, L55, doi: 10.1086/338119
Frederiks, D., Golenetskii, S., Aptekar, R., et al. 2016, GRB Coordinates Network, 20323, 1. https://ui.adsabs.harvard.edu/abs/2016GCN.20323....1F
—. 2020, GRB Coordinates Network, 27596, 1. https://ui.adsabs.harvard.edu/abs/2020GCN.27596....1F
Frederiks, D. D., Golenetskii, S. V., Palshin, V. D., et al. 2007, Astronomy Letters, 33, 1, doi: 10.1134/S106377370701001X
Fruchter, A. S., Levan, A. J., Strolger, L., et al. 2006, Nature, 441, 463, doi: 10.1038/nature04787
Fuentes-Fernández, J., Watson, A. M., Cuevas, S., et al. 2020, Journal of Astronomical Instrumentation, 9, 2050001, doi: 10.1142/S2251171720500014
Fukami, S., Berti, A., Loporchio, S., et al. 2022, in 37th International Cosmic Ray Conference. 12-23 July 2021. Berlin, 788
Fuller, J., & Lu, W. 2022, arXiv e-prints, arXiv:2201.08407. https://arxiv.org/abs/2201.08407
Fynbo, J. P. U., Perley, D. A., de Ugarte Postigo, A., et al. 2019, GCN, 26041, 1
Fynbo, J. P. U., Watson, D., Thöne, C. C., et al. 2006, Nature, 444, 1047, doi: 10.1038/nature05375
Fynbo, J. P. U., Thoene, C. C., Jensen, B. L., et al. 2006, GRB Coordinates Network, 5277, 1

Gal-Yam, A., Fox, D. B., Price, P. A., et al. 2006, Nature, 444, 1053, doi: 10.1038/nature05373
Galama, T. J., Vreeswijk, P. M., van Paradijs, J., et al. 1998, Nature, 395, 670, doi: 10.1038/27150
Galama, T. J., Wijers, R. A. M. J., Bremer, M., et al. 1998, ApJ, 500, L101, doi: 10.1086/311424
Gehrels, N., Chincarini, G., Giommi, P., et al. 2004a, ApJ, 611, 1005, doi: 10.1086/422091
—. 2004b, ApJ, 611, 1005, doi: 10.1086/422091
Gehrels, N., Sarazin, C. L., O'Brien, P. T., et al. 2005, Nature, 437, 851, doi: 10.1038/nature04142
Gehrels, N., Norris, J. P., Barthelmy, S. D., et al. 2006, Nature, 444, 1044, doi: 10.1038/nature05376
Gendre, B., Stratta, G., Atteia, J.-L., et al. 2013, ApJ, 766, 30, doi: 10.1088/0004-637X/766/1/30
Gevin, O., Baron, P., Coppolani, X., et al. 2009, IEEE Transactions on Nuclear Science, 56, 2351, doi: 10.1109/TNS.2009.2023989
Ghirlanda, G., Nava, L., & Ghisellini, G. 2010, A&A, 511, A43, doi: 10.1051/0004-6361/200913134
Godet, O. 2022, Suivi des versions des tables de configuration pour les essais sur le PFM-DPIX, Internal Report, EIC, IRAP
Godet, O., Nasser, G., Atteia, J. L., et al. 2014, in Society of Photo-Optical Instrumentation Engineers (SPIE) Conference Series, Vol. 9144, Proc. SPIE, 914424, doi: 10.1117/12.2055507
Goldstein, A., Connaughton, V., Briggs, M. S., & Burns, E. 2016, ApJ, 818, 18, doi: 10.3847/0004-637X/818/1/18
Goldstein, A., Veres, P., Burns, E., et al. 2017a, ApJ, 848, L14, doi: 10.3847/2041-8213/aa8f41
—. 2017b, ApJ, 848, L14, doi: 10.3847/2041-8213/aa8f41
Goldwurm, A., David, P., Foschini, L., et al. 2003, A&A, 411, L223, doi: 10.1051/0004-6361:20031395
Golenetskii, S., Aptekar, R., Mazets, E., et al. 2006a, GRB Coordinates Network, 5264, 1. https://ui.adsabs.harvard.edu/abs/2006GCN..5264....1G
—. 2006b, GRB Coordinates Network, 5890, 1. https://ui.adsabs.harvard.edu/abs/2006GCN..5890....1G
Golenetskii, S., Aptekar, R., Frederiks, D., et al. 2015a, GRB Coordinates Network, 17837, 1. https://ui.adsabs.harvard.edu/abs/2015GCN.17837....1G
—. 2015b, GRB Coordinates Network, 18198, 1. https://ui.adsabs.harvard.edu/abs/2015GCN.18198....1G
Gompertz, B. P., Levan, A. J., & Tanvir, N. R. 2020, ApJ, 895, 58, doi: 10.3847/1538-4357/ab8d24
Götz, D., Laurent, P., Lebrun, F., Daigne, F., & Bošnjak, Ž. 2009, ApJ, 695, L208, doi: 10.1088/0004-637X/695/2/L208
Gotz, D., Mereghetti, S., Beck, M., Borkowski, J., & Mowlavi, N. 2003, GRB Coordinates Network, 2459, 1. https://ui.adsabs.harvard.edu/abs/2003GCN..2459....1G

Götz, D., Osborne, J., Cordier, B., et al. 2014, in Society of Photo-Optical Instrumentation Engineers (SPIE) Conference Series, Vol. 9144, Proc. SPIE, 914423, doi: 10.1117/12.2054898
Graham, M. J., Kulkarni, S. R., Bellm, E. C., et al. 2019, PASP, 131, 078001, doi: 10.1088/1538-3873/ab006c
Granot, J., Ramirez-Ruiz, E., & Loeb, A. 2005, ApJ, 618, 413, doi: 10.1086/425899
Greiner, J., Peimbert, M., Esteban, C., et al. 2003, GRB Coordinates Network, 2020, 1. https://ui.adsabs.harvard.edu/abs/2003GCN..2020....1G
Greiner, J., Krühler, T., Klose, S., et al. 2011, A&A, 526, A30, doi: 10.1051/0004-6361/201015458
Guetta, D., Rahin, R., Bartos, I., & Della Valle, M. 2020, MNRAS, 492, 843, doi: 10.1093/mnras/stz3245
Guidorzi, C., & Virgili, F. 2013, GRB Coordinates Network, 15050, 1. https://ui.adsabs.harvard.edu/abs/2013GCN.15050....1G
Guillemot, P. 2022, SVOM/ECLAIRs bruit CCHP, Internal Report, CNES
Guiriec, S., Connaughton, V., Briggs, M. S., et al. 2011, ApJ, 727, L33, doi: 10.1088/2041-8205/727/2/L33
Hajdas, W., Eggel, C., Wigger, C., et al. 2004, in ESA Special Publication, Vol. 536, ESA Special Publication, 607
Hallinan, G., Corsi, A., Mooley, K. P., et al. 2017, Science, 358, 1579, doi: 10.1126/science.aap9855
Halpern, J. P., Mirabal, N., Halpern, J. P., & Mirabal, N. 2006, GCN, 5982, 1
Han, X., Xiao, Y., Zhang, P., et al. 2021, PASP, 133, 065001, doi: 10.1088/1538-3873/abfb4e
Hascoët, R., Daigne, F., & Mochkovitch, R. 2013, A&A, 551, A124, doi: 10.1051/0004-6361/201220023
He, J., Sun, J.-C., Wen, X., et al. 2020, Ap&SS, 365, 167, doi: 10.1007/s10509-020-03880-9
Heise, J., Zand, J. I., Kippen, R. M., & Woods, P. M. 2001, in X-Ray Flashes and X-Ray Rich Gamma Ray Bursts, ed. E. Costa, F. Frontera, & J. Hjorth, 16, doi: 10.1007/10853853
Heussaff, V., Atteia, J. L., & Zolnierowski, Y. 2013, A&A, 557, A100, doi: 10.1051/0004-6361/201321528
Higdon, J. C., & Lingenfelter, R. E. 1990, ARA&A, 28, 401, doi: 10.1146/annurev.aa.28.090190.002153
Hjorth, J., Sollerman, J., Møller, P., et al. 2003, Nature, 423, 847, doi: 10.1038/nature01750
Hjorth, J., Watson, D., Fynbo, J. P. U., et al. 2005, Nature, 437, 859, doi: 10.1038/nature04174
Holland, S. T., & Marshall, F. E. 2006, GRB Coordinates Network, 5898, 1
Hook, I. 2009, in Astrophysics and Space Science Proceedings, Vol. 9, Science with the VLT in the ELT Era, 225, doi: 10.1007/978-1-4020-9190-2_38
Huang, B.-Q., & Liu, T. 2021, arXiv e-prints, arXiv:2106.00826. https://arxiv.org/abs/2106.00826
Hulsman, J. 2020, in Society of Photo-Optical Instrumentation Engineers (SPIE) Conference Series, Vol. 11444, Society of Photo-Optical Instrumentation Engineers (SPIE) Conference Series, 114442V, doi: 10.1117/12.2559374

Hundman, K., Constantinou, V., Laporte, C., Colwell, I., & Soderstrom, T. 2018, arXiv e-prints, arXiv:1802.04431. https://arxiv.org/abs/1802.04431
Hunter, J. D. 2007, Computing in Science and Engineering, 9, 90, doi: 10.1109/MCSE.2007.55
Hurley, K. 2011a, Advances in Space Research, 47, 1326, doi: 10.1016/j.asr.2010.03.001
—. 2011b, Advances in Space Research, 47, 1337, doi: 10.1016/j.asr.2010.08.036
Hurley, K., Cline, T., Mazets, E., et al. 1999, Nature, 397, 41, doi: 10.1038/16199
Hurley, K., Boggs, S. E., Smith, D. M., et al. 2005, Nature, 434, 1098, doi: 10.1038/nature03519
Hurley, K., Rowlinson, A., Bellm, E., et al. 2010, MNRAS, 403, 342, doi: 10.1111/j.1365-2966.2009.16118.x
Hütsi, G., Raidal, M., Vaskonen, V., & Veermäe, H. 2021, J. Cosmology Astropart. Phys., 2021, 068, doi: 10.1088/1475-7516/2021/03/068
IceCube Collaboration. 2013, Science, 342, 1242856, doi: 10.1126/science.1242856
Inoue, S., Granot, J., O'Brien, P. T., et al. 2013, Astroparticle Physics, 43, 252, doi: 10.1016/j.astropartphys.2013.01.004
Ivezić, Ž., Kahn, S. M., Tyson, J. A., et al. 2019, ApJ, 873, 111, doi: 10.3847/1538-4357/ab042c
Izzo, L., Kann, D. A., Fynbo, J. P. U., et al. 2017, GCN, 22178, 1
Izzo, L., Rossi, A., Malesani, D. B., et al. 2018, GRB Coordinates Network, 23142, 1
Jager, R., Mels, W. A., Brinkman, A. C., et al. 1997, A&AS, 125, 557, doi: 10.1051/aas:1997243
Jenke, P. A., Linares, M., Connaughton, V., et al. 2016, ApJ, 826, 228, doi: 10.3847/0004-637X/826/2/228
Jespersen, C. K., Severin, J. B., Steinhardt, C. L., et al. 2020, ApJ, 896, L20, doi: 10.3847/2041-8213/ab964d
Jin, Z.-P., Covino, S., Liao, N.-H., et al. 2020, Nature Astronomy, 4, 77, doi: 10.1038/s41550-019-0892-y
Jin, Z.-P., Li, X., Cano, Z., et al. 2015, ApJ, 811, L22, doi: 10.1088/2041-8205/811/2/L22
Jin, Z.-P., Hotokezaka, K., Li, X., et al. 2016, Nature Communications, 7, 12898, doi: 10.1038/ncomms12898
Johnston, S., Taylor, R., Bailes, M., et al. 2008, Experimental Astronomy, 22, 151, doi: 10.1007/s10686-008-9124-7
Jonas, J. L. 2009, IEEE Proceedings, 97, 1522, doi: 10.1109/JPROC.2009.2020713
Kagra Collaboration, Akutsu, T., Ando, M., et al. 2019, Nature Astronomy, 3, 35, doi: 10.1038/s41550-018-0658-y
Kamble, A. 2015, GRB Coordinates Network, 17859, 1. https://ui.adsabs.harvard.edu/abs/2015GCN.17859....1K
Kann, D. A., Klose, S., Zhang, B., et al. 2011, ApJ, 734, 96, doi: 10.1088/0004-637X/734/2/96
Kawai, N., Kosugi, G., Aoki, K., et al. 2006, Nature, 440, 184, doi: 10.1038/nature04498
Kelson, D. D., Koviak, K., Berger, E., & Fox, D. B. 2004, GRB Coordinates Network, 2627, 1. https://ui.adsabs.harvard.edu/abs/2004GCN..2627....1K
Kennea, J. A., Sbarufatti, B., Burrows, D. N., et al. 2017, GRB Coordinates Network, 22183, 1

Kippen, R. M., Woods, P. M., Heise, J., et al. 2003, in American Institute of Physics Conference Series, Vol. 662, Gamma-Ray Burst and Afterglow Astronomy 2001: A Workshop Celebrating the First Year of the HETE Mission, ed. G. R. Ricker & R. K. Vanderspek, 244–247, doi: 10.1063/1.1579349
Klebesadel, R. W., Strong, I. B., & Olson, R. A. 1973, ApJ, 182, L85, doi: 10.1086/181225
Kocevski, D., Ryde, F., & Liang, E. 2003, ApJ, 596, 389, doi: 10.1086/377707
Kole, M., De Angelis, N., Berlato, F., et al. 2020, A&A, 644, A124, doi: 10.1051/0004-6361/202037915
Kouveliotou, C., Meegan, C. A., Fishman, G. J., et al. 1993, ApJ, 413, L101, doi: 10.1086/186969
Krause, M. 1979, Atomic Radiative and Radiationless Yields for K and L Shells, Journal of physical and chemical reference data: Reprint (American Chemical Society and the American Institute of Physics for the National Bureau of Standards). https://books.google.fr/books?id=iA8pnQEACAAJ
Krawczynski, H., & Beheshtipour, B. 2022, arXiv e-prints, arXiv:2201.07360. https://arxiv.org/abs/2201.07360
Krimm, H. A., Yamaoka, K., Sugita, S., et al. 2009, ApJ, 704, 1405, doi: 10.1088/0004-637X/704/2/1405
Kruehler, T., Wiseman, P., & Greiner, J. 2016, GRB Coordinates Network, 20299, 1
Kuin, N. P. M., & Troja, E. 2012, GRB Coordinates Network, 13248, 1
Kushnir, D., Zaldarriaga, M., Kollmeier, J. A., & Waldman, R. 2017, MNRAS, 467, 2146, doi: 10.1093/mnras/stx255
Lacombe, K., Dezalay, J. P., Houret, B., et al. 2018, Astroparticle Physics, 103, 131, doi: 10.1016/j.astropartphys.2018.08.002
Lacombe, K., Amoros, C., Atteia, J.-L., et al. 2019, Experimental Astronomy, 47, 245, doi: 10.1007/s10686-019-09626-y
Lamb, D. Q., Donaghy, T. Q., & Graziani, C. 2005, ApJ, 620, 355, doi: 10.1086/426099
Lamb, G. P., Kann, D. A., Fernández, J. J., et al. 2021, MNRAS, 506, 4163, doi: 10.1093/mnras/stab2071
Lamb, G. P., Tanvir, N. R., Levan, A. J., et al. 2019, ApJ, 883, 48, doi: 10.3847/1538-4357/ab38bb
Laporte, S. J., & Starling, R. L. C. 2018, GRB Coordinates Network, 23064, 1
Laskar, T., Berger, E., Zauderer, B. A., et al. 2013, ApJ, 776, 119, doi: 10.1088/0004-637X/776/2/119
Laxhammar, R., Falkman, G., & Sviestins, E. 2009, in 2009 12th International Conference on Information Fusion, 756–763
Le Floc'h, E., Duc, P. A., Mirabel, I. F., et al. 2003, A&A, 400, 499, doi: 10.1051/0004-6361:20030001
Lebrun, F., Leray, J. P., Lavocat, P., et al. 2003, A&A, 411, L141, doi: 10.1051/0004-6361:20031367
Leloudas, G., Fynbo, J. P. U., Schulze, S., et al. 2013, GCN, 14983, 1
Levan, A., Crowther, P., de Grijs, R., et al. 2016, Space Sci. Rev., 202, 33, doi: 10.1007/s11214-016-0312-x
Levan, A. J., Hjorth, J., Wiersema, K., et al. 2015, GCN, 17281, 1

Levan, A. J., Tanvir, N. R., Wiersema, K., & O'Brien, P. T. 2011, GRB Coordinates Network, 12414, 1
Levan, A. J., Tanvir, N. R., Jakobsson, P., et al. 2007, MNRAS, 384, 541, doi: 10.1111/j.1365-2966.2007.11953.x
Levan, A. J., Tanvir, N. R., Starling, R. L. C., et al. 2014, ApJ, 781, 13, doi: 10.1088/0004-637X/781/1/13
Levan, A. J., Wiersema, K., Tanvir, N. R., et al. 2016, GCN, 19846, 1
Lewis, A. R., Dolphin, A. E., Dalcanton, J. J., et al. 2015, ApJ, 805, 183, doi: 10.1088/0004-637X/805/2/183
Li, L., Liang, E.-W., Tang, Q.-W., et al. 2012, ApJ, 758, 27, doi: 10.1088/0004-637X/758/1/27
Li, L.-X. 2008, MNRAS, 388, 1487, doi: 10.1111/j.1365-2966.2008.13488.x
Liang, E., Zhang, B., Virgili, F., & Dai, Z. G. 2007, ApJ, 662, 1111, doi: 10.1086/517959
Liang, E. W., Zhang, B., O'Brien, P. T., et al. 2006, ApJ, 646, 351, doi: 10.1086/504684
Liao, Y., Shen, Z., Huang, Q., & Wang, Z. 2017, in Society of Photo-Optical Instrumentation Engineers (SPIE) Conference Series, Vol. 10399, Society of Photo-Optical Instrumentation Engineers (SPIE) Conference Series, ed. S. L. O'Dell & G. Pareschi, 103990L, doi: 10.1117/12.2272079
Lien, A., Sakamoto, T., Gehrels, N., et al. 2014, ApJ, 783, 24, doi: 10.1088/0004-637X/783/1/24
Lien, A., Sakamoto, T., Barthelmy, S. D., et al. 2016, ApJ, 829, 7, doi: 10.3847/0004-637X/829/1/7
LIGO Scientific Collaboration. 2018, LIGO Algorithm Library - LALSuite, free software (GPL), doi: 10.7935/GT1W-FZ16
LIGO Scientific Collaboration, Aasi, J., Abbott, B. P., et al. 2015, Classical and Quantum Gravity, 32, 074001, doi: 10.1088/0264-9381/32/7/074001
Lin, R. P., Dennis, B. R., Hurford, G. J., et al. 2002, Sol. Phys., 210, 3, doi: 10.1023/A:1022428818870
Lipunov, V., Kornilov, V., Kuvshinov, D., et al. 2005, GRB Coordinates Network, 4206, 1
Lü, H.-J., Zhang, H.-M., Zhong, S.-Q., et al. 2017, ApJ, 835, 181, doi: 10.3847/1538-4357/835/2/181
Lü, H.-J., Yuan, H.-Y., Yi, T.-F., et al. 2022, arXiv e-prints, arXiv:2201.06395. https://arxiv.org/abs/2201.06395
Lund, N., Budtz-Jørgensen, C., Westergaard, N. J., et al. 2003, A&A, 411, L231, doi: 10.1051/0004-6361:20031358
Lundman, C., Vurm, I., & Beloborodov, A. M. 2018, ApJ, 856, 145, doi: 10.3847/1538-4357/aab3e8
Lv, P., Xiong, S. L., Sun, X. L., Lv, J. G., & Li, Y. G. 2018, Journal of Instrumentation, 13, P08014, doi: 10.1088/1748-0221/13/08/P08014
Lyutikov, M., Pariev, V. I., & Blandford, R. D. 2003, ApJ, 597, 998, doi: 10.1086/378497
MacFadyen, A. I., & Woosley, S. E. 1999, ApJ, 524, 262, doi: 10.1086/307790
Macquart, J.-P., Bailes, M., Bhat, N. D. R., et al. 2010, Publ. Astron. Soc. Australia, 27, 272, doi: 10.1071/AS09082
MAGIC Collaboration, Acciari, V. A., Ansoldi, S., et al. 2019a, Nature, 575, 455, doi: 10.1038/s41586-019-1750-x

—. 2019b, Nature, 575, 459, doi: 10.1038/s41586-019-1754-6
Malanchev, K. L., Pruzhinskaya, M. V., Korolev, V. S., et al. 2021, MNRAS, 502, 5147, doi: 10.1093/mnras/stab316
Malesani, D., Levan, A. J., Tanvir, N. R., et al. 2011, GRB Coordinates Network, 12418, 1
Malesani, D., de Ugarte Postigo, A., Fynbo, J. P. U., et al. 2008, GRB Coordinates Network, 8190, 1
Malesani, D., Schulze, S., Kruehler, T., et al. 2012, GRB Coordinates Network, 13275, 1
Malesani, D. B., Izzo, L., Xu, D., et al. 2021, GRB Coordinates Network, 31324, 1
Mangano, V., Racusin, J., Morris, D., & Burrows, D. N. 2005, GRB Coordinates Network, 3885, 1
Mao, S., & Paczynski, B. 1992, ApJ, 388, L45, doi: 10.1086/186326
Marchant, P., Pappas, K. M. W., Gallegos-Garcia, M., et al. 2021, A&A, 650, A107, doi: 10.1051/0004-6361/202039992
Markwardt, C., Barbier, L., Barthelmy, S., et al. 2005, GRB Coordinates Network, 3888, 1
Marshall, F., Perri, M., Stratta, G., et al. 2006, GCN Report, 18, 1
Marshall, F. E., & D'Elia, V. 2015, GRB Coordinates Network, 18155, 1. https://ui.adsabs.harvard.edu/abs/2015GCN.18155....1M
Marshall, F. E., Markwardt, C., & Swank, J. H. 2003, GRB Coordinates Network, 2052, 1
Masetti, N., Palazzi, E., Pian, E., & Patat, F. 2006, GRB Coordinates Network, 4803, 1
Mate, S. 2021, PhD thesis. http://www.theses.fr/2021TOU30031
Mate, S., Bouchet, L., Atteia, J.-L., et al. 2019, Experimental Astronomy, 48, 171, doi: 10.1007/s10686-019-09643-x
Matheson, T., Garnavich, P. M., Stanek, K. Z., et al. 2003, ApJ, 599, 394, doi: 10.1086/379228
Matsuoka, M., Kawasaki, K., Ueno, S., et al. 2009, PASJ, 61, 999, doi: 10.1093/pasj/61.5.999
Mazaeva, E., Klunko, E., Volnova, A., Korobtsev, I., & Pozanenko, A. 2015, GRB Coordinates Network, 18205, 1
Mazets, E. P., Cline, T. L., Aptekar, R. L., et al. 2005, arXiv e-prints, astro
Mazets, E. P., Aptekar, R. L., Cline, T. L., et al. 2008, ApJ, 680, 545, doi: 10.1086/587955
McKernan, B., Ford, K. E. S., & O'Shaughnessy, R. 2020, MNRAS, 498, 4088, doi: 10.1093/mnras/staa2681
Meegan, C., Lichti, G., Bhat, P. N., et al. 2009a, ApJ, 702, 791, doi: 10.1088/0004-637X/702/1/791
—. 2009b, ApJ, 702, 791, doi: 10.1088/0004-637X/702/1/791
—. 2009c, ApJ, 702, 791, doi: 10.1088/0004-637X/702/1/791
Meegan, C. A., Fishman, G. J., Wilson, R. B., et al. 1992, Nature, 355, 143, doi: 10.1038/355143a0
Melandri, A., Pian, E., Ferrero, P., et al. 2012, A&A, 547, A82, doi: 10.1051/0004-6361/201219879
Mercier, K., Gonzalez, F., Götz, D., et al. 2018, in Society of Photo-Optical Instrumentation Engineers (SPIE) Conference Series, Vol. 10699, Space Telescopes and Instrumentation 2018: Ultraviolet to Gamma Ray, ed. J.-W. A. den Herder, S. Nikzad, & K. Nakazawa, 1069921, doi: 10.1117/12.2313561
Mereghetti, S., & Gotz, D. 2003, GRB Coordinates Network, 2460, 1

Mereghetti, S., Götz, D., Borkowski, J., Walter, R., & Pedersen, H. 2003, A&A, 411, L291, doi: 10.1051/0004-6361:20031289
Mészáros, P., & Rees, M. J. 1997, ApJ, 476, 232, doi: 10.1086/303625
Metzger, B. D., Martínez-Pinedo, G., Darbha, S., et al. 2010, MNRAS, 406, 2650, doi: 10.1111/j.1365-2966.2010.16864.x
Metzger, M. R., Djorgovski, S. G., Kulkarni, S. R., et al. 1997, Nature, 387, 878, doi: 10.1038/43132
Michałowski, M. J., Xu, D., Stevens, J., et al. 2018, A&A, 616, A169, doi: 10.1051/0004-6361/201629942
Miller-Jones, J. C. A., Bahramian, A., Orosz, J. A., et al. 2021, Science, 371, 1046, doi: 10.1126/science.abb3363
Minaev, P., & Pozanenko, A. 2020, arXiv e-prints, arXiv:2008.12752. https://arxiv.org/abs/2008.12752
Mirabal, N., Halpern, J. P., Mirabal, N., & Halpern, J. P. 2006, GCN, 4792, 1
Mirabal, N., Halpern, J. P., & O'Brien, P. T. 2007, Astrophys. J., 661, L127, doi: 10.1086/519006
Möller, A., Peloton, J., Ishida, E. E. O., et al. 2021, MNRAS, 501, 3272, doi: 10.1093/mnras/staa3602
Morawski, F., Bejger, M., Cuoco, E., & Petre, L. 2021, arXiv e-prints, arXiv:2103.07688. https://arxiv.org/abs/2103.07688
Murase, K., & Ioka, K. 2013, Phys. Rev. Lett., 111, 121102, doi: 10.1103/PhysRevLett.111.121102
Murase, K., Ioka, K., Nagataki, S., & Nakamura, T. 2008, Phys. Rev. D, 78, 023005, doi: 10.1103/PhysRevD.78.023005
Nakar, E. 2007, Phys. Rep., 442, 166, doi: 10.1016/j.physrep.2007.02.005
Narayana Bhat, P., Meegan, C. A., von Kienlin, A., et al. 2016, ApJS, 223, 28, doi: 10.3847/0067-0049/223/2/28
Nasser, G. 2015, PhD thesis, SDU2E. http://www.theses.fr/2015TOU30221
Nasser, G., Godet, O., Atteia, J. L., et al. 2014, in Society of Photo-Optical Instrumentation Engineers (SPIE) Conference Series, Vol. 9144, Space Telescopes and Instrumentation 2014: Ultraviolet to Gamma Ray, ed. T. Takahashi, J.-W. A. den Herder, & M. Bautz, 91443X, doi: 10.1117/12.2056354
Niu, B.-L., Liu, C.-Z., Li, Z.-W., Kang, Z., & Lv, Y. 2022, Research in Astronomy and Astrophysics, 22, 055009, doi: 10.1088/1674-4527/ac5afc
Norris, J. P., & Bonnell, J. T. 2006, ApJ, 643, 266, doi: 10.1086/502796
Norris, J. P., Bonnell, J. T., Kazanas, D., et al. 2005, ApJ, 627, 324, doi: 10.1086/430294
Norris, J. P., Nemiroff, R. J., Bonnell, J. T., et al. 1996, ApJ, 459, 393, doi: 10.1086/176902
Nouvel De La Flèche, A., Atteia, J.-L., & Gravrand, O. 2022, in Society of Photo-Optical Instrumentation Engineers (SPIE) Conference Series, Vol. 11444, Society of Photo-Optical Instrumentation Engineers (SPIE) Conference Series, 114445B, doi: 10.1117/12.2562311
Ofek, E. O., Cenko, S. B., Gal-Yam, A., et al. 2006, GRB Coordinates Network, 5123, 1
—. 2007, Astrophys. J., 662, 1129, doi: 10.1086/518082
Ofek, E. O., Muno, M., Quimby, R., et al. 2008, ApJ, 681, 1464, doi: 10.1086/587686
Olejak, A., & Belczynski, K. 2021, ApJ, 921, L2, doi: 10.3847/2041-8213/ac2f48

Osborne, J. P., Beardmore, A. P., Evans, P. A., & Goad, M. R. 2017, GRB Coordinates Network, 22179, 1
Pagani, C., Baumgartner, W. H., Beardmore, A. P., et al. 2008, GRB Coordinates Network, 8180, 1
Palmer, D. M., Barthelmy, S. D., Cummings, J. R., et al. 2015, GRB Coordinates Network, 18157, 1
Palmerio, J. T., & Daigne, F. 2021, A&A, 649, A166, doi: 10.1051/0004-6361/202039929
Parsons, A., Sarazin, C., Barbier, L., et al. 2005, GRB Coordinates Network, 3935, 1. https://ui.adsabs.harvard.edu/abs/2005GCN..3935....1P
Parsons, A. M., Cummings, J. R., Gehrels, N., et al. 2006, GRB Coordinates Network, 5252, 1
Parsons, A. M., Beardmore, A. P., Burrows, D. N., et al. 2008, GRB Coordinates Network, 7742, 1
Paul, J., Mandrou, P., Ballet, J., et al. 1991, Advances in Space Research, 11, 289, doi: 10.1016/0273-1177(91)90181-I
Pedregosa, F., Varoquaux, G., Gramfort, A., et al. 2011, Journal of Machine Learning Research, 12, 2825
Peebles, P. J., & Ratra, B. 2003, Reviews of Modern Physics, 75, 559, doi: 10.1103/RevModPhys.75.559
Pélangeon, A., Atteia, J. L., Nakagawa, Y. E., et al. 2008, A&A, 491, 157, doi: 10.1051/0004-6361:200809709
Perley, D. A., Bloom, J. S., Modjaz, M., et al. 2008, GRB Coordinates Network, 7889, 1
Perley, D. A., & Cockeram, A. M. 2019, GRB Coordinates Network, 25657, 1
Perley, D. A., Foley, R. J., Bloom, J. S., & Butler, N. R. 2006, GRB Coordinates Network, 5387, 1
Perley, D. A., Malesani, D. B., Levan, A. J., et al. 2019, GRB Coordinates Network, 26062, 1
Perley, D. A., Krühler, T., Schulze, S., et al. 2016, ApJ, 817, 7, doi: 10.3847/0004-637X/817/1/7
Perri, M., Evans, P. A., Osborne, J. P., et al. 2018, GRB Coordinates Network, 23049, 1
Peters, P. C. 1964, Physical Review, 136, 1224, doi: 10.1103/PhysRev.136.B1224
Peterson, B. A., & Price, P. A. 2003, GRB Coordinates Network, 1985, 1
Pian, E., Antonelli, L. A., Piro, L., & Feroci, M. 1998, GRB Coordinates Network, 158, 1
Pian, E., Amati, L., Antonelli, L. A., et al. 2000, ApJ, 536, 778, doi: 10.1086/308978
Pian, E., D'Avanzo, P., Benetti, S., et al. 2017, Nature, 551, 67, doi: 10.1038/nature24298
Pierre Auger Collaboration, Aab, A., Abreu, P., et al. 2017, Science, 357, 1266, doi: 10.1126/science.aan4338
Piran, Z., & Piran, T. 2020, ApJ, 892, 64, doi: 10.3847/1538-4357/ab792a
Piro, L., Frail, D. A., Gorosabel, J., et al. 2002, ApJ, 577, 680, doi: 10.1086/342226
Planck Collaboration, Aghanim, N., Akrami, Y., et al. 2018, arXiv e-prints, arXiv:1807.06209. https://arxiv.org/abs/1807.06209
Poole, T. S., & Troja, E. 2006, GRB Coordinates Network, 5069, 1
Portillo, S. K. N., Parejko, J. K., Vergara, J. R., & Connolly, A. J. 2020, AJ, 160, 45, doi: 10.3847/1538-3881/ab9644
Pozanenko, A., Mazaeva, E., Sergeev, A., et al. 2015, GRB Coordinates Network, 17903, 1

Predehl, P., Andritschke, R., Arefiev, V., et al. 2021, A&A, 647, A1, doi: 10.1051/0004-6361/202039313
Price, P. A., Berger, E., Fox, D. B., et al. 2006, GCN, 5275, 1
Price, P. A., Roth, K., Fox, D. W., et al. 2005, GCN, 3605, 1
Prochaska, J. X., Cooper, M., Newman, J., et al. 2005a, GRB Coordinates Network, 3390, 1
Prochaska, J. X., Bloom, J. S., Chen, H. W., et al. 2003, GCN, 2482, 1
—. 2005b, GCN, 3700, 1
Punturo, M., Abernathy, M., Acernese, F., et al. 2010, Classical and Quantum Gravity, 27, 194002, doi: 10.1088/0264-9381/27/19/194002
Qin, Y., Marchant, P., Fragos, T., Meynet, G., & Kalogera, V. 2019, ApJ, 870, L18, doi: 10.3847/2041-8213/aaf97b
Rees, M. J., & Meszaros, P. 1992, MNRAS, 258, 41, doi: 10.1093/mnras/258.1.41P
Reichart, D. 2003, GRB Coordinates Network, 2469, 1
Reitze, D., LIGO Laboratory: California Institute of Technology, LIGO Laboratory: Massachusetts Institute of Technology, LIGO Hanford Observatory, & LIGO Livingston Observatory. 2019, BAAS, 51, 141. https://arxiv.org/abs/1903.04615
Remoué, N., Barret, D., Godet, O., & Mandrou, P. 2010, Nuclear Instruments and Methods in Physics Research A, 618, 199, doi: 10.1016/j.nima.2010.02.137
Reva, I., Pozanenko, A., Krugov, M., et al. 2019, GRB Coordinates Network, 26036, 1
Rhodes, L., van der Horst, A. J., Fender, R., et al. 2020, arXiv e-prints, arXiv:2004.01538
Ricker, G. R., Atteia, J. L., Crew, G. B., et al. 2003, in American Institute of Physics Conference Series, Vol. 662, Gamma-Ray Burst and Afterglow Astronomy 2001: A Workshop Celebrating the First Year of the HETE Mission, ed. G. R. Ricker & R. K. Vanderspek, 3–16, doi: 10.1063/1.1579291
Riess, A. G., Filippenko, A. V., Challis, P., et al. 1998, AJ, 116, 1009, doi: 10.1086/300499
Romano, P., Perri, M., Beardmore, A., et al. 2005, GRB Coordinates Network, 3036, 1
Roming, P. W. A., Kennedy, T. E., Mason, K. O., et al. 2005, Space Sci. Rev., 120, 95, doi: 10.1007/s11214-005-5095-4
Rossi, A., Piranomonte, S., Savaglio, S., et al. 2014, A&A, 572, A47, doi: 10.1051/0004-6361/201423865
Rossi, A., Izzo, L., Milvang-Jensen, B., et al. 2018, GRB Coordinates Network, 23055, 1
Rowlinson, A., Wiersema, K., Levan, A. J., et al. 2010, Mon. Not. R. Astron. Soc., 408, 383, doi: 10.1111/j.1365-2966.2010.17115.x
Sakamoto, T., Lamb, D. Q., Graziani, C., et al. 2004, Astrophys. J., 602, 875, doi: 10.1086/381232
Sakamoto, T., Lamb, D. Q., Kawai, N., et al. 2005, ApJ, 629, 311, doi: 10.1086/431235
Sakamoto, T., Hullinger, D., Sato, G., et al. 2008, ApJ, 679, 570, doi: 10.1086/586884
Sakamoto, T., Serino, M., Nakahira, S., et al. 2015, GRB Coordinates Network, 17860, 1. https://ui.adsabs.harvard.edu/abs/2015GCN.17860....1S
Saleem, M., Rana, J., Gayathri, V., et al. 2022, Classical and Quantum Gravity, 39, 025004, doi: 10.1088/1361-6382/ac3b99
Salvaterra, R. 2015, Journal of High Energy Astrophysics, 7, 35, doi: 10.1016/j.jheap.2015.03.001
Salvaterra, R., Campana, S., Vergani, S. D., et al. 2012a, ApJ, 749, 68, doi: 10.1088/0004-637X/749/1/68

—. 2012b, ApJ, 749, 68, doi: 10.1088/0004-637X/749/1/68
Sanchez-Ramirez, R., Gorosabel, J., Perez-Ramirez, D., et al. 2015, GCN, 18177, 1
Santos-Lleo, M., Calderon, P., & Gotz, D. 2003, GRB Coordinates Network, 2464, 1
Sarria, D., Lebrun, F., Blelly, P.-L., et al. 2017, Geoscientific Instrumentation, Methods and Data Systems, 6, 239, doi: 10.5194/gi-6-239-2017
Savchenko, V., Ferrigno, C., Kuulkers, E., et al. 2017, ApJ, 848, L15, doi: 10.3847/2041-8213/aa8f94
Sazonov, S., Churazov, E., Sunyaev, R., & Revnivtsev, M. 2007, MNRAS, 377, 1726, doi: 10.1111/j.1365-2966.2007.11746.x
Sazonov, S. Y., Lutovinov, A. A., & Sunyaev, R. A. 2004, Nature, 430, 646, doi: 10.1038/nature02748
Sbarufatti, B., Evans, P. A., Osborne, J. P., Simpson, K. K., & Team, S.-X. 2019, GRB Coordinates Network, 26048, 1
Sbarufatti, B., Pagani, C., Beardmore, A. P., et al. 2015, GRB Coordinates Network, 17827, 1
Schanne, S., Dagoneau, N., Château, F., et al. 2019, Mem. Soc. Astron. Italiana, 90, 267. https://ui.adsabs.harvard.edu/abs/2019MmSAI..90..267S
Schmidt, M. 1968, ApJ, 151, 393, doi: 10.1086/149446
Schulze, S., Leloudas, G., Xu, D., et al. 2013, GRB Coordinates Network, 14994, 1
Schulze, S., Levan, A. J., Malesani, D., et al. 2012, GCN, 13257, 1
Senno, N., Murase, K., & Mészáros, P. 2016, Phys. Rev. D, 93, 083003, doi: 10.1103/PhysRevD.93.083003
Shahmoradi, A., & Nemiroff, R. J. 2011, MNRAS, 411, 1843, doi: 10.1111/j.1365-2966.2010.17805.x
Shirasaki, Y., Kawai, N., Yoshida, A., et al. 2003, PASJ, 55, 1033, doi: 10.1093/pasj/55.5.1033
Shreeram, S., & Ingram, A. 2020, MNRAS, 492, 405, doi: 10.1093/mnras/stz3455
Siegel, M. H., Baumgartner, W. H., Chester, M. M., et al. 2011, GRB Coordinates Network, 12720, 1
Singer, L. P., Cenko, S. B., Kasliwal, M. M., et al. 2013, ApJ, 776, L34, doi: 10.1088/2041-8205/776/2/L34
Skidmore, W., TMT International Science Development Teams, & Science Advisory Committee, T. 2015, Research in Astronomy and Astrophysics, 15, 1945, doi: 10.1088/1674-4527/15/12/001
Soderberg, A. M., & Frail, D. A. 2006, GRB Coordinates Network, 4794, 1
Soderberg, A. M., Nakar, E., Berger, E., & Kulkarni, S. R. 2006a, ApJ, 638, 930, doi: 10.1086/499121
Soderberg, A. M., Price, P. A., Fox, D. W., et al. 2002, GCN, 1554, 1
Soderberg, A. M., Kulkarni, S. R., Berger, E., et al. 2004a, Nature, 430, 648, doi: 10.1038/nature02757
—. 2004b, ApJ, 606, 994, doi: 10.1086/383082
Soderberg, A. M., Kulkarni, S. R., Fox, D. B., et al. 2005, ApJ, 627, 877, doi: 10.1086/430405
Soderberg, A. M., Kulkarni, S. R., Nakar, E., et al. 2006b, Nature, 442, 1014, doi: 10.1038/nature05087

—. 2006c, Nature, 442, 1014, doi: 10.1038/nature05087
Soffitta, P., Feroci, M., Piro, L., et al. 1998, IAU Circ., 6884, 1
Somiya, K. 2012, Classical and Quantum Gravity, 29, 124007, doi: 10.1088/0264-9381/29/12/124007
Stamatikos, M., Barthelmy, S. D., Baumgartner, W. H., et al. 2010, GRB Coordinates Network, 10496, 1
Stanbro, M., & Meegan, C. 2016, GRB Coordinates Network, 19843, 1. https://ui.adsabs.harvard.edu/abs/2016GCN.19843....1S
Stanek, K. Z., Latham, D. W., & Everett, M. E. 2003, GRB Coordinates Network, 2244, 1
Stanway, E. R., Levan, A. J., Tanvir, N., et al. 2015, MNRAS, 446, 3911, doi: 10.1093/mnras/stu2286
Starling, R. L., Wiersema, K., Levan, A. J., et al. 2011, Mon. Not. R. Astron. Soc., 411, 2792, doi: 10.1111/j.1365-2966.2010.17879.x
Stern, B. E., Tikhomirova, Y., Kompaneets, D., Svensson, R., & Poutanen, J. 2001, ApJ, 563, 80, doi: 10.1086/322295
Stratta, G., D'Avanzo, P., Piranomonte, S., et al. 2007, Astron. Astrophys., 474, 827, doi: 10.1051/0004-6361:20078006
Sunyaev, R. A., Babichenko, S. I., Goganov, D. A., Tabaldyev, S. R., & Iamburenko, N. S. 1990, Advances in Space Research, 10, 233, doi: 10.1016/0273-1177(90)90147-R
Svinkin, D., Hurley, K., Frederiks, D., et al. 2020, GRB Coordinates Network, 27585, 1. https://ui.adsabs.harvard.edu/abs/2020GCN.27585....1S
Tagliaferri, G., Malesani, D., Chincarini, G., et al. 2006, Advances in Space Research, 38, 1295, doi: 10.1016/j.asr.2005.05.040
Tagliaferri, G., Goad, M., Chincarini, G., et al. 2005, Nature, 436, 985, doi: 10.1038/nature03934
Tanaka, Y. T. 2007, in GEOTAIL observation of SGR 1900+14 giant flare on 27 August 1998, ed. W. Becker & H. H. Huang, 205
Tanaka, Y. T., Terasawa, T., Kawai, N., et al. 2007, Astrophys. J., 665, L55, doi: 10.1086/521025
Tanga, M., Krühler, T., Schady, P., et al. 2018, A&A, 615, A136, doi: 10.1051/0004-6361/201731799
Tanvir, N. R., Levan, A. J., Cucchiara, A., & Fox, D. B. 2012, GRB Coordinates Network, 13251, 1
Tanvir, N. R., Fox, D. B., Levan, A. J., et al. 2009, Nature, 461, 1254, doi: 10.1038/nature08459
Tanvir, N. R., Levan, A. J., Fruchter, A. S., et al. 2015, GRB Coordinates Network, 18100, 1. https://ui.adsabs.harvard.edu/abs/2015GCN.18100....1T
Tanvir, N. R., Kruehler, T., Wiersema, K., et al. 2016, GCN, 20321, 1
Tanvir, N. R., Levan, A. J., González-Fernández, C., et al. 2017, ApJ, 848, L27, doi: 10.3847/2041-8213/aa90b6
Tanvir, N. R., Levan, A. J., González-Fernández, C., et al. 2017, ApJ, 848, L27, doi: 10.3847/2041-8213/aa90b6
The LIGO Scientific Collaboration, The Virgo Collaboration, & The KAGRA Scientific Collaboration. 2021a, arXiv e-prints, arXiv:2111.03634. https://arxiv.org/abs/2111.03634

The LIGO Scientific Collaboration, the Virgo Collaboration, the KAGRA Collaboration, et al. 2021b, arXiv e-prints, arXiv:2111.03606. https://arxiv.org/abs/2111.03606
The LIGO Scientific Collaboration, the Virgo Collaboration, Abbott, R., et al. 2021c, arXiv e-prints, arXiv:2108.01045. https://arxiv.org/abs/2108.01045
Thoene, C. C., & de Ugarte Postigo, A. 2014, GRB Coordinates Network, 16079, 1
Thoene, C. C., Fynbo, J. P. U., Sollerman, J., et al. 2006, GCN, 5161, 1
Thompson, C. 1994, MNRAS, 270, 480, doi: 10.1093/mnras/270.3.480
Tinney, C., Stathakis, R., Cannon, R., et al. 1998, IAU Circ., 6896, 3
Tohuvavohu, A., Kennea, J. A., DeLaunay, J., et al. 2020, ApJ, 900, 35, doi: 10.3847/1538-4357/aba94f
Toma, K. 2013, arXiv e-prints, arXiv:1308.5733. https://arxiv.org/abs/1308.5733
Tominaga, N., Maeda, K., Umeda, H., et al. 2007, ApJ, 657, L77, doi: 10.1086/513193
Toy, V. L., Cenko, S. B., Silverman, J. M., et al. 2016, ApJ, 818, 79, doi: 10.3847/0004-637X/818/1/79
Troja, E., King, A. R., O'Brien, P. T., Lyons, N., & Cusumano, G. 2008, MNRAS, 385, L10, doi: 10.1111/j.1745-3933.2007.00421.x
Troja, E., Barthelmy, S. D., Boyd, P. T., et al. 2006, GRB Coordinates Network, 5055, 1
Troja, E., Piro, L., van Eerten, H., et al. 2017, Nature, 551, 71, doi: 10.1038/nature24290
Troja, E., Piro, L., Ryan, G., et al. 2018, MNRAS, 478, L18, doi: 10.1093/mnrasl/sly061
Troja, E., Ryan, G., Piro, L., et al. 2018, Nature Communications, 9, 4089, doi: 10.1038/s41467-018-06558-7
Troja, E., Castro-Tirado, A. J., González, J. B., et al. 2019, MNRAS, 489, 2104, doi: 10.1093/mnras/stz2255
Tsvetkova, A., Frederiks, D., Golenetskii, S., et al. 2017, ApJ, 850, 161, doi: 10.3847/1538-4357/aa96af
Turpin, D., Ganet, M., Antier, S., et al. 2020a, MNRAS, 497, 2641, doi: 10.1093/mnras/staa2046
Turpin, D., Wu, C., Han, X.-H., et al. 2020b, Research in Astronomy and Astrophysics, 20, 013, doi: 10.1088/1674-4527/20/1/13
Ubertini, P., Lebrun, F., Di Cocco, G., et al. 2003, A&A, 411, L131, doi: 10.1051/0004-6361:20031224
Ukwatta, T. N., Sakamoto, T., Stamatikos, M., Gehrels, N., & Dhuga, K. S. 2008, in American Institute of Physics Conference Series, Vol. 1000, American Institute of Physics Conference Series, ed. M. Galassi, D. Palmer, & E. Fenimore, 166–169, doi: 10.1063/1.2943435
Ulanov, M. V., Golenetskii, S. V., Frederiks, D. D., et al. 2005, Nuovo Cimento C Geophysics Space Physics C, 28, 351, doi: 10.1393/ncc/i2005-10058-8
Usov, V. V. 1992, Nature, 357, 472, doi: 10.1038/357472a0
Valeev, A. F., Castro-Tirado, A. J., Hu, Y. D., et al. 2019, GCN, 25565, 1
Valle, M. D., Chincarini, G., Panagia, N., et al. 2006, Nature, 444, 1050, doi: 10.1038/nature05374
van der Horst, A. J. 2013, GRB Coordinates Network, 14987, 1
van der Horst, A. J., Kamble, A., Wijers, R. A. M. J., et al. 2006, Nuovo Cimento B Serie, 121, 1605, doi: 10.1393/ncb/i2007-10327-5

van der Horst, A. J., Paragi, Z., de Bruyn, A. G., et al. 2014, Monthly Notices of the Royal Astronomical Society, 444, 3151, doi: 10.1093/mnras/stu1664
van der Walt, S., Colbert, S. C., & Varoquaux, G. 2011, Computing in Science and Engineering, 13, 22, doi: 10.1109/MCSE.2011.37
Vanderspek, R., Sakamoto, T., Barraud, C., et al. 2004, Astrophys. J., 617, 1251, doi: 10.1086/423923
Vedrenne, G., & Atteia, J.-L. 2009, Gamma-Ray Bursts (Springer Verlag Berlin Heidelberg), doi: 10.1007/978-3-540-39088-6
Vedrenne, G., Roques, J. P., Schönfelder, V., et al. 2003, A&A, 411, L63, doi: 10.1051/0004-6361:20031482
Vergani, S. D., D'Avanzo, P., Levan, A. J., et al. 2010, GRB Coordinates Network, 10512, 1
Vietri, M. 1995, ApJ, 453, 883, doi: 10.1086/176448
Villasenor, J. S., Lamb, D. Q., Ricker, G. R., et al. 2005, Nature, 437, 855, doi: 10.1038/nature04213
Virtanen, P., Gommers, R., Oliphant, T. E., et al. 2020, Nature Methods, 17, 261, doi: 10.1038/s41592-019-0686-2
Volonteri, M., Habouzit, M., & Colpi, M. 2021, Nature Reviews Physics, 3, 732, doi: 10.1038/s42254-021-00364-9
Vrba, F. J., Henden, A. A., Luginbuhl, C. B., et al. 2000, ApJ, 533, L17, doi: 10.1086/312602
Wanderman, D., & Piran, T. 2010, MNRAS, 406, 1944, doi: 10.1111/j.1365-2966.2010.16787.x
—. 2015, MNRAS, 448, 3026, doi: 10.1093/mnras/stv123
Wang, J., Dagoneau, N., Wei, J. Y., Schanne, S., & Han, X. H. 2020, GRB Coordinates Network, 27406, 1
Wang, K., & Wang, Y. 2018, in Advanced Manufacturing and Automation VII, ed. K. Wang, Y. Wang, J. O. Strandhagen, & T. Yu (Singapore: Springer Singapore), 1–9
Wang, Y., Rueda, J. A., Ruffini, R., et al. 2019, ApJ, 874, 39, doi: 10.3847/1538-4357/ab04f8
Wang, Y.-Z., Fan, Y.-Z., Tang, S.-P., Qin, Y., & Wei, D.-M. 2021, arXiv e-prints, arXiv:2110.10838. https://arxiv.org/abs/2110.10838
Watson, D., Hjorth, J., Levan, A., et al. 2004, Astrophys. J., 605, L101, doi: 10.1086/420844
Watson, D., Vaughan, S. A., Willingale, R., et al. 2006, ApJ, 636, 967, doi: 10.1086/498089
Waxman, E. 1995, Phys. Rev. Lett., 75, 386, doi: 10.1103/PhysRevLett.75.386
Wei, J., Cordier, B., Antier, S., et al. 2016, arXiv e-prints, arXiv:1610.06892. https://arxiv.org/abs/1610.06892
Wieringa, M., Soderberg, A., & Edwards, P. 2010, GRB Coordinates Network, 10533, 1
Wiersema, K., D'Avanzo, P., Levan, A. J., et al. 2010, GRB Coordinates Network, 10525, 1
Wijers, R. A. M. J., Rees, M. J., & Meszaros, P. 1997, MNRAS, 288, L51, doi: 10.1093/mnras/288.4.L51
Winkler, C., Courvoisier, T. J. L., Di Cocco, G., et al. 2003, A&A, 411, L1, doi: 10.1051/0004-6361:20031288
Wong, T.-W., Valsecchi, F., Fragos, T., & Kalogera, V. 2012, ApJ, 747, 111, doi: 10.1088/0004-637X/747/2/111

Woosley, S. E., & Bloom, J. S. 2006, ARA&A, 44, 507, doi: 10.1146/annurev.astro.43.072103.150558
Wu, B. 2021, in 43rd COSPAR Scientific Assembly. Held 28 January - 4 February, Vol. 43, 1272
Wu, C., Qiu, Y. L., & Cai, H. B. 2012, in IAU Symposium, Vol. 279, Death of Massive Stars: Supernovae and Gamma-Ray Bursts, ed. P. Roming, N. Kawai, & E. Pian, 421–422, doi: 10.1017/S1743921312013646
Xu, D., Malesani, D., de Ugarte Postigo, A., Gafton, E., & Losada, I. R. 2016, GRB Coordinates Network, 19834, 1
Xu, D., Michalowski, M., Stevens, J., & Edwards, P. 2011, GRB Coordinates Network, 12435, 1. https://ui.adsabs.harvard.edu/abs/2011GCN.12435....1X
Xu, D., Starling, R. L. C., Fynbo, J. P. U., et al. 2009, ApJ, 696, 971, doi: 10.1088/0004-637X/696/1/971
Xu, D., Levan, A. J., de Ugarte Postigo, A., et al. 2015, GCN, 17832, 1
Xu, H., Chen, W., Zhao, N., et al. 2018, arXiv e-prints, arXiv:1802.03903. https://arxiv.org/abs/1802.03903
Yamazaki, R., Ioka, K., & Nakamura, T. 2004, ApJ, 607, L103, doi: 10.1086/421872
Yamazaki, R., Yonetoku, D., & Nakamura, T. 2003, Astrophys. J., 594, L79, doi: 10.1086/378736
Yang, B., Jin, Z.-P., Li, X., et al. 2015, Nature Communications, 6, 7323, doi: 10.1038/ncomms8323
Yassine, M. 2021, SVOM/ECLAIRs response files, Internal Report, EIC, IRAP
Yi, T., Liang, E., Qin, Y., & Lu, R. 2006, MNRAS, 367, 1751, doi: 10.1111/j.1365-2966.2006.10083.x
Yonetoku, D., Murakami, T., Nakamura, T., et al. 2004, ApJ, 609, 935, doi: 10.1086/421285
Yuan, W., Zhang, C., Chen, Y., & Ling, Z. 2022, arXiv e-prints, arXiv:2209.09763, doi: 10.48550/arXiv.2209.09763
Zevin, M., Bavera, S. S., Berry, C. P. L., et al. 2021, ApJ, 910, 152, doi: 10.3847/1538-4357/abe40e
Zhang, B. 2018, The Physics of Gamma-Ray Bursts (Cambridge University Press), doi: 10.1017/9781139226530
Zhang, B., Dai, X., Lloyd-Ronning, N. M., & Mészáros, P. 2004, ApJ, 601, L119, doi: 10.1086/382132
Zhang, B., Fan, Y. Z., Dyks, J., et al. 2006, ApJ, 642, 354, doi: 10.1086/500723
Zhang, B., Zhang, B.-B., Liang, E.-W., et al. 2006, Astrophys. J., 655, L25, doi: 10.1086/511781
Zhang, H.-M., Liu, R.-Y., Zhong, S.-Q., & Wang, X.-Y. 2020a, arXiv e-prints, arXiv:2008.05097. https://arxiv.org/abs/2008.05097
Zhang, S. N., Feroci, M., Santangelo, A., et al. 2016, in Society of Photo-Optical Instrumentation Engineers (SPIE) Conference Series, Vol. 9905, Space Telescopes and Instrumentation 2016: Ultraviolet to Gamma Ray, ed. J.-W. A. den Herder, T. Takahashi, & M. Bautz, 99051Q, doi: 10.1117/12.2232034
Zhang, S.-N., Li, T., Lu, F., et al. 2020b, Science China Physics, Mechanics, and Astronomy, 63, 249502, doi: 10.1007/s11433-019-1432-6

Zhao, D., Cordier, B., Sizun, P., et al. 2012, Experimental Astronomy, 34, 705, doi: 10.1007/s10686-012-9313-2

Zhao, X., Gou, L., Dong, Y., et al. 2021, ApJ, 908, 117, doi: 10.3847/1538-4357/abbcd6

Zimmerer, D., Kohl, S. A. A., Petersen, J., Isensee, F., & Maier-Hein, K. H. 2018, arXiv e-prints, arXiv:1812.05941. https://arxiv.org/abs/1812.05941